Tidal turbine performance

in the offshore environment

Conor F. Fleming

St. Catherine's College

University of Oxford

A thesis submitted for the degree of

Doctor of Philosophy

Hilary Term 2014

Abstract

A three dimensional computational model of a full scale axial flow tidal turbine has been used to investigate the effects of a range of realistic environmental conditions on turbine performance. The model, which is based on the Reynolds averaged Navier-Stokes equations, has been developed using the commercial flow solver ANSYS Fluent.

A 1:30 scale tidal turbine is simulated in an open channel for comparison to existing experimental data. The rotor blades are directly resolved using a body-fitted, unstructured computational grid. Rotor motion is enabled through a sliding mesh interface between the rotor and the channel boundaries. Reasonably good agreement in thrust and power is observed. The computed performance curves are offset from the measured performance curves by a small increment in rotor speed.

Subsequently, a full scale axial flow turbine is modelled in a variety of conditions representative of tidal channel flows. A parametric study is carried out to investigate the effects of flow shear, confinement and alignment on turbine performance, structural loading, and wake recovery. Mean power and thrust are found to be higher in sheared flow, relative to uniform flow of equivalent volumetric flow rate. Large fluctuations in blade thrust and torque occur in sheared flow as the blade passes through the high velocity freestream flow in the upper portion of the profile and the lower velocity flow near the channel bed. A stronger shear layer is formed around the upper portion of the wake in sheared flow, leading to enhanced wake mixing.

Mean power and thrust are reduced when the turbine is simulated at a lower position in a sheared velocity profile. However, fluctuations in blade loading are increased due to the higher velocity gradient. The opposite effects are observed when the turbine operates at greater heights in sheared flow.

Flow misalignment has a negative impact on mean rotor thrust and power, as well as on unsteady blade loading. Although the range of unsteady loading is not increased significantly, additional perturbations are introduced due to interactions between the blade and the nacelle.

A deforming surface is introduced using the volume-of-fluid method. Linear wave theory is combined with the existing free surface model to develop an unsteady inflow boundary condition prescribing combined sheared flow and free surface waves. The relative

effects of the sheared profile and wave-induced velocities on turbine loading are identified through frequency analysis. Rotor and blade load fluctuations are found to increase with wave height and wave length.

In a separate study, the performance of bi-directional ducted tidal turbines is investigated through a parametric study of a range of duct profiles. A two dimensional axisymmetric computational model is developed to compare the ducted geometries with an unducted device under consistent blockage conditions. The best-performing ducted device achieves a peak power coefficient of approximately 45% of that of the unducted device. Comparisons of streamtube area, velocity and pressure for the flow through the ducted device shows that the duct limits the pressure drop across the rotor and the mass flow through the rotor, resulting in lower device power.

Acknowledgements

I would like to thank my supervisor, Prof. Richard Willden, for his guidance and support throughout this project. It has been a privilege to work with and learn from him, and I feel I have gained valuable experience for my future career. In addition, I am very grateful to my examiners, Prof. Mike Graham and Prof. Li He, for their thorough review of my work.

I would also like to thank my colleague and friend, Dr. Simon McIntosh. With his enthusiasm, optimism and generosity he set an example for the rest of our research group. Working with him has been a highlight of my PhD experience.

Thirdly, I wish to express my gratitude to my colleagues in the tidal energy research group Susannah, Justine and Chris, as well as my brother Cathal for their reviewing of this thesis. Their feedback, both technical and typographical, was invaluable.

Thank you also to my other colleagues in the tidal energy research group, for many useful discussions and encouragement, in particular Tom, Taka, Sena, William, Clarissa and Ross. Additionally, I would like to thank my friends and colleagues in the wider Civil Engineering Group.

I would like to formally acknowledge colleagues with whom I worked during the PerAWaT project: Clément Buvat at EDF, Clym Stock-Williams and Kester Gunn at E.ON, Dr. Tim Stallard and Dr. Tong Feng at the University of Manchester, Dr. Gareth Gretton at the University of Edinburgh, and Steven Parkinson, Mat Thomson and Rob Rawlinson-Smith at DNV GL.

Many of the simulations reported in this thesis were run on high-performance computing clusters managed by Advanced Research Computing at the University of Oxford, and I would like to acknowledge the help of their staff.

I am grateful to Prof. Chris Martin for giving me the opportunity to teach at Mansfield College during my PhD. I thoroughly enjoyed this experience, and have benefited greatly from it.

Thank you to my good friends, Gearóid, Brendan and Colin, for their company, friendship and support over the last few years.

Finally, I would like to thank my parents Seán and Phil, my brothers Enda, Cathal and Kieran, and my girlfriend Liz.

Contents

Nomenclature

Symbol	Unit	Definition
A	m^2	Area
a	-	Axial induction factor, or
	m	Wave amplitude
a'	-	Tangential induction factor
B	-	Blockage ratio
c	m	Blade chord length
c_f	-	Coefficient of friction
C_M	-	Moment coefficient
C_P	-	Power coefficient
c_p	-	Pressure coefficient
C_T	-	Thrust coefficient
D	m	Diameter, or
	N	Drag force
F	N	Force
f	Hz	Frequency
Fr	-	Froude number
g	$m\,s^{-2}$	Acceleration due to gravity
h	m	Water depth, or
	m	Computational grid spacing
H	m	Wave height

Symbol	Unit	Definition
K	-	Momentum loss coefficient
k	$\mathrm{J\,kg^{-1}}$	Turbulence kinetic energy, or
	$\mathrm{m^{-1}}$	Wave number, or
	-	Disc porosity
L	N	Lift force, or
	m	Duct length
l	m	Turbulence length scale
λ_w	m	Wave length
M	$\mathrm{kg\,m\,s^{-1}}$	Momentum, or
	$\mathrm{N\,m}$	Bending moment
p	Pa	Static pressure, or
	-	Order of convergence of numerical scheme
P	W	Power
Q	$\mathrm{N\,m}$	Torque, or
	$\mathrm{s^{-1}}$	Q-criterion, or
	$\mathrm{m^3\,s^{-1}}$	Volumetric flow rate
q	$\mathrm{N\,m^{-1}}$	Distributed force
r	m	Radial coordinate, or
	-	Grid refinement ratio
R	m	Rotor radius
Re	-	Reynolds number
s	m	Turbine spacing, or
	m	channel width
T	N	Thrust
t	s	Time
T	s	Rotor period
TI	%	Turbulence intensity

Symbol	Unit	Definition
u, v, w	$\mathrm{m\,s^{-1}}$	Cartesian components of velocity
u^+	-	Dimensionless velocity
u_τ	$\mathrm{m\,s^{-1}}$	Friction velocity
U	$\mathrm{m\,s^{-1}}$	Velocity relative to the blade
V	N	Shear force on beam
x, y, z	m	Cartesian coordinates
y^+	-	Dimensionless wall distance
α	$^\circ$	Angle of attack
α_w	rad	Wave phase
β	$^\circ$	Duct internal angle
γ	-	Fluid phase
Γ	$\mathrm{m^2\,s^{-1}}$	Diffusion coefficient
δ	m	Displacement thickness
ε	$\mathrm{J\,kg^{-1}\,s^{-1}}$	Turbulence dissipation rate
ζ	m	Free surface position
η	-	Normalised depth, or
	-	Hydrodynamic efficiency
θ	$^\circ$	Azimuthal coordinate
κ	-	Von Kármán constant
λ	-	Tip speed ratio
μ	Pa s	Dynamic viscosity
μ_t	Pa s	Eddy viscosity
ν	$\mathrm{m^2\,s^{-1}}$	Kinematic viscosity
ρ	$\mathrm{kg\,m^{-3}}$	Density
σ	$\mathrm{rad\,s^{-1}}$	Intrinsic wave frequency
τ_w	Pa	Wall shear

Symbol	Unit	Definition
ϕ	$^\circ$	Yaw angle, or
	-	Generic scalar
ω	$\mathrm{rad\,s^{-1}}$	Blade angular velocity, or
	$\mathrm{s^{-1}}$	Turbulence specific dissipation rate, or
	$\mathrm{rad\,s^{-1}}$	observed wave frequency
Ω	$\mathrm{rad\,s^{-1}}$	Wake angular velocity

Chapter 1

Introduction

1.1 The case for tidal energy

There has been renewed focus on renewable and sustainable sources of energy in recent years, driven by a number of issues. The first issue is the steady increase in mean atmospheric temperatures since the industrial revolution in the 18th century. This temperature rise is attributed to the Greenhouse Effect, where solar radiation reflected away from the surface of the earth is partially absorbed in the atmosphere and re-radiated back towards the earth (Solomon et al., 2007). The effect is exacerbated by the presence of so-called greenhouse gases, such as carbon dioxide and methane, in the atmosphere. The concentration of atmospheric carbon dioxide has been measured continuously by the US National Oceanic and Atmospheric Administration at Mauna Loa Observatory in Hawaii since 1958 (NOAA, 2014). Since then, values have increased from circa 310 parts per million (ppm) to current values of 400 ppm, as shown in figure 1.1 (a). Ancient records indicate that this value has never previously exceeded 300 ppm (Petit et al., 1999). The correlation between the concentration of atmospheric carbon dioxide and global temperature rise is indicated in figure 1.1 (b) (Hansen et al., 2006; NASA, 2014), where 'temperature anomaly' indicates the deviation of global annual mean surface temperature from reference values in the period 1951-1980. In order to mitigate the negative impacts of climate change,

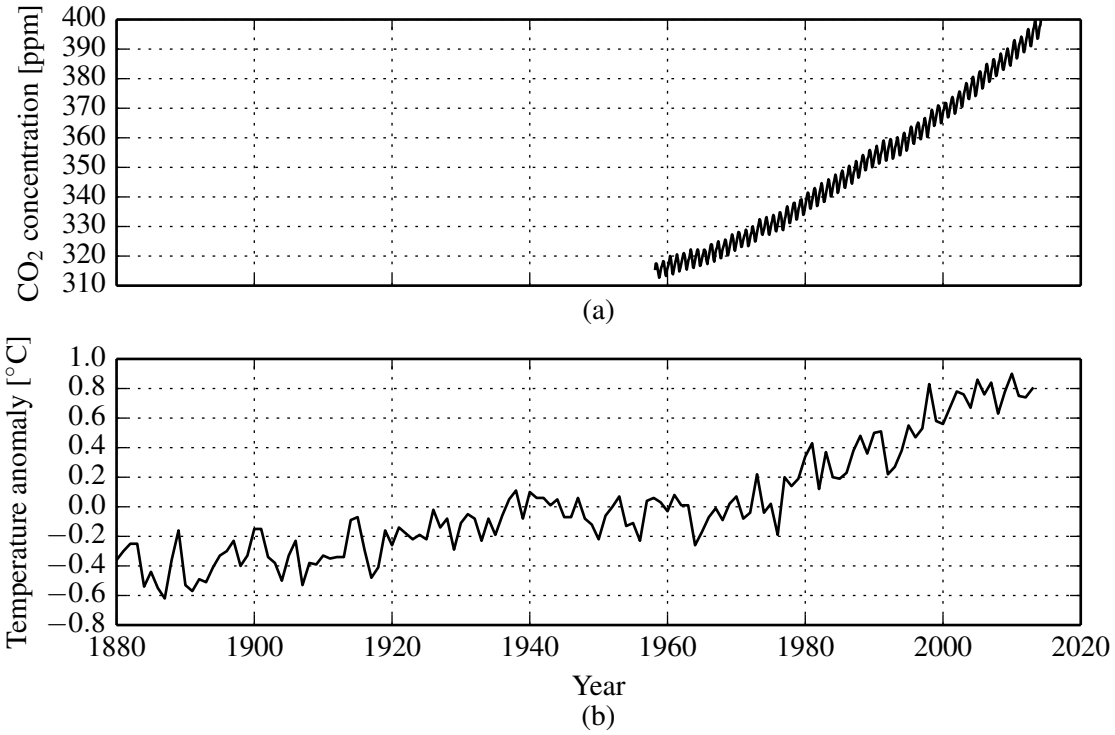

Figure 1.1: (a) History of monthly mean atmospheric carbon dioxide concentration at Mauna Loa Observatory for the period 1958 - 2014 (NOAA, 2014), and (b) global annual mean surface temperature anomalies for the period 1880 - 2014 (NASA, 2014).

the Intergovernmental Panel on Climate Change (IPCC) has recommended that efforts to reduce greenhouse gas emissions be made across all industrial sectors (i.e. energy, transport, agriculture) and all regions (IPCC, 2014). Our current reliance on fossil fuels as an energy source can be reduced through the development and adoption of renewable sources such as tidal energy.

A second issue driving the development of renewable sources of energy is the depletion of existing fossil fuel reserves. While a range of projections for future fossil fuel production and consumption exist (e.g. the annual report by EIA (2014)), it is generally accepted that these resources are finite and must ultimately be replaced. MacKay (2009) evaluates the potential of a variety of sustainable energy resources for the UK, including wind, solar, biomass and tidal, and concludes that a combination of such resources would be necessary to produce sufficient energy in the absence of fossil fuels. The UK has a relatively rich tidal resource, estimated at 20.6 TWh per year, or 5–6% of its annual electricity demand (Carbon

Trust, 2011). A detailed study of the available resource in the Pentland Firth by Adcock et al. (2013) explores a selection of energy extraction scenarios within practical constraints, and calculates mean available power of 1.9 GW for the best performing case. If the resource at the Pentland Firth and at other high energy tidal sites around the UK is harnessed, tidal energy can make a meaningful contribution to the country's energy supply, and reduce dependence on non-renewable resources.

1.2 Technical challenges in tidal energy research

There are three main challenges relating to the development of tidal energy. Firstly, the available resource must be calculated. This requires consideration of basin scale tidal dynamics, and how energy extraction at one site may affect the available energy at other sites within the same tidal system. Secondly, the optimal arrangement of tidal turbines at a particular site must be determined. This involves the analysis of the effects of device spacing and thrust on the performance of the array as a whole. The third challenge concerns the design and analysis of individual tidal energy converters, which is the focus of this thesis.

A brief overview of previous research at each of these scales is now given. In subsequent sections, the particular methods used and topics examined in this thesis are discussed in detail.

1.2.1 Basin scale

In order to estimate the available energy at a tidal site with reasonable confidence, the effect of energy extraction on the tidal dynamics must be examined. Many analytical models have been developed to find general limits to power extraction based on bed resistance (Garrett and Cummins, 2005), tidal forcing (Garrett and Cummins, 2005; Vennell, 2010, 2011), flow confinement (Garrett and Cummins, 2007; Houlsby et al., 2008) and free surface deformation (Houlsby et al., 2008; Whelan et al., 2009). Energy extraction from multi-

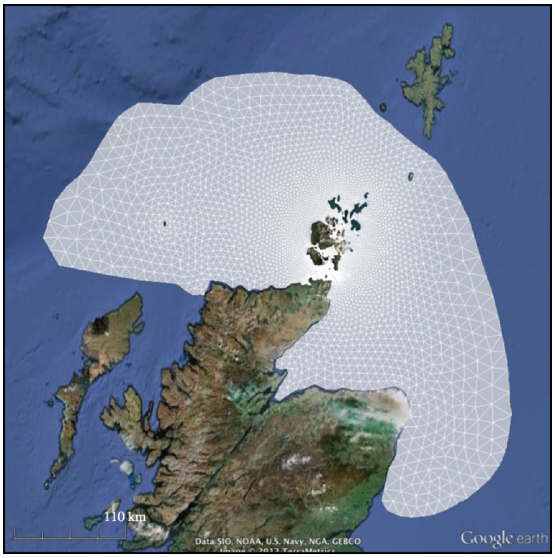

(a) Full domain

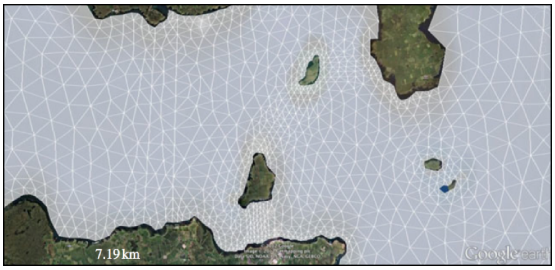

(b) Close-up view of region where energy extraction is modelled

Figure 1.2: Figures from the paper by Adcock et al. (2013), showing the computational grid used in their model of the Pentland Firth. Permission to reproduce this figure has been granted by The Royal Society.

channel systems has been modelled by Atwater and Lawrence (2010), Cummins (2013) and Draper et al. (2014).

While these models are very important for obtaining general limits to power extraction and understanding fundamental interactions between tidal farms and tidal channels, real tidal sites are usually modelled numerically. Specific details for a tidal site, such as coastline geometry, bathymetry, tidal forcing and turbine location can be prescribed, and the flow field can be computed through numerical solution of the equations governing shallow water flows. Energy extraction can be modelled by increasing bed friction in the region of the tidal farm (Bryden et al., 2007; Divett et al., 2013). Draper et al. (2010) present an improved method of representing energy extraction based on an analytical model of power extraction (Houlsby et al., 2008), and which has subsequently been adopted by other authors. (Adcock et al., 2013) use this turbine representation in a shallow water solver to model a range of power extraction scenarios in the Pentland Firth, Scotland (see figure 1.2), and Serhadlıoğlu et al. (2013) use the same model to model power extraction at the Anglesey Skerries, Wales.

Limited experimental studies have been carried out for energy extraction at basin scale;

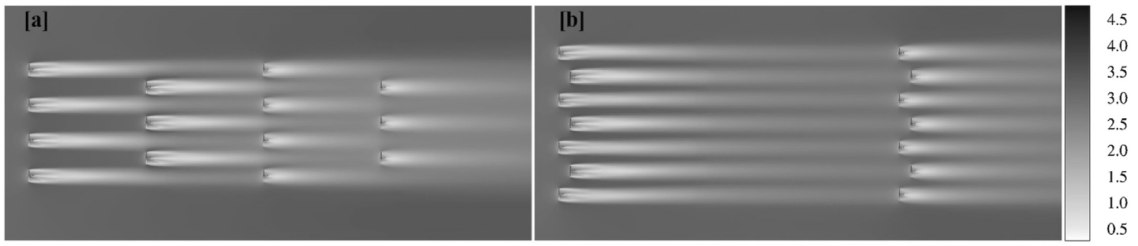

Figure 1.3: Figure from Malki et al. (2014) showing velocity fields (in metres per second) for two array layouts. Layout (b) is reported to produce 10% more power than layout (a). This result has been computed using a RANS-BEM model, described in section 1.4.1.2. Permission to reproduce this figure has been granted by Elsevier.

one such study is that of Draper et al. (2013).

1.2.2 Array scale

At the array scale, the layout of a farm must be optimised to maximise array power and efficiency (the ratio of useful mechanical power to the total power given up by the flow, including mixing losses). The input conditions for array scale modelling, such as flow velocity and channel geometry, are determined from basin scale assessments of a tidal site. Individual devices are usually represented in an idealised manner, e.g. a one-dimensional momentum sink.

Nishino and Willden (2012*a*) extend the model of Garrett and Cummins (2007) to account for fences of turbines partially blocking a wide channel, and identify the relationship between inter-device spacing, power extraction and efficiency. Further work has been carried out to extend the model to shorter fences of fewer turbines, and compared results to computations (Nishino and Willden, 2013).

Using a computational model, Hunter et al. (2013) investigate how array power and efficiency may be optimised by varying the operating points of individual devices within an array. Many computational studies have examined the effect of wakes on downstream devices within an array, for example those by Bai et al. (2009) and Malki et al. (2014). Figure 1.3 is taken from Malki et al. (2014), and shows velocity fields for two array configurations. The second array, labelled ‘b’ produces approximately 10% more power.

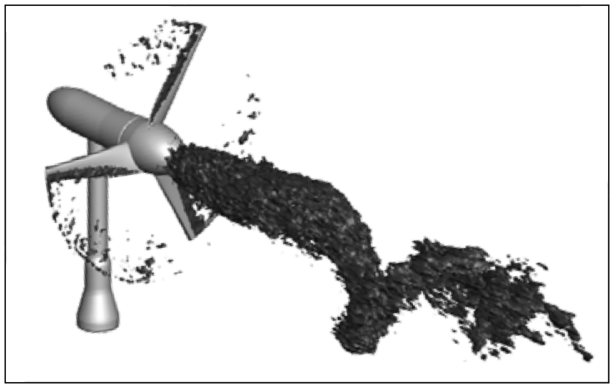

Figure 1.4: Figure from Kang et al. (2014) showing the structure of a vortex core downstream of a tidal turbine. The flow direction is from the top left to the bottom right. This result has been computed using a large eddy simulation where the turbine geometry is directly resolved, and is discussed further in section 1.4.1.4. Permission to reproduce this figure has been granted by Cambridge University Press.

An experimental study of wake merging for three adjacent turbines has been presented by Stallard et al. (2013).

1.2.3 Device scale

The challenge at the device scale is to maximise power and efficiency while maintaining structural strength and reliability. Device power and thrust must be determined so that an effective support structure can be designed. However support structure design affects turbine performance by exerting additional drag on the flow and reducing the power available to other devices in an array. The behaviour of the wake is also of interest, as it affects flow conditions for downstream devices. Figure 1.4 is taken from a study into the fluid mechanics of wake meandering by Kang et al. (2014). This model is discussed further in section 1.4.1.4. These performance metrics are affected by conditions in the tidal environment such as the velocity profile, freestream turbulence, flow alignment and waves.

A range of device types have been proposed for tidal energy extraction. Axial flow devices, similar to wind turbines, have been developed by Marine Current Turbines (2014)*, Tidal Generation Ltd. (2014)† and Verdant Power (2014). Variations of this type of device

*now owned by Siemens
†now owned by Alstom

include ducted turbines (Clean Current Power Systems Inc., 2014; Lunar Energy, 2014; Atlantis Resources, 2014) and ducted open-centre turbines (OpenHydro Group Ltd., 2014). Cross flow devices, similar to the Darrieus wind turbine, have been developed by Kepler Energy Ltd. (2014) and the Ocean Renewable Power Company (2014).

This thesis focuses on the computational modelling of axial flow devices in a variety of flow conditions representative of the tidal environment. The particular aims of this research are outlined in the next section, followed by a detailed review of relevant turbine and flow modelling methods in section 1.4.

1.3 Research objectives

The first aim of this research is to develop a three dimensional computational model of an axial flow turbine which predicts rotor power and structural loading with reasonable accuracy. Initial development work is carried out at model scale so that results can be compared to experimental measurements, and a full scale turbine model is subsequently developed.

The second objective is to examine the performance of the full scale turbine in flow conditions representative of the tidal environment. Computational techniques for modelling highly sheared, turbulent, confined and yawed flows are described, and a method for modelling free surface waves is developed. Turbine performance is evaluated generally in terms of mean rotor power and thrust and wake development. Subsequently the unsteady loading on turbine blades is examined in detail.

The final objective is to gain further insight into the fluid mechanics of ducted tidal turbines. A simplified computational model is used to compare the performance of a range of parameterised duct geometries.

This work has been carried out as part of the PerAWaT project (Rawlinson-Smith et al., 2010). Funded by the Energy Technologies Institute*, this project was a collaboration

*www.eti.co.uk

between a number of industrial and academic institutions, and involved numerical and physical modelling of wave and tidal energy generation.

1.4 Computational methods for predicting and evaluating turbine performance

A review of existing literature relevant to the aims of this thesis is now presented. The computational framework for the models in this thesis is the Reynolds averaged Navier Stokes (RANS) equation solver ANSYS Fluent (ANSYS Inc., 2012*b*). The RANS equations are a filtered form of the equations governing unsteady fluid flow, where semi-empirical closure models are employed to account for high-frequency turbulent motion which is impractical to calculate directly. Details of discretisation and solution of the RANS equations are given in chapter 2.

Analytical and computational methods for predicting and evaluating the performance of axial flow tidal turbines are reviewed in two parts. Firstly, a series of approaches to the analysis of rotor performance of increasing complexity are introduced. The simplest approach, where the rotor is represented as a porous disc, is used in chapter 5 where the performance of a range of ducted devices is evaluated.

The most elaborate rotor model, where the geometry is resolved dynamically, is used to examine turbine performance in a variety of flow conditions in chapters 3 and 4 and hence is discussed in detail. Details of spatial and temporal resolution, turbulence modelling, and computational load are compared where available.

In the second part of this review, methods of reproducing characteristic features of tidal flows are examined. In particular, existing methods of modelling sheared, turbulent flow and free surface deformation are reviewed.

Finally, a selection of experimental and computational studies of ducted turbines are reviewed and compared.

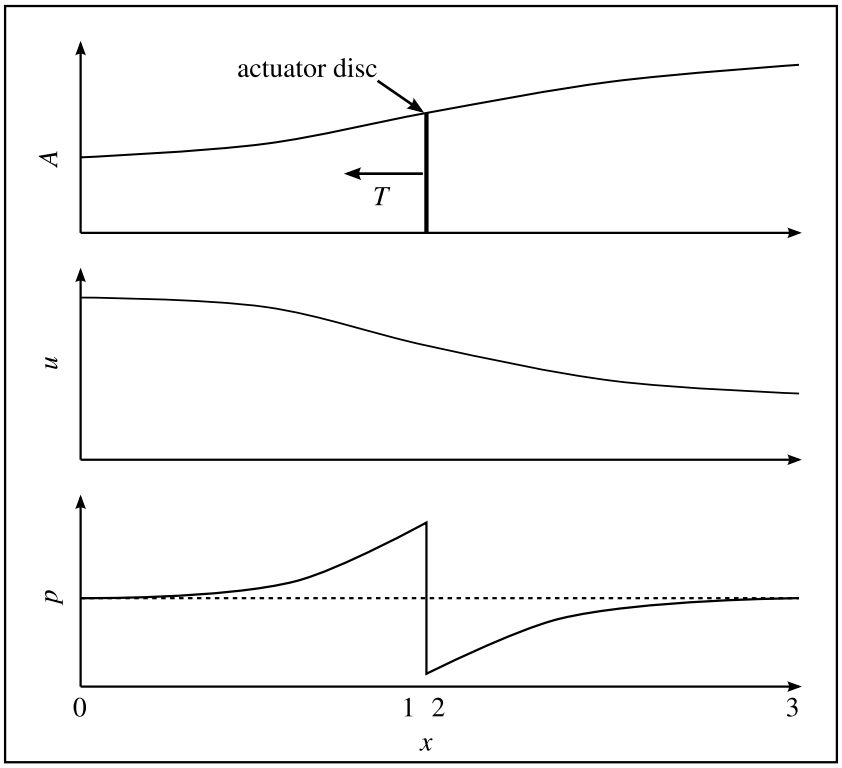

Figure 1.5: Distributions of streamtube area A, velocity u and static pressure p according to actuator disc theory.

1.4.1 Rotor modelling

1.4.1.1 Actuator disc

The simplest approach for the analysis of flow through an axial rotor is to reduce the problem to one dimension, neglecting the radial and tangential components of the flow. Lanchester (1915), Betz (1920) and Joukowsky (1920) independently developed this method for the analysis of propellers and wind turbines in unconstrained flow (van Kuik, 2007). The rotor is represented as an actuator disc, i.e. an infinitely thin disc which presents a uniform resistance to the oncoming flow. The physical analogue of the actuator disc is a porous disc, examples of which are tested by Graham (1976), Whelan et al. (2009) and Draper et al. (2013). Numerical implementations of actuator disc theory are often termed 'numerical porous discs'. Far upstream, the flow has a uniform velocity u_0 which reduces as the flow approaches and passes through the actuator disc. The cross-sectional area of the core streamtube A expands upstream of the turbine to satisfy continuity, and

the static pressure p increases. The resistive force of the disc T is balanced by a pressure change across the disc,

$$T = (p_2 - p_1)\, A_\mathrm{d} \tag{1.1}$$

where stations 1 and 2 correspond to the locations immediately upstream and downstream. Between stations 2, where the core flow pressure is below that of the bypass flow (which remains constant with a value of $p = p_0$) and station 3 (far downstream) where the core pressure has recovered to p_0, the flow decelerates further with a corresponding increase in streamtube area. This model is used to derive the theoretical limit of power extraction from an unbounded flow (see Burton et al. (2001)), which is

$$C_P = \frac{P}{\frac{1}{2}\rho u_0^3 A_\mathrm{d}} = \frac{16}{27} \tag{1.2}$$

where C_P is the non-dimensional power coefficient, and ρ is fluid density. At this operating point, the velocity through the disc is $u_1 = u_2 = \frac{2u_0}{3}$ and the velocity far downstream is $u_3 = \frac{u_0}{3}$.

This model has been extended to account for flow confinement by Houlsby et al. (2008) and Garrett and Cummins (2007), who find that peak power coefficient is increased by a factor of $(1 - B)^{-2}$, where the blockage ratio B is the ratio of the turbine area to the channel area.

A rotor can be represented numerically in an analogous manner, where the turbine is represented as a thin porous disc. The resistance of the disc in the axial direction takes the form of a momentum sink M,

$$M = \frac{1}{2} K \rho u_\mathrm{d}^2 \tag{1.3}$$

where K is a momentum loss coefficient. While this representation of a rotor is extremely simple, it has been used successfully in a wide range of computational studies of tidal turbines. Batten et al. (2013) used this method within a RANS model to compare predictions of wake development with measurements from a physical rotor model between $5D$ and $10D$ downstream, observing good agreement in profiles of velocity and turbulence

intensity. Nishino and Willden (2012*a*) examine the effect of blockage and turbulent wake mixing on power extraction by a porous disc, finding good agreement with previous analytical predictions (Houlsby et al., 2008; Garrett and Cummins, 2007).

Due to its simplicity, the porous disc model is not computationally demanding and hence can be practically applied in parametric studies, where other aspects of the flow can be examined. For example, Hunter et al. (2013) apply the model to investigate local blockage effects in arrays of up to 8 devices, arranged in single and multiple rows. Sun et al. (2008) use it in conjunction with a volume-of-fluid method to examine the effect of energy extraction on the free surface of the flow. The performance of ducted and open centre tidal turbines, in aligned and yawed flow has been studied by Belloni et al. (2013) and Belloni (2013). Various uni-directional ducted turbine geometries are compared by Shives and Crawford (2012) in order to identify an optimum design. A similar approach is applied to the design of a bi-directional ducted turbine in chapter 5, following on from preliminary work in Fleming et al. (2011).

1.4.1.2 Blade element momentum theory

The primary limitation of the theoretical and computational actuator disc models is that a radial variation in thrust is not allowed. Additionally, the swirl induced by a real rotor is not reproduced. These issues are addressed in blade element momentum (BEM) theory, where the sectional lift and drag forces of the rotor blade are distributed azimuthally across a thin disc. In the analytical model, the flow is divided into a series of concentric annuli, which are assumed to be independent of one other (i.e. radial flow is assumed to be negligible). While it is valid for wind and tidal turbine rotors, this assumption would not be appropriate for situations where a significant radial imbalance exists, for example in a gas turbine.

At each annulus, fluid momentum is balanced with the blade forces in the streamwise and azimuthal direction to calculate the velocities induced in the streamwise and azimuthal directions. Hence non-uniform distributions of thrust and torque are permitted along the

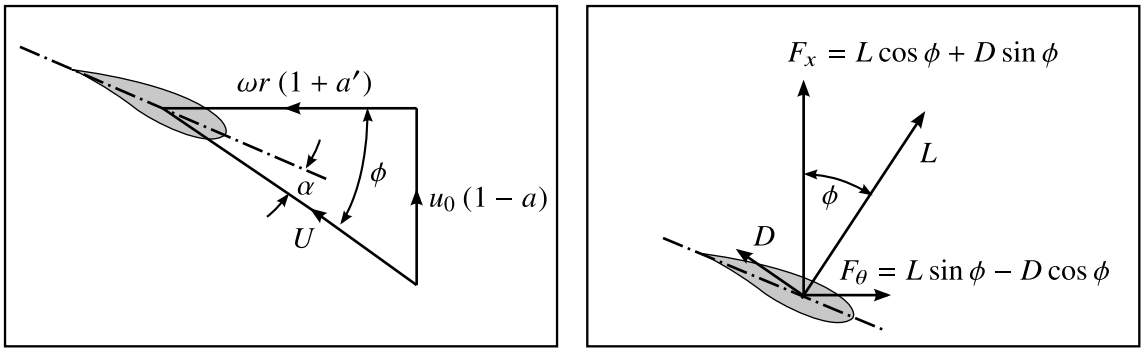

(a) (b)

Figure 1.6: (a) Velocity vectors and (b) force vectors according to blade element momentum theory. The blade element is travelling from left to right.

rotor blade. The induced velocities are expressed as induction factors,

$$a = \frac{u_0 - u_1}{u_0} \tag{1.4}$$

$$a' = \frac{\Omega}{2\omega} \tag{1.5}$$

where a is the axial induction factor, a' is the tangential induction factor, Ω is the angular velocity of the wake and ω is the angular velocity of the blade. These induction factors are used to calculate annular power and thrust, which are then integrated over the full rotor (Burton et al., 2001). Appropriate blade forces for a given angle of attack are obtained from measurements of the blade profile in two-dimensional flow. It is often necessary to extrapolate lift and drag force values for angles of attack outside the range of the available data, using methods such as that suggested by Viterna and Corrigan (1981).

Velocity and force diagrams for a blade element are presented in figure 1.6. The relative velocity at the blade, U, is the sum of the axial velocity, $u_0\,(1 - a)$, and radial velocity, $\omega r\,(1 + a')$. The lift force, L, and drag force, D, for that angle of attack, α, are obtained from experimental data. These sectional forces are then resolved into a streamwise component, F_x, and an azimuthal component, F_θ.

The basic model is applicable to unconfined flow only; Whelan et al. (2009) propose a correction to the axial induction factor to address this. Additionally, the model is axi-symmetric, and semi-empirical corrections are often applied to account for yawed or

sheared flow (Burton et al., 2001).

The flexibility of the model is greatly improved when implemented as a momentum source within a RANS model, referred to hereafter as RANS-BEM. The shortcomings of the analytical model, e.g. artificial corrections for blockage, shear and yaw, are overcome as the general flow field is computed numerically, with BEM theory applied only to the rotor disc region. While this method is more elaborate than the computational porous disc model in that it includes wake rotation, it is still lightweight enough to be suitable for array scale modelling and parametric studies.

Models of this type have been developed by a number of authors for various applications. Ammara et al. (2002) uses such a model to investigate the effect of upstream wakes on turbine performance in a wind turbine array. Similar studies on arrays of tidal turbines have been carried out by Turnock et al. (2011) and Malki et al. (2014). Malki et al. investigate the effect of device layout on total array power, and identify favourable array configurations. Velocity fields for two array layouts from this study are presented in figure 1.3.

Batten et al. (2013) develop a RANS-BEM model for comparison to physical measurements by Myers and Bahaj (2009), and achieve good agreement in rotor performance and wake recovery. More elaborate applications of this type of rotor model include the investigation of bend-twist coupling in a composite blade (Nicholls-Lee et al., 2013) and cavitation inception (Buckland et al., 2013).

McIntosh et al. (2011) implement an inverse BEM model for rotor design within a RANS simulation. The method is applied to rotor design for a ducted turbine, showing that the bespoke ducted rotor design outperforms a generic rotor designed for operation in unbounded flow. Belloni (2013) uses this model to design rotors for ducted and open centre turbines which are subsequently simulated in aligned and yawed flow. A study of the effect of blockage by Schluntz and Willden (2013) shows that a rotor designed for one particular level of blockage outperforms rotors designed for other blockage values.

1.4.1.3 Actuator line

A limitation of RANS-BEM models is that streamwise and tangential rotor forces are distributed across the rotor disc area. Discrete blade effects, such as blade-tower interaction and near wake flow structure, cannot be reproduced.

Individual rotor blades can be modelled using actuator line theory, where a rotor blade is represented as a radial line sink of momentum. Local velocity magnitude and angle of attack are calculated at a series of radial locations (collocation points) along the line, and appropriate streamwise and azimuthal forces are applied to the flow based on two dimensional lift and drag data for the blade profile. This type of model typically requires a greater computational resource than the foregoing models, as an unsteady numerical scheme is required to track the motion of the rotor blades. Additionally, actuator line models are often used to examine the structure of the near wake, which can require higher spatial resolution and higher-order techniques for turbulence closure. However, it is not as costly as methods where the blade geometry is resolved.

An actuator line model has been developed for wind turbine rotors by Sørensen and Shen (2002), which predicts rotor power very well and reveals the helical structure of the near wake. This implementation has subsequently been combined with large eddy simulation (LES) to examine the performance of wind and tidal turbines in unsteady flow fields (Churchfield et al., 2012, 2013).

One shortcoming in the model by Sørensen and Shen (2002) is that, for stability reasons, the momentum source cannot be applied at a singular point, as the velocity at that point will be inaccurate. Instead, it must be distributed over a certain volume, dependent on grid resolution, and the velocity can then be read at the collocation point. Schluntz and Willden (2014) have recently presented a more robust method for the introduction of the momentum source, where velocity is sampled at several points adjacent to the location of the momentum source. This information is used to deduce the velocity magnitude and angle of attack, from which the appropriate momentum source can be applied based on the reference aerofoil data. This approach requires no assumption about the distribution of

the momentum source; the appropriate distance between the momentum source and the velocity sampling points has been determined through a simple grid convergence study. A distance of one local chord length, c, is found to be appropriate for a local mesh resolution of $c/4$.

1.4.1.4 Direct resolution of rotor geometry

A criticism of RANS-BEM and actuator line models is that they rely on lift and drag measurements for aerofoil sections in two-dimensional flow to calculate local momentum sources, which are then applied to a three-dimensional flow field. This approach is not applicable to situations involving static stall, dynamic stall or stall delay. For flow angles beyond the point of static stall, sectional force data must be extrapolated. Dynamic stall, which may occur as a rotor blade interacts with a non-uniform velocity profile, cannot be predicted due to the quasi-steady assumption of these models. Stall delay is a three-dimensional phenomenon, observed in experimental and numerical models of rotating wind turbine blades (Butterfield et al., 1992; Hu et al., 2006). Additionally, BEM theory does not account for unsteady flow effects and hence is not suitable in cases where the inflow velocity is unsteady or where wake dynamics influence blade loading.

Direct resolution of the rotor is necessary when the flow field around the blade is likely to depart from the steady, planar assumptions of the RANS-BEM and actuator line models, or when particular flow features at the blade scale are to be investigated. Such models, also termed 'blade-resolved' models, are more computationally demanding due to the degree of spatial resolution necessary to capture the high velocity gradients in the boundary layers at the blade surfaces. One technique commonly used to reduce computational load is to simulate rotor motion by recasting the governing equations in terms of a moving reference frame (MRF). The MRF approach can be used in conjunction with periodic boundary conditions along planes of axial symmetry in the domain to further reduce the computational load.

In a blind comparison with the NREL Phase VI wind turbine experiment, Sørensen

et al. (2002) use a steady state MRF approach to predict the performance of the turbine at a range of free stream velocities. Good agreement is observed for rotor torque as well as for the radial distribution of streamwise force for the lowest velocity case ($7\,\mathrm{m\,s^{-1}}$). Poor agreement at higher freestream velocities is attributed to stalled conditions at the rotor blades (Hand et al., 2001).

Hu et al. (2006) use a moving reference frame model of the NREL Phase II 'Combined Experiment' wind turbine to reproduce and investigate the stall delay observed in that experiment.

The MRF method has also been used by Ferrer and Munduate (2007) in a study of three-dimensional flow around a selection of blade tip geometries. In a validation case against the NREL Phase VI wind turbine experiment the authors achieve excellent agreement in streamwise force coefficient and chordwise pressure distribution along the middle sections of the blade, while streamwise force is over-predicted at the root and tip sections.

The steady MRF model has been applied to a tidal turbine rotor by O'Doherty et al. (2009), who match the power and thrust characteristics of a model scale device using a variety of turbulence models. This model is developed further by Mason-Jones et al. (2012) and is used to identify appropriate methods of normalising turbine performance coefficients in sheared flow conditions. However, the MRF model is not ideal for use in conjunction with a sheared velocity profile. The rotor geometry does not move, so a particular blade will only encounter a portion of the incoming flow, rather than interact with the full velocity profile. For cases such as this, a dynamic rotor model should be used. This type of model is employed in studies of a full scale tidal turbine in sheared flow in chapter 3 and with a deforming free surface in chapter 4; hence previous work is reviewed here.

Typically, rotor motion is enabled in a blade-resolved RANS model by subdividing the computational domain into rotating and stationary portions, which are separated by a sliding interface. An additional computational load is introduced, as blade motion must be simulated using an unsteady scheme where the geometry is advanced incrementally at

discrete intervals of time (timesteps). The entire flow field must be solved at every timestep, so computational cost is directly proportional to the number of timesteps. The expense of this method is such that it is necessary to compromise between various objectives based on the available computational resource:

- Spatial resolution should be sufficiently high to adequately resolve high gradients in the flow field, particularly at boundary layers.
- Temporal resolution should be sufficiently high to adequately resolve unsteady flow features and geometry motion.
- The turbulence model should be capable of predicting flow behaviour in turbulent boundary layers, e.g. velocity profile, wall shear and flow separation.
- The simulation should be continued for sufficient time to allow transient flow features to dissipate and a periodic solution to develop.
- Upon reaching a periodic state, the simulation should be continued further to enable the extraction of time-averaged performance metrics.
- Multiple cases should be simulated so that the effect of a model parameter can be studied.

A measure that is often used to address the first point above, the high spatial resolution required to resolve boundary layers, is wall modelling. Rather than directly resolving high velocity gradients at a wall boundary, a theoretical model is used to calculate the velocity at a larger distance from the wall. With this method, discussed further in section 2.1.8, a larger distance is permitted between the wall and the first grid point, resulting in considerable savings of computational expense. The distance in the normal direction (y) between the wall and the first grid point is measured in non-dimensional units, $y^+ = u_\tau y/\nu$, where ν is kinematic viscosity, $u_\tau = \sqrt{\tau_w/\rho}$ is friction velocity, τ_w is wall shear and ρ is density. Where wall resolution is mentioned in the following review of blade-resolved models, values below $y^+ = 11$ indicate that direct resolution of the boundary layer was

attempted (although y^+ should be lower than 5 for proper resolution of the boundary layer, as discussed in section 2.1.8), and values above this indicate that wall functions were employed.

It is rare that all of the modelling objectives listed above are met simultaneously; a recent example is the study of the mechanism underlying experimentally-observed tidal turbine wake meandering by Kang et al. (2014) (see figure 1.4). In their model, the computational domain is discretised into 165 million grid points. Large eddy simulation is used for turbulence closure, and the turbine is simulated in operation for 70 revolutions (56×10^3 timesteps) following the dissipation of start-up transients. The authors show how wake meandering is initiated through an interaction between an inner vortex core shed from the hub and the outer shear layer of the wake. The application of a geometry-resolving LES model is justified by showing that lower order actuator disc and actuator line rotor models do not predict this mechanism correctly.

Gómez-Iradi et al. (2009) reproduce the NREL Phase VI experiment (Hand et al., 2001) using a blade-resolved model. Two types of sliding mesh interface are used. In the first case, a cylindrical interface extends from the upstream to the downstream boundaries, inside of which the turbine rotates relative to the boundaries of a rectangular-section domain. This method does not allow the supporting tower to be included. They achieve good agreement in blade root bending moment and shaft torque using a computational grid of 7 million elements. The boundary layers are directly resolved, with the k-ω model used for turbulence closure, and a timestep size such that the rotor advances 0.25° every timestep. In a second case the turbine is simulated in a cylindrical domain, and the tower geometry is included. The sliding mesh interface is located in a plane perpendicular to the flow, between the rotor and tower. Using a grid of similar size, they match measurements of the tower wake reasonably well.

Mason-Jones et al. (2013) add a sliding mesh interface to their previous MRF model (Mason-Jones et al., 2012) and examine the effect of velocity shear and support structure geometry on rotor performance and loading. They use the Reynolds stress model (RSM)

for turbulence closure, based on previous comparisons of turbulence models in an MRF model (O'Doherty et al., 2009) (although considerable scatter exists in the experimental reference data, and the realisable and renormalisation group k-ε models tested yielded similar results). While this model is more computationally costly than the k-ε and k-ω families of turbulence models, it enables the reproduction of turbulence-driven phenomena, e.g. secondary flows in rectangular channels (Nezu, 2005). However, the authors do not investigate turbulence-driven flow features. The computational domain is discretised with 1.84 million elements, and wall functions are used to resolve the boundary layers. The timestep size is not reported, but the rotor appears to advance by 45° every timestep for the case where no support structure is modelled, and 23° for the cases where a support structure is included. Due to the large timesteps used, this model should be considered as a series of steady simulations with different rotor orientations, rather than a continuous unsteady simulation. The sheared velocity profile is taken into account when comparing rotor performance in uniform and sheared flows, where the reference velocity is calculated based on the volumetric flow rate through the rotor. The results show that mean rotor power and thrust is reduced when a support structure is included. Additionally, the authors attribute periodic fluctuations in blade thrust and torque to the sheared velocity profile, and show how the magnitude of these fluctuations increase when a support structure is introduced.

Using a grid of 8×10^5 elements and the k-ω SST turbulence model, McSherry et al. (2011) simulate the model scale tidal turbine experiment by Bahaj et al. (2007). They report good agreement in computed and measured power at low and moderate rotor speeds, and attribute discrepancies at high rotor speeds to cavitation effects.

McNaughton et al. (2014) implement a new sliding mesh method in an open-source finite volume flow solver, and use it to simulate a tidal turbine in a towing tank as tested by Bahaj et al. (2007). They compare predictions of power and thrust by RANS models with k-ω SST, k-ε and RSM turbulence closure and an LES model against experimental measurements. A related study by Afgan et al. (2013) compares flow field data computed

by the k-ω SST and LES models. For the RANS models, the computational domain is discretised by 3.7 million elements, and the boundary layers are directly resolved. The LES model uses a grid of 7.4 million elements. In each case the model is run for 24 rotations, requiring 5×10^5 timesteps (equivalent to less than 0.02° degrees per timestep). Computational loads of 0.14×10^6 and 4.4×10^6 CPU-hours are quoted for the RANS and LES models respectively.

The best results are achieved with the LES model, which predicts power and thrust well across all rotor operating points. The k-ω SST and RSM models perform similarly to one another, predicting power and thrust well at the peak power operating point, and under-predicting power at other operating points. Very poor results are observed with the k-ε model, with peak power under-predicted by nearly 50%. In fact, the poor performance of this turbulence model in adverse pressure gradients, as often occurs for aerofoil flows, was the motivation for the development of the k-ω SST model (Menter et al., 2003).

McNaughton (2013) simulates a full scale turbine in sheared velocity profiles based on physical measurements at a tidal site reported by Gunn and Stock-Williams (2013). A grid of 8.4 million elements is used to discretise the geometry, with 2.8 million of these within the sliding mesh region. Wall functions are used to model the boundary layers, with a maximum dimensionless wall distance of $y^+ = 500$ reported. The effect of freestream turbulence, velocity profile, and flow alignment on rotor performance and loading is examined, where power and thrust are normalised on the mean velocity across the swept area of the rotor.

Two blade-resolved models are presented later in this thesis. In chapter 2, a model of a 1:30 scale turbine is developed and compared with results from an experimental study. Details of the domain dimensions, grid resolution, timestep size and flow time are given in section 2.2.2. In chapters 3 and 4, a full scale turbine is modelled in a variety of flow conditions. Spatial and temporal resolution of the model is described in section 3.2.

1.4.2 Computational modelling of environmental conditions

Another important aspect of computational modelling of tidal energy converters is the representation of the tidal environment. Measurements reported by Gunn and Stock-Williams (2013) and Mason-Jones et al. (2013) show that tidal flows exhibit a high degree of velocity shear and free stream turbulence. Additional environmental factors, such as turbine spacing and waves, affect turbine performance and loading.

1.4.2.1 Sheared and turbulent inflow

The majority of the device-scale studies cited in section 1.4 have been carried out in uniform flow. Tidal turbine performance in sheared flow has been examined by Batten et al. (2008), Mason-Jones et al. (2013), and McNaughton (2013). In the first two models a $\frac{1}{7}$ power law is used to represent the velocity profile, while in the third model polynomial profiles based on site data are used. In the absence of a turbulence-generating mechanism such as bed shear (as opposed to a no-slip condition), high levels of turbulence intensity (e.g. on the order of 10%) are not sustainable, and free stream turbulence decays between the inlet and the rotor plane. This is often addressed by prescribing a higher value of turbulence at the inlet to achieve a target value at the rotor plane (Nishino and Willden, 2012*a*; Batten et al., 2013). McNaughton (2013) reports that the prescription of high turbulence intensity (10%) in conjunction with a sheared velocity profile causes the velocity profile to change as the flow progresses downstream. Hence, studies of the effects of sheared flows are carried out in low free stream turbulence.

Gant and Stallard (2008) use an unsteady upstream boundary condition to generate large scale structures in the flow past a numerical porous disc. They report that a 9:1 ratio of resolved turbulence (via the unsteady boundary condition) to modelled turbulence (via the k-ε turbulence model) results in a turbulent flow field which is sustained well in the downstream direction. The resolved eddies dissipate as they are convected downstream, with a corresponding increase in modelled turbulent kinetic energy. Wake mixing is enhanced relative to a reference case where a steady inflow condition is prescribed. The

computational cost of this method is not reported, but it is likely to be high due to the timestep required to generate coherent structures at the inlet boundary.

For the model scale turbine simulations in chapter 2, a logarithmic law velocity profile is specified, with matching profiles of turbulence parameters. Rough wall conditions are applied at the bed and sides of the channel to maintain these profiles in the streamwise direction. For the full scale model in chapters 3 and 4, a self-sustaining sheared flow profile is applied, based on an assumed linear shear profile between the channel bed and free surface. A shear force is directly imposed at the channel bed, which maintains the velocity profile in the downstream direction and assist turbulence generation.

1.4.2.2 Effect of blockage

Blockage, which is the ratio of the swept area of the rotor to the local flow channel, greatly influences device performance. As discussed previously, Garrett and Cummins (2007) and Houlsby et al. (2008) show that the peak power increases by a factor of $(1 - B)^{-2}$. Nishino and Willden (2012*b*) extend the Garrett and Cummins model in a different direction, examining the effect of local turbine spacing on the maximum power extracted by a single row of equally-spaced turbines extending partially across a tidal channel, and show that the Betz limit of $C_P = 0.593$ can be increased to a new maximum of $C_P = 0.798$ for this type of array.

A number of computational studies on blockage effects have been carried out using actuator disc and RANS-BEM rotor models, e.g. the studies by Nishino and Willden (2012*a*) and Schluntz and Willden (2013), previously mentioned in the context of rotor modelling. Additionally, Nishino and Willden (2013) use a RANS actuator disc model to validate an extension to their momentum theory for partial arrays which is applicable to relatively short turbine fences.

In this thesis, the effect of blockage on turbine performance, structural loading and wake development is examined in section 3.6.

1.4.2.3 Effect of yawed flow

McNaughton (2013) examines the performance of a full scale tidal turbine in yawed flows of up to 15° and shows how mean power and thrust can be renormalised to account for flow misalignment using a method by Bahaj et al. (2007). Maximum fluctuations in rotor power and thrust of 15% and 6.4% respectively are observed, and blade power and thrust fluctuate by up to 20% and 30% respectively. These fluctuations are attributed to the alteration of the local velocity magnitude and angle at the blade as it sweeps through the yawed oncoming flow. The supporting tower is identified as the source of asymmetry in the wake.

Turbine operation in yawed flows of 15° and 30° is modelled in section 3.7. The unsteady loading of turbine blades and the development of the wake are examined.

1.4.2.4 Free surface deformation and waves

The behaviour of an open channel flow is dependent on the non-dimensional Froude number, $\mathrm{Fr} = u/\sqrt{gh}$, where u is velocity, g is gravitational acceleration, and h is water depth (Chaudhry, 2007). In supercritical flow, when $\mathrm{Fr} > 1$, the streamwise velocity is greater than the speed at which disturbances can travel along the free surface, and hence information cannot be transmitted in the upstream direction. When $\mathrm{Fr} < 1$ the flow is subcritical, and disturbances can travel in all directions. Typical Froude numbers for flows past tidal turbines range from $\mathrm{Fr} \approx 0.05$ for a flow of velocity $u = 1\,\mathrm{m\,s^{-1}}$ in water of depth $h = 40\,\mathrm{m}$, to $\mathrm{Fr} \approx 0.2$ for a $u = 3\,\mathrm{m\,s^{-1}}$ flow in 20 m deep water. A rigid lid boundary condition, applied in the many of the rotor models previously discussed, implies a Froude number of $\mathrm{Fr} = 0$.

As mentioned in the previous section, Whelan et al. (2009) show how the free surface height change and turbine power can be calculated analytically for an actuator disc rotor operating at given values of blockage, thrust and Froude number. In computational models involving more complex geometry and which include the effects of viscosity and turbulence, the thrust on the device is not known *a priori* and hence the appropriate height difference between the upstream and downstream boundaries corresponding to a steady-state solution

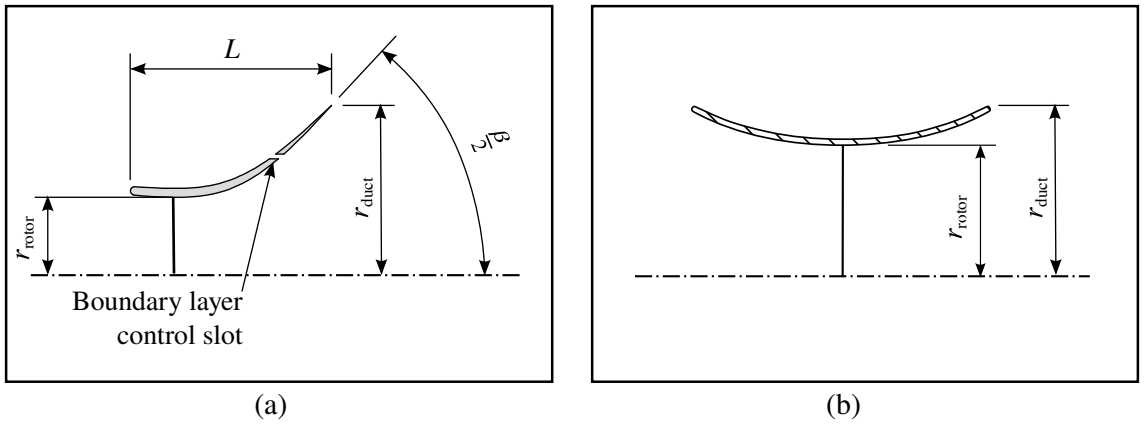

(a) (b)

Figure 1.7: Schematic diagrams of (a) uni-directional and (b) bi-directional ducted turbines.

cannot be prescribed in advance. Sun et al. (2008) circumvent this issue using a RANS-based volume-of-fluid model. The volumetric flow rate of water is prescribed at the upstream boundary, and the solver allows the downstream water depth to reduce to balance the turbine thrust. Consul et al. (2013) present an alternative approach, which allows for a velocity profile to be prescribed (although this was not demonstrated in their investigation). As a difference in upstream and downstream water depth is developed during the solution of their model, the water depth at the downstream boundary is adjusted iteratively to ensure the upstream water depth is unaffected. This method was considered for the deforming free surface study presented in chapter 4, but was found not to be suitable for unsteady free surface conditions, i.e. waves. As a result, low frequency error waves are observed in the domain, but do not influence the general findings of this study.

1.4.2.5 Ducted turbines

Many tidal energy converters currently in development feature a ducted rotor due to perceived advantages over an unducted rotor (Lunar Energy, 2014; Clean Current Power Systems Inc., 2014; OpenHydro Group Ltd., 2014). The primary effect of a duct, when its internal surface is cambered appropriately, is to accelerate the flow at the rotor plane beyond the free-stream velocity. However this effect is reduced when the rotor is in operation, as its thrust will oppose the flow. Other beneficial effects include realignment of yawed flow studied in detail by (Belloni et al., 2013), and protection of the rotor blades.

Early experimental work has been carried out on uni-directional ducts by Foreman and Gilbert (1983) in an effort to improve wind turbine performance by increasing the flow velocity at the rotor, whilst also increasing the pressure drop across it. Conventionally, the internal duct angle β must be small in order to avoid an overly high pressure gradient within the duct, as this would cause boundary layer separation and render the diffuser ineffective. Foreman and Gilbert (1983) find that the internal angle can be increased and the diffuser length reduced through the introduction of boundary layer control slots, which allow higher momentum fluid from the bypass flow to re-energise the boundary layer on the internal surface of the duct. Experiments are carried out on a range of steel and aluminium ducts, with the rotor represented by a wire mesh (Foreman et al., 1983). The internal angle and location of boundary layer control slots are varied. The best performing duct tested achieved a reported power coefficient based on disk area of 1.93, which surpasses the Betz limit by a factor of 3.25.

Phillips (2003) claims that the results reported by Foreman et al. (1983) are overly optimistic, as factors such as area blockage (5% for that case) and inaccuracies in velocity measurement were not accounted for. The author recalculates the reported performance metrics to arrive at an adjusted maximum C_P of 1.2. In the same body of work, a range of ducted devices are tested, again taking advantage of a slotted design to enable use of a shorter diffuser with a wider internal angle. The best performing device achieved a reported C_P of 1.03.

Computational studies have also indicated that ducts can be used to increase the power coefficient of wind and tidal turbines. The duct geometry developed by Hansen et al. (2000) is based on a NACA 0015 aerofoil section, with camber introduced to achieve an internal angle of 30° at the duct exit. While boundary layer control slots are not used, a small gap is allowed between the rotor tips and duct wall of $0.004D$ to delay separation. A peak power coefficient of 0.94 is reported.

Following the methodology of Hansen et al. (2000), Shives and Crawford (2012) simulate a range of uni-directional duct geometries based on a solid NACA 0015 section,

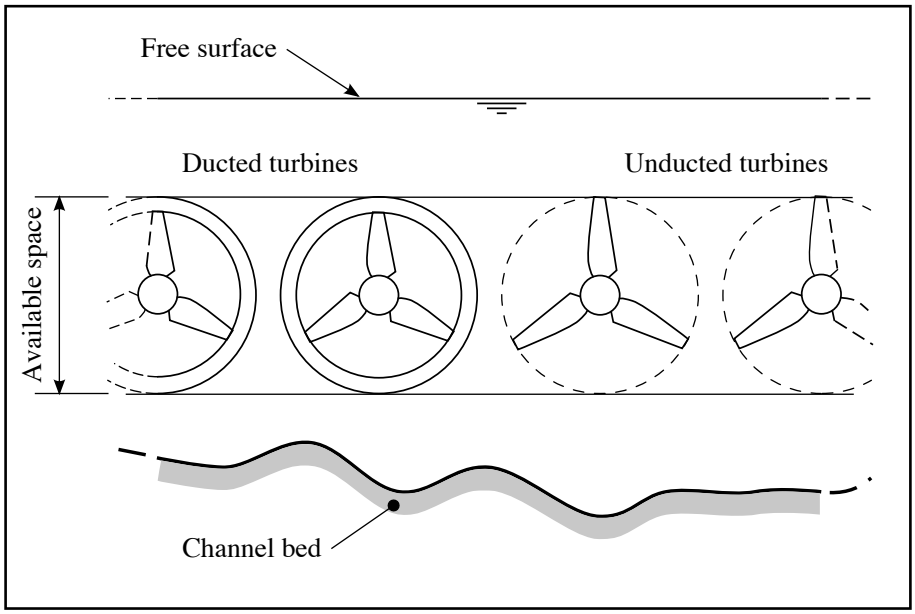

Figure 1.8: Schematic diagram showing how the diameter of an axial flow tidal turbine may be limited, typically by tidal levels above and channel geometry below.

where thickness, camber and angle of attack are varied. Again, the device features a gap of $0.004D$ between the rotor tips and duct wall. The maximum C_P achieved is approximately 1.2.

The experimental and computational investigations cited above imply that the Betz limit of $C_{P\,\max} \approx 0.593$ may be exceeded through the use of a flow-concentrating device. However, the comparison is unfair for a number of reasons. Firstly, as the projected frontal area of an unducted device is increased with the addition of a duct, the blockage B is increased. This may lead to a considerable increase in C_P, as discussed earlier in section 1.4.2.2. Secondly, basing C_P on rotor area is unfair if the ducted device is larger than the unducted device. The power coefficient should express the power generated to that available in an unperturbed flow intersected by the entire device, whether or not a duct is employed. Further, it is likely that channel depth will dictate the maximum external dimension of the device, so this dimension, and not rotor diameter, would be held constant in a candidate device study for a real tidal site. Figure 1.8 shows how the diameter of an axial flow device would typically be constrained by the geometry of a channel.

In table 1.1, the power coefficients of the aforementioned devices are recalculated on

the new basis of total projected area. Details of the geometry, such as duct length L, ratio of duct exit area to rotor area $A_{\text{exit}}/A_{\text{rotor}}$, duct internal angle β and Reynolds number are reported where available. Duct length and Reynolds number are given in terms of rotor diameter D. Note that blockage is based on the maximum projected frontal area, i.e. A_{exit}.

Examining the reported values for $C_{P\,\text{rotor}}$, the ducted devices all appear to exceed the Betz limit by factors greater than 1.0. However, when C_P is renormalised on total frontal area (by scaling by the area ratio $A_{\text{exit}}/A_{\text{rotor}}$), more modest performance metrics result. Note that the entry in the first row in table 1.1 is the original result reported by Foreman et al. (1983), and was believed to be erroneous by Phillips (2003), whose adjusted value of Foreman's power coefficient is given in the second row. The device of Hansen et al. (2000) achieves the highest value: $C_P = 0.51$. However, it still does not surpass the performance of an ideal unducted rotor in unbounded flow, which is $C_P \approx 0.593$.

A similar comparison of ducted turbine performance has been presented by Belloni (2013), which also emphasises inconsistencies in blockage ratios in the evaluation of ducted turbine performance. The additional parameter 'blockage bias' is compared, which accounts for the difference in blockage ratio in comparisons of bare and ducted rotors. The author uses actuator disc and RANS-BEM methods to model ducted and open centre turbines in aligned and yawed flow. Two modes of operation are identified for a bi-directional ducted turbine in aligned flow. When rotor thrust is low, the flow follows the contours of the duct geometry, and acceleration effects are observed. When thrust is increased beyond a particular threshold, the flow separates from the exterior of the leading edge, generating a large region of recirculating flow around the duct which increases the

Table 1.1: Comparison of uni-directional ducted devices.

	Author	$C_{P\,\text{rotor}}$	$\frac{A_{\text{exit}}}{A_{\text{rotor}}}$	C_P	B	L	β	Re_D
Exp.	Foreman	1.93	2.62	0.74	open-jet	$0.49D$	90°	-
	Foreman (adj.)	1.20	2.62	0.46	open-jet	$0.49D$	90°	-
	Phillips	1.03	3.00	0.34	6.0%	$0.48D$	110°	2.4×10^5
Comp.	Hansen	0.94	1.84	0.51	0.4%	$1.06D$	31°	5×10^7
	Shives	~ 1.2	2.87	~ 0.4	2.7%	$1.03D$	83°	-

effective blockage of the device. Power coefficient can be improved, depending on the degree of effective blockage, but energy is also lost to viscous effects in the recirculation zone.

A duct design exercise is carried out in chapter 4, based on an initial comparison of various duct geometries with a bare rotor at consistent blockage ratios by Fleming et al. (2011). This revised study adopts some modelling techniques from Shives and Crawford (2012), namely a two-dimensional axi-symmetric domain and a structured computational grid.

1.5 Outline of thesis

The remainder of this thesis is presented in five chapters.

The computational framework is introduced in chapter 2. Details are given of the discretisation and numerical schemes used in ANSYS Fluent to solve the governing flow equations. A computational model of a 1:30 scale tidal turbine is developed for comparison with experimental data. Methods used to reproduce the appropriate levels of shear and turbulence in the free stream flow are described. Predictions of turbine performance by the model are compared with physical measurements. The structure of the wake in the near field of the modelled turbine is examined.

In chapter 3, a model of a full scale tidal turbine is generated. A method of modelling sustainable sheared profiles of velocity and turbulence is described. The effects of shear, elevation in sheared flow, blockage and yaw are examined in a parametric study. In particular, the effects of these conditions on the unsteady loading of the turbine blades are quantified.

This model is extended to include a deforming free surface in chapter 4. A theoretical model for free surface wave motion is combined with the existing sheared profile model. The turbine is simulated in conditions of combined velocity shear and waves, and the effects of wave height and length on turbine performance and loading are examined.

In a separate study in chapter 5, the effect of a bi-directional duct on tidal turbine performance is examined. A set of duct geometries is generated parametrically and evaluated relative to an unducted turbine under constant blockage conditions. Streamwise profiles of streamtube area, velocity and pressure are compared to identify the mechanisms behind poorly performing and well performing duct profiles. A 1:60 scale three-dimensional computational model of one of the parameterised geometries is produced, and predictions of total device thrust are compared to experimental data.

The conclusions of the various studies in this thesis are summarised in chapter 6, and suggestions are made for future work.

Chapter 2

Methods and validation

In this work, computational models are used to simulate the operation of tidal turbines in a variety of flow conditions. The purpose of this chapter is to describe the general features of the computational models, and steps taken to assess the accuracy of these models.

The first part of the chapter begins with a presentation of the governing equations, before describing techniques employed for their numerical solution, such as time-averaging, turbulence modelling, and spatial and temporal discretisation. Algorithms for the simultaneous solution of the discretised continuity, momentum and turbulence equations are discussed. Following this, methods of spatial discretisation of the computational domain are introduced. Unstructured and structured grid generation is discussed, as both methods are used later in this work. This part ends with a discussion of wall modelling, where the highly-sheared flow at a no-slip wall is accounted for.

The second part of this chapter focuses on the validation of a three-dimensional model of a tidal turbine. The geometry and flow conditions are based on a physical experiment at model scale. Spatial discretisation of the domain is based on a grid convergence study of a two-dimensional section of the rotor blade. Numerical predictions of rotor power and thrust are compared with experimental data, as well as velocity profiles in the wake region. Finally, the wake structure of the computed flow field is examined and prominent flow features are highlighted.

2.1 Computational methods

2.1.1 The Navier-Stokes equations

The mathematical description of a fluid element in motion is based on three physical considerations: conservation of mass, Newton's second law, and conservation of energy. Mass conservation requires that the rate of increase of mass of an inertially fixed control volume of fluid must be balanced by the net rate of mass flow into that volume.

$$\frac{\partial \rho}{\partial t} + \rho \frac{\partial u_i}{\partial x_i} = 0 \tag{2.1}$$

where ρ is density, t is time, and u_i and x_i are the velocity and position tensors. Water flowing in a tidal channel may be treated as incompressible, so the continuity equation reduces to

$$\frac{\partial u_i}{\partial x_i} = 0. \tag{2.2}$$

Newton's second law dictates that the sum of surface and body forces on a fluid element must be balanced by the rate of change of momentum of that element. Pressure and viscous forces act on the surface of a fluid element, and are accounted for with separate terms in the momentum equation (equation 2.3). Where present, gravitational, centrifugal, electromagnetic and Coriolis forces act throughout the fluid element, and are accounted for collectively per unit mass by the source term f_i. Assuming that the dynamic viscosity μ is spatially constant and the flow is incompressible, momentum transport in a fluid can be described by the following conservative form of the Navier-Stokes equations (Wilcox, 1994)

$$\rho \frac{\partial u_i}{\partial t} + \rho \frac{\partial}{\partial x_j}\left(u_j u_i\right) = -\frac{\partial p}{\partial x_i} + \mu \left(\frac{\partial^2 u_i}{\partial x_j \partial x_j} + \frac{\partial^2 u_j}{\partial x_j \partial x_i} \right) + \rho f_i \tag{2.3}$$

where p is the static pressure. The two terms on the left hand side are inertial, representing unsteady and convective acceleration respectively. On the right hand side, the pressure gradient term $\frac{\partial p}{\partial x_i}$ acts against the direction of acceleration, as indicated by its negative

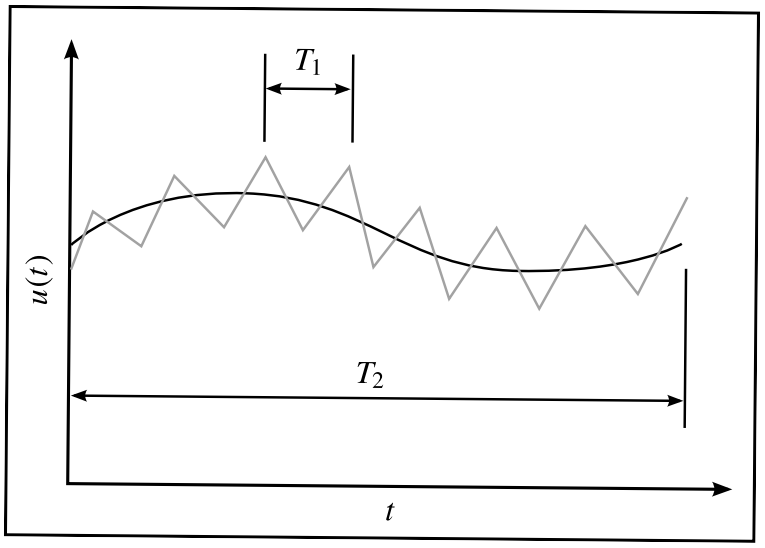

Figure 2.1: A time history of velocity at a point, showing fluctuations of a small timescale, T_1, and large timescale, T_2, after Wilcox (1994).

sign. The second term on the right hand side represents the diffusive effect of viscosity.

Heat transfer in tidal flows at the scale of tidal devices is negligible, and hence the transport of energy is not modelled.

2.1.2 Reynolds-averaged Navier-Stokes equations

The velocity of an unsteady flow is a function of both position and time. At a given point in a typical tidal flow, the velocity will fluctuate with a range of timescales, e.g. monthly and diurnal periods related to tidal forcing, the period of rotor revolution, the timescales of vortex-shedding from the turbine blades and support structure. At the smallest timescales, those of turbulent eddies within boundary layers and free shear layers, kinetic energy is converted to heat through viscous action. The timescales of this mechanism are several orders of magnitude lower than those related to the blade and rotor. Figure 2.1 illustrates velocity fluctuations on two distinct timescales, a small scale denoted T_1 and a large scale denoted T_2. In many practical cases, the small scale fluctuations may be represented through a turbulence model.

The flow velocity may be expressed as the sum of a time mean component $\overline{u_i}$ (which includes slowly varying oscillations, e.g. vortices shed from the blades and support structure)

and a fluctuating component u_i'.

$$u_i(\mathbf{x},t) = \overline{u_i}(\mathbf{x}) + u_i'(\mathbf{x},t) \tag{2.4}$$

Substitution for the instantaneous pressure and velocity in equation 2.3 in terms of their mean and fluctuating components, followed by time averaging, results in the Reynolds-averaged Navier Stokes (RANS) equations in conservation form.

$$\frac{\partial \overline{u_i}}{\partial x_i} = 0 \tag{2.5}$$

$$\rho\frac{\partial \overline{u_i}}{\partial t} + \rho\frac{\partial}{\partial x_j}\left(\overline{u_j}\,\overline{u_i}\right) = -\frac{\partial \overline{p}}{\partial x_i} + \mu\left(\frac{\partial^2 \overline{u_i}}{\partial x_j x_j} + \frac{\partial^2 \overline{u_j}}{\partial x_j \partial x_i}\right) - \frac{\partial}{\partial x_j}\left(\rho\overline{u_j' u_i'}\right) + \rho\overline{f_i} \tag{2.6}$$

Comparison of equations 2.3 and 2.6 highlights the Reynolds stress tensor, denoted by $\tau_{ij} = -\rho\overline{u_j' u_i'}$. This symmetrical tensor introduces six additional unknowns, which must be solved along with the three velocity components and the pressure. Closure of the existing system of four equations (the continuity equation and the three momentum equations) is achieved through the introduction of a turbulence model.

Turbulence models generally make use of the Boussinesq approximation, or an extension thereof, where Reynolds stresses may be linked to mean rates of deformation (Versteeg and Malalasekera, 1995)

$$\tau_{ij} = \mu_t\left(\frac{\partial \overline{u_i}}{\partial x_j} + \frac{\partial \overline{u_j}}{\partial x_i}\right) - \frac{2}{3}\rho k \delta_{ij} \tag{2.7}$$

where μ_t is known as the eddy viscosity and k is the specific kinetic energy of the turbulent fluctuations,

$$k = \frac{1}{2}\overline{u_i' u_i'}. \tag{2.8}$$

The Kronecker delta ($\delta_{ij} = 1$ if $i = j$ and $\delta_{ij} = 0$ for $i \neq j$) is used to account for the normal Reynolds stresses (for which $i = j$) correctly.

A variety of turbulence models exist which may introduce zero, one, two, or more

equations to relate μ_t to flow parameters such as specific turbulent kinetic energy k, specific dissipation rate ω, and the turbulence dissipation rate ε. For example, in the standard $k-\omega$ model, $\mu_t = \rho k/\omega$. Transport equations are then used to account for the production and dissipation of the turbulence parameters throughout the flow field. The turbulence model provides the additional information necessary to close the system, which can be fully described by equations for conservation of mass (equation 2.5), conservation of momentum (2.6), the Boussinesq approximation (equation 2.7), transport of turbulence modelling terms (equations 2.9 and 2.10), and the relationship between the turbulence model terms (k and ω in the current case) and the eddy viscosity, $\mu_t = f(k,\omega)$.

Throughout this work, the shear stress transport (SST) k-ω turbulence model (Menter, 1994) is employed, as it is capable of modelling flow separations, which can occur in flows past slender bodies such as aerofoils, rotor blades and turbine ducts. This model blends two constituent turbulence models, the k-ω and k-ϵ models, using a blending function based on wall distance. In near-wall regions, the former model dominates, and the latter model dominates in the far field. The transport equations for this model are presented below in a simplified form (ANSYS Inc., 2012*a*).

$$\rho\frac{\partial k}{\partial t} + \rho\frac{\partial}{\partial x_i}(k u_i) = \frac{\partial}{\partial x_j}\left[\left(\mu + \frac{\mu_t}{\sigma_k}\right)\frac{\partial k}{\partial x_j}\right] + G_k - Y_k + S_k \tag{2.9}$$

$$\rho\frac{\partial \omega}{\partial t} + \rho\frac{\partial}{\partial x_i}(\omega u_i) = \frac{\partial}{\partial x_j}\left[\left(\mu + \frac{\mu_t}{\sigma_\omega}\right)\frac{\partial \omega}{\partial x_j}\right] + G_\omega - Y_\omega + D_\omega + S_\omega \tag{2.10}$$

where σ_k and σ_ω are the turbulent Prandtl numbers for k and ω respectively, the term G represents generation, Y represents dissipation, D is a cross-diffusion term and S is a user-defined source term. The cross-diffusion term results from the translation of the standard k-ϵ transport equations into equations based on k and ω. Empirical coefficients are used in the equations describing the terms G, Y and D, thus closing the turbulence model and the RANS equations. Values for turbulence intensity and length scale are chosen by the user, based on assumptions about the flow environment, and applied as inlet boundary conditions to the model.

Two-equation turbulence models, such as the k-ω SST model used here, assume that the boundary layer is fully turbulent from the point of its initial development. In reality, as a boundary layer develops from the leading edge of an aerofoil section it is initially laminar. After some distance, dependent on Reynolds number, the boundary layer flow becomes unstable and a turbulent boundary layer develops. At high Reynolds numbers ($\mathrm{Re} > 10^6$ for an aerofoil (Lissaman, 1983)) this transition point is close to the leading edge and the assumption of a fully turbulent boundary layer is reasonable. However, at lower Reynolds numbers the extent of the laminar boundary layer becomes significant. The skin friction is lower in this region, and hence the assumption of a turbulent boundary layer may result in the over-prediction of drag. It is possible to predict the point of transition using a more sophisticated turbulence closure, such as the Transition SST model by Menter et al. (2004). However such models usually require the solution of additional transport equations, increasing the computational load. The full scale rotor blades simulated in chapters 3 and 4 are in the fully turbulent regime, and hence the k-ω SST model is considered appropriate. For the model scale turbine examined later in this chapter, the rotor blades operate in a transitional Reynolds number range. However, the physical model on which the current simulations are based was tested in a highly turbulent flow. Given the added expense of a transition model, and the possibility that free-stream turbulence would trigger early transition of the boundary layer, the k-ω SST turbulence model is used.

In the blade-resolved dynamic rotor models presented in this thesis, the unsteady form of the RANS equations (URANS) is solved. The instantaneous flow field is computed for a series of discrete points in time (timesteps). At each timestep, the rotor geometry is rotated by an increment and the flow field is updated. Unsteady flow features at the scale of the turbine, such as vortices shed from the rotor blades and supporting structure, may be directly resolved, while small-scale turbulent fluctuations are modelled as regions of increased effective viscosity. This assumption of separable scales of turbulence, which is the basis of URANS modelling, is not strictly correct. In a real tidal channel, no such distinction between large and small scale turbulence can be made, as a continuous spectrum

of turbulence scales exists. However a URANS-modelled flow field can be considered as an ensemble average of many real flows, and the tidal turbine models developed here are useful for predicting average turbine performance and wake development in that context.

2.1.3 The finite volume method

The simulations presented here are carried out using the commercial Reynolds Averaged Navier-Stokes (RANS) flow solver ANSYS Fluent (ANSYS Inc., 2012*b*). The discretisation and solution of the RANS equations is considerably complicated, due to unsteadiness, the inter-dependence of the velocity and pressure fields, and the non-linear transport of momentum. For the sake of clarity, the finite volume method is demonstrated for one-dimensional, steady state convection and diffusion of a scalar ϕ, following (Versteeg and Malalasekera, 1995). Subsequently, methods for temporal discretisation and pressure-velocity coupling are discussed.

Steady convection and diffusion of a scalar ϕ in one dimension is described as

$$\frac{\mathrm{d}}{\mathrm{d}x}\left(\rho u \phi\right) = \frac{\mathrm{d}}{\mathrm{d}x}\left(\Gamma \frac{\mathrm{d}\phi}{\mathrm{d}x}\right) \tag{2.11}$$

where u is velocity, ρ is density and Γ is the diffusion coefficient. Continuity must also be satisfied,

$$\frac{\mathrm{d}\rho u}{\mathrm{d}x} = 0. \tag{2.12}$$

Integration of equations 2.11 and 2.12 over the control volume ΔV on a uniform grid (illustrated in figure 2.2) yields

$$\left(\rho u A \phi\right)_e - \left(\rho u A \phi\right)_w = \left(\Gamma A \frac{\mathrm{d}\phi}{\mathrm{d}x}\right)_e - \left(\Gamma A \frac{\mathrm{d}\phi}{\mathrm{d}x}\right)_w \tag{2.13}$$

$$\left(\rho u A\right)_e - \left(\rho u A\right)_w = 0. \tag{2.14}$$

The derivative terms at the faces e and w are approximated by taking a central difference

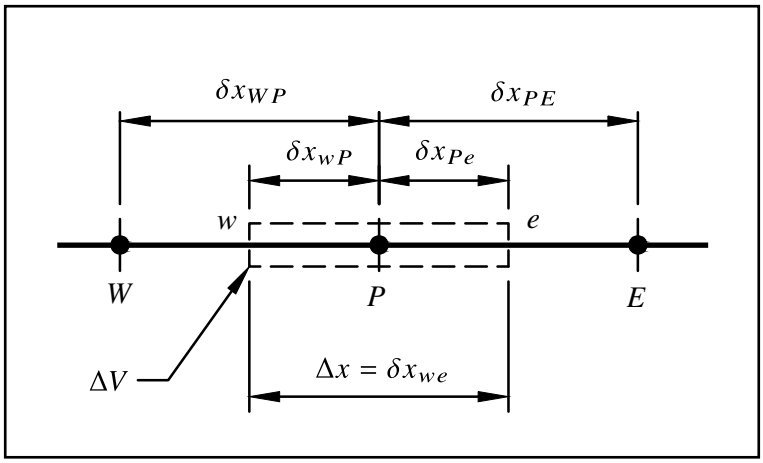

Figure 2.2: One-dimensional domain divided into discrete control volumes, adapted from Versteeg and Malalasekera (1995). The control volume ΔV around the node of interest P is indicated by a broken line. The west and east faces of the control volume are designated w and e respectively, while the neighbouring nodes are labelled W and E.

of the adjacent nodal values. Defining the convective mass flux per unit area as $F = \rho u$ and the diffusion conductance as $D = \Gamma/\delta x$, the transport and continuity equations become

$$F_e\phi_e - F_w\phi_w = D_e\left(\phi_E - \phi_P\right) - D_w\left(\phi_P - \phi_W\right) \tag{2.15}$$

$$F_e - F_w = 0 \tag{2.16}$$

The values of ϕ at the faces are also approximated by central differences, e.g. $\phi_e = \left(\phi_P + \phi_E\right)/2$. With some algebraic manipulation, the discretised transport equation can then be presented in a general form,

$$a_P\phi_P = a_W\phi_W + a_E\phi_E \tag{2.17}$$

where the coefficients a are

$$a_W = D_w + \frac{F_w}{2} \tag{2.18}$$

$$a_E = D_e + \frac{F_e}{2} \tag{2.19}$$

$$a_P = a_W + a_E + \left(F_e - F_w\right). \tag{2.20}$$

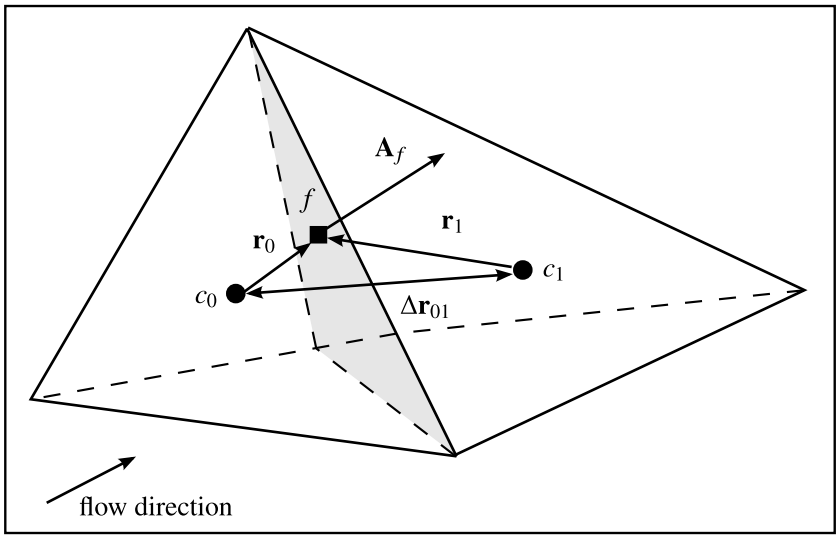

Figure 2.3: Illustration of two neighbouring tetrahedral elements within an unstructured grid, after ANSYS Inc. (2012*a*). The common face is shaded in grey.

A shortcoming of the central differencing scheme is that the influence of flow direction is not taken into account. In a strongly convective flow, the value of ϕ at a cell face should be influenced to a greater degree by the upstream nodal values, known as upwinding. ANSYS Fluent uses a second-order upwind discretisation scheme.

2.1.4 Discretisation for unstructured grids

While the preceding one-dimensional model serves as a useful introduction to the finite-volume method, discretisation methods employed by ANSYS Fluent are now discussed in the context of a three-dimensional unstructured grid, following ANSYS Inc. (2012*a*).

Two neighbouring tetrahedral elements from an unstructured grid are illustrated in figure 2.3. Scalar variables ϕ are stored at element centroids c. These values are used directly for the calculation of diffusion terms in the finite volume equations, which are discretised to second-order accuracy using a central differencing approach. The values of convection terms in the governing equation however are required at the element faces f, and are interpolated using a second-order upwind differencing scheme.

$$\phi_f = \phi_{c_0} + (\nabla\phi)_{c_0} \cdot \mathbf{r}_0 \tag{2.21}$$

$\nabla\phi$ is calculated using a least squares cell-based method as follows. The change in ϕ between the current centroid c_0 and the centroids of neighbouring cells c_i is expressed as

$$(\nabla\phi)_{c_0} \cdot \Delta\mathbf{r}_{0i} = (\phi_{c_i} - \phi_{c_0}) \tag{2.22}$$

where $\Delta\mathbf{r}_{0i}$ is the vector between the centroids c_0 and c_i. The procedure is repeated for each centroid surrounding c_0, yielding an over-determined system of equations which can be solved using the least-squares approach.

2.1.5 Temporal discretisation

For unsteady flow, the time-dependent term $\mathrm{d}\phi/\mathrm{d}t$ must also be discretised. ANSYS Fluent uses a fully-implicit scheme for temporal discretisation, where the solution variable ϕ at the current timestep n appears on both sides of the finite volume equation, e.g.

$$\frac{\phi^n - \phi^{n-1}}{\Delta t} = F\left(\phi^n\right) \tag{2.23}$$

where F represents the discretised finite volume equation. The sliding-mesh interface in ANSYS Fluent, used in the unsteady tidal turbine models in this thesis, is compatible with first-order discretisation only. Fully-implicit time discretisation is unconditionally stable; however an overly large timestep will be detrimental to solution accuracy.

2.1.6 Solution algorithm

The solution of the RANS equations is complicated due to the inter-dependence of the pressure and velocity fields. The continuity and momentum equations are intricately coupled, and must be solved through iterative methods. One such method, available in ANSYS Fluent and used throughout this work, is the SIMPLE algorithm (Patankar and Spalding, 1972), and is described in detail by Versteeg and Malalasekera (1995).

The SIMPLE algorithm begins with estimations of the pressure and velocity fields. A

pressure correction equation is used to calculate a pressure correction field, The pressure and velocity fields are then updated, and additional transport equations (e.g. for turbulence modelling terms) are solved. The procedure is repeated iteratively until the velocity and pressure fields converge to an acceptable degree. Under-relaxation, where a fraction of the old value of a variable is combined with its new value, is employed to avoid divergence of the solution. Following convergence, time is incremented by the timestep Δt, and the procedure is repeated.

The procedure is repeated, with the newly computed pressure and velocity fields providing the initial values for the next iteration (step 2e). This algorithm is continued in an iterative manner, until the pressure and velocity fields have converged to an acceptable degree. Under-relaxation, where a fraction of the old value of a variable is combined with its new value, is employed to avoid divergence of the solution. Following convergence, time is incremented by the timestep Δt, and the procedure is repeated (step 3).

2.1.7 Mesh types

The geometrical domain in which the flow field is to be calculated is discretised into an array of elements over which the finite volume equations are solved. Two approaches to domain discretisation are generally used – structured and unstructured mesh generation.

Structured meshes consist of regular rectangular or hexahedral elements which are mapped to the boundaries of the domain in a continuous manner. To generate a structured mesh, the domain is subdivided into a number of 'blocks', and element distributions are specified along the edges of each block. Hence the modeller has a high degree of control over mesh density throughout the domain. However refinement at one location, e.g. a boundary layer, will continue in each coordinate direction throughout the domain. This can lead to unnecessarily high resolution of the flow in the far field, with a consequent waste of computer storage and load. Additionally, highly skewed and high aspect ratio elements can occur, which may lead to poor convergence of the solver. The structured approach is described in further detail in chapter 5, where it is used for the simulation of a

series of two-dimensional duct profiles for a tidal turbine.

Good quality structured meshes are difficult to generate for complex three-dimensional geometries, such as the tidal turbine rotor modelled in this work. In this approach, maximum element dimensions are specified at surface and volume regions throughout the computational domain. The domain is then subdivided into unstructured triangular or tetrahedral elements in an automated fashion. Two algorithms are used for the three-dimensional models in this work. The octree algorithm is a 'top-down' method, where the domain is subdivided into many tetrahedra, of uniform size based on the smallest dimension specified in the domain. Where an element is smaller then the local size limit, groups of 8 elements are merged to produce larger elements. This process is repeated recursively, until element sizes are just below the specified local size limits. An example of this approach is the three-dimensional model of a ducted turbine in figure 5.23 of chapter 5.

The second approach to three-dimensional unstructured mesh generation is the Delaunay algorithm (ANSYS Inc., 2012*c*). Beginning with a mesh consisting solely of two-dimensional triangular surface elements, layers of tetrahedral elements are grown from the surface elements, with the elements of subsequent layers increasing in volume by a constant ratio, until the domain is filled. Node locations in a new layer are determined by Delaunay triangulation of the nodes in the preceding layer. In a similar manner to the octree approach, element size can be limited in local volume regions throughout the domain. The Delaunay method has been used for the turbine model later in this chapter, as well as the models in chapters 3 and 4.

The boundary layer flows adjacent to the rotor and support structure geometry require very high mesh resolution in the wall-normal direction. This is achieved by generating layers of high aspect ratio prismatic elements from the triangular elements on these surfaces. The pre-existing tetrahedral elements are either displaced in the wall-normal direction or deleted.

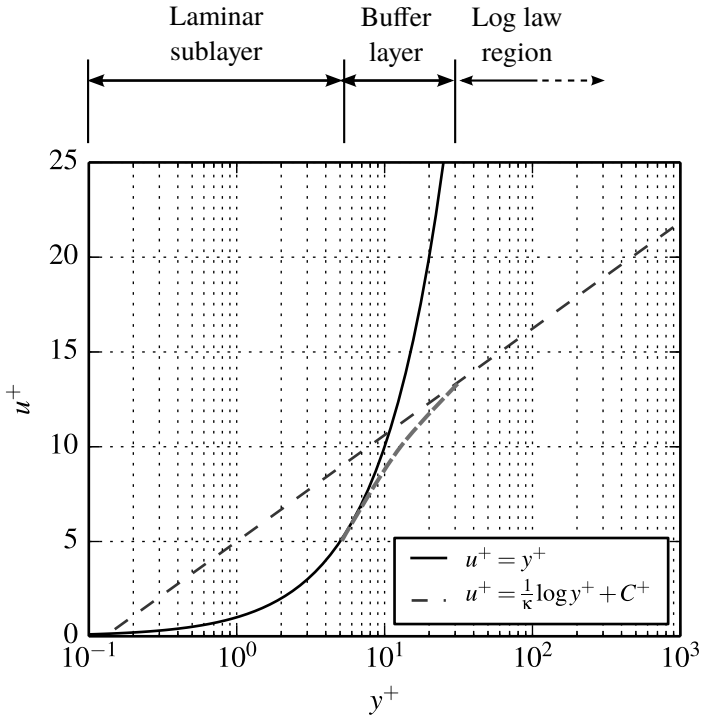

Figure 2.4: Non-dimensional velocity u^+ as a function of non-dimensional wall distance y^+.

2.1.8 Wall modelling

Approaches to modelling the turbulent velocity profile near a wall boundary are discussed now, following Schlichting (2000) and Versteeg and Malalasekera (1995). Velocity is expressed in non-dimensional form as $u^+ = u/u_\tau$, where the friction velocity is defined as $u_\tau = \sqrt{\tau_w/\rho}$, and τ_w is wall shear and ρ is fluid density. Wall distance is non-dimensionalised as $y^+ = yu_\tau/\nu$, where ν is the kinematic viscosity of the fluid. The region very close to the wall, $y^+ < 5$, is known as the laminar sublayer, where velocity is dependent on wall distance and fluid viscosity. In dimensionless form, this relationship is expressed as $u^+ = y^+$. Further from the wall, in the range $y^+ > 25$, the velocity profile can be expressed by the law of the wall,

$$u^+ = \frac{1}{\kappa} \ln y^+ + C^+ \tag{2.24}$$

where $\kappa = 0.41$ is the von Kármán constant and C^+ is an empirically determined constant with a value of approximately 5 for a smooth wall.

Two methods are used in RANS modelling to account for the high velocity gradient in a turbulent boundary layer. Firstly, the boundary layer can be resolved explicitly. This approach requires that the wall-adjacent centroid lies within the laminar sublayer, i.e. $y^+ < 5$, and the laminar sublayer velocity relationship is used to calculate velocity. The rate of increase of centroid spacing in the wall normal direction must be limited such that the velocity gradient is adequately captured. This can lead to high numbers of elements in the computational grid, increasing the computational cost of the simulation.

The second approach to account for the boundary layer velocity gradient is to set a larger wall normal distance, such that the wall-adjacent centroid falls within the logarithmic law layer, $y^+ > 25$. In this case, the logarithmic law of the wall is used to calculate the velocity at the wall-adjacent centroid. If the wall-adjacent centroid falls within the buffer layer, neither wall law is appropriate, and the accuracy of the solution suffers. The implementation of the k-ω SST turbulence model in ANSYS Fluent includes an 'enhanced wall treatment', whereby the laminar sublayer law is blended smoothly through the buffer layer into the logarithmic law region (ANSYS Inc., 2012*a*). This method mitigates the adverse effects which would otherwise occur when the wall-adjacent centroid falls within the buffer layer.

Both of these approaches are used for various models in this work. In the blade-resolved model of a tidal turbine at experimental scale in section 2.2.2, the boundary layers at the blade surfaces are fully resolved. Wall functions are used to model the boundary layers for the full scale turbine simulations in chapters 3 and 4. Two models of a ducted tidal turbine are presented in chapter 5. In the two dimensional axi-symmetric model, used for a comparative study of a range of duct geometries, the boundary layers at the duct surfaces are resolved. In the second case, a model scale ducted turbine is simulated in a three-dimensional domain, and wall functions are employed at the duct surfaces.

2.2 Validation

A primary aim of this thesis is to investigate the effects of flow conditions such as shear, confinement, alignment and waves on the power and loading of an axial flow tidal turbine through computational modelling. Development of the computational techniques, such as grid generation and the application of boundary conditions was carried out at model scale. Predictions of turbine performance and wake development were compared to experimental data to assess the effectiveness of the developed methods, which were subsequently applied in the full scale simulations.

Details of the physical model are not publicly available (Buvat et al., 2012) so a description of the experiment is given here. The computational approaches to reproduce the experimental conditions are then described, and the results of the two models are compared.

2.2.1 Physical model

A model scale tidal turbine was built and tested as part of the PerAWaT project (Rawlinson-Smith et al., 2010). Testing was carried out by project partners Électricité de France (EDF) at the National Hydraulic and Environment Laboratory (NHEL) at Chatou, Paris (Buvat et al., 2012).

2.2.1.1 Water channel

The recirculating water channel at NHEL of length 80 m, width $s = 1.5$ m, with a working section of approximately 72 m and maximum water depth of $h = 1.2$ m. The bottom and one side wall of the flume are lined with concrete, and the other side wall is constructed from transparent perspex. For these tests, the centreline flow velocity was $u_{\mathrm{cl}} = 0.55\,\mathrm{m\,s^{-1}}$ and the depth was $h = 0.8$ m, resulting in a Froude number (based on centreline velocity) of $\mathrm{Fr} = u_{\mathrm{cl}}/\sqrt{gh} = 0.196$. These conditions are equivalent to the full scale turbine (with diameter $D = 18$ m) operating in flow of velocity $u_{\mathrm{cl}} = 3\,\mathrm{m\,s^{-1}}$ and depth $h = 25$ m. The

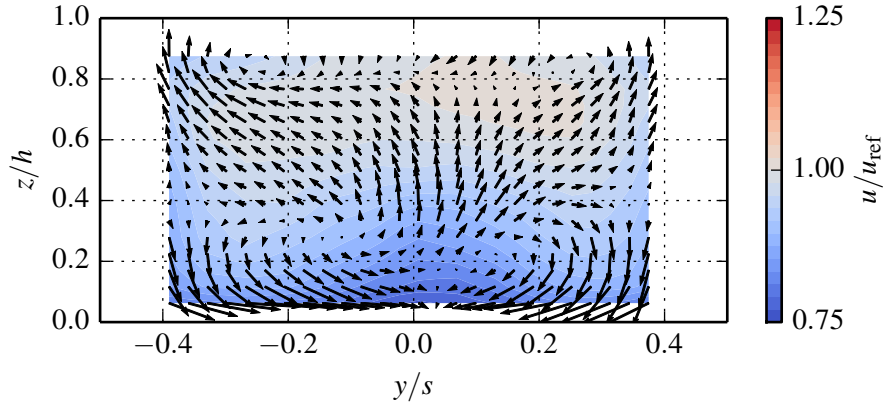

Figure 2.5: Contours of time-averaged streamwise velocity at the rotor plane in the absence of a turbine. The vectors indicate the direction and magnitude of spanwise flow, with the largest vectors corresponding to $0.02u_{\text{ref}}$.

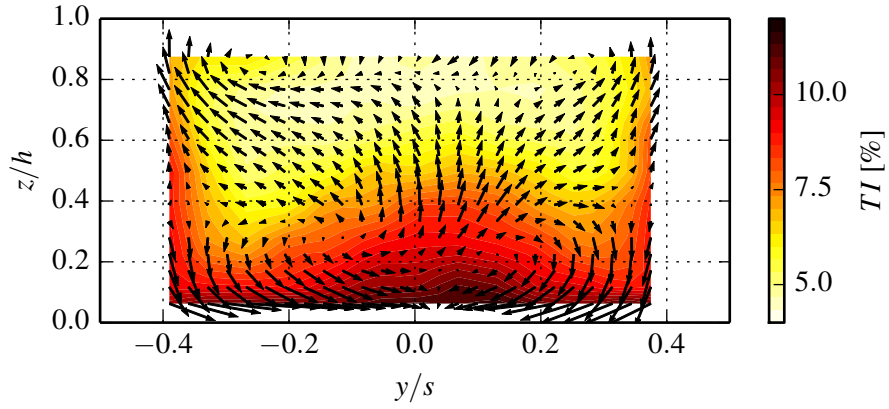

Figure 2.6: Contours of time-averaged turbulence intensity at the rotor plane in the absence of a turbine.

flow is conditioned by a series of grids at the flume entrance, and a polystyrene block is used to stabilise the free surface. The flow is allowed to develop for a distance of 32 m before encountering the rotor.

Three orthogonal components of velocity are measured using a SonTek acoustic Doppler velocimeter (ADV). The measurement volume is less than 0.1 cm^3, and the precision of the sensor is 1% of the velocity magnitude. Velocity measurements are taken at a frequency of 25 Hz over a period of 120 s. A manually-operated traversing rig is used to set the position of the ADV at prescribed locations in the flow field while a test is in progress. The precision of the sensor location is 0.001 m.

A two-dimensional profile of streamwise velocity at the rotor plane in the absence of

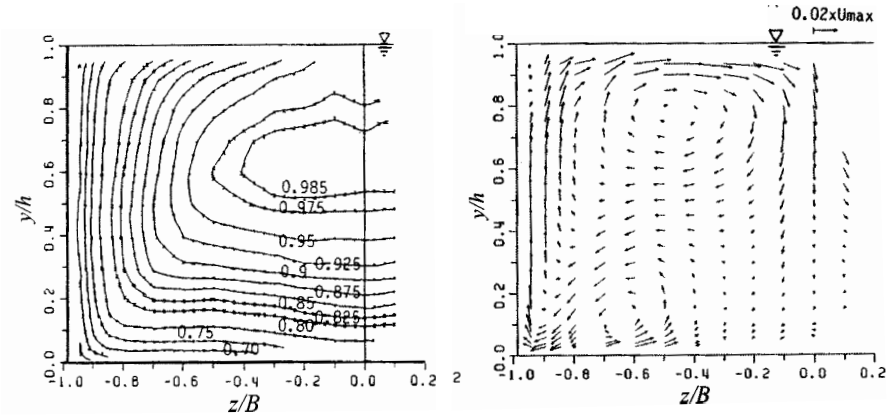

(a) Streamwise velocity (b) Spanwise velocity

Figure 2.7: (a) Contours of time-averaged streamwise velocity and (b) vectors indicating spanwise flow magnitude and direction for open channel flow measurements by Nezu and Rodi (1986)[†].

the turbine is presented in figure 2.5. Velocity does not increase monotonically from the channel boundaries to the centre of the free surface, as would be expected for laminar channel flow. Instead, maximum velocity occurs in a region between 60% and 80% of the water depth. A region of low velocity is present around the vertical midplane ($y = 0$) of the flow, extending from the channel bed up to a depth of approximately $z = 0.3h$. It is clear from figure 2.6 that this low velocity region is also highly turbulent.

Nezu (2005) explains that secondary currents in turbulent flow through a straight channel[‡] are affected by spanwise gradients in Reynolds stresses. Specifically, the generation of secondary currents is related to the gradient of the difference between the normal Reynolds stresses in the cross-stream plane, $\frac{\partial^2}{\partial y \partial z}\left(\overline{v'^2} - \overline{w'^2}\right)$. These secondary currents then affect the spanwise distribution of the mean streamwise velocity u.

Measurements of flow in an open channel by Nezu (2005) are shown in figure 2.7, showing similar features to the velocity field in figure 2.5. In both cases, a clockwise circulation is observed in the upper left hand corner, along with an anti-clockwise circulation in the lower left hand corner of the channel. Note also that the magnitude of the secondary flows is similar; the maximum spanwise velocity is approximately 2% of the reference streamwise velocity.

[†]With permission from ASCE. This material may be downloaded for personal use only. Any other use requires prior permission of the American Society of Civil Engineers.

[‡]Note that secondary currents can be generated by channel curvature for laminar or turbulent flow.

Turbulence-related secondary flows cannot be predicted numerically by turbulence models based on the Boussinesq approximation, as this hypothesis assumes that the normal Reynolds stresses are equal, $\overline{u'^2} = \overline{v'^2} = \overline{w'^2}$ (Versteeg and Malalasekera, 1995; Schmitt, 2007), and hence the Reynolds stress term related to secondary currents, $\frac{\partial^2}{\partial y \partial z}\left(\overline{v'^2} - \overline{w'^2}\right)$, cannot arise. The k-ε and k-ω families of turbulence models fall into this category. Algebraic stress and Reynolds stress turbulence models are capable of predicting such flows, but are more costly in terms of computational demand. Time-averaged secondary currents do not usually occur when the aspect ratio of the channel is greater than $h/s = 5$, although they can develop over time due to sediment transport at the channel bed. Such flows are not expected to be a significant issue for tidal turbines, as the aspect ratio of a tidal channel would typically greatly exceed $h/s = 5$, and long-term secondary flow patterns are unlikely to occur due to the periodic variations in velocity magnitude and direction. Hence it is considered unnecessary to attempt to reproduce secondary flows in the full scale tidal turbine modelling undertaken later in this work, and an isotropic turbulence model is used. Some disagreement in velocity profiles will occur between the velocity and turbulence profiles measured in the EDF flume and the current computational model.

2.2.1.2 Turbine

The model turbine has a three-bladed axial flow rotor with a radius of $R = 0.3\,\text{m}$. The resulting area blockage, defined as the ratio of the swept area of the rotor to the cross-sectional area of the channel, is $B \approx 23.6\%$.

A NACA 4415 profile is used for the rotor blades. The chord length varies linearly from $c = 0.025\,\text{m}$ at the radial location $r = 0.2R$ up to a maximum value of $c = 0.095\,\text{m}$ at $r = 0.4R$, and then varies linearly down to $c = 0.037\,\text{m}$ at $r = 0.93R$. Beyond this radius, the chord length reduces to 0.033 m at the blade tip. Blade section twist, β, varies linearly from 30° at $r = 0.2R$ down to 5° at $r = 0.93R$. The Reynolds number at the radial location $r = 0.8R$ ranges from $\text{Re} \approx 7.2 \times 10^4$ for a tip speed ratio $\lambda = u_{\text{tip}}/u_\infty = 3$, to

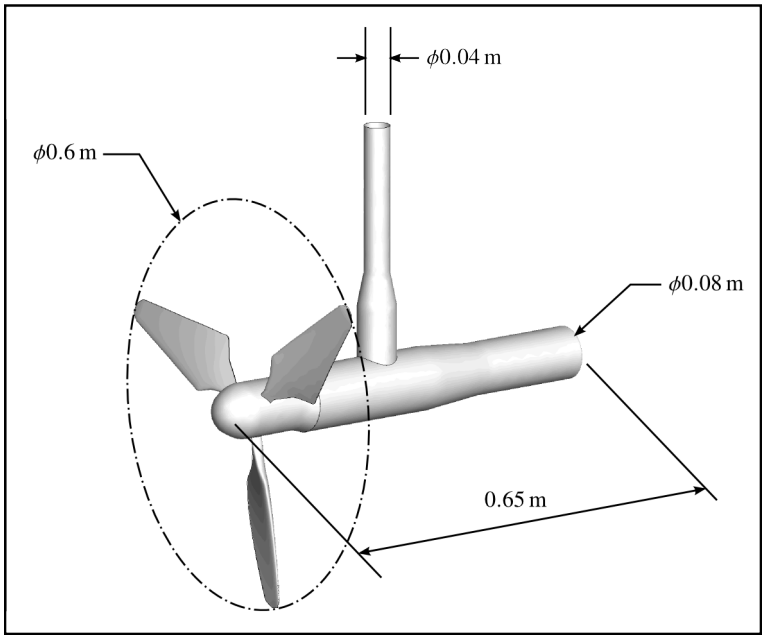

Figure 2.8: CAD rendering of the model turbine with the major dimensions indicated. The rotor rotates anti-clockwise from this perspective.

$\mathrm{Re} \approx 1.2 \times 10^5$ for a tip speed ratio of $\lambda = 5$. The rotor blades are manufactured by casting a hard polymer-glass powder composite around a tapered steel spar.

The rotor speed is connected to a speed-controlled Maxon RE30 generator. Thrust and torque sensors, manufactured and calibrated by Futek and each with an accuracy of 0.06%, are connected to the main rotor shaft. These signals are amplified on-board to maintain signal quality. The instrumentation is calibrated by measuring the rotor speed via a tachometer, and cross-referencing it to the voltage applied by the controller. Shielded cables are used to minimise electromagnetic interference from the generator.

The generator is housed within a cylindrical nacelle measuring approximately 0.65 m in length and 0.08 m in diameter. The rotor features a rounded nosecone of radius 0.4 m. The turbine is suspended from above by a tower of diameter 0.04 m.

The turbine is tested at 26 tip speed ratios in the range $0.25 < \lambda < 7.5$. Measurements of wake velocity are taken at a finite set of locations for tip speed ratios of $\lambda = 3.5$ and $\lambda = 4.5$.

2.2.2 Computational model

A computational model of the turbine is developed using the flow solver ANSYS Fluent. Pertinent aspects of the model are described in this section, and predictions of rotor performance and wake development are compared with experimental measurements.

2.2.2.1 Velocity and turbulence profiles

As discussed previously, the velocity profile observed in the EDF flume cannot be reproduced using an isotropic turbulence model. In this computational model, the velocity profile is based on a logarithmic law of the wall,

$$u = \frac{u_\tau}{\kappa} \ln \frac{\eta}{\eta_0} \tag{2.25}$$

$$u_\tau = \sqrt{\frac{\tau_w}{\rho}}, \tag{2.26}$$

where u_τ is the friction velocity, η is the distance from the nearest wall normalised by total profile height, η_0 is the wall roughness height, and τ_w is the shear force at the wall. A modification is made to the profile beyond a certain distance from the wall, η_{blend} so that the gradient tends to zero at the upper boundary. The following adjustment is made to the profile when $\eta > \eta_{blend}$, and is illustrated in figure 2.9.

$$u_{adj} = -\frac{(1-\eta_{blend})^2 - (1-\eta)^2}{2\eta_{blend}\,(1-\eta_{blend})} \tag{2.27}$$

Horizontal and vertical velocity profiles are blended to produce a two-dimensional profile with the same reference (e.g. centreline) value.

$$u\,(y,z) = \frac{\frac{u(y)}{y} + \frac{u(z)}{z}}{\frac{1}{y} + \frac{1}{z}} \tag{2.28}$$

The same wall roughness height used to derive the velocity profile is prescribed in the corresponding rough wall boundary condition at the bed and sides of the computational domain. A wall roughness height of $y_0 = z_0 = 3.307 \times 10^{-4}\,\mathrm{m}$ is used, based on a

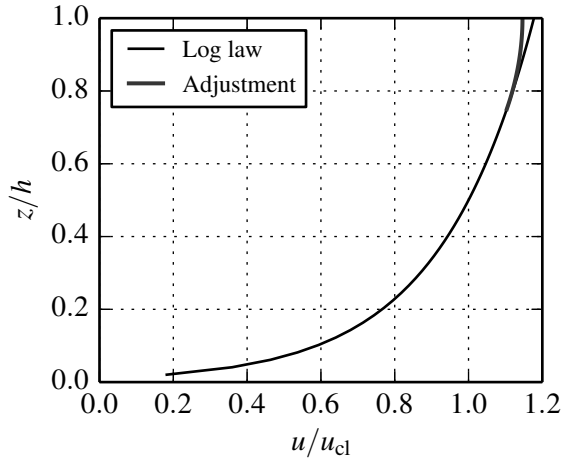

Figure 2.9: Illustration of the correction (thick line) made to the logarithmic velocity profile to force the velocity gradient to zero at the upper boundary.

least squares fit of a logarithmic velocity profile to the measured profile along the vertical midplane $y = 0$. The same wall roughness height is applied at each wall boundary, despite the fact that two boundaries are of concrete and the other is of perspex. A symmetry condition is applied to the upper boundary to approximate the free surface as a rigid lid.

Differences between the computed and measured velocity profiles are dominated by the presence of secondary currents in the physical case, and will not be reduced significantly by changes to the wall roughness parameter. A cross-section of the computed velocity profile, extracted from the turbine simulation at the plane $x = -2D$ is presented in figure 2.10. The contour scale is identical to the experimental case in figure 2.5 so that direct comparison can be made. While the experimental velocity profile is irregular due to secondary currents, the discrepancy within the rotor region (marked by the broken line) is generally less than 5%.

Profiles of turbulent kinetic energy k and specific dissipation rate ω are prescribed at the inlet boundary, based on the inlet velocity profile. The algebraic turbulence model of Cebeci and Smith (1974) is used to calculate kinematic eddy viscosity, ν_t, based on

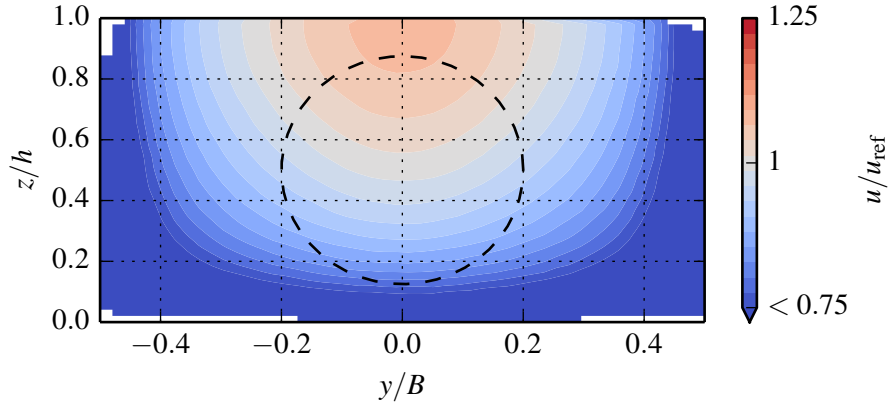

Figure 2.10: Contours of computed normalised streamwise velocity at the plane $x = -2.5D$, for comparison with figure 2.5. The velocity tends to zero at the lower and lateral boundaries and are included in the contour level $u/u_{\text{ref}} < 0.75$ so that the same colour scale as figure 2.5 may be used. The broken line marks the outline of the rotor.

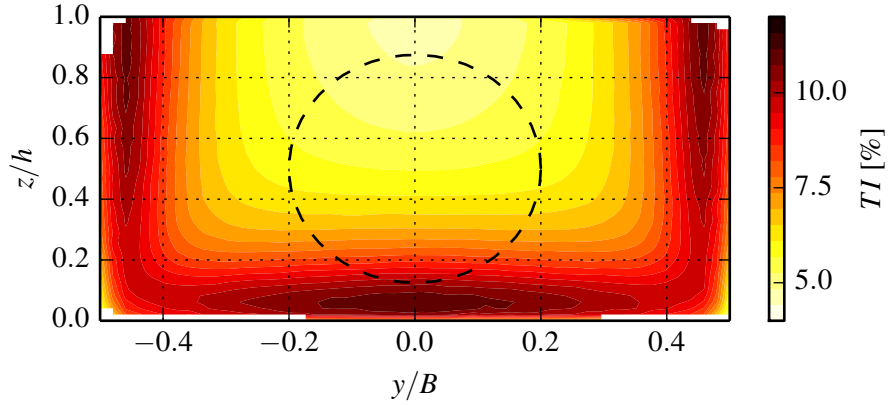

Figure 2.11: Contours of computed turbulence intensity at the plane $x = -2.5D$. The broken line marks the outline of the rotor.

velocity gradient and wall distance.

$$\nu_t = \begin{cases} \kappa^2 z^2 \left|\frac{\partial \bar{u}}{\partial z}\right| & \text{if } 0 < z < z_c \\ \alpha U_e \delta & \text{if } z_c \leq z \end{cases} \tag{2.29}$$

where z_c is the smallest wall distance where both equations return the same value, $\alpha = 0.016$ is a constant, U_e is the velocity at the edge of the boundary layer (in this case the velocity at the free surface $z = h$ or along the midplane $y = 0$, and δ is the displacement thickness. The turbulent length scale, l, is calculated by rearranging the mixing length

model of (Prandtl, 1925),

$$\nu_t = l^2 \left| \frac{\partial \overline{u}}{\partial z} \right| \tag{2.30}$$

The turbulent kinetic energy, k, may be related to the turbulent length scale and eddy viscosity by dimensional considerations Schlichting (2000); Prandtl (1945)

$$\nu_t = c_P l \sqrt{k} \tag{2.31}$$

where c_P is a constant with a value of 0.55. Finally, the specific dissipation rate is calculated from turbulent viscosity and turbulent kinetic energy using the definition of ν_t from the k-ω SST turbulence model Wilcox (1994); Menter (1994)

$$\nu_t = \frac{k}{\omega}. \tag{2.32}$$

A computed profile of turbulence intensity at the plane $x = -2.5D$ is presented in figure 2.11, and compares reasonably well with the corresponding experimental profile in figure 2.6.

2.2.2.2 Spatial discretisation

Discretisation of the computational domain is driven by two opposing considerations. Firstly, grid resolution should be sufficiently high that relevant physical flow features at the rotor and wake can be captured, and the prediction of turbine performance is satisfactory. Secondly, it is desirable to minimise the computational cost of the model by limiting the total number of elements, so that it can be run multiple times to facilitate the investigation of various operating conditions.

The sensitivity of rotor performance to grid resolution is examined through a grid convergence study on a two-dimensional aerofoil profile based on the rotor operating conditions. At a tip speed ratio of $\lambda = 4$, corresponding to peak power extraction, the blade Reynolds number at the radial position $r = 0.8R$ is $\mathrm{Re} = 9.6 \times 10^4$.

Three two-dimensional unstructured grids of increasing refinement are generated about a NACA 4415 profile. Views of the 'coarse' resolution grid are presented in figure 2.12. The largest element size at the blade surface is $0.08c$, reducing to $0.01c$ at the leading edge and $0.0025c$ at the trailing edge. Element size is limited to $0.64c$ in the far field.

Several layers of high aspect ratio quadrilateral elements are used to resolve the boundary layers at the blade surfaces. As discussed in section 2.1.8, wall functions can be used to model the boundary layer within the wall-adjacent elements. This typically enables larger wall-adjacent elements (with wall-normal height of $y^+ > 25$) and fewer layers of quadrilateral boundary layer elements, thereby reducing computational load. However, wall functions are intended for steady, attached flow, and do not predict boundary layer separation well (Versteeg and Malalasekera, 1995). It is likely that boundary layer separation will occur at portions of the rotor blades during operation. It may be necessary to capture these features of the flow in order to achieve good agreement in rotor performance with the physical model. Hence a wall-resolved approach is taken, with the wall-adjacent element heights corresponding to $y^+ < 11.25$ (ANSYS Inc., 2012*a*).

For the coarse grid, the wall normal cell height is 1×10^{-4} and the height of subsequent layers increases by a factor of 1.5.

The 'medium' resolution grid is generated by subdividing each element in the high resolution area around the aerofoil to produce four 'child' elements. Elements in the far field are not subdivided. Mesh quality, i.e. element aspect ratio and transitions in size, is improved through the application of a smoothing algorithm. This procedure of subdivision and smoothing is repeated to produce the 'fine' mesh. The resultant refinement ratio across the set of grids is $r = 2.0$. Dimensions for each grid are listed in table 2.1.

Table 2.1: Element size limits in terms of the chord length c for the grid refinement study. The three columns on the right hand side describe the resolution of the boundary layer region.

Mesh	Aerofoil	Leading edge	Trailing edge	1st cell height	Layers	Growth ratio
Coarse	0.08	0.01	2.5×10^{-3}	1×10^{-4}	12	1.5
Medium	0.04	5×10^{-3}	1.25×10^{-4}	5×10^{-5}	24	1.22
Fine	0.02	2.5×10^{-3}	6.25×10^{-5}	2.5×10^{-5}	48	1.1

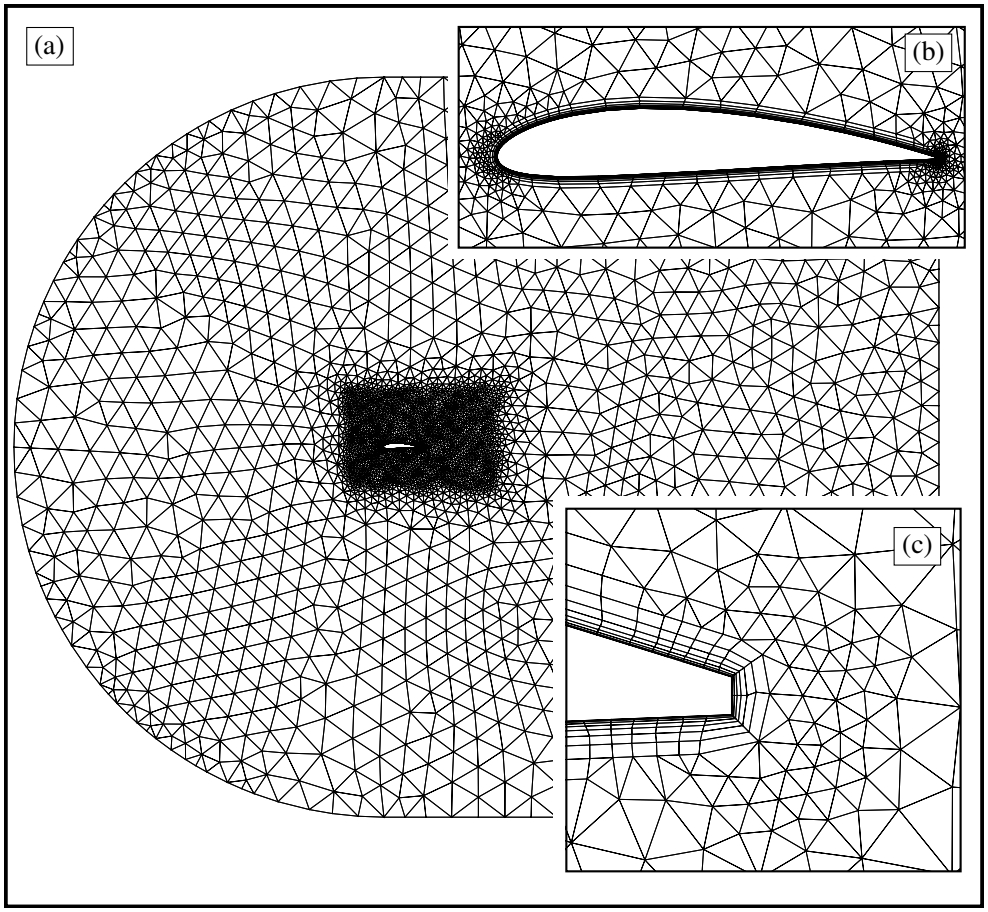

Figure 2.12: (a) The coarse computational grid for the aerofoil convergence study with inset close-up views of (b) the aerofoil section and (c) the trailing edge. The flow direction is generally from left to right, at an angle of attack α relative to the blade chord. The distance between the leading edge and the domain boundaries is 15 chord lengths.

Each aerofoil grid is simulated in steady flow at $\mathrm{Re} = 8.3 \times 10^4$ for consistency with available experimental data (Miley, 1982). Velocity magnitude and direction are specified along the upper and lower domain boundaries as well as the curved upstream boundary (see figure 2.12). The aerofoil is simulated at angles of attack in the range $-6° < \alpha < 12°$ by altering the direction of the velocity at the inflow boundaries. Information on the freestream turbulence intensity is not available; a relatively low, uniform value of $TI = 2\%$ is prescribed at the inflow boundary along with a turbulence length scale of $l = 0.1c$. A uniform pressure condition of $p = 0\,\mathrm{Pa}$ is applied at the downstream boundary.

The flow field is calculated using the steady solver of ANSYS Fluent, which is valid for cases where the flow remains attached. The k-ω SST turbulence model is used. A second

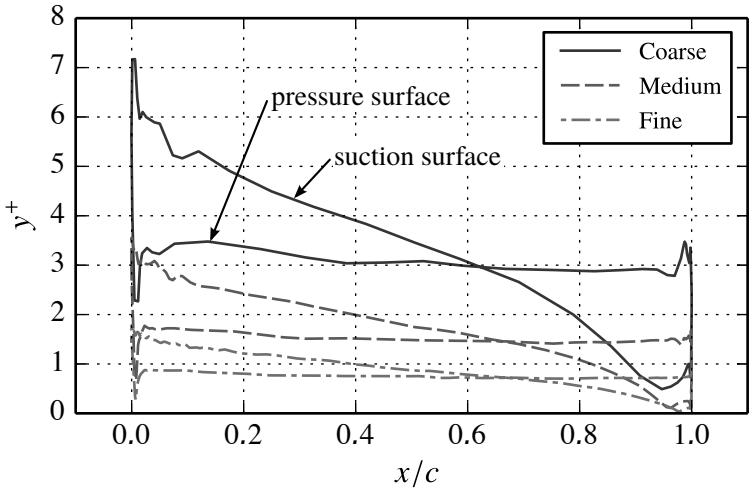

Figure 2.13: Distribution of non-dimensional wall distance y^+ at the aerofoil surface for three levels of grid resolution.

order upwind scheme is used for the discretisation of momentum and turbulence terms. The SIMPLE algorithm is used for pressure-velocity coupling (Patankar and Spalding, 1972). Lift and drag forces are monitored during the solution, as well as residual values of the transport equations returned by the solver. Convergence is determined primarily when the relative error of lift or drag changes by less than 0.1% in 100 iterations. This typically occurs within 1000 to 3000 iterations for the coarse and medium grids, and between 3000 - 6000 iterations for the fine grid. In this time, the residual values from the solution of the continuity and momentum equations reduce by 6 orders of magnitude, whereas those for the turbulent kinetic energy and dissipation rate reduce by 4 - 5 orders of magnitude.

For effective resolution of the boundary layer, at least one cell centroid should lie within the viscous sublayer, corresponding to $y^+ < 5$. This is the case for the three grids (apart from a portion at the leading edge of the coarse grid), as shown in figure 2.13.

Plots of lift coefficient, $C_L = L/\frac{1}{2}\rho u_\infty^2 c$ and drag coefficient, $C_D = D/\frac{1}{2}\rho u_\infty^2 c$ are displayed in figures 2.14 (a) and (b), with comparison to experimental data (Miley, 1982). Solutions on the three grids generally exhibit good numerical convergence for moderate angles of attack, $-6° < \alpha < 6°$. At higher angles of attack, the flow separates from the upper surface of the aerofoil upstream of the trailing edge. Grid convergence is affected in this range as the separation point is highly dependent on local grid resolution. The separation

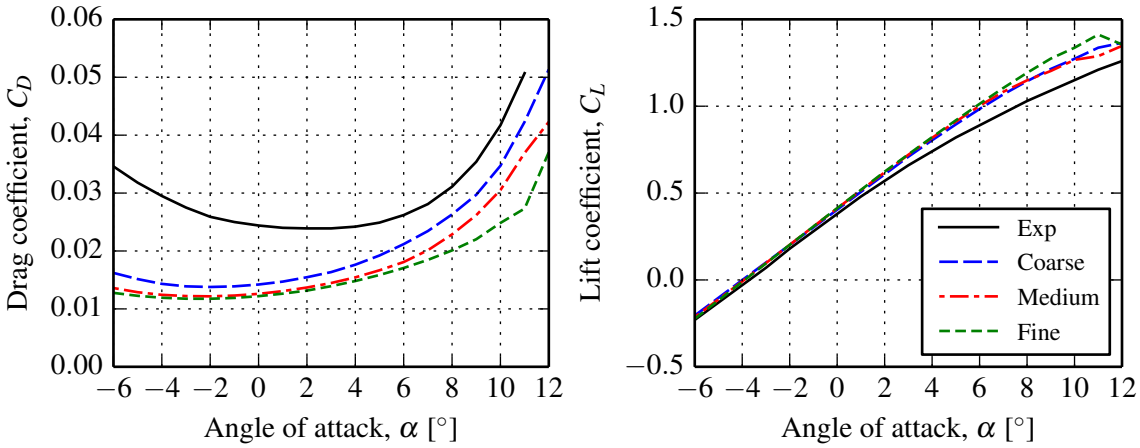

(a) (b)

Figure 2.14: Comparison of computed results from coarse, medium and fine resolution grids with experimental measurements of (a) drag coefficient and (b) lift coefficient for a NACA 4415 profile at Re = 8.3×10^4.

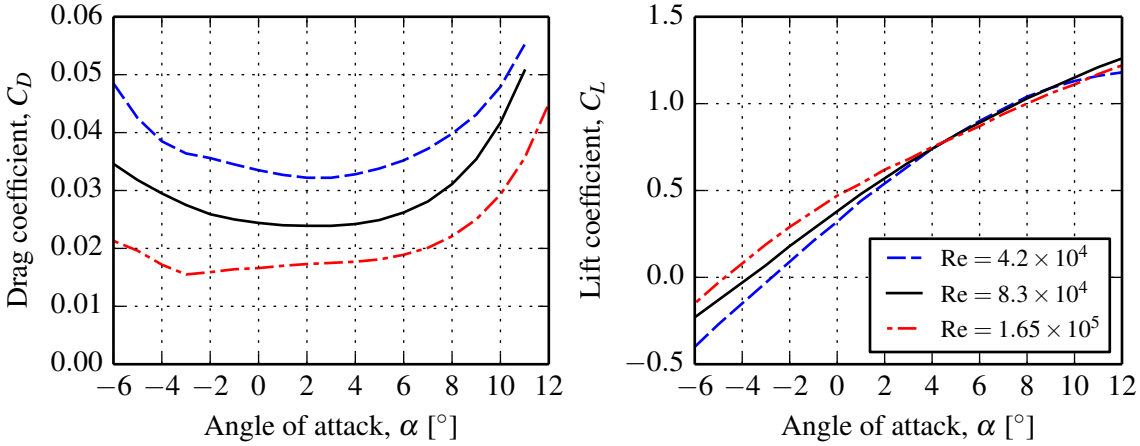

(a) (b)

Figure 2.15: Effect of Reynolds number on physical measurements of (a) drag coefficient and (b) lift coefficient for a NACA 4415 aerofoil (Miley, 1982). The data at Re = 8.3×10^4, indicated by the solid black line, corresponds to the experimental data in figure 2.14 above.

point can only occur at discrete locations along the aerofoil surface corresponding to grid points, and may not be consistent between the three levels of grid resolution. Unsteady vortex-shedding will also result from flow separation, and is outside the scope of this model as it cannot be captured accurately by a steady flow solver. Additionally, it is unlikely that it will be feasible to capture flow features at this scale in the three-dimensional rotor model.

Significant differences are present between the numerical predictions and experimental measurements of lift and drag. The lift coefficient is slightly over-predicted for the full range of angles of attack, with the grids converging to values away from the experimental data. For flow angles below about 4°, drag is under-predicted, and at higher angles it is over-predicted. Drag coefficient is under-predicted at all flow angles, and again the computed values tend to reduce further with increasing spatial resolution. This disagreement is due to the fact that the turbulence model is applicable to fully-turbulent flow only, whereas the aerofoil is operating in a transitional Reynolds number regime. The forces on the physical model in the transitional Reynolds regime are extremely sensitive to free stream turbulence and surface roughness. At higher Reynolds numbers the measured drag decreases and tends towards the computed values, as shown in figure 2.15.

A three-dimensional unstructured grid is generated for the model scale rotor using the dimensions of the coarse grid presented above. Maximum element sizes at the blade surface correspond to those in table 2.1. Twelve layers of prismatic elements are generated at the blade surfaces, with a wall-adjacent cell height of 5×10^{-6} m, and a growth ratio of 1.5. This results in a dimensionless wall distance of $y^+ < 3$ at the blades when the flow field has been solved. The maximum element size in the near field, defined as the region bounded by the planes $x = -0.1D$, $x = D$, $y = -0.6D$ and $y = 0.6D$, is $0.25c$. Beyond this region, element size increases to $0.5c$. A summary of element size limits is given in table 2.2. The total numer of elements is 4.75 million. An oblique view of the surface mesh on the rotor and sliding mesh interface is presented in figure 2.16.

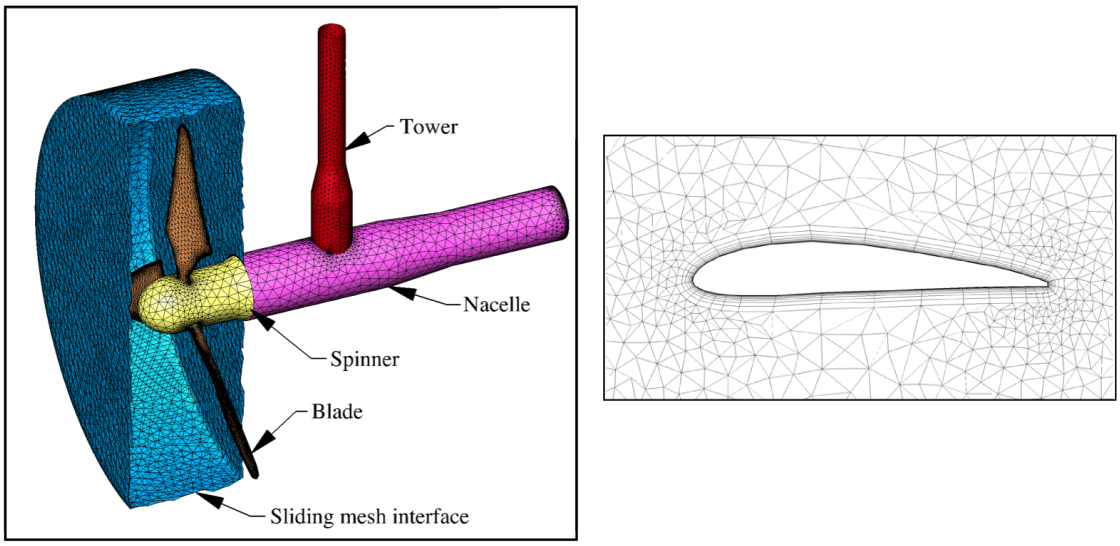

(a) (b)

Figure 2.16: (a) Oblique view of the surface mesh on the experimental scale turbine model, also showing the sliding mesh interface, and (b) a cross-section through the volume mesh around a rotor blade at the radial location $r = 0.8R$. Element sizes in this region are based on the coarse grid in figure 2.12.

2.2.2.3 Rotor motion

A sliding mesh interface is used to enable angular motion of the rotor relative to the domain boundaries. The rotor and spinner are enclosed within a cylindrical region which is lined with non-conformal surface meshes of two-dimensional triangular elements on either side, as shown in figure 2.16. The timestep size is $\Delta t = 0.0034$ s, corresponding to an angluar increment of the rotor of $\Delta\theta = 0.6°$. This is equivalent to the $r = 0.8R$ blade section advancing linearly by $0.1c_{0.8R}$, where $c_{0.8R}$ is the local chord length.

Table 2.2: Element size limits in terms of the blade chord length c at the radial location $r = 0.8R$ for the three dimensional rotor mesh.

Location	Element size limit
Spinner	$0.20c$
Nacelle	$0.25c$
Tower	$0.15c$
Near field	$0.25c$
Far field	$0.50c$

2.2.3 Comparison of model scale simulation and experiment

The turbine is simulated at tip speed ratios of 3, 4 and 5. Velocity, turbulence and wall boundary conditions are as described in section 2.2.2.1. A uniform pressure profile of $p = 0\,\mathrm{Pa}$ is specified at the outlet boundary, six diameters downstream of the rotor. A symmetry condition is applied at the upper boundary of the domain, approximating the free surface as a rigid lid. The rotor is simulated at a constant tip speed ratio for at least two 'flow-through' periods, i.e. the length of time taken for a fluid parcel to travel from the rotor plane to the outlet boundary, which typically takes 20 seconds in total, or approximately 6000 timesteps. Ten sub-iterations are taken per timestep, in which time the solution residuals reduce by at least four orders of magnitude. The total computational load is approximately 900 CPU-hours on a high-performance computing cluster with a clock rate of 2.0 MHz.

Rotor performance is reported in terms of thrust and power coefficients, defined respectively as

$$C_T = \frac{T}{\frac{1}{2}\rho A_\mathrm{r} u_\mathrm{ref}^2};\; C_P = \frac{P}{\frac{1}{2}\rho A_\mathrm{r} u_\mathrm{ref}^3}, \tag{2.33}$$

where ρ is the density of the fluid, A_r is the swept rotor area and u_ref is a reference velocity. The reference velocity for the current experiment and model is taken as the freestream velocity along the rotor centreline, $u_\mathrm{ref} = u_\mathrm{cl} = 0.55\,\mathrm{m\,s^{-1}}$.

The operating point of the turbine is presented non-dimensionally as a tip speed ratio,

$$\lambda = \frac{u_\mathrm{tip}}{u_\mathrm{ref}} \tag{2.34}$$

where the tip velocity of the blade is defined as $u_\mathrm{tip} = \omega R$ and ω is angular velocity.

The computed and experimental results are compared in figure 2.17 (a) and (b). Thrust is over-predicted by the computational model at all operating points. This can be attributed to the over-prediction of sectional lift at the rotor blades, evident from the results of the two-dimensional model in figure 2.14.

Reasonable agreement in power is achieved at tip speed ratios of $\lambda = 3$ and $\lambda = 4$, but

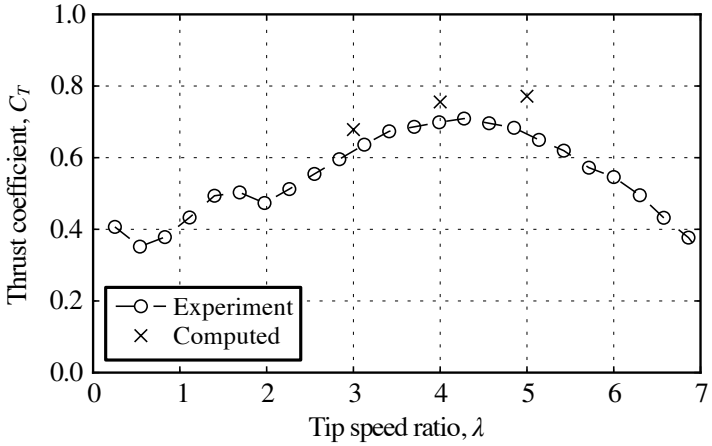

(a)

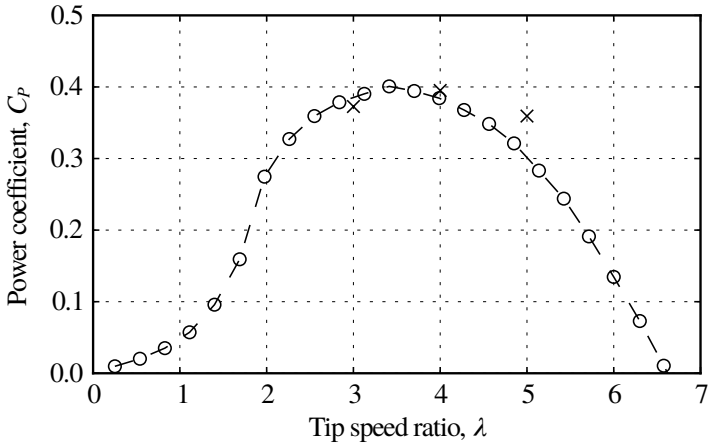

(b)

Figure 2.17: Comparison of computed and measured (a) thrust coefficient and (b) power coefficient for the model scale turbine.

power is over-predicted at $\lambda = 5$. Overall, the computed power curve is shifted to the right of the measurements by $\Delta\lambda = 0.5$. The peak power point occurs where the rotor blade is operating at the angle of attack corresponding to a maximum ratio of lift force to drag force. Computed and measured lift-to-drag ratios, L/D, for the NACA 4415 profile from the preceding convergence study are plotted as a function of angle of attack in figure 2.18. The computed result is produced from the coarse grid, which is similar to the resolution of the rotor blade. The angle for maximum L/D is about $\alpha = 7°$ for the experimental data, while it is reduced to $\alpha = 5°$ in the numerical model. The numerically modelled rotor will

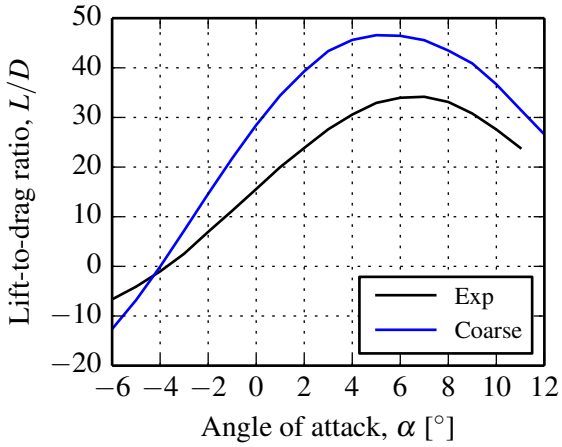

Figure 2.18: Comparison of computed and measured lift-to-drag ratio for the NACA 4415 aerofoil studied in section 2.2.2.2. The computed result is produced on the coarse grid from the convergence study.

consequently reach its optimum operating point at a higher tip speed ratio (lower angle of attack) than the experimental case.

Wake measurements were taken at the streamwise locations $x = -4.67D$, $2.33D$, $3.33D$, $4.83D$, and $6.33D$ for the rotor tests at the operating points $\lambda = 3.5$ and 4.5. Velocity was measured for periods of 2 minutes at a frequency of 25 Hz at points spaced roughly $0.1h$ apart along the planes $y = 0$ and $z = h/2$. The computations were run concurrently with the experiments, at tip speed ratios of $\lambda = 3$, 4 and 5, and hence computed wake data is not available at exactly the same operating points. The flow field for the $\lambda = 4$ simulation is time-averaged over one-third of a rotor revolution, and wake data is extracted along lines corresponding to the experimental wake traverses. As the computational domain extends only $3D$ upstream and $6D$ downstream, data is extracted at $x = -2.5D$ and $5.5D$ ($0.5D$ inside the domain boundaries) for comparison with the experimental measurements at $x = -4.67D$ and $6.33D$ respectively. Streamwise velocity is presented in non-dimensional form, with the velocity profile upstream of the rotor plane (at $x = -4.67D$ for the experimental data and at $x = -2.5D$ for the computational data) used for normalisation.

Vertical profiles of computed and measured streamwise velocity are presented in figure 2.19. The computational model generally predicts a larger velocity deficit than the

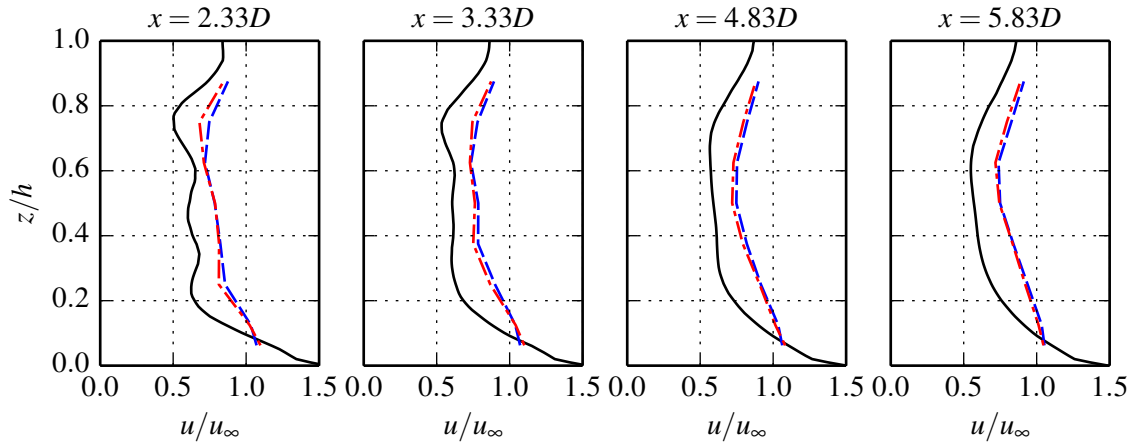

Figure 2.19: Profiles of streamwise velocity u normalised by the upstream profile $u_\infty(z)$ at a series of downstream locations along the vertical midplane $y = 0$. Solid black line, —— : computational data at $\lambda = 4$; dashed blue line, – – – : experimental data at $\lambda = 3.5$; dash-dot red line, – · – · – : experimental data at $\lambda = 4.5$.

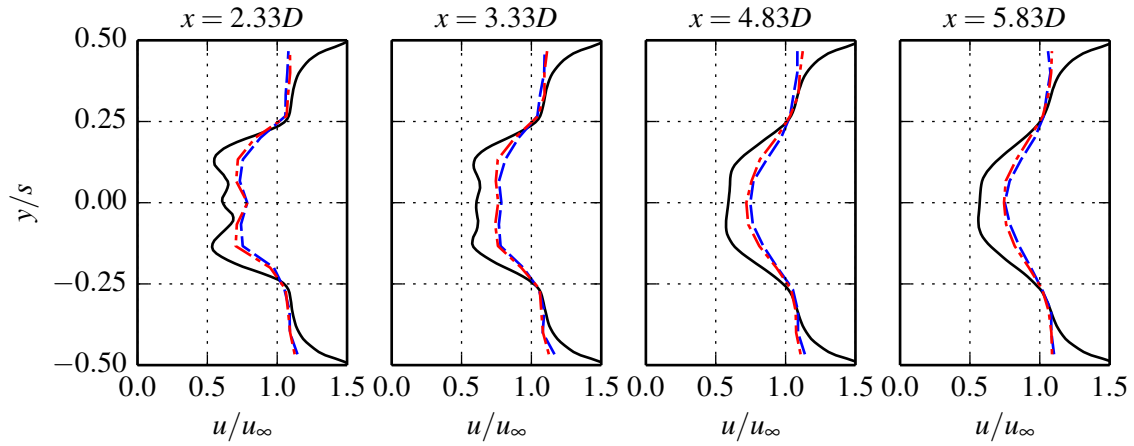

Figure 2.20: Profiles of streamwise velocity u normalised by the upstream profile $u_\infty(y)$ at a series of downstream locations along the horizontal midplane $z = 0.5h$. Legend as above.

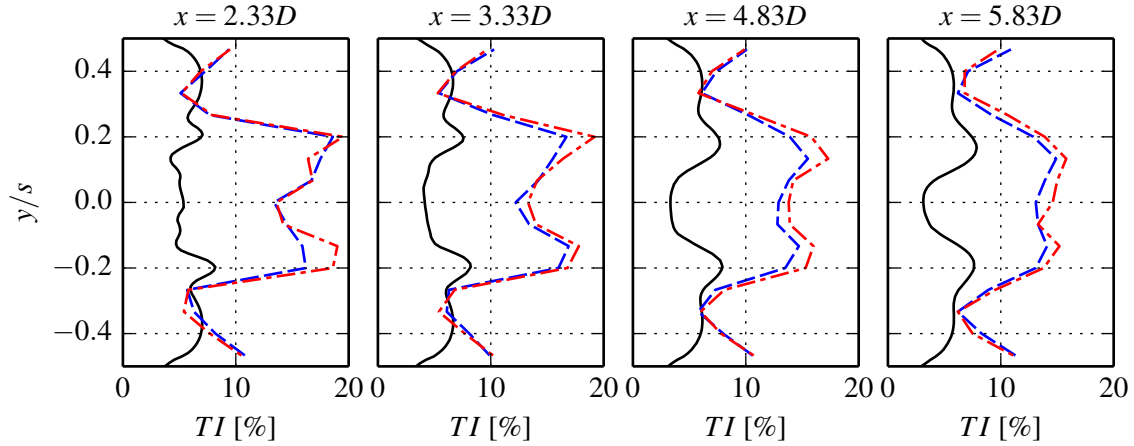

Figure 2.21: Profiles of turbulence intensity TI at a series of downstream locations along the horizontal midplane $z = 0.5h$. Legend as above.

physical model, which is consistent with the general over-prediction of thrust in figure 2.17 (a). In the physical model, the wake deficit is greater at the higher tip speed ratio, $\lambda = 4.5$, due to increased rotor thrust. At $x = 2.33D$, both models features local minima in velocity at elevations of $z = 0.25h$ and $z = 0.75h$ which correspond to the outboard radial sections of the rotor where thrust is highest. An additional minimum is observed in the computational data at mid-depth corresponding to the nacelle. These undulations in the wake velocity profile mix out by $x = 4.83D$ in the physical model, and $x = 5.83D$ in the computational model, indicating weaker wake mixing in the latter case. This is also visible in the horizontal velocity profiles in figure 2.20.

The vertical profiles show that the wake occupies most of the vertical distance in the channel, due to the large size of the rotor relative to the water depth, $D = 0.75h$. Comparison of the vertical and horizontal profiles indicates that greater bypass flow acceleration occurs at either side of the wake than above and below.

The computational model over-predicts bypass acceleration, which follows from the over-prediction of the device thrust and wake deficit. Note that the upstream velocity close to the walls is very low, so small increases in velocity in this region appear large due to normalisation. Despite this, it is apparent that the wall boundary does not impart sufficient shear on the flow. A new sheared flow model with an improved boundary condition is described in chapter 3, where the operation of a full scale tidal turbine in a variety of flow conditions is investigated.

Horizontal profiles of turbulence intensity are compared in figure 2.21. Turbulence intensity is defined as

$$TI = \frac{U'}{\overline{U}} \tag{2.35}$$

where $\overline{U}$ is the time mean of velocity magnitude and U' is the fluctuation of velocity about the mean. In the experimental case, U' is taken as the root mean square of the directional velocity fluctuations,

$$U' = \sqrt{\frac{1}{3}\overline{u_i'^2}}. \tag{2.36}$$

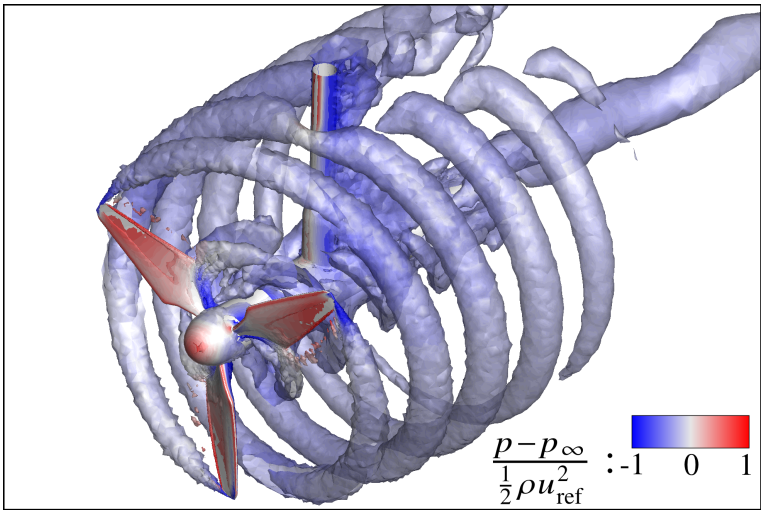

Figure 2.22: Instantaneous iso-surface of $Q = 2\,\text{s}^{-1}$, coloured by pressure coefficient, for a rotor speed of $\lambda = 4$.

where the index i indicates summation over the three directions x, y and z. In the computational model, turbulence intensity is calculated from the turbulence kinetic energy k, which is calculated by the k-ω SST turbulence model.

$$U' = \frac{2}{3}\sqrt{k} \tag{2.37}$$

Figure 2.21 highlights that turbulence intensity is greatly under-predicted by the computational model.

As the experimental measurements are relatively sparse, greater insight into the behaviour of the flow around the turbine can be gained through visualisation of the computed flow field. Coherent structures in the flow field can be identified by Q-criterion (Jeong and Hussain, 1995),

$$Q = -\frac{1}{2}\left(S_{ij}S_{ij} - \Omega_{ij}\Omega_{ij}\right) \tag{2.38}$$

where S_{ij} and Ω_{ij} are the symmetric and anti-symmetric parts of the velocity gradient tensor $\frac{\partial \overline{u_i}}{\partial x_j}$. This parameter is more effective for the isolation of vortex structures than pressure and vorticity. Although the local pressure at the core of a vortex is lower than the surrounding fluid, such local pressure differences will be outweighed by large variations of the pressure field due to the operation of the turbine. Vortex structures can be identified by

constant values of vorticity; however in this case such structures cannot be isolated from vorticity due to shear in the freestream flow.

An instantaneous iso-surface of $Q = 2\,\mathrm{s}^{-1}$ is presented for the turbine operating at $\lambda = 4$ in figure 2.22, where the rotor speed is $\lambda = 4$. The wake has a helical structure, formed as vorticity is shed from the blade tips and convected downstream with the mean flow. This structure is interrupted by the tower and ultimately fades downstream as the wake mixes. Vorticity is also shed from the sharp corner near the blade root. The resulting root vortices wrap around the nacelle, where the pressure is lower due to wake rotation, and merge together before departing from the rear of the nacelle. The iso-surfaces are coloured by pressure coefficient,

$$c_p = \frac{p - p_\infty}{\frac{1}{2}\rho u_{\mathrm{ref}}^2} \tag{2.39}$$

where p_∞ is the pressure far upstream. Highest pressure occurs at the upstream sides of the rotor blades, the front of the spinner, and at a stagnation line along the upstream surface of the supporting tower. In general, pressure is lower downstream of the rotor, with the lowest values occurring during the formation of the tip and root vortices, and in the shear layers of the tower.

2.3 Conclusion

This chapter has introduced the general numerical methods which are used throughout this work. The equations governing incompressible, unsteady fluid flow have been presented, and techniques for their numerical solution have been described.

A validation exercise has been carried out at model scale for comparison with experimental data. Steps taken to reproduce the flow and geometry have been described. The sensitivity of the solution to the resolution of the computational grid has been examined for the case of a two-dimensional blade section.

A three-dimensional model has been produced to simulate the operation of a 1:30 scale tidal turbine. Over-prediction of thrust and a shift in the power curve are attributed to

under-prediction of blade drag, which was observed in the two-dimensional convergence study.

The computed flow field for the model scale turbine has been compared to the experimental case, and differences have been highlighted and discussed. The lower velocities observed in the wake of the computed flow field relative to measurements are attributed to the over-prediction of rotor thrust and a lower rate of wake mixing. Finally, the complex structure of the wake has been examined using the numerical model, and the helical structure of the near wake has been highlighted.

This model is further extended to account for highly sheared, turbulent flow at full scale in chapter 3. Subsequently, in chapter 4, a free surface model is introduced and the effect of waves on turbine performance is examined.

Chapter 3

Effect of environmental conditions on turbine performance at full scale

3.1 Introduction

The experimental scale computational model from chapter 2 is now used to simulate a full scale tidal turbine in a variety of flow and blockage conditions. A different sheared flow model, consisting of self-sustaining profiles of velocity and turbulence parameters, is described and implemented. The sensitivity of computed results to spatial and temporal resolution is assessed. A series of parametric investigations are then carried out, where velocity shear, turbine spacing, and flow alignment are perturbed. The effects of such environmental factors on power extraction, structural loading and wake development are identified and analysed.

3.2 Computational model

3.2.1 Turbine geometry

The full scale turbine features a three bladed, axial flow rotor of diameter $D = 18\,\text{m}$. The centrebody consists of a spinner and a nacelle, with a diameter of 3 m and total length of

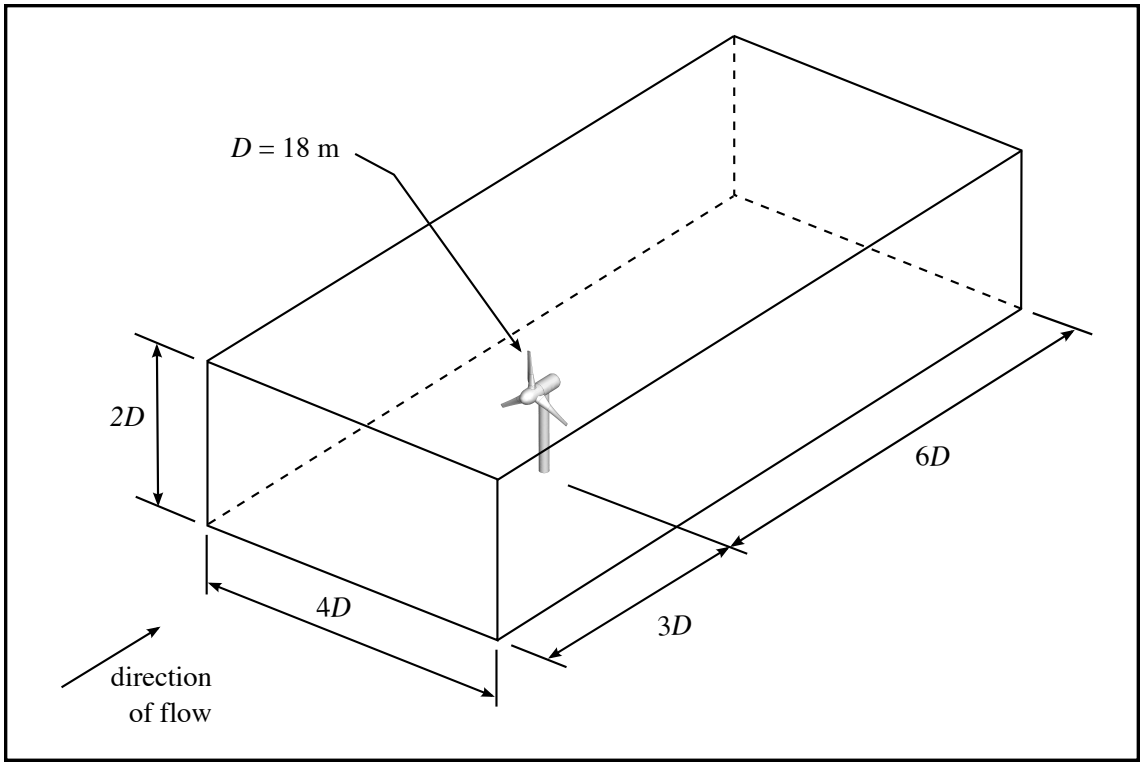

Figure 3.1: Isometric view of the turbine in the computational domain.

approximately 10 m. The spinner has a semi-ellipsoidal profile with a major-to-minor axis ratio of 1.5 : 1. A cylindrical monopile of diameter $D_{\text{tower}} = 2\,\text{m}$ supports the device from below. The hub height is $h_{\text{hub}} = 18\,\text{m} = 1D$. This corresponds to mid-depth in the flow, which has a total depth of $h = 2D = 36\,\text{m}$.

The rotor geometry is based on a proprietary design obtained through the PerAWaT project. The blade section is based on a NACA 63_3-$4x$ aerofoil, where the thickness x ranges from 55% at the root to 18% at the tip.

The computational domain has a rectangular cross section of width $y = 4D$ and depth $z = 2D$, resulting in a blockage ratio of $B = 0.0982$. An isometric view of the turbine within the computational domain is presented in figure 3.1.

3.2.2 Spatial discretisation

In order to determine the potential sensitivity of computed data from the three-dimensional turbine model to grid resolution, a convergence study is carried out on a two-dimensional

aerofoil. The geometry and Reynolds number for the convergence study are based on those at a radial section through the blade at $r = 0.8R$, a rotor tip speed ratio of $\lambda = 4.5$, and a reference velocity of $2\,\mathrm{m\,s^{-1}}$. At this location, the local Reynolds number based on chord length is $\mathrm{Re} = 7.2 \times 10^6$ and the blade section is 26% thick (NACA 63_3-426). Experimental data is available from Abbot and von Doenhoff (1959) for the 18% thick NACA 63_3-418 profile, so this section is used for the convergence study.

The computational domain is discretised using the same approach detailed in section 2.2.2.2. 'Coarse', 'medium' and 'fine' resolution grids are generated, with resolution increasing uniformly by a refinement ratio of $r = 1.5$ between each grid. Due to the high Reynolds number of the flow, direct resolution of the boundary layers would require a degree of wall-normal resolution that will be impractical in the three-dimensional rotor model. Hence wall functions are used to model the velocity profile in the boundary layers, and the target range for non-dimensional wall distance is $y^+ > 25$. Further details on wall modelling are given in section 2.1.8. Element size limits for each of the three grids are listed in table 3.1. Domain dimensions and boundary conditions are equivalent to the grid resolution study in section 2.2.2.2. A close-up view of the aerofoil as discretised by the coarse grid is presented in figure 3.4 (a). The full grid is not shown, as it is very similar to the low Reynolds number grid in figure 2.12 (a).

The aerofoil is simulated in steady flow for a series of angles of attack in the range $-6° < \alpha < 12°$. Profiles of non-dimensional wall distance y^+ at the aerofoil surface are compared for each of the three grids at an angle of attack of $\alpha = 6°$ in figure 3.2. The wall-adjacent centroids in each case are located in the logarithmic law region of the

Table 3.1: Element size limits in terms of the chord length c for the grid refinement study. The three columns on the right hand side describe the resolution of the boundary layer region, where '1^{st} cell' denotes the wall normal distance of the wall adjacent cell, N_{lay} is the number of boundary layer elements and G.R. is the growth ratio of the boundary layer elements.

Mesh	Leading edge	Trailing edge	Near field	Far field	1^{st} cell	N_{lay}	G.R.
Coarse	0.02	1.8×10^{-3}	0.12	0.46	1×1^{-3}	6	1.5
Medium	0.013	1.2×10^{-3}	0.08	0.31	6.67×10^{-4}	9	1.3
Fine	8.67×10^{-3}	8×10^{-4}	0.032	0.20	4.45×10^{-4}	12	1.23

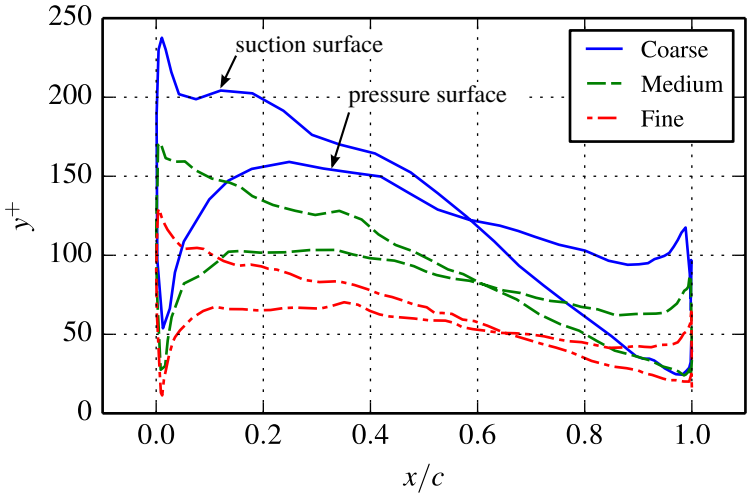

Figure 3.2: Distribution of non-dimensional wall distance y^+ at the aerofoil surface for three levels of grid resolution.

boundary layer, and hence wall functions can be used appropriately.

Lift and drag coefficients are presented as a function of angle of attack for each grid in figure 3.3. Experimental data for the same profile operating at a Reynolds number of $\mathrm{Re} = 1 \times 10^6$ (Abbot and von Doenhoff, 1959) is also plotted. Good numerical convergence is observed across the series of grids, i.e. at a given angle of attack, the difference between the medium and fine grid solutions is much less than that between the coarse and medium grid solutions. Numerical predictions of lift coefficient compare well with experimental data for flow angles $-6^\circ < \alpha < 5^\circ$. At higher angles of attack, lift is under-predicted in the coarse grid solution. Drag is over-predicted on all grids, with little performance improvement between the medium and fine grids. The lift-to-drag ratio is under-predicted by the three numerical solutions, indicating that a three-dimensional rotor model based on these grid dimensions will under-predict power and over-predict thrust.

A three-dimensional rotor grid is generated based on the dimensions of the coarse aerofoil grid, using the Delaunay algorithm detailed in section 2.1.7. Six layers of high aspect ratio prismatic elements are grown from each surface. The first cell height is allowed to float so that a gradual transition is ensured between the uppermost layer of prismatic elements and the adjacent tetrahedral elements. This improves solution convergence, but increases y^+ at the blade surface. A cross-section of the rotor grid, showing the 26% thick

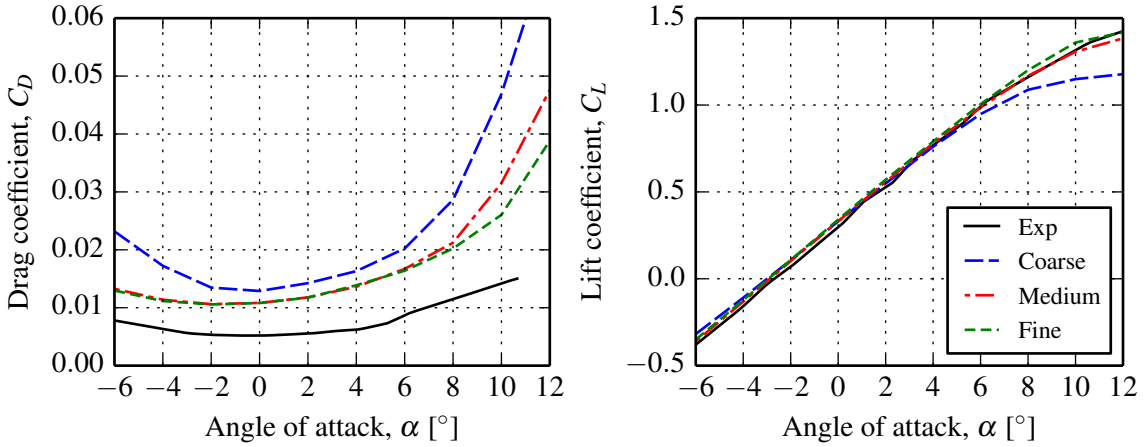

(a) (b)

Figure 3.3: Comparison of computed results from coarse, medium and fine resolution grids with experimental measurements (Abbot and von Doenhoff, 1959) of (a) drag coefficient and (b) lift coefficient for a NACA 63_3-418 profile. The computational data is at Re = 7.2×10^6 and the experimental data is at Re = 6×10^6.

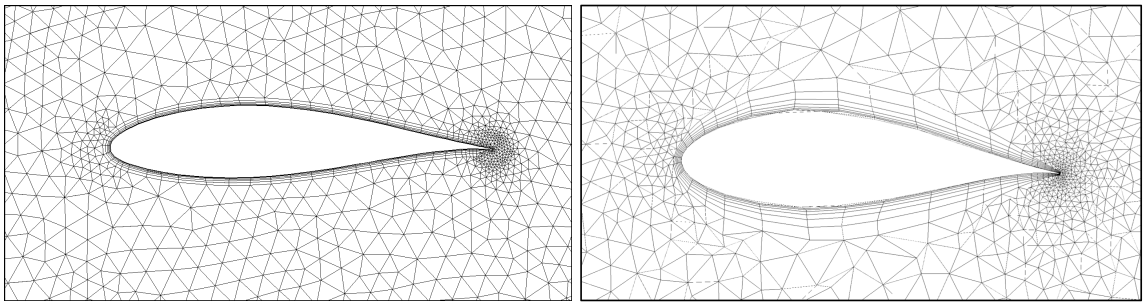

(a) 2D grid (b) 3D grid

Figure 3.4: (a) A close-up view of the coarse grid from the two-dimensional grid convergence study, showing the NACA 63_3-418 profile. (b) Cutplane through the full scale computational domain showing mesh resolution in the vicinity of the rotor blade at the 80% radial station. The blade section at this station is equivalent to a NACA 63_3-426.

blade section at $r \approx 0.8R$, is compared with the coarse version of the two-dimensional 18% thick convergence study grid in figure 3.4. Contours of y^+ at the rotor surfaces are presented in figure 3.5. The surface mesh and the sliding mesh interface are also shown. The maximum tetrahedral element size in the near field region is $1.0c$, and in the far field region is $2.0c$, where c is the blade chord length at $r = 0.8R$. The total number of elements in the rotor region (within the sliding mesh interface) is approximately 5.2×10^6. The far field, outside of the sliding mesh interface, is discretised by 5×10^5 elements, resulting in a total element count of 5.7×10^6.

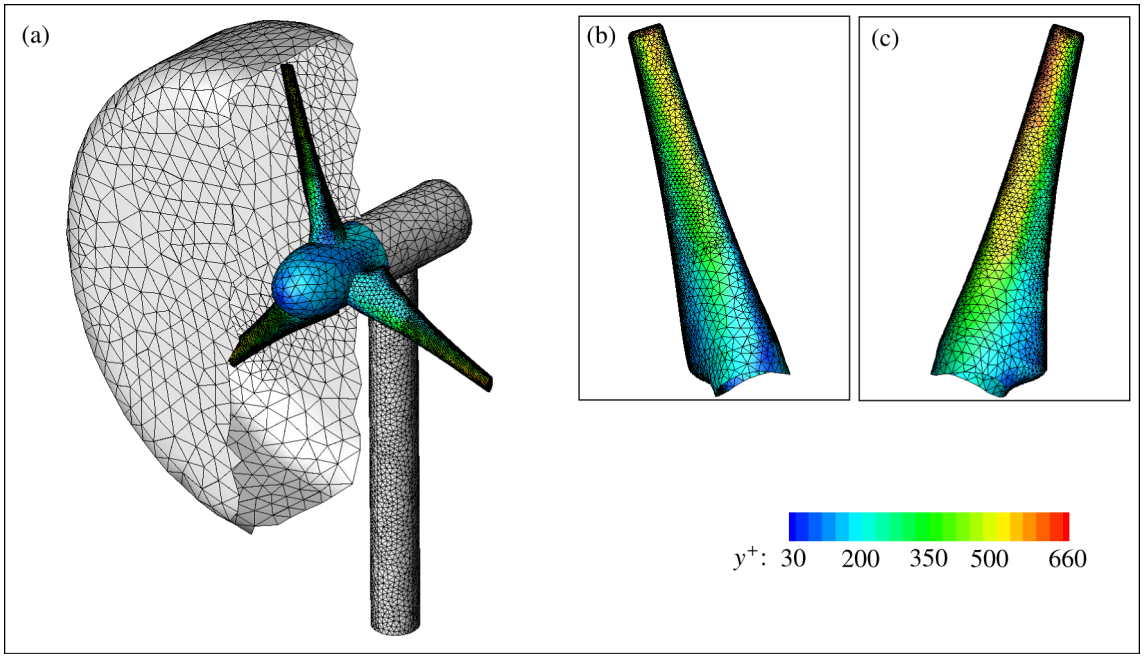

Figure 3.5: (a) Oblique view of the turbine showing the triangular surface mesh and contours of non-dimensional wall distance y^+. The sliding mesh interface is also shown. (b) Front view showing the suction surface of the uppermost blade. (c) Reverse view showing the suction surface of the uppermost blade. The turbine is operating at $\lambda = 4.5$ in uniform flow of $u_{\text{ref}} = 2\,\text{m}\,\text{s}^{-1}$.

3.2.3 Sheared flow model

As discussed in the review on RANS modelling of sheared flow in section 1.4.2.2, modelled turbulence tends to decay between the inlet boundary and the rotor plane. McNaughton (2013) reports that high levels of inlet turbulence ($TI = 10\%$) affect the prescribed sheared velocity profile as the flow develops in the downstream direction. In order to preserve the desired velocity profile, a low level of turbulence intensity must be specified at the domain inlet. Gant and Stallard (2008) address this issue by prescribing an unsteady flow field at the upstream boundary. The resolved unsteady structures introduce shear throughout the flow, and as they dissipate the level of modelled turbulent kinetic energy is maintained. The timestep required for this method will depend on the timescales of the resolved turbulence, and could add additional expense to the current model, which already has a high cost due to the blade-resolved sliding mesh rotor mode.

An alternative method for prescribing a sheared velocity profile, which is self-sustaining and features moderate levels of turbulence ($5\% < TI < 10\%$) has been developed by

McIntosh (reported in Fleming, McIntosh and Willden (2013)). The model is described and demonstrated in the following sections, and is used later to investigate the effects of sheared flow on the performance, loading and wake development of the current full scale tidal turbine.

3.2.3.1 RANS modelling of sheared flow

Analytical profiles of streamwise velocity, u, turbulent kinetic energy, k, and specific dissipation rate, ω, are derived for planar open channel flow following Schlichting (2000), and applied at a boundary three diameters upstream of the rotor plane. The velocity profile is a function of bed friction coefficient, c_f, and reference velocity u_{nom} (defined formally in equation 3.6). The friction velocity, u_τ, is defined as

$$u_\tau = u_{\text{nom}}\sqrt{\frac{c_f}{2}}, \tag{3.1}$$

from which the applied bed shear, τ_{w}, is calculated,

$$\tau_{\text{w}} = \rho u_\tau |u_\tau|. \tag{3.2}$$

We assume a linear variation of shear from a maximum of τ_{w} at the channel bed to a minimum of $\tau = 0$ at the free surface. This shear profile may be expressed as a function of dimensionless depth, $\eta = z/h$, where h is water depth,

$$\tau(\eta) = \tau_{\text{w}}(1-\eta) = \rho\nu_{\text{t}}\frac{\mathrm{d}u}{\mathrm{d}\eta}\frac{\mathrm{d}\eta}{\mathrm{d}z}, \tag{3.3}$$

as shown in figure 3.6. The shear τ_w is applied as a boundary condition to the bed of the computational model. For high shear cases, reversed flow can occur in the elements adjacent to the channel bed. Such flow is unphysical; however it is necessary to obtain a physically sensible profile throughout the rest of the water column. For stability of the numerical model, the bed shear is reduced to $\tau_w = 0\,\text{Pa}$ close to the outlet boundary of the

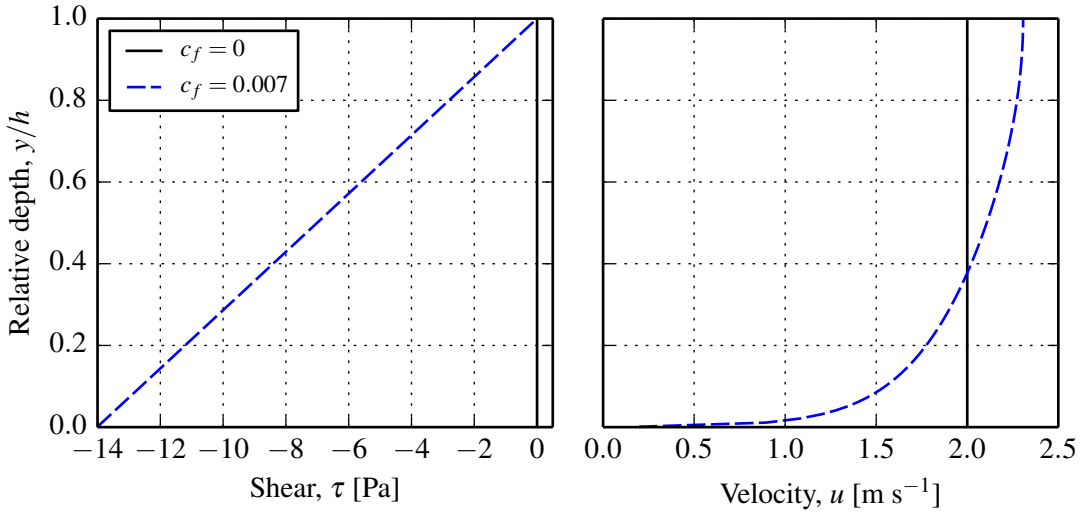

Figure 3.6: Variation of shear and velocity with depth for uniform flow ($c_f = 0$) and a sheared flow case ($c_f = 0.007$).

domain.

Using an ansatz for turbulent eddy viscosity, ν_t (Schlichting, 2000),

$$\nu_t = \frac{1}{6} u_\tau h \kappa \left[1 - (1-\eta)^2\right] \left[1 + 2(1-\eta)^2\right], \tag{3.4}$$

equation 3.3 can be integrated to yield the velocity profile for a turbulent open channel flow,

$$u(\eta) = \frac{u_\tau}{\kappa} \ln\left(\frac{\eta(2-\eta)}{2\eta^2 - 4\eta + 3}\right) + u_h \tag{3.5}$$

where $\kappa = 0.41$ is the von Kármán constant and u_h is the streamwise velocity at the free surface.

The reference flow velocity (used previously in equation 3.1) is defined as the average of the velocity profile,

$$u_{\text{nom}} = \int_0^1 u(\eta) \mathrm{d}\eta, \tag{3.6}$$

which is solved for u_h,

$$u_h = u_{\text{nom}} - \overline{c}, \tag{3.7}$$

where

$$\bar{c} = \frac{u_\tau}{\kappa}\left(\ln\frac{4}{3} - \frac{\pi}{\sqrt{2}} + \sqrt{2}\arctan\frac{1}{\sqrt{2}}\right), \tag{3.8}$$

which closes the model.

A bed friction coefficient of $c_f = 0.007$ is chosen throughout the remainder of this study, as this value leads to a velocity profile within the bounds of the flow measurements at a real tidal site reported by Gunn and Stock-Williams (2013). Velocity profiles for uniform flow ($c_f = 0$) and sheared flow ($c_f = 0.007$) are plotted in figure 3.6, which are derived from the linear shear profiles in figure 3.6. The velocity profiles are matched in terms of volumetric flow rate. However, the velocity at mid-depth is higher in sheared flow, which will be reflected in higher loads on a tidal turbine placed at that depth.

The profile of turbulent kinetic energy, k, resulting from this velocity distribution is calculated using the one-equation turbulence model of Bradshaw et al. (1967),

$$k = \frac{\tau_\mathrm{t}}{a\rho} = \frac{u_\tau^2\,(1-\eta)}{a}, \tag{3.9}$$

where $a = 0.3$ is a turbulence constant. Subsequently, a profile of specific turbulence dissipation rate, ω, may be calculated using equation 3.10.

$$\omega = \frac{k}{\nu_\mathrm{t}}. \tag{3.10}$$

The profile of turbulence intensity, TI, is also calculated from the profile of turbulent kinetic energy,

$$TI = 100\sqrt{\frac{2}{3}k}. \tag{3.11}$$

3.2.3.2 Demonstration of sheared flow model

A brief demonstration of this sheared flow model is now given. Sheared flow is simulated in an empty channel, showing that profiles of velocity and turbulence parameters are sustained in the streamwise direction. The domain is two dimensional, extending $20h$ downstream,

where $h = 36\,\mathrm{m}$ is the domain height (equivalent to water depth). It is discretised by a structured grid consisting of uniform quadrilateral elements. There are 360 evenly spaced nodes (element boundaries) in the streamwise (x) direction and 72 evenly spaced nodes in the vertical (z) direction. A friction coefficient of $c_f = 0.007$ is chosen to derive the bed shear and the inlet flow profiles (velocity and turbulence parameters). The equivalent uniform bulk flow is $2\,\mathrm{m\,s^{-1}}$, corresponding to a Reynolds number (based on water depth h) of $\mathrm{Re} = 7.2 \times 10^7$. The free surface is modelled as a rigid lid, and a uniform pressure of $p = 0\,\mathrm{Pa}$ is applied at the domain outlet.

The shear force applied at the channel bed acts in the upstream direction, which may lead to reversed flow at the bed for highly-sheared velocity profiles. This is a physically unstable situation which cannot be accurately captured using a steady RANS solver. Hence an unsteady RANS solver is used, with the timestep size chosen such that the flow field residuals reduce by at least four orders of magnitude at each timestep during the calculation. A timestep size of 0.1 s was used, and the total simulation time was 720 s (equivalent to a flow passage of twice the domain length).

Vertical profiles of velocity and turbulence parameters are compared at a range of distances downstream of the channel inlet in figure 3.7. In each case, the blue line represents the profile prescribed at the inlet boundary ($x = 0h$). It is important to note that the turbulence profiles are not quite in equilibrium with the velocity profile at this point, due to the simple algebraic turbulence model employed in their derivation at the boundary. A more elaborate two-equation turbulence model (k-ω SST) is employed by the RANS solver, so some relaxation of the velocity and turbulence profiles is observed between $0h$ and $4h$ downstream. The velocity profile is sustained very well beyond this point, although some further development of the turbulence parameters k and ω occurs. Note that the velocity at the channel bed is actually negative; this is a consequence of the high shearing force applied at this boundary, which is necessary to achieve the desirable profile through the rest of the water depth. Notably, the turbulence intensity TI remains within a reasonably high range of $4\% < TI < 8\%$; the higher levels of turbulence intensity

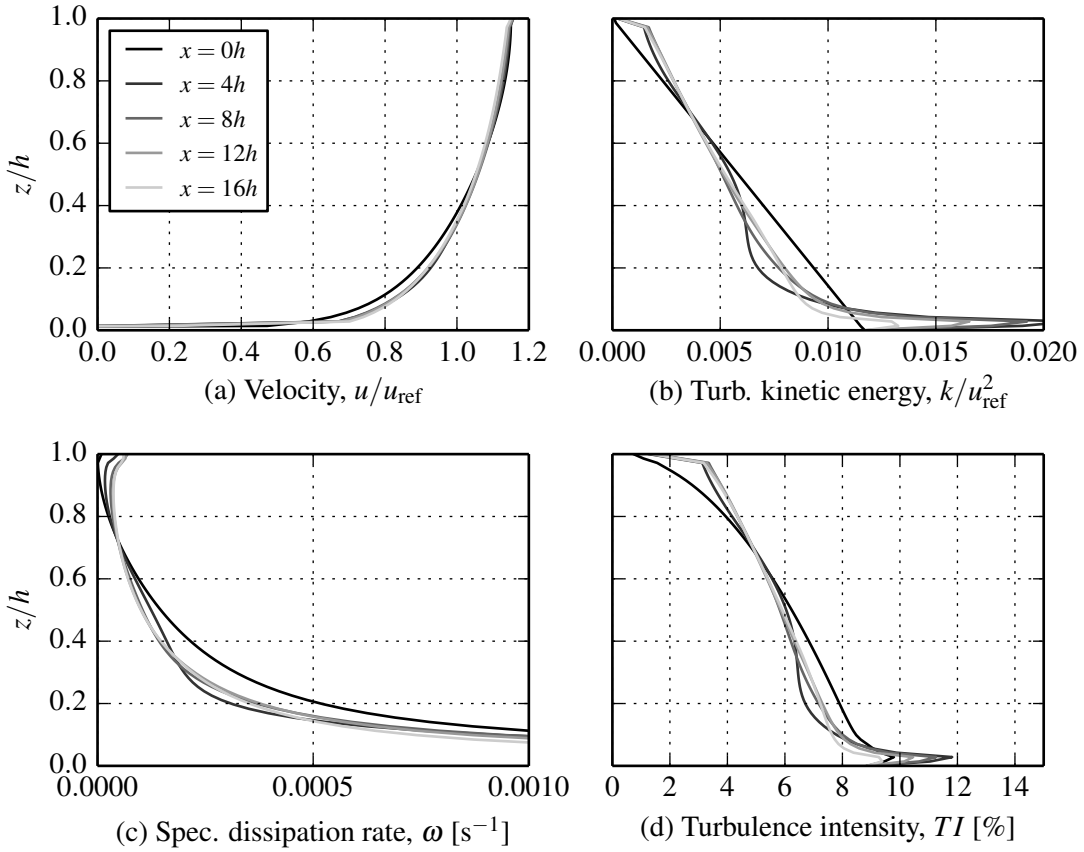

Figure 3.7: Development of velocity and turbulence profiles for two dimensional open channel flow using the current sheared flow model, where $u_{\text{ref}} = 2\,\text{m}\,\text{s}^{-1}$.

observed in real tidal channels are likely due to additional influences such as bathymetry.

3.3 General details of full scale turbine model

The turbine is now simulated at a range of operating points in a variety of flow conditions. Velocity and turbulence profiles from the sheared flow model presented in section 3.2.3 are applied at the upstream boundary, $3D$ from the rotor plane. A corresponding shear force is applied at the lower boundary to represent the channel bed. A symmetry condition is applied at the upper boundary of the domain, approximating the free surface as a rigid lid. A uniform pressure of $p = 0\,\text{Pa}$ is prescribed at the downstream boundary which is $6D$ from the rotor plane. Periodicity is prescribed at the lateral boundaries of the channel, simulating an in finite fence of turbines. A sliding mesh interface is used to allow motion

of the rotor relative to the channel boundaries. The rotor advances by 2° every timestep: ten timesteps are required for the blade to travel a circumferential distance of one chord length at the radial location $r = 0.8R$. Typical timestep size is $\Delta t = 0.03\,\mathrm{s}$, and simulations are run for at least 80 s of flow time to allow the wake to convect beyond the domain outlet. Computations take approximately 80 hours to complete when run in parallel on four 2.3 GHz CPUs on a high performance computing cluster, equivalent to 320 CPU-hours.

3.4 Turbine performance in sheared flow

The turbine is simulated at tip speed ratios of $\lambda = 3.5$, 4.5 and 5.5 in uniform flow, where $c_f = 0$, and sheared flow, where $c_f = 0.007$. Tip speed ratio is usually defined with reference to the freestream velocity, which poses a difficulty for sheared flow cases. While the sheared and uniform profiles are based on the same reference velocity of $2\,\mathrm{m\,s^{-1}}$, the velocity in the rotor region $h/4 < z < 3h/4$ differs as can be seen in figure 3.6. To ensure the rotor is turning at the same angular velocity relative to the flow directly upstream in both flow cases, it is defined as follows,

$$\lambda = \frac{R\omega}{\frac{1}{A_\mathrm{r}} \int_{A_\mathrm{r}} u_\infty(y,z)\,\mathrm{d}A} \tag{3.12}$$

where the upstream velocity is averaged over the projected area of the rotor, A_r (which includes the centrebody).

Instantaneous contours of normalised streamwise velocity u/u_ref are plotted on a vertical midplane through the computational domain for two operating cases in figure 3.8. In figure (a), the tip speed ratio is $\lambda = 4.5$ and the bed friction coefficient is $c_f = 0$, corresponding to uniform flow of $2\,\mathrm{m\,s^{-1}}$. The corresponding thrust coefficient, based on the reference velocity $u_\mathrm{ref} = 2\,\mathrm{m\,s^{-1}}$, is $C_T = 0.81$. The turbine is operating at the same tip speed ratio in sheared flow ($c_f = 0.007$) in figure (b). The thrust coefficient in this case, $C_T = 0.85$, is slightly higher than for uniform flow.

Features common to both flows include the reduction of velocity as the flow approaches

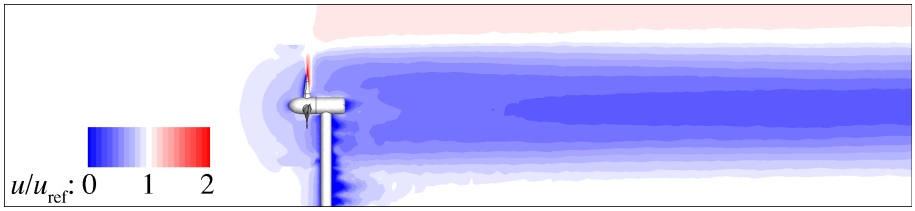

(a) Uniform flow; $c_f = 0$

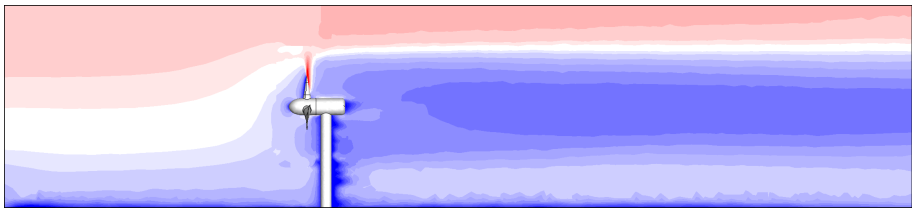

(b) Sheared flow; $c_f = 0.007$

Figure 3.8: Contours of normalised velocity u/u_{ref} at the vertical midplane through the turbine operating at $\lambda = 4.5$ in uniform and sheared flow. The direction of flow is from left to right.

the turbine, the reduced velocity in the wake of the rotor, and the increased velocity in the bypass flow above the wake. The bypass acceleration is not visible directly below the wake due to the presence of the tower.

Although the volumetric flow rate for both profiles is the same, the velocity across the rotor $0.25h < z < 0.75h$ is higher for the sheared profile (see figure 3.6). Correspondingly the wake velocity is slightly higher in the sheared flow case.

3.4.1 Wake development in sheared and uniform flow

Wake mixing is examined by comparing time-averaged fields of velocity and turbulence intensity. Data is interpolated onto a uniform grid of spacing $0.1D$ in each direction and averaged over a period of one third of a revolution, corresponding to the period of axial symmetry of the rotor. As the interpolation grid does not capture the turbine geometry or sliding mesh interface exactly, some unphysical artefacts arise in those areas. However, the time-averaged data is valid away from the turbine (outside the range $-D/2 < x < D/2$).

Contours of time-averaged normalised velocity are presented at the vertical midplane $y = 0$ in figure 3.9 (a). Velocity is normalised on the upstream profile, $u(z)/u_\infty(z)$. For the sheared flow case, the velocity at a particular elevation, $u(z)$, is normalised by the

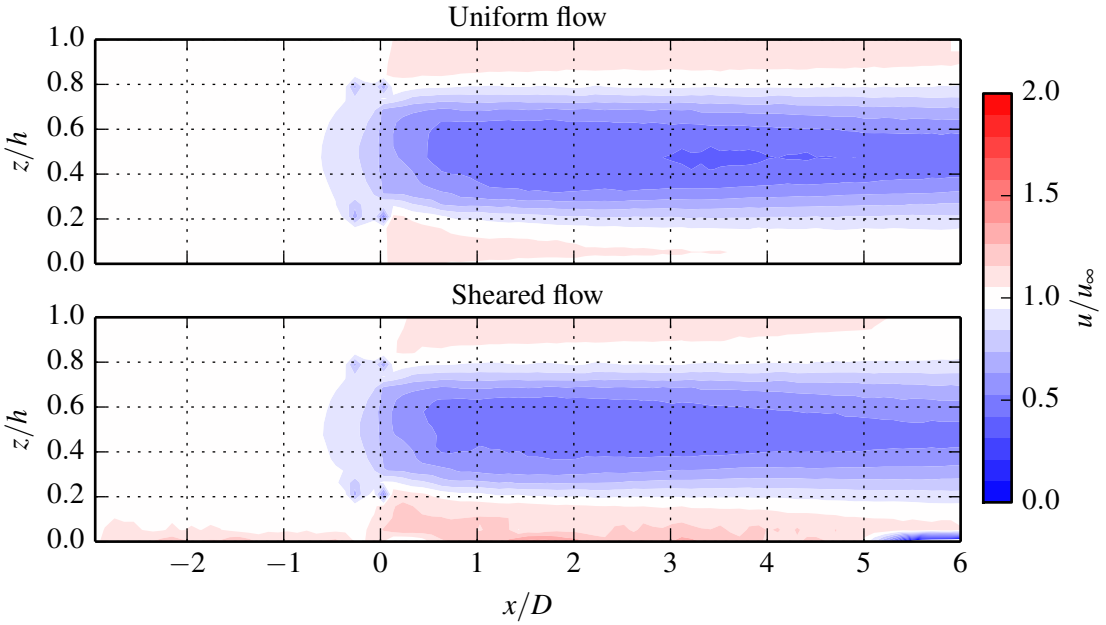

(a) Normalised velocity, u/u_∞

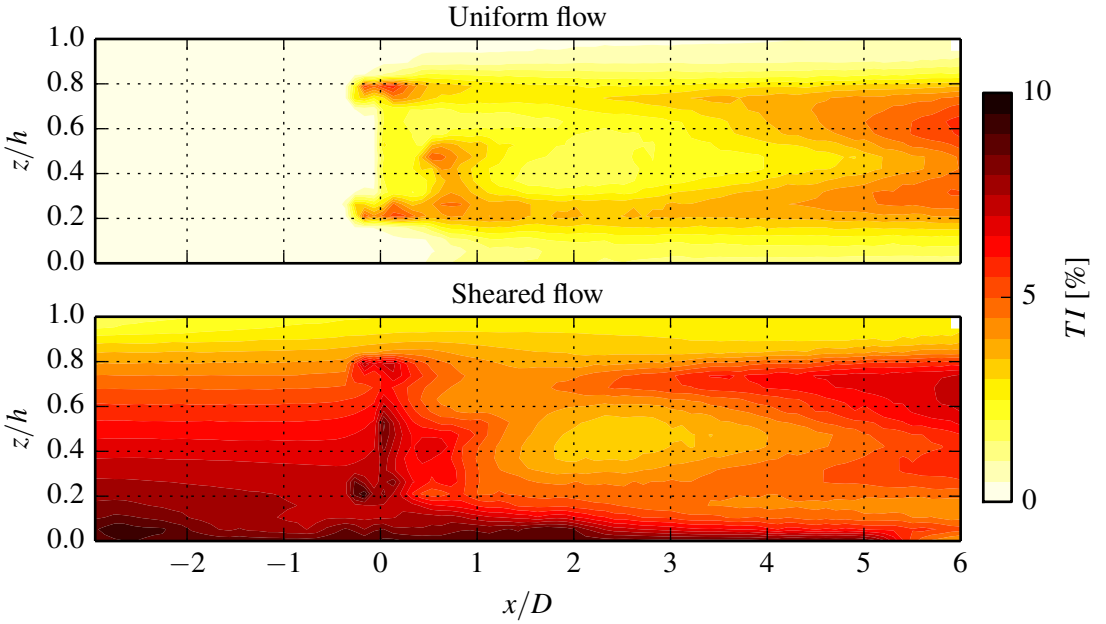

(b) Turbulence intensity, TI

Figure 3.9: Comparison of (a) time-averaged normalised velocity u/u_∞ and (b) turbulence intensity TI at the vertical midplane of the channel, $y = 0$, in uniform and sheared flow. The turbine geometry has been obscured due to the interpolation and time-averaging process, but is present at $x = 0D$. The rotor speed is $\lambda = 4.5$.

velocity directly upstream at the same elevation, $u_\infty(z)$, enabling the wake deficit to be directly compared with the uniform flow case. Comparison of the flow fields in the region $5D < x < 6D$ reveals a higher rate of mixing in the sheared flow case. The velocity of the bypass flow above the wake is higher in sheared flow, due to the higher freestream velocity in the upper portion of the channel. This leads to higher shear between the wake and the bypass flow above it, generating increased turbulence in that region and enhancing wake mixing, as shown in figure 3.9.

Wake mixing is also enhanced by the higher ambient turbulence in sheared flow. Ambient turbulence in the range of $4\% < TI < 10\%$ is observed in the sheared flow case, whereas the turbulence intensity is around 1% in uniform flow. In uniform flow, the bypass flow is accelerated evenly above and below the wake, resulting in greater symmetry of the shear layer about the mid-depth plane.

3.4.2 Rotor performance and loading

Power and thrust coefficients are compared for a single blade and the full rotor in sheared and uniform flow in figure 3.10, where each data point represents a mean value and the errorbar tails represent the 5^{th} and 95^{th} percentile values. The first observation to be made from these results is that a single blade undergoes a larger relative load fluctuation than the rotor in both uniform and sheared velocity profiles. This can be investigated further by comparing load fluctuations on a single blade and rotor in figure 3.11, where the unsteady thrust and torque histories are normalised by their respective mean values. The rotor is operating at a tip speed ratio of $\lambda = 4.5$, corresponding to peak power extraction.

In uniform flow (figures (a) and (c)), the blade undergoes a sharp dip of about 10% in axial load and 33% in torque once every revolution as it passes upstream of the tower. A region of elevated static pressure and reduced freestream velocity exists just upstream of the tower. As a rotor blade encounters this region, the angle of attack and the local velocity magnitude are reduced, resulting in lower sectional lift and drag, and consequently thrust and torque.

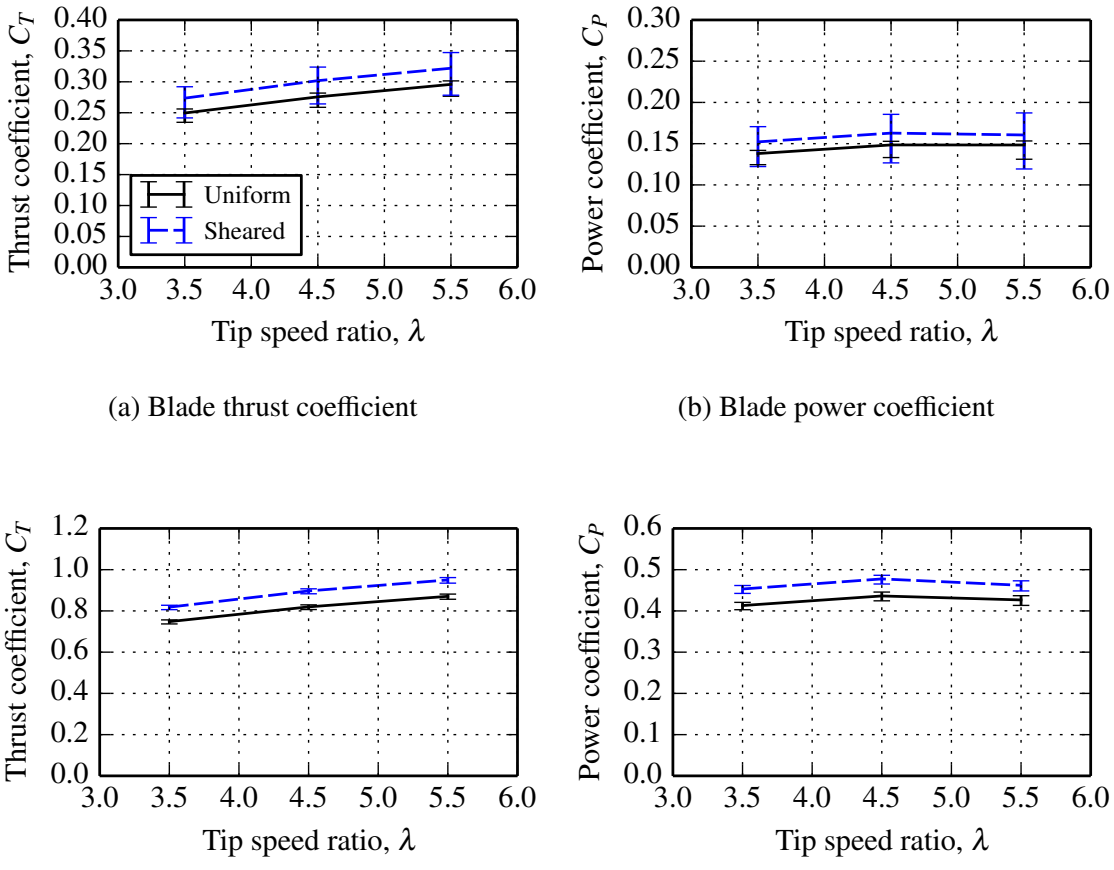

(a) Blade thrust coefficient

(b) Blade power coefficient

(c) Rotor thrust coefficient

(d) Rotor power coefficient

Figure 3.10: Blade and rotor thrust and power coefficients in uniform and sheared flow. The errorbars represent the 5th and 95th percentiles of the fluctuations in thrust and power.

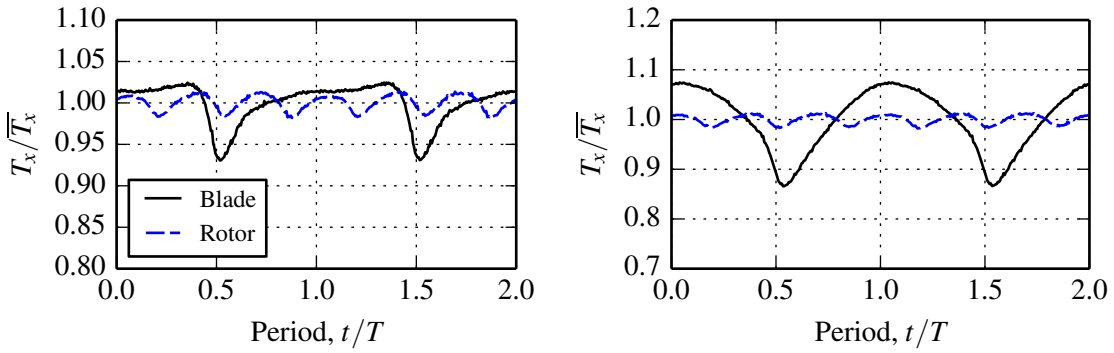

(a) Thrust in uniform flow

(b) Thrust in sheared flow

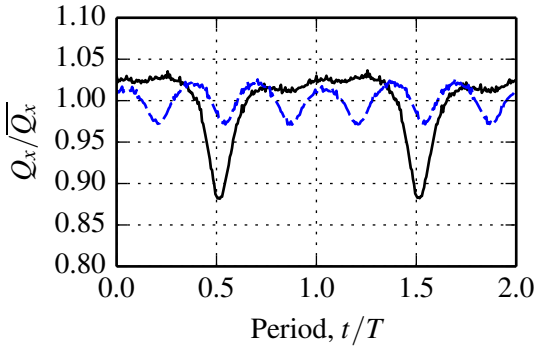

(c) Torque in uniform flow

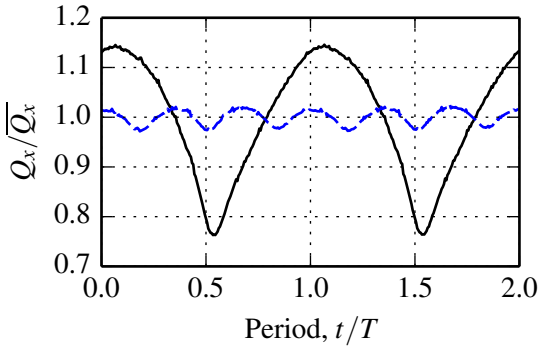

(d) Torque in sheared flow

Figure 3.11: Loading history on a blade and the rotor in uniform and sheared flow. The rotor speed is $\lambda = 4.5$.

The loading pattern on the single blade is qualitatively different in sheared flow, exhibiting a more continuous pattern of loading and unloading. The highest loading occurs when the blade is in the upper portion of the flow where streamwise velocity is highest. The asymmetry in the loading history on either side of the mean load is due to the variation of the velocity profile. The gradient of the velocity profile increases with depth, so the blade loads change more rapidly in the lower portion of a revolution. When the loads on the three blades are summed together, the relative load is greatly reduced. The influence of shear appears to be cancelled out, with the tower remaining as the only source of unbalanced load on the rotor.

A further observation from the power and thrust curves in figure 3.10 is that the load fluctuations on the blade are influenced by the velocity profile, whereas those on the rotor are not. Thrust and torque histories are compared in uniform and sheared flow in figure 3.12. Examining the effect of shear on a single blade (figures (a) and (c)), we see that the magnitude of the thrust and torque forces are similar during the tower interaction at $t/T = 0.5$ and $t/T = 1.5$. At this azimuthal position, the blade extends from $h/4 < z < h/2$, where the undisturbed velocity of the sheared profile is close to $2\,\mathrm{m\,s^{-1}}$, as shown in the comparison of velocity profiles in figure 3.6. Hence the local velocity just upstream of the tower is similar for both flow cases, resulting in similar blade loads.

In sheared flow, the forces on the blade are higher while it passes through the upper portion of the flow, peaking at the top-dead-centre position ($t/T = \{0, 1, 2\}$). This local increase in load occurs because the velocity in the sheared profile in this region ($h/2 < z < 3h/4$) is greater than $2\,\mathrm{m\,s^{-1}}$, again illustrated by figure 3.6.

The nature of the loading history on the rotor appears to be unaffected by the velocity profile (figures (b) and (d)). When the loading histories for each blade are summed, the portion of load fluctuation due to the velocity profile appears to be balanced across the rotor, while the influence of the tower remains. The mean thrust and torque (and power coefficient) on the rotor is increased in the sheared velocity profile, due to the higher kinetic flux passing through the rotor.

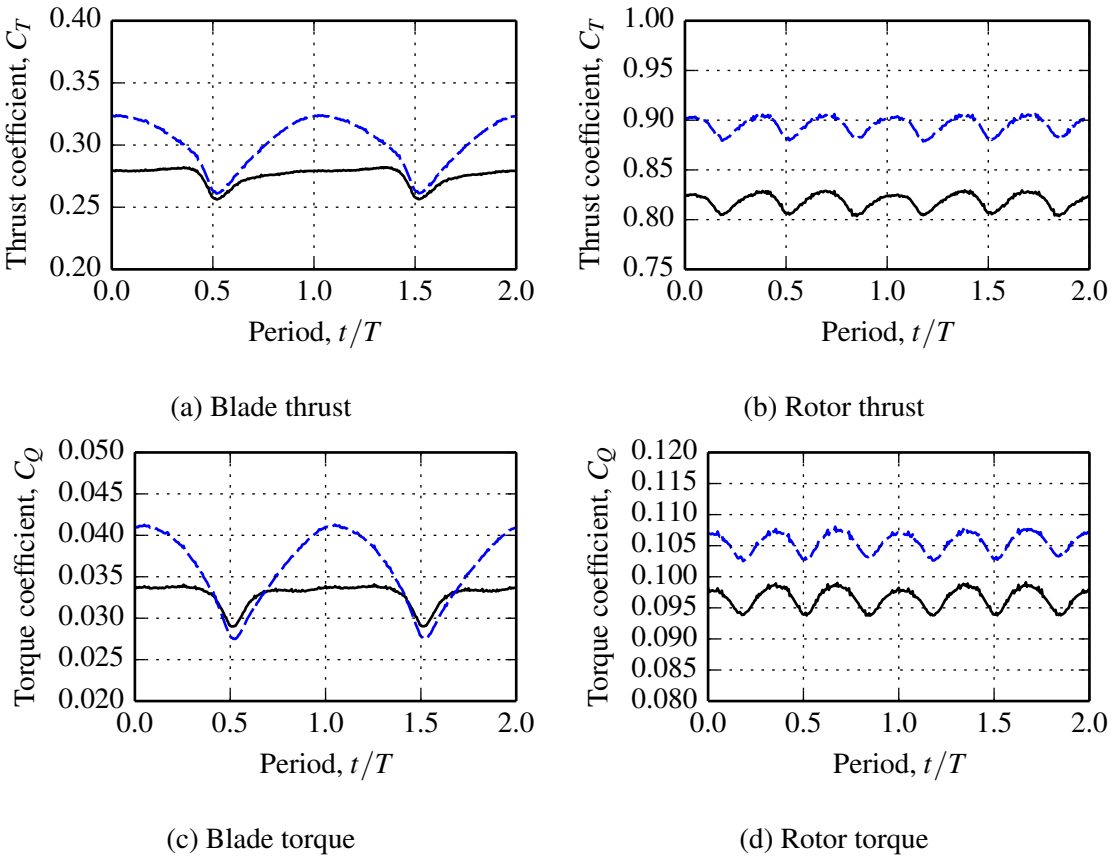

(a) Blade thrust

(b) Rotor thrust

(c) Blade torque

(d) Rotor torque

Figure 3.12: Loading history on a single blade and the rotor in uniform flow (solid line, —) and sheared flow (broken line, - - -). The rotor speed is $\lambda = 4.5$.

3.4.3 Shear force and bending moment distribution

The increase in magnitude of the load fluctuations on the rotor blade in sheared flow has consequences for the fatigue life of the blade. Fatigue life is proportional to the number of load cycles, and inversely proportional to the magnitude of the stress cycles. The stress in the blade is a function of its geometry and the bending moment distribution. As the blade is a cantilevered beam, the highest local bending moment is expected to occur at the root. The distribution of bending moment M is calculated by integrating the distribution of shear force V from the tip to the root of the blade following equation 3.14. The shear force is calculated following equation 3.13 from the distributed load q which is retrieved from

the simulation results.

$$\frac{\mathrm{d}V}{\mathrm{d}r} = -q \tag{3.13}$$

$$\frac{\mathrm{d}M}{\mathrm{d}r} = V \tag{3.14}$$

Distributions of axial, azimuthal and radial loads on a blade oriented at an azimuthal angle of $\theta = -125°$ is presented in figure 3.13 (a). These load distributions are produced by segmenting the blade into radial sections and summing the directional forces at each surface element within a segment. The rotor loading is highest in the axial direction, peaking at approximately $r = 0.8R$. The radial load is strongest in the region $0.2 < r/R < 0.6$, as the blade surface elements have a significant component of area in the radial direction due to the reduction in blade thickness. Radial loads are directed outward as suction forces dominate at each radial segment and at the blade tip. Contours of pressure coefficient on the rotor blade are projected in the spanwise direction in figure 3.13 (b), highlighting the areas where radial forces are significant. The negative pressure forces on the downstream surface (upper surface in diagram) exert a radial load on the blade, as well as axial and tangential loads. Note that the magnitude of the limits of c_p are high as it is based on the freestream velocity rather than the local velocity in the rotating reference frame.

The range of magnitudes of the distributed axial loads q_x over a full revolution in uniform and sheared flow are presented in figure 3.14. In the uniform flow case, the peak load (occurring at $r = 0.8R$) varies by 8.6% due to tower shadow. A much larger variation of peak load of 22.4% is observed in sheared flow.

The distribution of sheared force is calculated by integrating the distributed load along the blade from tip to root. The only reaction force occurs at the blade root, so the shear is largest at this location. The shear force reduces to zero at the tip of the blade, where no reaction is provided.

The flapwise bending moment distribution is calculated by integrating the sheared force distribution. The largest bending moment occurs where the blade is supported at its

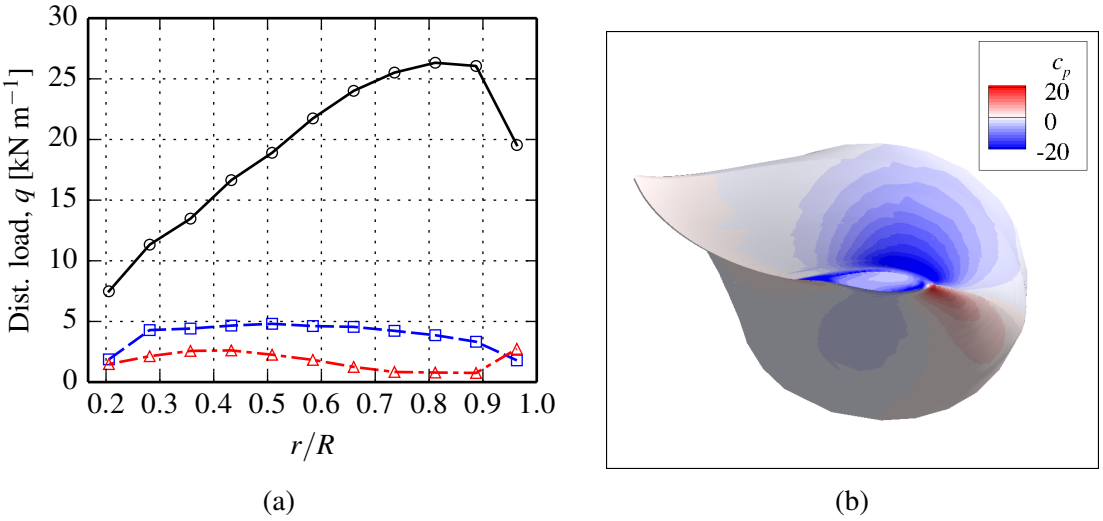

(a) (b)

Figure 3.13: (a) Distributions of axial (○), azimuthal (□) and radial loads (△) on a single blade, along with (b) an end view of rotor blade rotating at $\lambda = 4.5$ in uniform flow, showing the distribution of pressure on the blade surface.

root, and reduces to zero towards the blade tip which is unsupported.

The effect of velocity profile on blade stress can be examined by comparing distributions of bending moment, as this parameter contributes directly to blade stress. The comparison of bending moment distributions in figure 3.14 show that the magnitude and fluctuations are higher in sheared flow. The root bending moment has an average magnitude of 1.28 MN m and a fluctuation of 8.6% in uniform flow which is due to tower shadow. In sheared flow, the mean root bending moment increases by 10% to 1.41 MN m, due ultimately to the higher kinetic flux through the rotor. Additionally, the sheared profile increases the range of root bending moment to 21%.

Distributed load, shear force and bending moments in the azimuthal direction are affected by sheared flow in a similar manner, as shown in figure 3.15. The mean edgewise root bending moment is increased by 9.5% from uniform to sheared flow. The fluctuation in bending moment increases from 14.5% to 39%.

3.4.4 Renormalisation for sheared flow

For comparison of turbines in sheared flow, alternative definitions of thrust and power coefficient can be defined, taking the level of flow shear into account. The distributed thrust

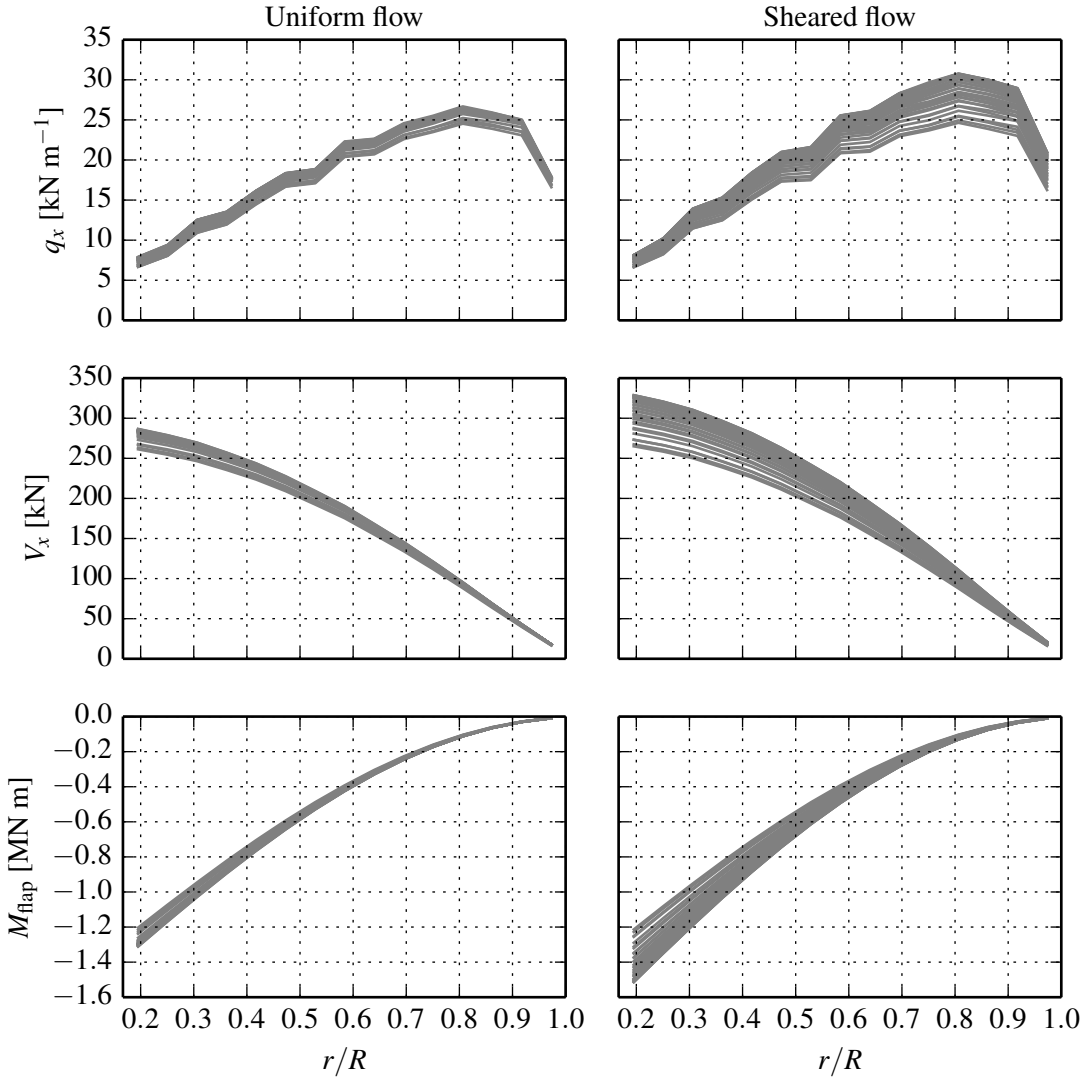

Figure 3.14: Distributed axial load q_x, axial shear force V_x, and flapwise bending moment M_{flap} on a blade in uniform flow (left) and sheared flow (right) over a full revolution at $\lambda = 4.5$.

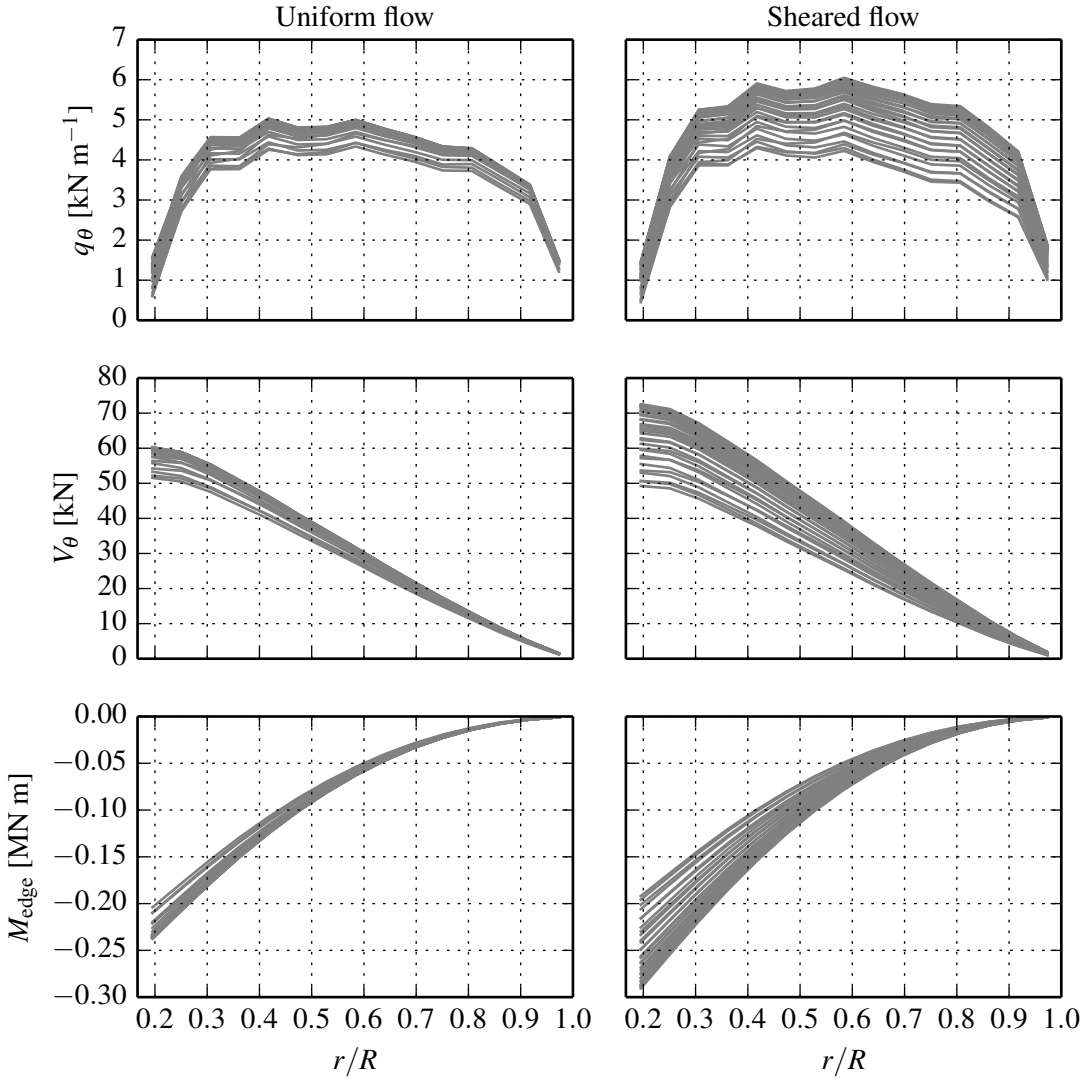

Figure 3.15: Distributed azimuthal load q_θ, axial shear force V_θ, and edgewise bending moment M_{edge} on a blade in uniform flow (left) and sheared flow (right) over a full revolution at a rotor operating point of $\lambda = 4.5$.

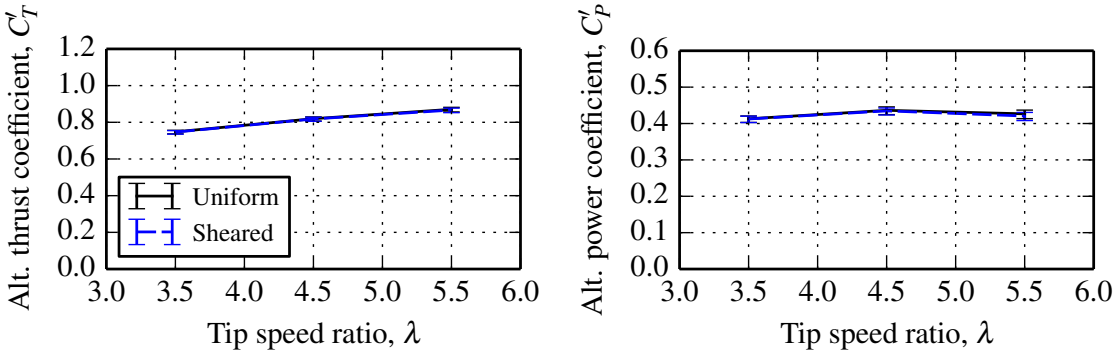

Figure 3.16: Comparison of turbines in different shear profiles from figure 3.10 (b) and (d) with renormalised performance coefficients.

on the rotor can be normalised by the second moment of the upstream velocity profile (area-average of velocity squared),

$$C'_T = \frac{T}{\frac{1}{2}\rho \int_{A_r} [u_\infty(y,z)]^2 \, \mathrm{d}A}, \tag{3.15}$$

where the integration is performed on the undisturbed profile far upstream of the rotor over the area which is intersected by the projected swept area of the rotor, A_r. Similarly, power can be normalised by the third moment of the upstream profile,

$$C'_P = \frac{P}{\frac{1}{2}\rho \int_{A_r} [u_\infty(y,z)]^3 \, \mathrm{d}A}. \tag{3.16}$$

These alternative performance coefficients enable direct comparison of turbines operating in different velocity profiles. The various moments of the current velocity profile are listed in table 3.2. The comparison of turbines in different sheared flow profiles is now repeated using the new definitions of power and thrust coefficient. Note that the definition of tip speed ratio in equation 3.12 already takes velocity shear into account.

Table 3.2: List of the various moments of the velocity profile

Profile details			Velocity moments [m s^{-1}]		
u_{ref} [m s^{-1}]	c_f	z_{hub}	1$^{\mathrm{st}}$	2$^{\mathrm{nd}}$	3$^{\mathrm{rd}}$
2.0	0.0	$0.5h$	2.0	2.0	2.0
2.0	0.007	$0.5h$	2.09177	2.09409	2.09636

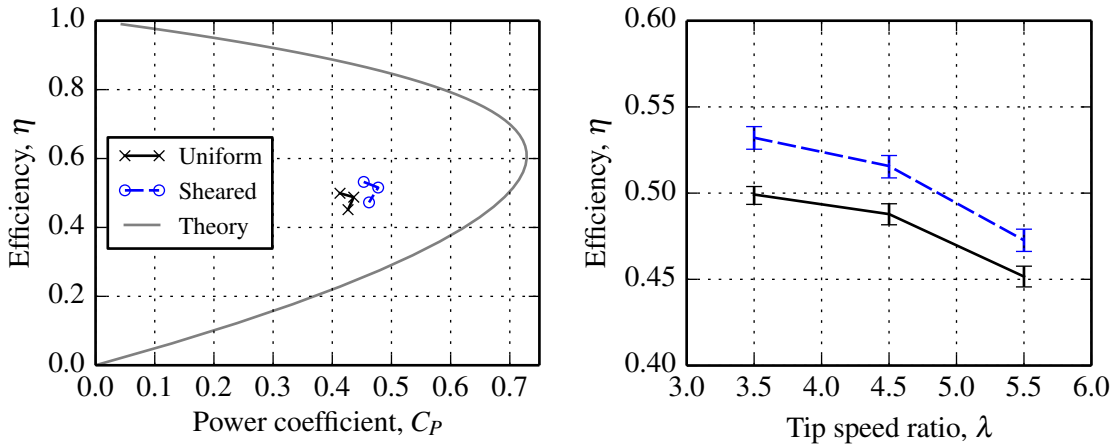

(a) (b)

Figure 3.17: Comparison of turbine efficiency in uniform and sheared flow. The theoretical result in figure (a) is calculated for an ideal turbine using momentum theory (Garret and Cummins, 2007). The tails in figure (b) represent the 5th and 95th percentiles of efficiency.

The respective thrust and power curves, shown in figure 3.16 collapse, showing that the differences in upstream velocity profile are properly accounted for. This result implies that turbine performance in a given velocity profile can be predicted based on knowledge of performance in a different velocity profile, including uniform flow.

3.4.5 Turbine efficiency

The efficiency of a tidal turbine is a measure of the mechanical power relative to the total power lost by the flow. Losses include the transfer of momentum to the rotor blades, and conversion of momentum to heat through viscous action in the wake of the turbine and supporting structure. This metric is also used in chapter 5 to show how a ducted turbine has additional viscous losses relative to an unducted turbine, and hence is less efficient. As the rotor is now resolved, rather than modelled by a porous disc, efficiency can be defined as

$$\eta = \frac{P_{\text{mech}}}{P_{\text{lost}}} = \frac{\omega Q}{P_{\text{lost}}} \tag{3.17}$$

where ω is angular velocity, Q is rotor torque, and T_{tot} is the total streamwise thrust on the structure.

In uniform flow, the total power lost can be found simply by multiplying the total thrust on the device by the freestream velocity. In sheared flow however, the power lost is a function of depth, so the product of the thrust on the device and the upstream velocity must be integrated in the vertical direction.

$$P_{\text{lost}} = \int_0^h T(z) u_\infty(z)\, \mathrm{d}z \tag{3.18}$$

The turbine geometry from the simulation solution should be discretised in the vertical direction into thin strips, and the power lost at each elevation calculated. This process should be repeated and averaged over one third of a revolution, so that every rotor orientation is accounted for. While this method of calculation of efficiency is formally correct, errors are likely to be introduced through the discretisation and averaging process. Instead, the turbine forces and velocity profile are integrated separately and then multiplied together to provide an estimate of efficiency.

$$P_{\text{lost}} = \int_0^h T(z)\, \mathrm{d}z \int_0^h u_\infty(z)\, \mathrm{d}z = T_{\text{tot}} u_{\text{ref}} \tag{3.19}$$

As the sheared velocity profile is based on the same reference velocity as the uniform profile, it integrates to $u_{\text{ref}} = 2\,\mathrm{m\,s^{-1}}$. The reference velocity is a constant, always equal to $2\,\mathrm{m\,s^{-1}}$, so this definition of efficiency is effectively the ratio of rotor power to total turbine thrust. It is desirable to maximise rotor power and minimise total device thrust.

Efficiency is plotted as a function of power coefficient for uniform and sheared flow cases in figure 3.17 (a). The same relationship is calculated for an ideal turbine using one-dimensional momentum theory (Garret and Cummins, 2007). Both computed results yield much lower power and efficiency than the theoretical limits due to viscous losses at the rotor and tower surfaces and in the wake. As previously shown in figure 3.10, the turbine produces more power in sheared flow, due to the higher freestream velocity at the rotor height. The turbine also performs at higher efficiency in sheared flow, indicating that the parasitic drag of the supporting structure is lower. By examining the flow fields in figure 3.8

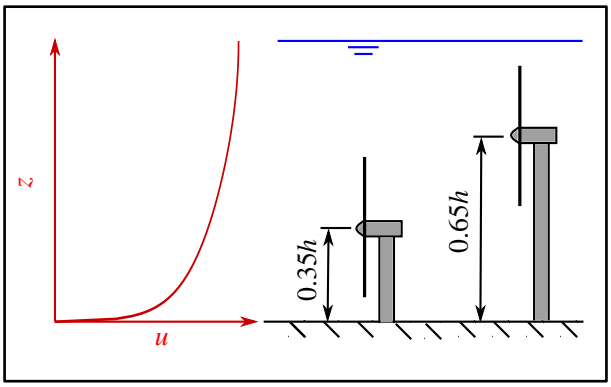

Figure 3.18: The turbine is simulated at elevations of $z = 0.35h$ and $z = 0.65h$ in a sheared velocity profile based on a reference velocity of $u_{\text{ref}} = 2\,\text{m}\,\text{s}^{-1}$ and bed friction coefficient of $c_f = 0.007$.

we can see that the tower encounters lower velocity flow in a sheared profile, resulting in lower thrust. At the three tip speed ratios 3.5, 4.5, and 5.5, the time-averaged tower thrust is higher in uniform flow by 22%, 14% and 10% respectively. The corresponding increases in efficiency in sheared flow are 6.6%, 5.7% and 4.7%.

3.5 Effect of elevation on turbine performance

When installing a tidal turbine at a site where sheared flow occurs, a compromise may arise with regard to the elevation of the turbine from the sea bed. In sheared flow profiles where the velocity increases with distance from the channel bed, a rotor will produce more mechanical power if positioned towards the water surface. However, the axial rotor thrust and the length of the support structure will also increase, resulting in a higher overturning moment at the foundation. Additionally, device efficiency may be reduced due to the increase in relative size of the support structure. The trade-off between mechanical power and structural loading at different elevations in sheared flow is examined in this section.

The turbine is simulated at two hub heights in sheared flow: close to the channel bed ($z_{\text{hub}} = 0.35h$) and close to the free surface ($z_{\text{hub}} = 0.65h$), as illustrated in figure 3.18. The velocity profile corresponds to a bed friction coefficient of $c_f = 0.007$, consistent with the previous study in section 3.4.

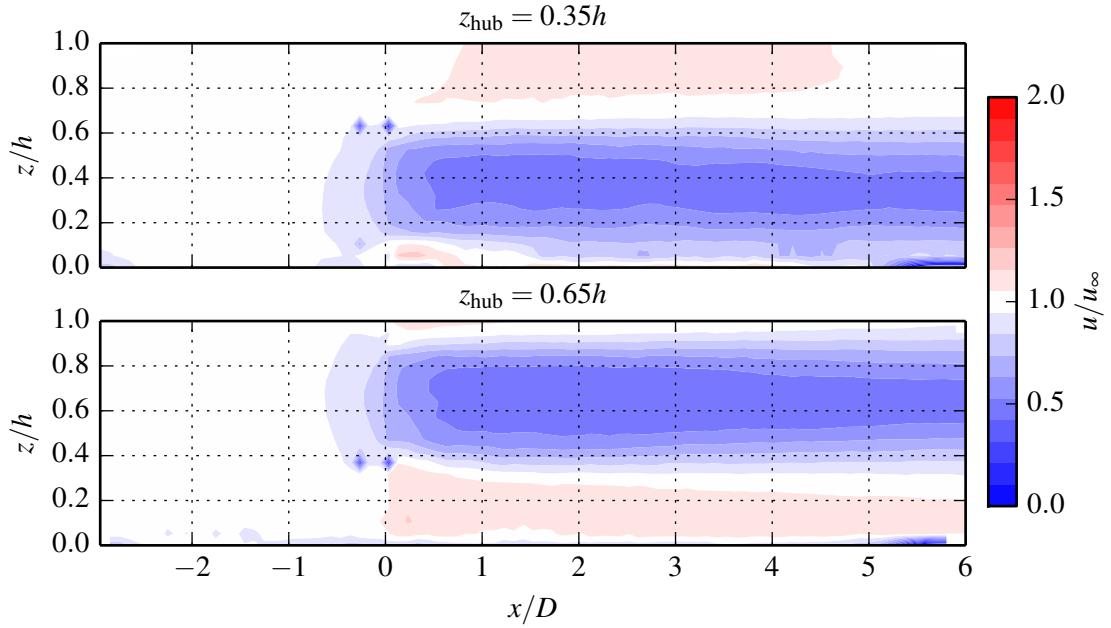

Figure 3.19: Comparison of time-averaged normalised velocity u/u_∞ at the vertical midplane of the channel, $y = 0$, at low ($z_{\text{hub}} = 0.35h$) and high ($z_{\text{hub}} = 0.65h$) elevation. The turbine geometry has been obscured due to the interpolation and time-averaging process, but is present at $x = 0D$. The rotor speed is $\lambda = 4.5$.

3.5.1 Wake development

Qualitatively, the flow fields are quite similar to that shown in figure 3.8, where the hub height is at mid-depth in the profile, $z_{\text{hub}} = h/2$. Velocity and turbulence data for each case is averaged over one third of a revolution so that the time-averaged effects of elevation on wake development can be examined. In figure 3.19, contours of time-averaged velocity at the vertical midplane through the rotor are compared for each elevation. Velocity is normalised on the upstream profile, so that differences to the undisturbed flow are highlighted.

In both the low and high rotor cases, insufficient space exists between the rotor and the nearest bounding surface (the bed or surface respectively) for a strong shear layer to develop. This has greater consequences for the wake in the low rotor case (upper figure), as the velocity close to the bed is low due to flow shear and hence wake mixing is weak in that region. Mixing is visible at the upper boundary of the wake, where the velocity contours spread out between the downstream locations $x = D$ and $x = 6D$. No such

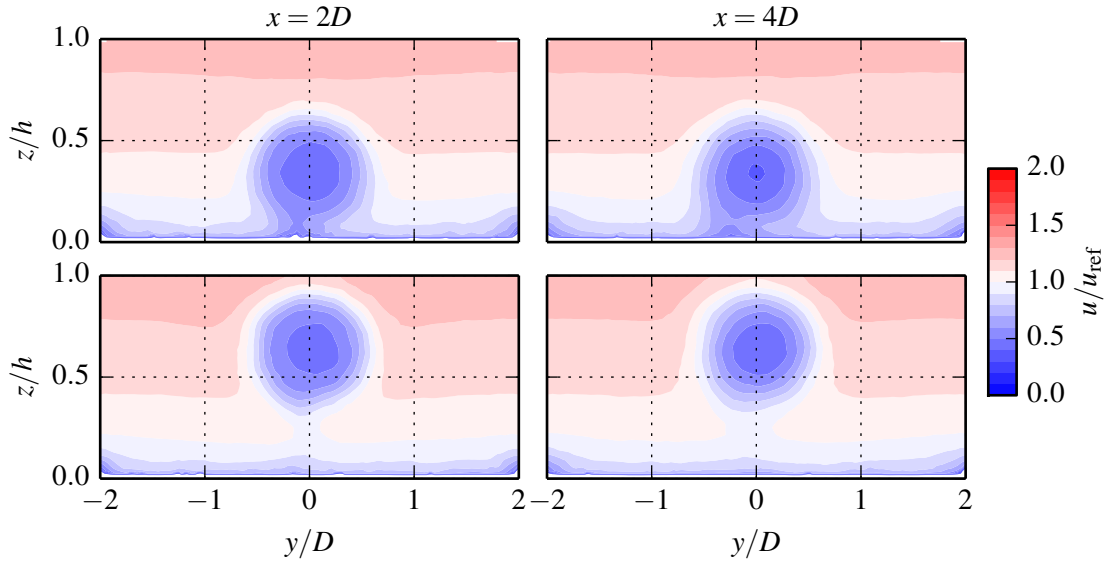

(a) Normalised velocity, u/u_{ref}

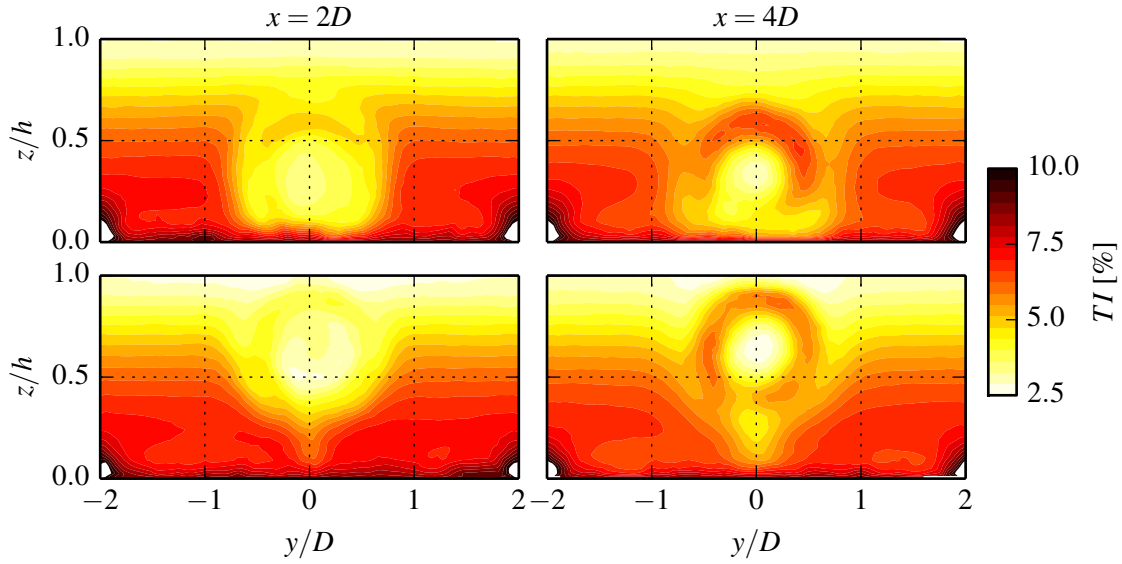

(b) Turbulence intensity, TI

Figure 3.20: Comparison of time-averaged velocity and turbulence intensity at downstream planes $x = 2D$ and $x = 4D$ for a turbine operating at $\lambda = 4.5$ at low ($z_{\mathrm{hub}} = 0.35h$) and high ($z_{\mathrm{hub}} = 0.65h$) elevation.

mixing is apparent at the lower boundary; the velocity contour lines remain at the same vertical locations throughout the downstream region. In contrast, the wake in the high rotor case is surrounded by higher-velocity flow, which generates shear around the full circumference of the wake. Mixing is evident at both the upper and lower wake boundaries between $x = D$ and $x = 6D$.

The extent of the shear layer between the wake and bypass flows in the circumferential direction is examined by comparing cross-stream sections of the velocity field at $x = 2D$ and $x = 4D$ in figure 3.20 (a). In the lower turbine case (upper figure), the wake merges with the low-velocity flow at the channel bed. Mixing of the wake occurs only at the shear layers at the sides and top of the wake, and not underneath it. This is particularly evident when comparing the turbulence generated by wake mixing in figure 3.20 (b). At $x = 4D$, turbulence is generated at the sides and upper portions of the wake for the low rotor case. However at the same downstream location for the high rotor case, turbulence is generated all around the wake.

Although wake mixing occurs only at the upper and side portions of the wake for the low rotor case, it is stronger due to the increased vertical shear at low elevations in the velocity profile. Hence wake mixing begins earlier at the upper side of the wake, as can be seen by comparing the turbulence intensity contours at $x = 2D$ in figure 3.20 (b). At $x = 4D$, the turbulence intensity in the upper portion of the low turbine wake is stronger than that in the corresponding location of the high turbine wake.

3.5.2 Rotor performance and loading

Rotor power and thrust coefficients are compared for the two turbine elevations in figure 3.21. The highest values of thrust and power are observed for the high elevation case, as the rotor encounters higher velocity flow in this region. At $\lambda = 4.5$, the mean axial thrust on the high rotor is 24.6% greater than that on the low rotor. The overturning moment at the base of the tower increases correspondingly from $C_M = 0.58$ to $C_M = 1.35$, where the

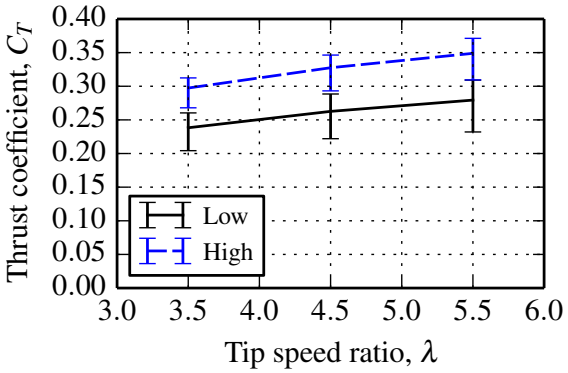

(a) Blade thrust coefficient

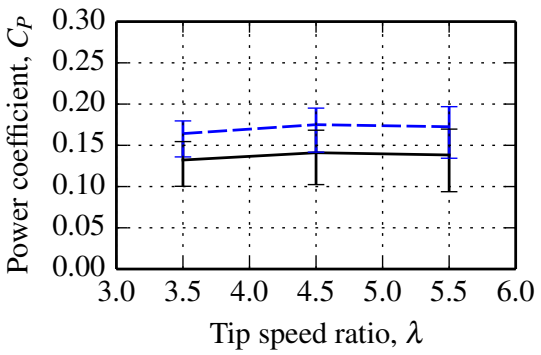

(b) Blade power coefficient

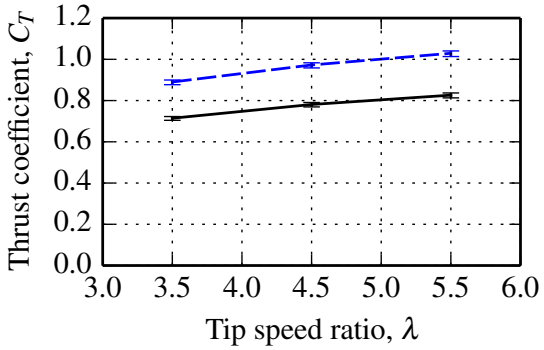

(c) Rotor thrust coefficient

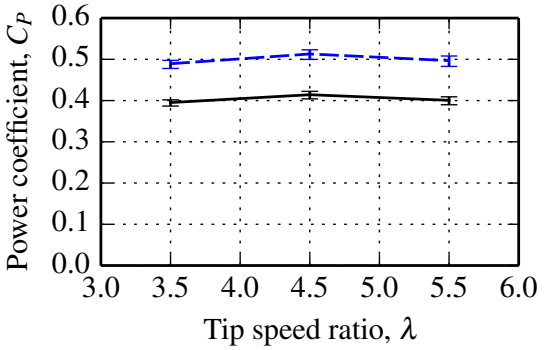

(d) Rotor power coefficient

Figure 3.21: Blade and rotor thrust and power coefficients at low ($z_{\text{hub}} = 0.35h$) and high ($z_{\text{hub}} = 0.65h$) elevations. The errorbars represent the 5th and 95th percentiles of the fluctuations in thrust and power.

moment coefficient is defined as

$$C_M = \frac{M_{\text{tower}}}{\frac{1}{2}\rho u_{\text{ref}}^2 A_{\text{ref}} L_{\text{ref}}}. \tag{3.20}$$

M_{tower} represents the moment at the base of the tower due to the loads on the entire structure. The reference area A_{ref} is the swept rotor area (including the centrebody) and the reference length L_{ref} is the rotor diameter.

Although the mean load is lower, the blades undergo higher fluctuations in loading in the low rotor case, due to the greater differential in the velocity profile at the corresponding rotor height range, $0.1 < z/h < 0.6$. Flapwise and edgewise bending moment distributions along a single rotor blade for a full revolution in each flow case are compared in figure 3.22.

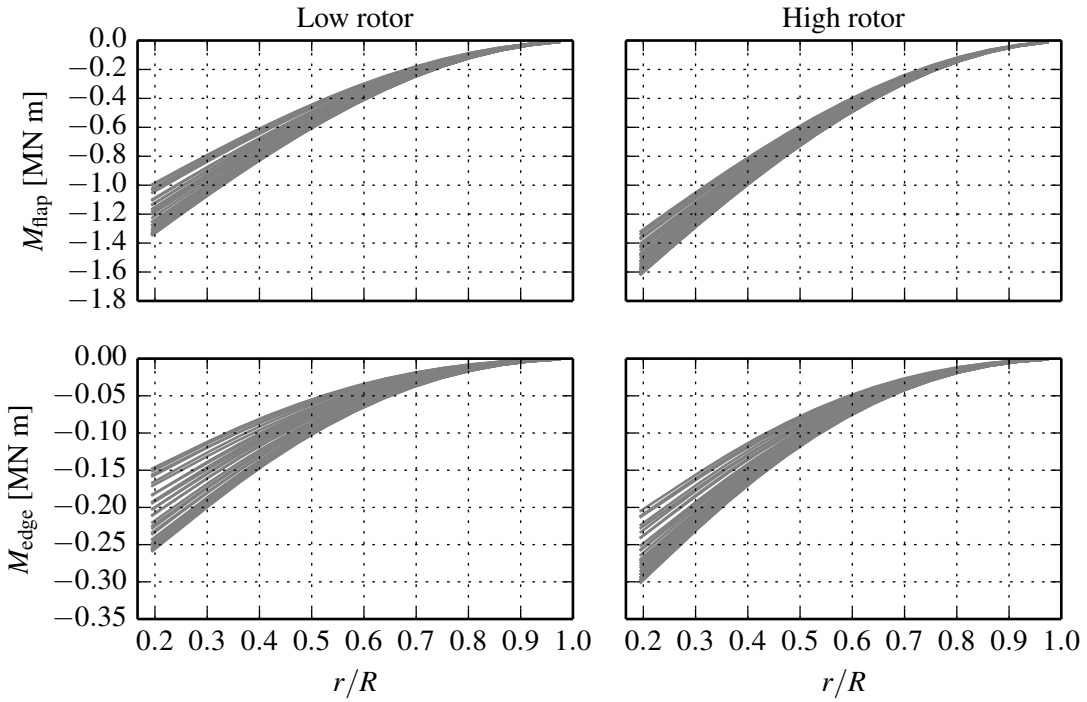

Figure 3.22: Distribution of flapwise (upper figures) and edgewise (lower figures) bending moments for the low rotor and high rotor case over one revolution at a rotor speed of $\lambda = 4.5$. Note that the edgewise bending moments use a smaller scale on the vertical axis.

The highest stress in the blade material will occur at the root, where the maximum bending moment occurs. We can see that the mean flapwise root bending moment for the low rotor case is 20.0% lower than that for the high rotor case, consistent with the load fluctuations in figures 3.21 (a) and (b). The fluctuation in flapwise root bending moment, which is an important parameter for fatigue design, is 29.0% for the low rotor case and 19.7% for the high rotor case. The reduction in edgewise bending moment between the high and low rotor cases is 19.7%, while the respective fluctuations increase from 36.0% to 51.7%.

It is clear that the vertical position of a rotor in a sheared velocity profile has consequences for the structural design of a rotor blade. If a turbine is to be positioned away from the channel bed, the mean velocity is likely to be higher, and the shear across the rotor is likely to be lower. When the rotor is sited close to the channel bed, the blades will undergo lower mean loading due to the lower freestream velocity, but more severe fatigue loading due to the velocity differential across the rotor.

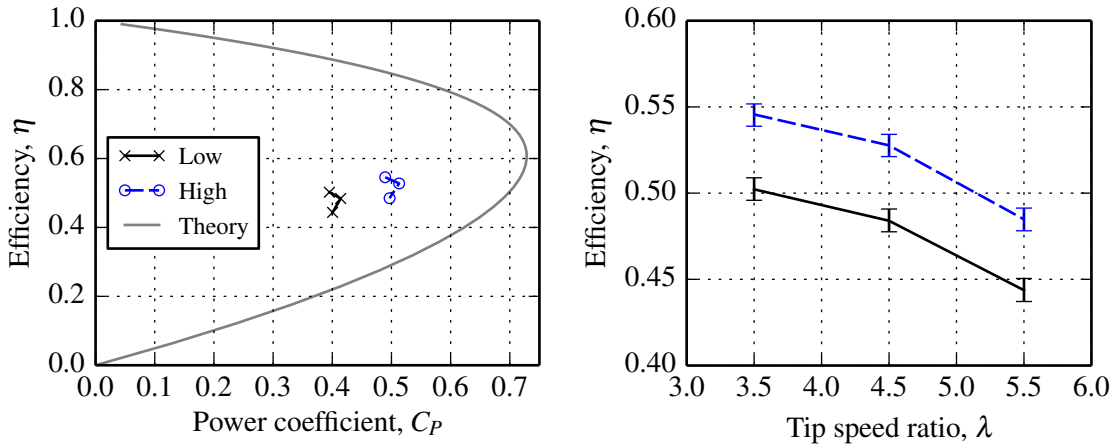

(a) (b)

Figure 3.23: Comparison of turbine efficiency at low and high rotor elevations. The theoretical result in figure (a) is calculated for an ideal turbine using momentum theory (Garret and Cummins, 2007). The tails in figure (b) represent the 5^{th} and 95^{th} percentiles of efficiency.

3.5.3 Turbine efficiency

Efficiency is plotted as a function of power coefficient for the low rotor and high rotor flow cases in figure 3.23 (a). The same relationship is calculated for an ideal turbine using one-dimensional momentum theory (Garret and Cummins, 2007). Both computed results yield much lower power and efficiency than the theoretical limits due to viscous losses at the rotor and tower surfaces and in the wake. As previously shown in figure 3.21, the higher rotor produces more power, due to the greater kinetic flux in the upper portion of the velocity profile. The increase in power available to the rotor outweighs the additional parasitic drag associated with the longer tower, resulting in greater device efficiency.

3.5.4 Renormalisation for sheared flow

The comparison of turbines in sheared flow at different elevations is now repeated using the alternative definitions of power and thrust coefficient in equations 3.15 and 3.16. Again, the respective thrust and power curves collapse, showing that the differences in upstream velocity profile are properly accounted for. This result indicates that turbine performance in a given velocity profile can be predicted based on knowledge of performance in a different

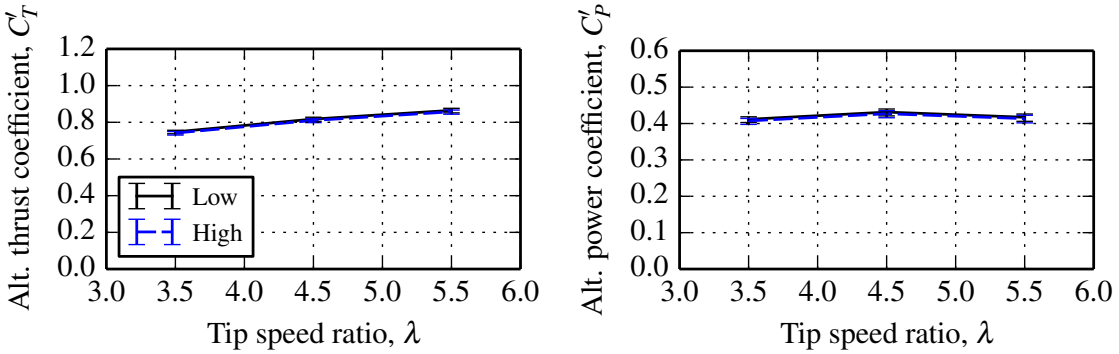

Figure 3.24: Comparison of turbines at different hub heights from figure 3.21 (c) and (d) with renormalised performance coefficients.

velocity profile, including uniform flow.

3.6 Performance in highly blocked flow

The effect of blockage on turbine performance is examined by changing the centre-to-centre spacing of the turbines. This equates to altering the width of the computational domain, due to the employment of periodic boundary conditions at the lateral boundaries of the domain, as illustrated in figure 3.25. The sheared flow simulations from section 3.4 are chosen as a base case, where the device spacing is $s = 4D$ and blockage is $B = 0.0981$. A high-blockage case of $B = 0.262$ is produced by reducing the width of the domain to $s = 1.5D$. Sheared flow velocity and turbulence profiles based on a bed friction coefficient of $c_f = 0.007$ are used for both cases, and the turbine is simulated at tip speed ratios of $\lambda = 3.5, 4.5$ and 5.5.

Table 3.3: List of the various moments of the velocity profile at each hub height.

Profile details			Velocity moments [m s^{-1}]		
u_{ref} [m s^{-1}]	z_f	z_{hub}	1$^{\text{st}}$	2$^{\text{nd}}$	3$^{\text{rd}}$
2.0	0.007	$0.35h$	1.94933	1.95460	1.95970
2.0	0.007	$0.65h$	2.19033	2.19144	2.19253

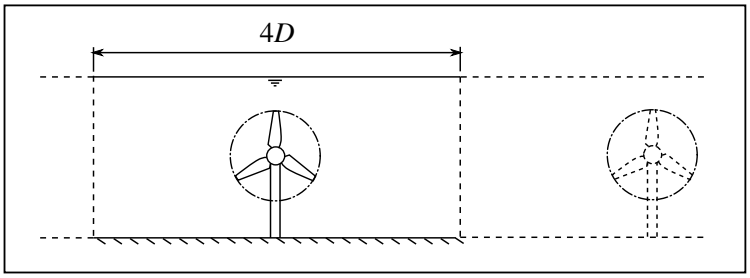

(a) Base case

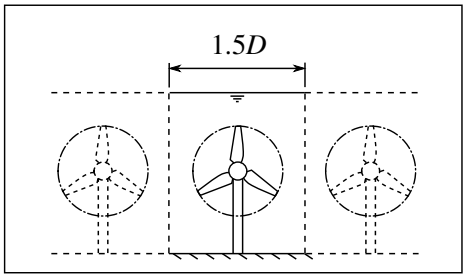

(b) High blockage case

Figure 3.25: The device spacing is altered by modifying the domain width.

3.6.1 Rotor performance and loading

Thrust and power on the rotor and a single blade are integrated over a number of revolutions and are presented in figure 3.26. The results follow the same trend as previous studies of the blockage effect, for example those by Whelan et al. (2009) and Nishino and Willden (2012*a*), where mean thrust and power increase with blockage.

The error bars indicate the 5% and 95% percentiles of the load fluctuations. The fluctuations in blade loading are driven by the sheared velocity profile and the tower interaction. It is apparent from figures (c) and (d) that blockage does not affect unsteady fluctuations in thrust and torque loads, and consequently the range of fluctuation in root bending moment.

Nishino and Willden (2012*a*) explain the mechanism behind the increase in thrust and power in the context of a three-dimensional numerical porous disc model. At higher blockage ratios, the velocity of the flow which bypasses the rotor is increased and its pressure is reduced. Far upstream and far downstream of the rotor plane the flow is parallel. As no pressure gradient can be supported in the cross-stream direction at these locations,

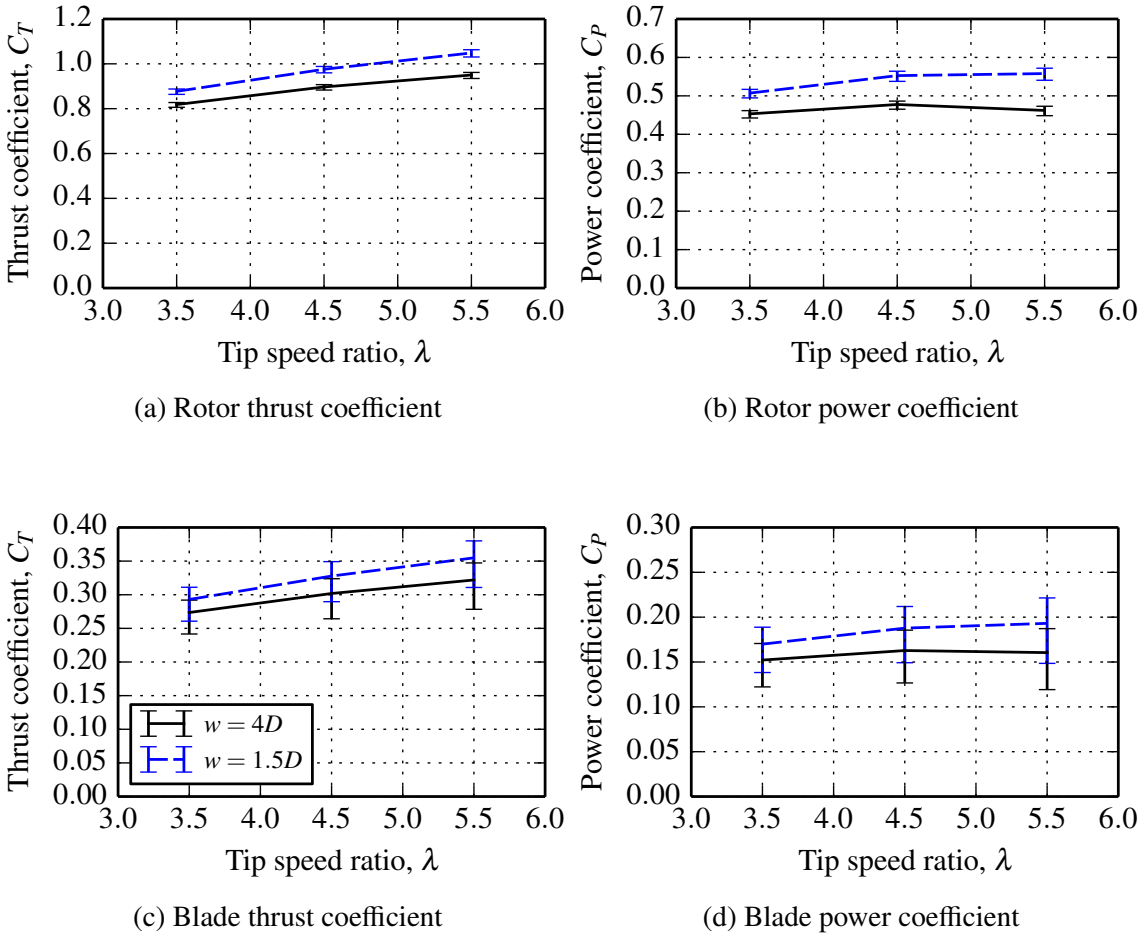

(a) Rotor thrust coefficient

(b) Rotor power coefficient

(c) Blade thrust coefficient

(d) Blade power coefficient

Figure 3.26: Rotor and blade thrust and power coefficients at low blockage ($w = 4D$) and high blockage ($w = 1.5D$). The errorbars represent the 5th and 95th percentiles of the fluctuations in thrust and power.

pressure must be equal in the core and bypass flow channels. Hence the higher pressure drop occurring in the bypass flow due to blockage leads to an increase in the pressure reduction in the core flow across the rotor, and consequently higher thrust and power.

3.6.2 Wake development

The increase in pressure drop with blockage is evident in figure 3.27 (a), where contours of time-averaged pressure are plotted at the vertical midplane $y = 0$ for each flow case at a rotor speed of $\lambda = 4.5$. Pressure is expressed in coefficient form as $c_p = (p - p_\infty) / \frac{1}{2}\rho u_{\text{ref}}^2$. A higher pressure drop is visible in the $w = 1.5D$ case, both locally across the rotor plane and overall between the upstream and downstream boundaries. Figure 3.27 (b) shows the

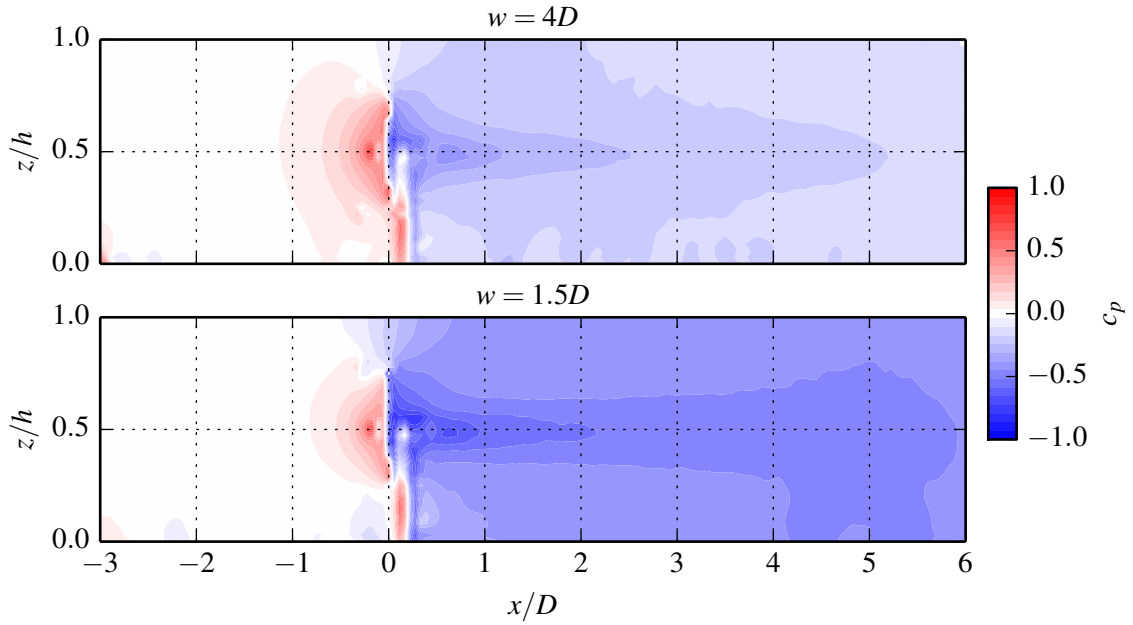

(a) Pressure

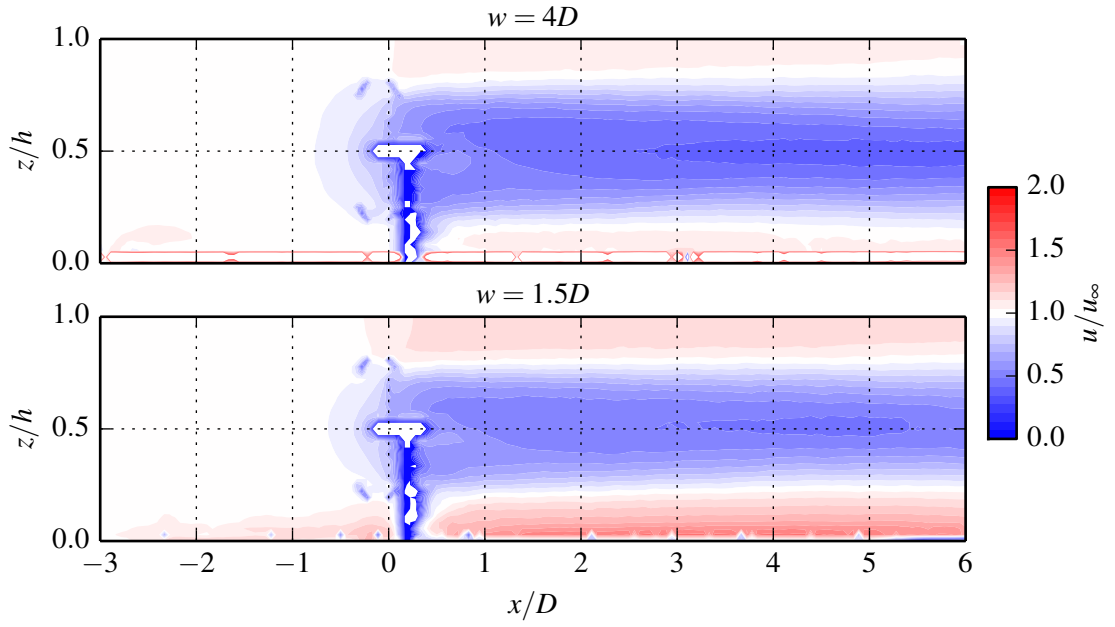

(b) Streamwise velocity

Figure 3.27: Comparison of time-averaged normalised velocity u/u_∞ and pressure coefficient c_p at the vertical midplane of the channel, $y = 0$, for turbine spacings of $w = 4D$ and $w = 1.5D$. The turbine geometry has been partially obscured due to the interpolation and time-averaging process, but is present at $x = 0D$. The rotor speed is $\lambda = 4.5$.

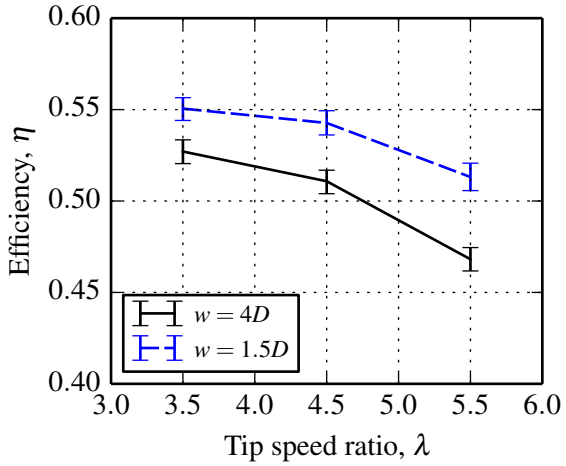

Figure 3.28: Comparison of turbine efficiency at low blockage ($w = 4D$) and high blockage ($w = 1.5D$). The errorbar tails represent the 5th and 95th percentiles of efficiency.

corresponding velocity fields, normalised by the upstream profile $u_\infty(z)$. The increased bypass velocity in the high blockage case is visible above and below the wake in figure (b) (save for the interruption of the tower beneath the rotor). Higher velocity in the bypass flow results in higher shear at the interface between the bypass and core flows, increasing the rate of wake recovery. This is noticeable by comparing the regions of minimum wake velocity which begin around $x = 3D$ in both cases. At $x = 5.5D$, this region has mixed out in the high blockage case, whereas it continues beyond $x = 6D$ in the low blockage case. Figure (b) also shows that at higher blockage the velocity through the rotor and in the wake generally is increased.

Further reduction of the flow velocity through the rotor is possible by increasing the tip speed ratio (which increases rotor resistance, as shown in figure 3.26 (a)). This leads to increased power removal, and hence the optimum tip speed ratio is elevated, as indicated in figure 3.26 (b).

3.6.3 Turbine efficiency

Further examination of figures 3.26 (a) and (b) reveals a greater relative increase in rotor power than rotor thrust when the turbine spacing is altered from $w = 4D$ to $1.5D$. This difference is reflected in a small increase in efficiency, shown in figure 3.28.

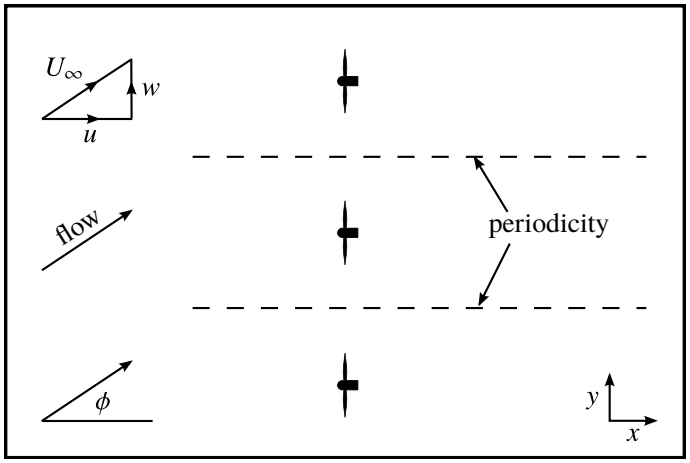

Figure 3.29: Illustration of yawed flow approaching an infinite fence of tidal turbines.

3.7 Performance in yawed flow

Tidal flows are not strictly bi-directional. For example, Gunn and Stock-Williams (2013) present measurements of tidal sites at the Fall of Warness, indicating misalignment between flood and ebb tides in the range of 30°. The effect of flow alignment on turbine performance is examined here. An illustration of the model is given in figure 3.29.

Slight modifications are made to the reference sheared flow case from section 3.4 to accommodate flow at arbitrary angles of alignment ϕ. The turbine and domain geometry is not altered, and continues to represent an infinite fence of tidal turbines with a centreline spacing of $4D$. The desired velocity profile $u_\infty(z)$ is decomposed into an along-channel (x) component of $u = u_\infty \cos\phi$ and a cross-channel (y) component of $v = u_\infty \sin\phi$. Similar modifications are made to the shear boundary condition at the channel bed, so that the resultant bed shear acts directly upstream. The periodic condition at the sides of the channel allows flow to pass out of one side of the domain and re-enter at the opposite side in a continuous manner. The turbine is simulated at tip speed ratios of $\lambda = \{3.5, 4.5, 5.5\}$ at flow alignments of $\phi = \{0°, 15°, 30°\}$.

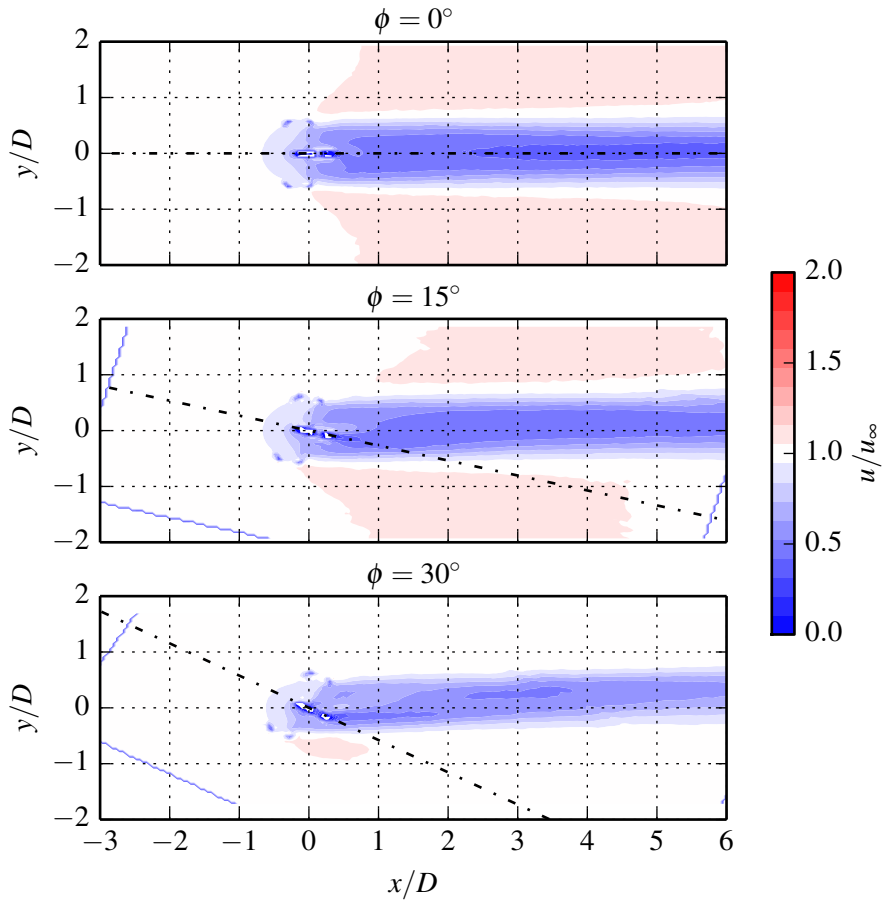

Figure 3.30: Comparison of time-averaged streamwise velocity at mid-depth in the flow, $z = h/2$, for flow alignment angles of $\phi = 0°$, 15°, and 30°. Velocity is normalised on the upstream profile $u_\infty(z)$. The turbine geometry has been partially obscured due to the interpolation and time-averaging process, but is present at $x = 0D$. The rotor speed is $\lambda = 4.5$.

3.7.1 Wake development

The development of the wake in yawed flow is presented in figure 3.30. Time-averaged contours of normalised velocity u/u_∞ are plotted at a horizontal plane at mid-depth in the flow for flow angles of 0° (reference case), 15° and 30°. The domains have been rotated and presented in the reference frame of the oncoming flow to allow direct comparison of the wakes. As the yaw angle is increased, the local flow channel reduces in width by a factor of $\cos\phi$. The projected area of the rotor and tower also reduces by $\cos\phi$, and hence blockage is almost constant (a small increase occurs due to the projected area of the nacelle).

The yawed wakes are narrower in the horizontal direction, corresponding to the reduc-

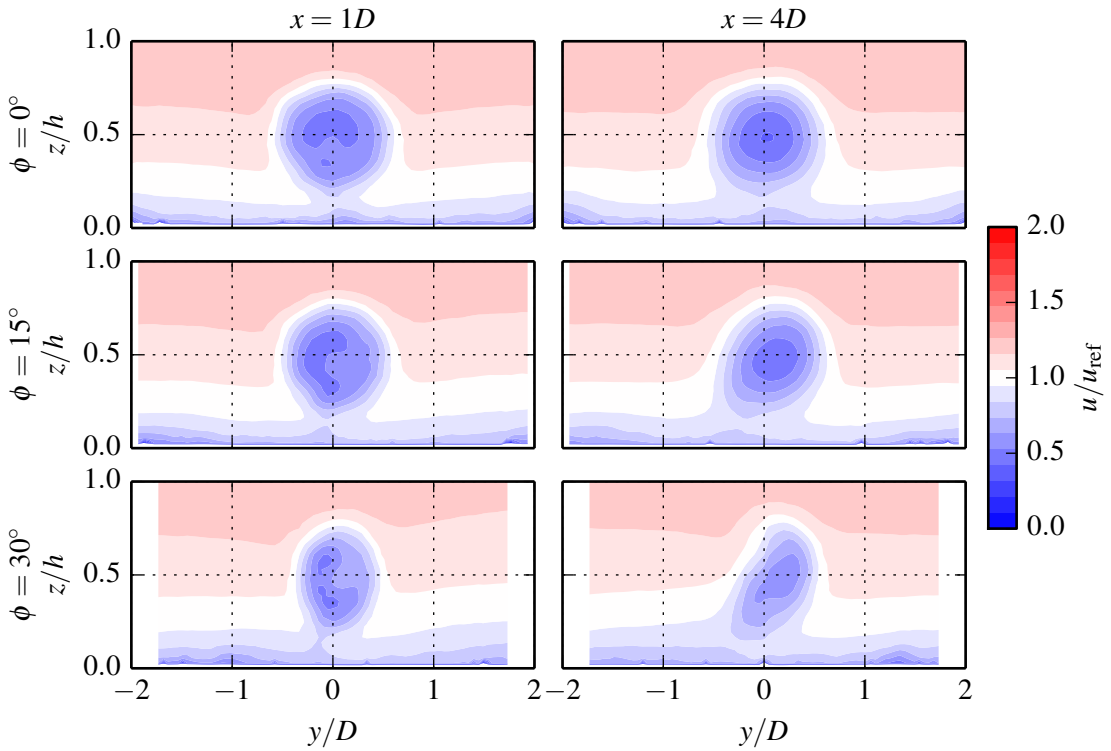

Figure 3.31: Contours of normalised velocity u/u_{ref} at cross-stream planes located $1D$ and $4D$ downstream of the rotor in flows aligned at $\phi = 0°$, $15°$ and $30°$ to the rotor axis. The rotor speed is $\lambda = 4.5$.

tion in projected width of the rotor. The magnitude of the velocity reduction in the wake decreases in yawed flow. This is due to the rotor blades encountering off-design local flow angles, where the lift-to-drag ratio is non-optimal, and hence torque and thrust are reduced.

There is an apparent drift of the wake in the direction of positive yaw (anti-clockwise) which increases with the yaw angle. This is examined further by viewing cross-sections of the flow at $1D$ and $4D$ downstream in figure 3.31. Contours of velocity, normalised by the reference value of $u_{\mathrm{ref}} = 2\,\mathrm{m\,s^{-1}}$, are plotted at these planes for cases where flow is aligned at 0°, 15°, and 30°. The direction of flow is out of the page. The apparent drift observed in figure 3.30 is possibly due to the rotating wake interacting with its respective images through the bed plane and free surface plane. Greater vorticity is generated in the upper portion of the wake as the local velocity at the blade is higher (and the wake rotates slowly). Hence the upper image will have a stronger influence on the wake, causing the upper portion to distort in the direction of rotation. This effect is very slight for unyawed

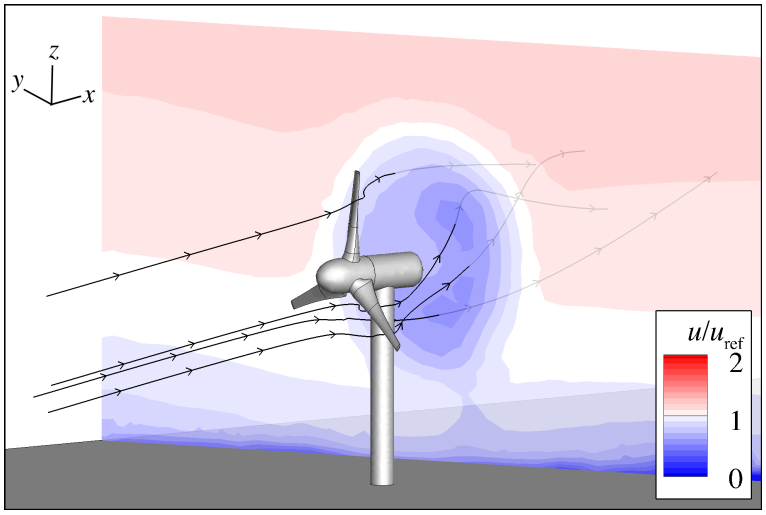

Figure 3.32: An oblique view of the rotor and wake at a plane $1D$ downstream of the rotor and normal to the mean flow direction, colored by normalised velocity u/u_{ref}. The instantaneous pathlines highlight the rotation of the wake and show the local effects of the nacelle and tower. The rotor speed is $\lambda = 4.5$.

flow, but is visible for the $\phi = 0°$ case at $x = 4D$, where the point of minimum velocity at the centre of the wake has drifted to the right of the $y = 0D$ line. The distortion is more pronounced for yawed wakes due to their narrower, elliptical shape.

The cause of the horizontal asymmetry in the yawed wakes at the $1D$ downstream plane is identified by examining the velocity field at that plane in relation to the turbine geometry. An oblique view of this plane from the upstream direction is presented in figure 3.32 for the $\phi = 30°$ flow case. Contours of instantaneous normalised velocity are displayed on the plane, corresponding to the time-averaged contours in the lower-left-hand plot in figure 3.31. The pathlines highlight the rotation of the wake in the opposite direction to that of the rotor, and indicate that the low-velocity regions within the wake are due to the nacelle and the upper portion of the tower.

3.7.2 Rotor performance and loading

Forces on the individual blades and the whole rotor are presented in figure 3.33. Thrust loading is defined in the streamwise direction, and azimuthal forces are calculated relative to the axis of revolution of the rotor. Examining the integrated rotor loads (figures (c) and

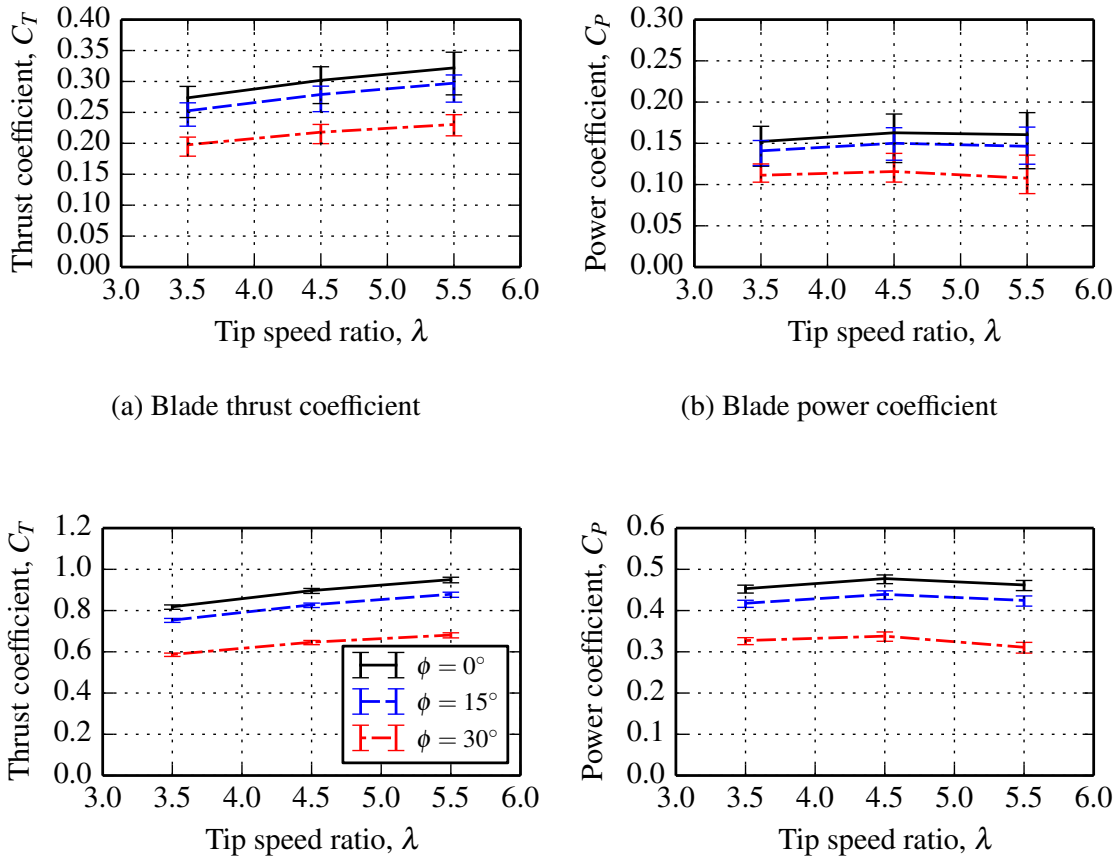

(a) Blade thrust coefficient

(b) Blade power coefficient

(c) Rotor thrust coefficient

(d) Rotor power coefficient

Figure 3.33: Blade and rotor thrust and power coefficients for flow alignment angles of $\phi = 0°$, $\phi = 15°$ and $\phi = 30°$. The errorbars represent the 5th and 95th percentiles of the fluctuations in thrust and power.

(d)), it is clear that rotor thrust and power are reduced in yawed flow. There is a non-linear relationship between the angle of flow alignment and rotor performance: doubling the yaw angle increases the power reduction by a factor of 3.6 at $\lambda = 4.5$. The small fluctuations observed in rotor thrust and power are attributed to the blade-tower interaction.

A reduction in blade thrust and torque due to flow misalignment is observed in the blade loading plots in figures 3.33 (a) and (b). At $\lambda = 4.5$, the blade thrust fluctuations relative to the mean reduce from 21% in aligned flow to 16% in both yawed flow cases. Corresponding blade torque fluctuations are reduced from 38% at $\phi = 0°$ to 28% and 31% at respective yaw angles of 15° and 30°.

The quality of the blade loading history is affected by flow alignment, as shown in

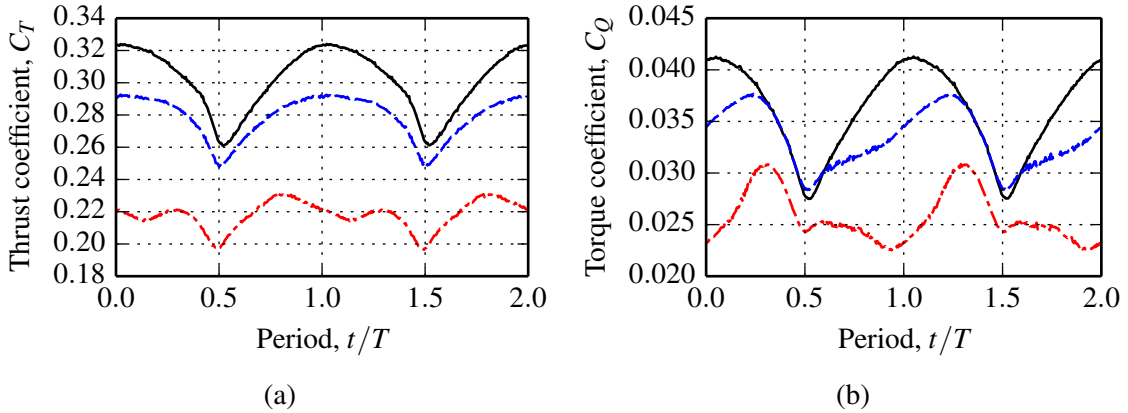

Figure 3.34: Loading history on a single blade in flow aligned at $\phi = 0°$ (—), $\phi = 15°$ (- - -) and $\phi = 30°$ (· – ·). The rotor operating point is $\lambda = 4.5$.

figures 3.34 (a) and (b). Here, the thrust and torque on a single blade are traced over two full revolutions in aligned and yawed flow. While the mean thrust and torque loads are reduced in yawed flow, additional perturbations in thrust and torque are observed. The black line in both figures represents the reference case of aligned flow, also shown earlier in figure 3.11. The blade-tower interaction is identifiable as the minimum in thrust and torque at $t = 0.5T$, and occurs earlier in yawed flow (for the positive angles of yaw examined here, $0° < \phi < 30°$). The oblique view of the rotor in figure 3.32 shows that the blade passes upstream of the tower prior to reaching the bottom of its stroke ($\theta = 180°$). After the blade passes the tower, the thrust increases as the blade moves up through the sheared profile and encounters higher velocity freestream flow. During the up-stroke in yawed flow, the torque history is perturbed as the blade passes behind the nacelle. The blade performs well, with a reduction in thrust and increase in torque, after it passes through its highest position ($t = 0, T, 2T, \ldots$) where it encounters undisturbed freestream flow. At the highest yaw angle, $\phi = 30°$, the blade undergoes a secondary thrust fluctuation in the 'upstream' portion of a revolution due to interaction with the nacelle.

Distributed blade loads are integrated to produce moment distributions over a full revolution in figure 3.35. While the magnitude of the mean flap-wise bending moment at the blade root is reduced in yawed flow by approximately 15%, the relative fluctuations increase from 23% to 35%. Although the edge-wise root bending moment is reduced both

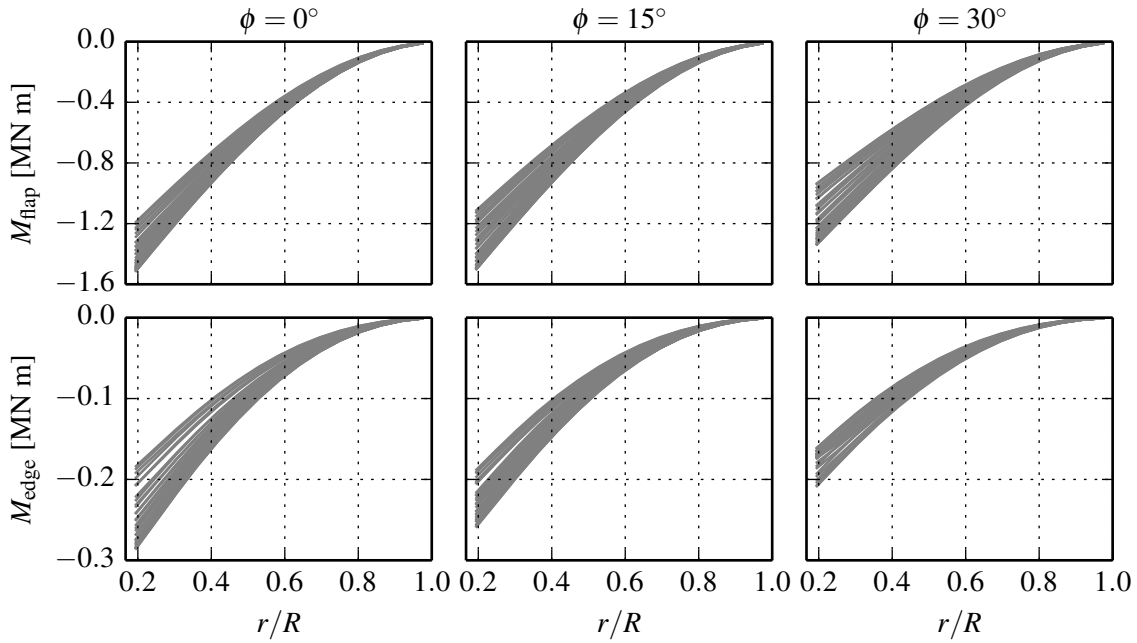

Figure 3.35: Distribution of flapwise (upper figures) and edgewise (lower figures) bending moments for flow yaw angles of 0°, 15° and 30° over one revolution. Note that the edgewise bending moments use a smaller scale on the vertical axis.

in terms of mean value and relative fluctuation in yawed flow. At $\phi = 30°$ the frequency of the root bending moment is the rotational frequency, due to the additional interaction with the nacelle, shown in figure 3.34.

3.7.3 Turbine efficiency

As discussed in section 3.4.5, efficiency is a form of the ratio of turbine power to thrust. Relatively large support structures and poorly designed rotor blades are associated with low efficiency.

The centrebody is streamlined for aligned flow, but behaves as a bluff body at large yaw angles. Unsteady vortex shedding from the nacelle will result in additional viscous losses and reduce the efficiency of the turbine. Additionally, in yawed flow the blades perform in off-design conditions for much of the revolution, as indicated by the loading history plots in the previous section. Hence it may be expected that the efficiency of the turbine would be greatly reduced in yawed flow. However, figures 3.36 (a) and (b) show that at low angles of yaw ($\phi = 15°$) efficiency is hardly effected, indicating that the reduction in

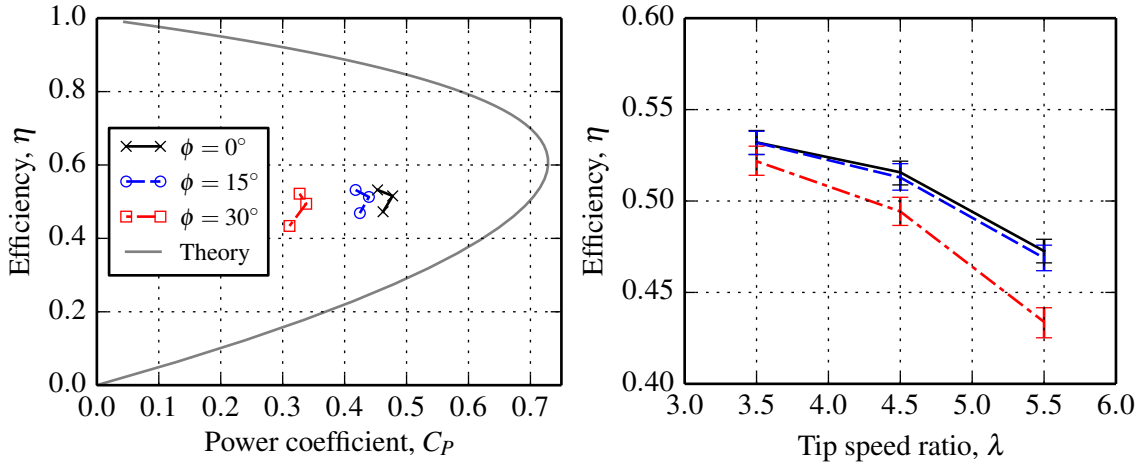

(a) (b)

Figure 3.36: Comparison of turbine efficiency in uniform and sheared flow. The theoretical result in figure (a) is calculated for an ideal turbine using momentum theory (Garret and Cummins, 2007). The tails in figure (b) represent the 5th and 95th percentiles of efficiency.

power is accompanied by an identical reduction in total thrust. At the higher yaw angle of $\phi = 30°$, there is sufficient exposure of the nacelle to affect efficiency. At tip speed ratios of 3.5, 4.5 and 5.5, efficiency is reduced by 2%, 4% and 8% respectively.

3.8 Conclusions

Tidal turbine performance has been examined under a variety of flow conditions as part of a parametric study. The effects of velocity shear, turbine position, blockage and flow alignment have been examined.

Sheared flow has been found to increase mean power and efficiency relative to uniform flow. However the fatigue life of a blade would be reduced, due the higher amplitude of the unsteady loads on the blades. As well as the slight reduction in blade loading due to the tower interaction, a larger load fluctuation occurs as the blade rotates between the high velocity flow in the upper profile and low velocity flow in the lower profile. Wake mixing occurs at a higher rate in sheared flow due to increased velocity in the upper bypass flow as well as higher ambient turbulence.

The power coefficient will be increased if a turbine is positioned higher up in a sheared

velocity profile, due to the greater kinetic flux. For the type of velocity profiles examined, the velocity gradient reduces towards the free surface, and consequently the amplitude of the unsteady blade loads are reduced. The root bending moment on the tower is increased due to the higher mean rotor load and the greater lever length. Despite the increase in relative size of the support structure, device efficiency is improved slightly, as the increase in power outweighs the increase in parasitic drag.

When the rotor is positioned close to the channel bed, power and thrust are reduced due to the lower momentum at that elevation. No shear layer forms at the underside of the wake, and hence the rate of wake mixing is reduced.

The effects of velocity shear on rotor power and thrust can be accounted for through an alternative method of normalisation. The squared or cubed reference velocity term is replaced by the second or third statistical moment of the undisturbed velocity profile, taken over the swept area of the rotor.

When the lateral spacing of a row of turbines is reduced, mean thrust and power are increased due to the blockage effect, where the higher velocity in the bypass flow enables a greater pressure change across the rotor plane. The tip speed ratio corresponding to peak power is increased. No significant increases in the relative amplitude of the unsteady components of thrust and torque are observed. The higher bypass velocity also causes stronger shear in the wake between the bypass and core flows, enhancing wake mixing.

Turbine performance in freestream flow aligned at 15° and 30° relative to the rotor axis has been investigated. Rotor thrust and power are reduced with increasing yaw angle as the blade operates at off-design local flow angles for significant sections of a revolution. During the ‘downstream’ portion of a revolution, a relative increase in blade thrust and a relative decrease in blade torque are observed, indicating stalled conditions. The relative amplitudes of the unsteady components of blade loads are not affected greatly by misaligned flow. However, at high yaw angles, an additional perturbation of the blade loading can occur in the ‘upstream’ portion of a revolution due to interaction with the nacelle. Device efficiency is reduced in yawed flow due to the reduction in power and the

increase in parasitic drag because of the exposure of the side of the nacelle to the oncoming flow.

Chapter 4

Effect of waves on tidal turbine performance

4.1 Introduction

The full scale turbine model is now extended to include the effects of free surface waves on performance. A two-fluid model is used to simulate air and water in an open channel flow, and the volume-of-fluid (VOF) model is employed for free surface tracking. Linear (Airy) wave theory is combined with the existing sheared flow model to calculate unsteady velocity profiles as well as water depth at the upstream boundary. Various numerical techniques required for the stability of the model, such as wave damping and variable time-stepping, are described. A schematic representation of the main features of the model is presented in figure 4.1.

The effect of a deforming free surface (without waves) is examined through comparison with a rigid free surface case from chapter 3. The turbine is then simulated in a variety of wave conditions, with perturbations on wave height and length. Rotor and blade loading are compared to identify the effects of wave height and length. Loading histories are presented for further evaluation of performance, and the influences of velocity shear, tower interaction and waves are identified through frequency analysis.

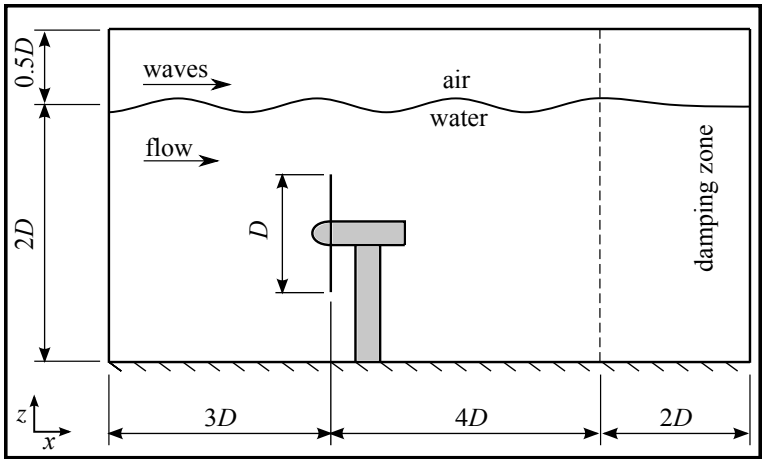

Figure 4.1: Schematic diagram of computational model showing general dimensions and free surface location.

4.2 Volume of fluid model

4.2.1 Phase equation

The full scale tidal turbine model developed in chapter 3 is modified to include the effects of a deforming free surface by the volume-of-fluid (VOF) method. The height of the computational domain is increased so that a volume of air can be simulated above the water flow. The fluid is identified by its phase γ, which has a value of $\gamma = 0$ for air (the primary phase) or $\gamma = 1$ for water (the secondary phase). Phase values in the range $0 < \gamma < 1$ indicate a mixture of fluids in the cell, which occurs at the free surface. The air-water interface is tracked through the solution of the following continuity equation for the volume fraction of the secondary phase (ANSYS Inc., 2012*a*),

$$\frac{1}{\rho_w}\left[\frac{\partial}{\partial t}\left(\gamma_w \rho_w\right) + \nabla \cdot \left(\gamma_w \rho_w \mathbf{u}_w\right)\right] = 0. \tag{4.1}$$

The Fluent solver can account for mass generation and transfer through additional terms in the volume fraction equation, but this is outside the scope of the current study. The air phase volume fraction is calculated as the remaining volume of the cell,

$$\gamma_a = 1 - \gamma_w. \tag{4.2}$$

4.2.2 Discretisation scheme

The volume fraction equation is discretised using an explicit scheme,

$$\frac{\gamma_w^{n+1}\rho_w^{n+1} - \gamma_w^n \rho_w^n}{\Delta t} V + \sum_f \left(\rho_w U_f^n \gamma_{w,f}^n\right) = 0 \tag{4.3}$$

where n is the previous time step, the subscript f denotes a value acting on the face of an element, and U_f is the volume flux through the face based on normal velocity. A local timestep is used to calculate the motion of the free surface, and is set according to a Courant number (named after the Courant-Friedrichs-Lewy condition (Courant et al., 1928)) of $CFL = \Delta t/\Delta t_{\text{char}} = 0.25$, where the characteristic timestep is

$$\Delta t_{\text{char}} = \min\left(\frac{\Delta x_i}{U_i}\right), \quad i = 1, \ldots, N_{\text{elem}} \tag{4.4}$$

where Δx_i is the dimension of cell i in the direction of fluid motion, U_i is the velocity of the fluid through cell i and N_{elem} is the number of elements in the domain. The minimum value calculated by equation 4.4 becomes the characteristic timestep. Face fluxes are interpolated using the 'geo-reconstruct' scheme, which is based on work by Youngs (1982) and has been adapted for unstructured grids (ANSYS Inc., 2012*a*).

Representative values for density and viscosity are calculated based on the balance of phases within a given cell. For example, density is calculated as

$$\rho = \gamma_w \rho_w + (1 - \gamma_w)\, \rho_a. \tag{4.5}$$

Transport equations for momentum and turbulence scalars are solved in each cell using representative material properties for the air and water phases. The second-order upwind scheme is used for interpolation at cell faces, as described in chapter 2.

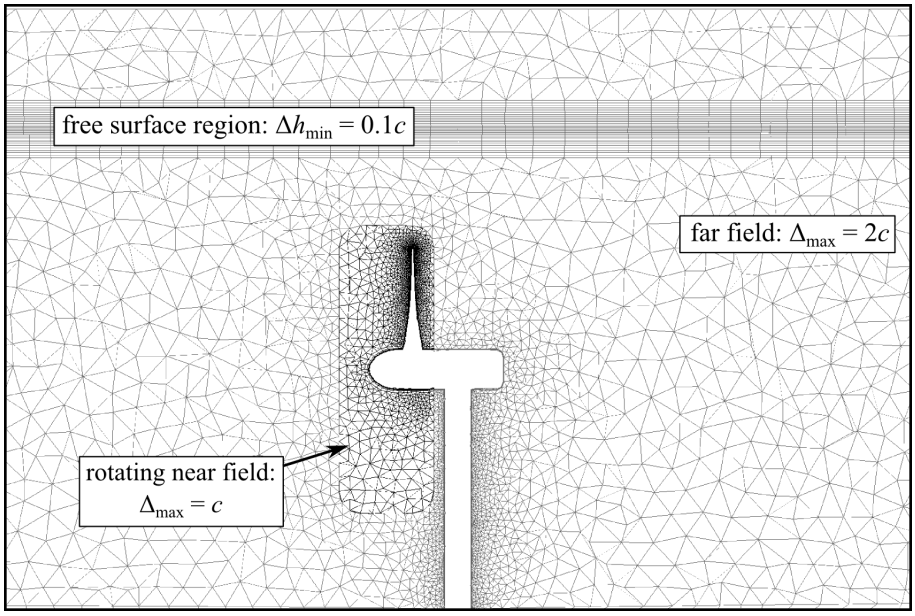

Figure 4.2: Cross section through the computational grid at the vertical midplane $y = 0$, showing element size limits at various locations in terms of the blade chord length at $r = 0.8R$, $c = 1$ m. The domain extends three rotor diameters to the left and six rotor diameters to the right.

4.2.3 Spatial discretisation

The computational grid from the full scale turbine model in chapter 3 is modified to include an air channel of height $h_{air} = 0.5D$. Thirty layers of high aspect ratio prism elements are generated in the free surface region to ensure high resolution of the phase gradient between the air and water flows. The central layers, located at $z = h$, measure $0.1c$ in the vertical direction, where c is the blade chord length at the radial location $r = 0.8R$. This is equivalent to $0.1H$ for a wave height of $H = 1$ m and $0.05H$ for a wave height of 2 m. Successive layers of elements increase in thickness by a factor of 1.05.

A device spacing of $s = 1.5D$ is chosen for consistency with the high blockage case in section 3.6 of chapter 3 and to minimise computational load. The resulting element count is approximately 5.6×10^6. For comparison, the total number of elements in the equivalent rigid lid case is 5.5×10^6.

4.2.4 Turbulence damping

Wave motion at the free surface may cause large local differences in velocity between the air and water phases, leading to unphysical turbulence generation. Stability of the VOF model is improved by damping turbulence in the vicinity of the free surface through the introduction of a source term to the transport equation for specific dissipation rate ω,

$$S_i = A_i \Delta n \beta \rho_i \left(\frac{6B\mu_i}{\beta \rho_i \Delta n^2} \right)^2 \tag{4.6}$$

where the subscript i identifies the phase, $A = 2\gamma_i \left| \nabla \gamma_i \right|$ is the interfacial area density, Δn is the cell height normal to the interface, $\beta = 0.075$ is the coefficient of destruction in the k-ω model, and the turbulence damping factor is tuned to a value of $B = 10^5$ based on preliminary simulations.

4.2.5 Variable time stepping

Stability of the VOF model is improved through the use of variable time stepping. The global timestep size for solution of the transport equations, Δt_{global}, is altered depending on the velocity of the air-water interface and the local mesh density according to the following equation

$$\Delta t_{\text{global}} = CFL_{\text{global}} \Delta t_{\text{char}}. \tag{4.7}$$

where the characteristic timestep Δt_{char} is set for the phase continuity equation based on a Courant number of $CFL = 0.25$ (equation 4.4) and the global Courant number is set to $CFL_{\text{global}} = 2.0$. If the local velocity at a point along the free surface interface increases, the global timestep will be reduced and vice versa. Changes to timestep size are limited to ±2% per timestep. At the beginning of the simulation, timestep size is ramped from $\Delta t_{\text{global}} = 10^{-5}$ s to a typical value of $\Delta t_{\text{global}} = 0.012$ s (with slight variation to maintain the global Courant number at $CFL_{\text{global}} = 2.0$) over the first 400 timesteps.

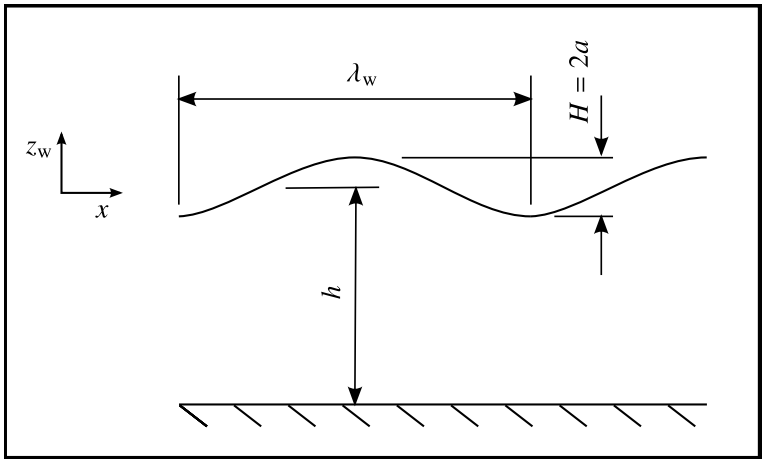

Figure 4.3: Characterisation of linear waves.

4.3 Boundary conditions

4.3.1 Upstream boundary condition

The sheared velocity boundary conditions introduced in chapter 3 are extended to include the unsteady induced velocities and water depth associated with free surface waves. Water depth can be described as a function of time t and streamwise distance x using linear wave theory (Airy, 1841),

$$\zeta\,(x,t) = a\cos\alpha_w \tag{4.8}$$

where the wave amplitude is equal to half the wave height, $a = H/2$, and the wave phase is defined as

$$\alpha_w = kx - \omega t. \tag{4.9}$$

The height of the water phase is specified as an unsteady boundary condition at the domain inlet,

$$h_w\,(t) = h + \zeta. \tag{4.10}$$

The wave number k is the spatial frequency of the wave, i.e. the number of radians per unit distance,

$$k = \frac{2\pi}{\lambda_w} \tag{4.11}$$

and λ_{w} is the wavelength (see figure 4.3).

The intrinsic wave frequency σ is related to wavelength (or wave number) through the dispersion relation,

$$\sigma = \sqrt{gk \tanh(kh)} \tag{4.12}$$

where g is acceleration due to gravity and h is mean water depth ($h = 36$ m for the current model for consistency with the rigid lid model in chapter 3). The dispersion relation can be simplified to $\omega = k\sqrt{gh}$ for cases of shallow water waves, where $h < \lambda_w/20$ and to $\omega = \sqrt{gk}$ for deep water waves, where $h > \lambda/2$. The waves examined in this study fall into the intermediate depth category, and hence the general form of the dispersion relation is used.

The frequency of waves travelling on a current of velocity U is altered due to the Doppler effect. The observed wave frequency ω in a stationary frame of reference is

$$\omega = \sigma + kU. \tag{4.13}$$

In the present model, where the underlying flow is sheared, the current speed is taken as the velocity at the free surface in the absence of waves, $U = u_{\mathrm{fs}}$.

The profiles of horizontal and vertical wave-induced velocities are

$$u_{\mathrm{w}}(z) = \sigma a \frac{\cosh(k(z_w + h))}{\sinh(kh)} \sin\alpha_w \tag{4.14}$$

$$v_{\mathrm{w}}(z) = \sigma a \frac{\sinh(k(z_w + h))}{\sinh(kh)} \cos\alpha_w \tag{4.15}$$

where the origin of the vertical coordinate in the wave reference frame z_{w} is zero at the mean water height $z = h$. It is considered acceptable to superimpose these wave-induced velocities upon a sheared velocity profile, as the velocity gradient is low in the upper portions of the flow where the effect of waves is greatest (see figures 3.6 and 4.12).

The underlying sheared velocity profile is based on a bed friction coefficient of $c_f = 0.007$ and reference velocity of $2\ \mathrm{m\,s^{-1}}$ for consistency with the rigid lid model in chapter 3.

The corresponding free surface velocity, upon which the observed angular frequency is based, is $u_{\mathrm{fs}} \approx 2.2\,\mathrm{m\,s^{-1}}$. A constant velocity of $u = u_{\mathrm{fs}}$ is prescribed for the air phase at the inlet.

During a revolution, the minimum distance from a blade tip to the free surface is $D/4$. At this distance, the rotor blades do not cause any measurable local disturbances to the free surface, and hence resonance between the waves and rotor is not expected.

4.3.2 Downstream boundary condition

The downstream boundary condition presents a difficulty in RANS modelling of a tidal turbine in open channel flow, as the depth change due to energy extraction, and hence the reduced water depth at the downstream boundary, is not known *a priori*. One method of addressing this issue is to prescribe the volumetric flow rate and upstream water depth, and allow the downstream depth to adjust accordingly. However the existing sheared flow model from chapter 3 is based on a prescribed-velocity boundary condition, and hence would be incompatible. The method presented by Consul et al. (2013) allows a velocity profile to be prescribed, and adjusts the downstream depth iteratively until the turbine thrust is balanced by the change in water depth. However this approach is only suitable where a steady solution exists. Hence it is necessary in the current model to fix the water depth at the downstream boundary ($h = 36\,\mathrm{m}$). A hydrostatic pressure gradient corresponding to the downtream water depth applied along the downstream boundary.

Waves are damped prior to reaching the outlet boundary, in the region $4D < x < 6D$, to suppress reflections in the upstream direction. In this region, also known as a 'numerical beach', The following sink term is added to the momentum equation,

$$S = -C\left(\frac{1}{2}\rho\,|w|\,w\right) f\,(x)\,f\,(z) \tag{4.16}$$

where w is the vertical component of velocity and C is a damping coefficient. A value of $C = 10^5$ is used for all cases in this study, based on preliminary simulations of an empty

channel. The damping functions in the streamwise and vertical directions are

$$f(x) = \left(\frac{x - x_\mathrm{s}}{x_\mathrm{e} - x_\mathrm{s}} \right)^2 \tag{4.17}$$

$$f(z) = 1 - \frac{z - z_\mathrm{fs}}{z_\mathrm{b} - z_\mathrm{fs}} \tag{4.18}$$

where the subscripts 's' and 'e' denote the start and end of the damping zone, and 'b' and 'fs' correspond to the channel bottom and free surface.

4.3.3 Other boundary conditions

The remaining boundary conditions are consistent with the rigid lid model in chapter 3. Periodicity is applied to the lateral boundaries, and a symmetry condition is applied at the upper boundary (adjacent to the air flow). A shear force is prescribed along the channel bed to achieve a bed friction coefficient of $c_f = 0.007$.

4.4 Simulated cases

The turbine is simulated in operation in sheared flow and a variety of wave conditions, listed in table 4.1. The tip speed ratios are increased for all cases, apart from the cross-comparison case with no waves, so that the peak in the power curve can be captured. Simulations are run for a flow time of 100 seconds, to allow the wake to convect through the downstream boundary and to allow a sufficient number of waves to pass through the domain for statistical analysis. The wake takes approximately 80 seconds to reach the downstream boundary. Waves travel at the phase velocity of

$$c_p = \sqrt{\frac{g}{k} \tanh(kh)}. \tag{4.19}$$

Waves of length 36 m take approximately 21.6 seconds to pass from the upstream to the downstream boundary, while the longer 72 m waves take 15.3 seconds. Depending

on the size of the variable time steps, the total number of time steps required for 100 seconds of flow time varies in the range 6000 – 8000. Running on a 16-core node of a high performance computing cluster with a clock rate of 2.0 GHz, each simulation takes approximately 130 hours of wall time to complete, resulting in a computational cost of 2000 CPU-hours.

4.5 Wave decay

The water depth, h, identified by a fluid phase value of $\gamma = 0.5$, is recorded at discrete locations along the vertical midplane $y = 0$ at every timestep during the simulation. Histories of water depth are plotted for each wave condition in figure 4.4, indicating the vertical range of motion of the free surface due to waves. The rotor speed is $\lambda = 5.5$ in each case. In case (a), where no waves are modelled but free surface deformation is allowed, some free surface motion is evident. This is attributed to low-frequency error waves, which are caused by the inconsistency between the fixed water depths at the upstream and downstream boundaries and energy extraction by the turbine. The effect of energy extraction at the rotor plane, $x = 0D$, is visible as a small reduction in mean water depth downstream of this plane. A similar reduction in mean water depth occurs for the other three wave cases, (b), (c) and (d). A wave height of $H = 1$ m is prescribed in case (b), but the observed wave height at the upstream boundary ($x = -3D$) is slightly smaller by about 10%. The reason for this is unclear; one possible cause is insufficient grid resolution across the wave envelope, particularly at the minimum and maximum depths. The observed wave height is well-maintained as far as the wave damping zone at $x > 4D$, indicating low

Table 4.1: List of wave operating cases simulated.

Wave height, H [m]	Wavelength, λ_w [m]	Tip speed ratio, λ
0	N/A	3.5, 4.5, 5.5
1	36	4.5, 5.5, 6.5
2	36	4.5, 5.5, 6.5
1	72	4.5, 5.5, 6.5

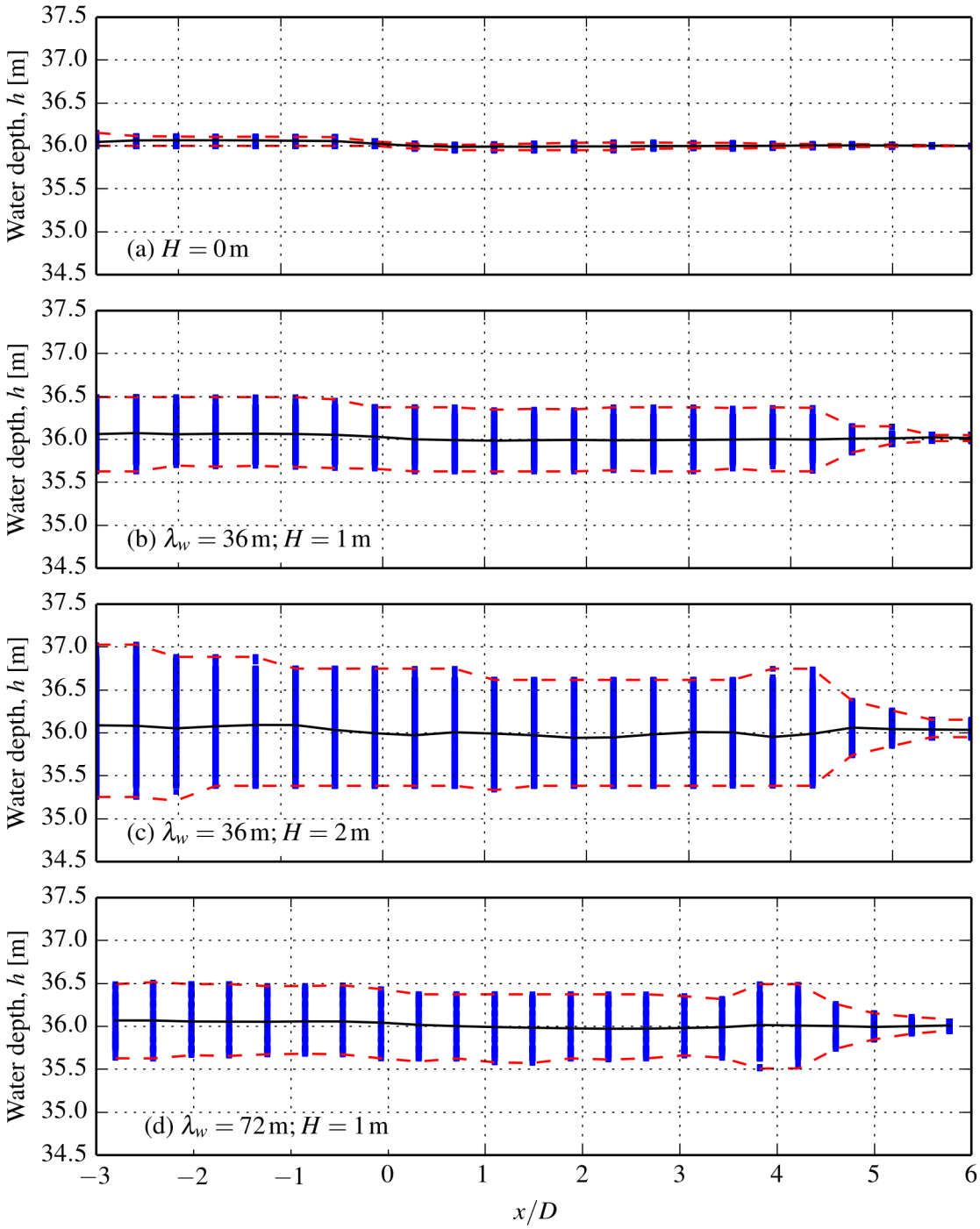

Figure 4.4: Histories of water depth h during the simulation of three wave cases: (a) $H = 0$ m; (b) $\lambda_w = 36$ m and $H = 1$ m; (c) $\lambda_w = 36$ m and $H = 2$ m; (d) $\lambda_w = 72$ m and $H = 1$ m. Instantaneous samples of the free surface, where $\gamma = 0.5$, are indicated by the blue squares which overlap to form vertical bands. The reference water depth is $h = 36$ m. Mean free surface depth is indicated by the solid black line (—), and the upper and lower bounds of the wave envelope are marked by the broken red lines (– – –). The rotor speed is $\lambda = 5.5$ in each case.

numerical diffusion.

When the prescribed wave height is increased to $H = 2\,\mathrm{m}$ (figure (b)), the observed wave height at the inlet boundary is 15% lower at 1.7 m. A higher initial rate of decay relative to case (a) is also apparent, before the wave height stabilises around $x = -D$. The increase in wave height at the beginning of the numerical beach zone at $x = 4D$ could indicate the presence of a standing wave caused by the sudden introduction of wave damping. While the damping functions (equations 4.17 and 4.18) are continuous, the numerical beach could act like a discontinuity if the damping coefficient C (equation 4.16) is overly high. While a standing wave would interfere constructively and destructively with the prescribed waves over time, only the constructive interference (i.e. increase of wave peaks and decrease of wave troughs) would be visible in figure 4.4. At the same time, it appears that the $H = 2\,\mathrm{m}$ waves are insufficiently damped prior to reaching the downstream boundary at $x = 6D$, which is expected to cause some reflection of waves in the upstream direction. These issues suggest that a longer numerical beach zone with a lower damping coefficient would be appropriate for these wave conditions.

The waves in case (d), where $\lambda_\mathrm{w} = 72\,\mathrm{m}$ and $H = 1\,\mathrm{m}$, behave similarly to those in case (b). The only difference is at the interface to the numerical beach, where again the effects of a standing wave are observed. A longer damping zone and a lower damping coefficient may reduce this effect.

4.6 Comparison of the rigid lid and volume-of-fluid models

Prior to the investigation of the influence of waves on turbine performance, it is necessary to identify differences due to the free surface model in isolation. To this end, the turbine is simulated under a deforming free surface (volume-of-fluid model) but in the absence of waves, for direct comparison with the rigid lid model from chapter 3. Illustrations of the rigid lid and free surface models are given in figure 4.5. The key difference between

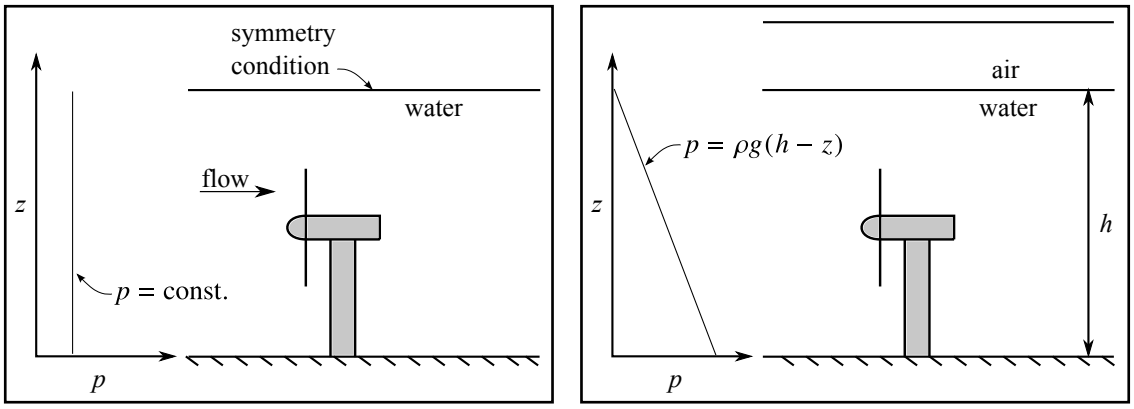

(a) Rigid lid model (b) Volume of fluid model

Figure 4.5: Illustrations of (a) the constant pressure profile for the rigid lid model and (b) the hydrostatic pressure gradient in the volume-of-fluid model.

the models is the depthwise pressure profile. In the rigid lid case, the effect of gravity is not modelled, and the pressure profile is uniform across the upstream flow. In the volume-of-fluid model, the free surface is allowed to deform, and gravity is included as a body force. The corresponding pressure profile is hydrostatic, described by the relation $p(z) = \rho g\,(h - z)$.

Thrust and power coefficients for the blade and rotor are presented in figure 4.6. Generally, a decrease in thrust and an increase in power are observed on a single blade and the full rotor in the deforming free surface case.

A slight reduction in blockage occurs in the deforming free surface case. In this model, a fixed air-water interface height of $h = 36\,\text{m}$ and a hydrostatic pressure gradient are prescribed at the downstream boundary. Because energy extraction by the rotor causes a change in free surface elevation, the upstream water depth must increase accordingly (note that the downstream water depth is fixed in this model), reducing the area blockage. However, the increase in water depth is only 0.22% at $\lambda = 4.5$, with a corresponding blockage reduction of 0.22%, which is unlikely to affect rotor performance.

The improvement in power-to-thrust ratio observed in the deforming free surface case is more likely to be due to a change in the wake induction factor. The local flow angles at the rotor blades are altered so that they operate at a higher lift-to-drag ratio for a given rotor speed, shifting the peak power operating point to a higher tip speed ratio.

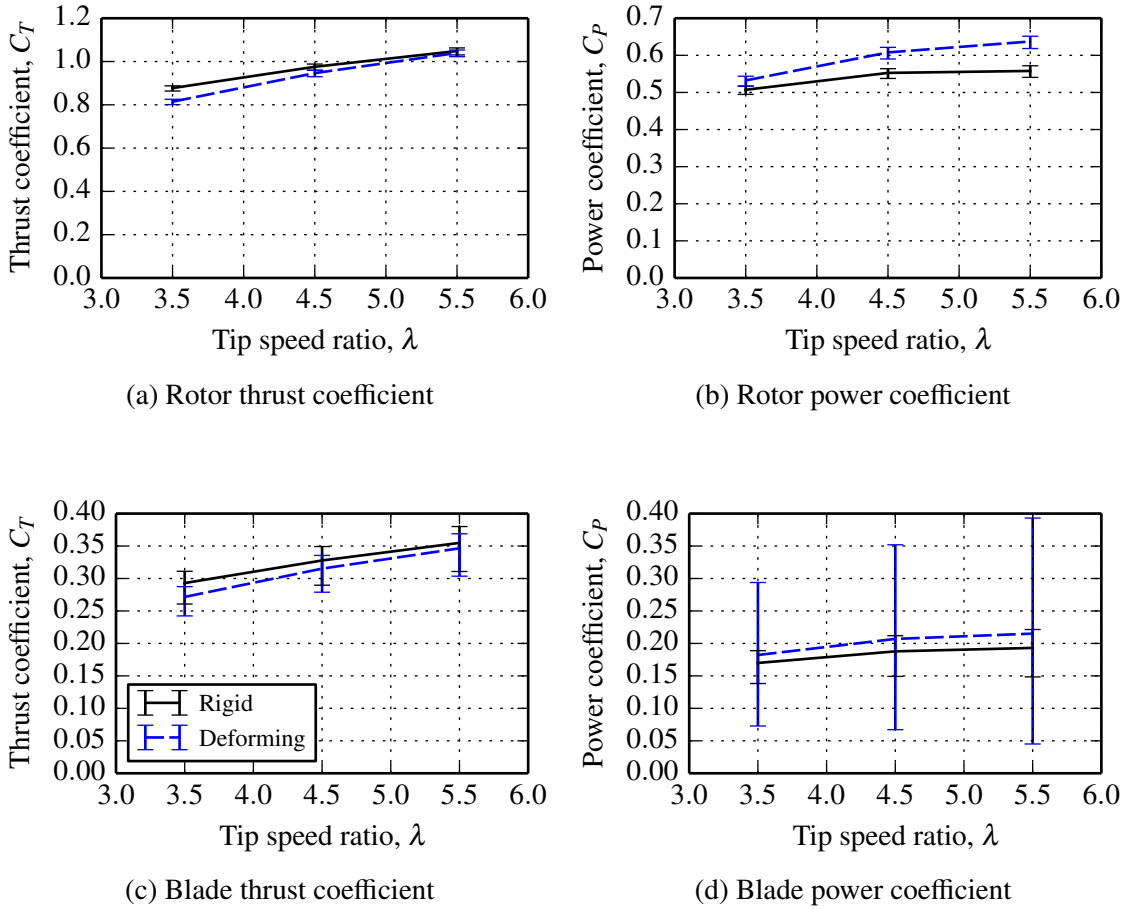

(a) Rotor thrust coefficient

(b) Rotor power coefficient

(c) Blade thrust coefficient

(d) Blade power coefficient

Figure 4.6: Blade and rotor thrust and power coefficients with rigid and deforming free surfaces. The error bars represent the 5$^{\text{th}}$ and 95$^{\text{th}}$ percentiles of the fluctuations in thrust and power.

The fluctuations in rotor power and thrust, indicated at the 5$^{\text{th}}$ and 95$^{\text{th}}$ values by the error bars in figure 4.6, are not affected by the free surface model. While blade thrust is likewise unaffected, fluctuations in blade power are increased dramatically in the deforming free surface case. Figure 4.7 shows histories of thrust and torque on a single blade over two revolutions, beginning at the top-dead-centre ($\theta = 0°$) position. Whereas the blade thrust history for both cases is qualitatively the same, the blade torque history is greatly affected in the deforming free surface model. In addition to the increase in torque amplitude, the location of the extreme loads on the blade is shifted. The tower interaction still occurs at the same point, just after the bottom of the revolution, $t/T = 0.5, 1.5, \ldots$, and can be identified in the torque plot as a slight inflection.

The increase in torque amplitude in the volume-of-fluid model is due to the hydrostatic

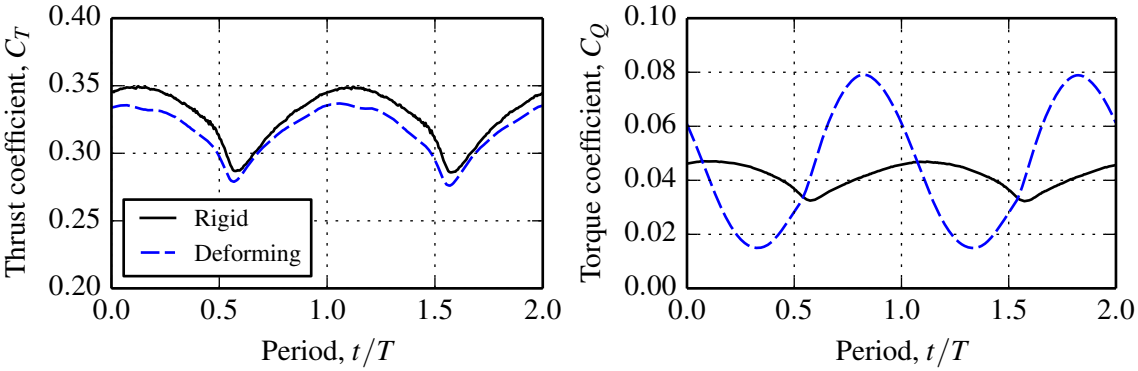

(a) Blade thrust (b) Blade torque

Figure 4.7: Loading history on a single blade over two revolutions for the rigid and deforming free surface models. The rotor speed is $\lambda = 4.5$.

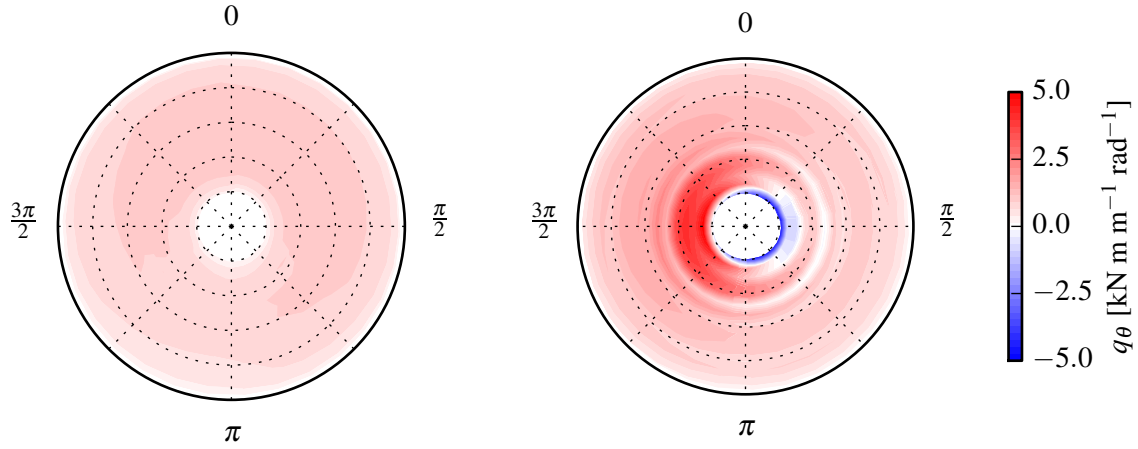

(a) Rigid free surface (b) Deforming free surface

Figure 4.8: Comparison of blade torque over a single revolution with rigid lid and volume-of-fluid models for a rotor speed of $\lambda = 4.5$.

pressure gradient, which is not present in the rigid free surface case. A buoyancy force acts on each blade in the positive vertical (z) direction. The blade geometry is treated as a void in the computational domain and hence does not experience any gravitational force to counteract the bouyancy force. The effect of buoyancy on blade torque is illustrated in figure 4.8, where the torque on a single blade over a full revolution is compared for both free surface models. The blade rotates clockwise, in the direction of increasing angular coordinate θ. In figure (a), the local distributed torque q_θ varies within the range $0.25 < q_\theta < 1.25$, remaining positive at all radial stations and blade orientations. Minimum torque occurs where the blade interacts with the tower just beyond the $\theta = \pi$ point, and

torque is highest in the upper portion of the flow in the sector $0 < \theta < \frac{\pi}{2}$. The effect of buoyancy is visible in figure (b), particularly at the inboard radial stations where local blade volume is largest. During the downstroke ($0 < \theta < \pi$), the hydrostatic pressure gradient acts against the blade and reduces torque. In fact, torque is negative at the blade root, as indicated by the blue contour levels. During the upstroke ($\pi < \theta < 2\pi$), the buoyancy force assists the blade and increases torque, with local values of distributed torque q_θ at the root increasing by a factor of five.

Fluctuations in blade torque are also frequency dependent, and increase with rotor velocity as shown in figure 4.6 (d). Note that this result is not truly representative of the physical scenario, as the turbine geometry is modelled as a void in the fluid and therefore has zero mass. Neutrally-buoyant blades, for example, would be expected to undergo torque loading similar to that predicted by the rigid free surface model.

It is interesting to note that the blade positions where buoyancy has no net effect on torque occur before the blade reaches the vertical positions of $\theta = 0$ and $\theta = \pi$, as shown in figure 4.7. The vertical pressure gradient is converted into positive or negative contributions to local torque depending on the orientation of the local surface normal vector. Hence the blade angles corresponding to peak load will change for different blade geometries.

Velocity fields at the vertical midplane $y = 0$ are compared for the rigid and deforming free surface models at an operating point of $\lambda = 4.5$ in figure 4.9. In both cases, streamwise velocity is normalised by the velocity profile at $x = -3D$ and averaged over one third of a rotor revolution. While the bypass velocity above the wake is similar for both cases, lower acceleration is observed in the bypass flow below the wake for the deforming free surface case. This appears to be due to differences in the way the velocity profile develops upstream of the turbine. In the rigid free surface case, some acceleration occurs upstream of the turbine near the channel bed ($z < 0.15h$) as the profile develops between the upstream boundary and the rotor plane. This is also observed in the lower blockage case studied in chapter 3 (see figure 3.27). The development of the velocity profile is slightly different with a deforming free surface and hydrostatic pressure gradient, with some reduction occurring

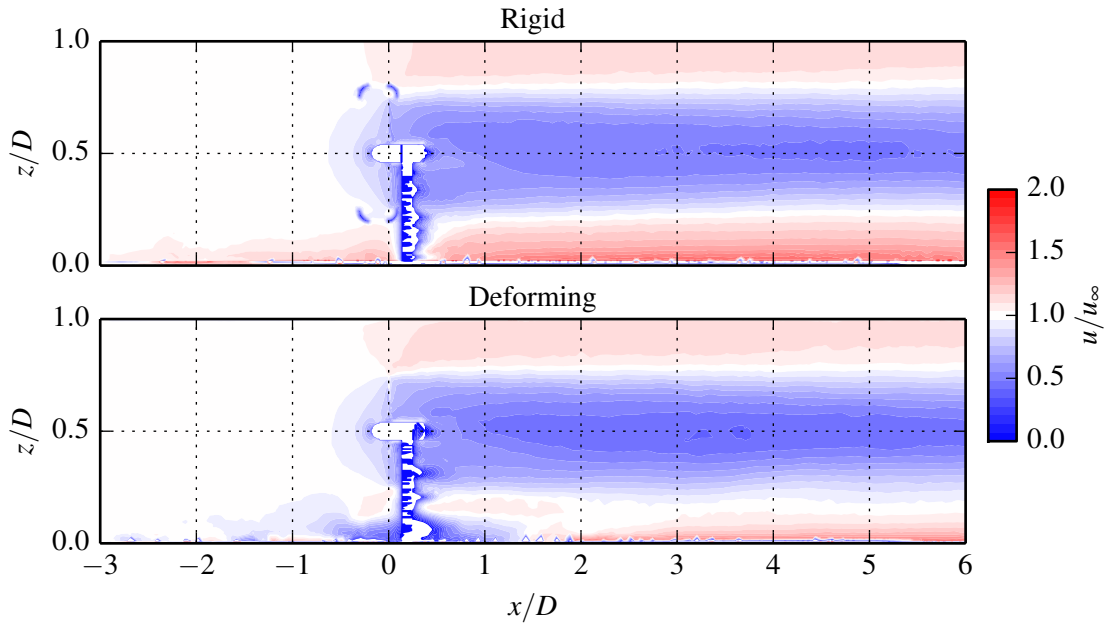

Figure 4.9: Contours of normalised time-averaged velocity u/u_∞ at the vertical midplane $y = 0$ for the rigid and deforming free surface models. The rotor speed is $\lambda = 4.5$.

in the region $z < 0.15h$ upstream of the tower. This deceleration somewhat masks the acceleration in velocity further downstream in the bypass flow beneath the wake.

4.7 Effect of wave height

The deforming free surface model is now used to investigate the effect of wave height on rotor power and loading. Wave heights of $H = 1\,\mathrm{m}$ and $H = 2\,\mathrm{m}$ are modelled, both with a wavelength of $\lambda_\mathrm{w} = 36\,\mathrm{m}$.

An instantaneous view of the turbine in operation under free surface waves of height $H = 1\,\mathrm{m}$ and length $\lambda_\mathrm{w} = 36\,\mathrm{m}$ is presented in figure 4.10. Contours of velocity, normalised by a reference value of $u_\mathrm{ref} = 2\,\mathrm{m\,s^{-1}}$, are plotted on the vertical midplane $y = 0$. The free surface is identified by an iso-surface of constant phase, $\gamma = 0.5$. The local streamwise velocity is elevated immediately beneath each wave crest and decreased beneath wave troughs due to the wave-induced orbital velocities. These wave-induced velocity components also affect the wake of the turbine, and are visible as undulations in the wake velocity contours. Downstream of the plane $x = 4D$, the numerical beach model is active and the

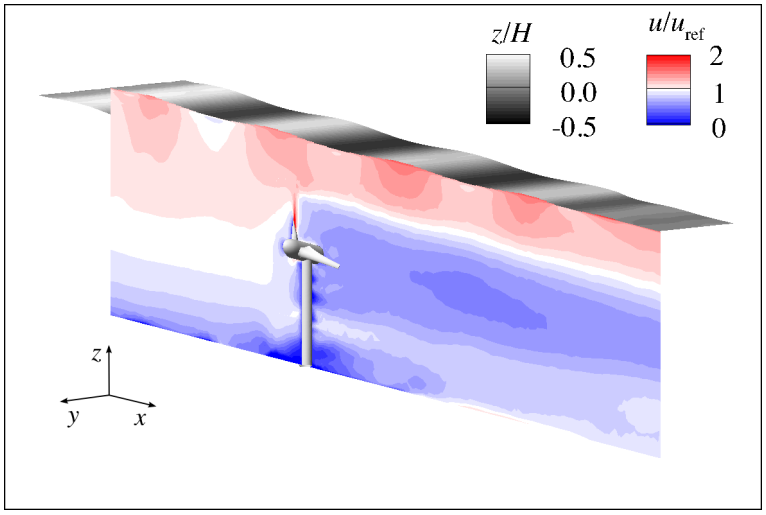

Figure 4.10: Isometric view of the turbine operating at $\lambda = 5.5$, showing the instantaneous velocity field at the vertical midplane $y = 0$ with free surface waves of height $H = 1$ m and length $\lambda_w = 36$ m. The free surface is highlighted by a surface of constant phase, $\gamma = 0.5$, shaded according to depth z/h.

waves are damped.

Rotor and blade power and thrust are presented in figure 4.11, where the data points represent mean values and the error bars indicate the 5th and 95th percentile values. While there is no consistent trend in mean values of power and thrust, fluctuations increase generally with wave height. This increase is due to wave-induced velocities in the horizontal and vertical directions, which alter the local flow angles along a rotor blade, particularly while it is in the upper portion of a revolution. Profiles of maximum and minimum profiles of induced velocities in the horizontal and vertical directions are compared for different wave heights in figure 4.12. The rotor extends from $z = 0.25h$ to $z = 0.75h$, as marked by the broken black lines. An increase of wave height causes increases to the maximum horizontal and vertical induced velocities, consistent with equations 4.14 and 4.15, where the amplitude term arises in the numerator.

It is observed in figures 4.11 (a) and (c) that fluctuations in thrust are relatively larger for an individual blade than the full rotor. Thrust histories for each blade and the rotor in the absence of waves (the deforming free surface case from section 4.6) are presented in figure 4.13. The rotor is operating at a tip speed ratio of $\lambda = 6.5$, and in each case measurements are presented for an integer number of revolutions within the interval

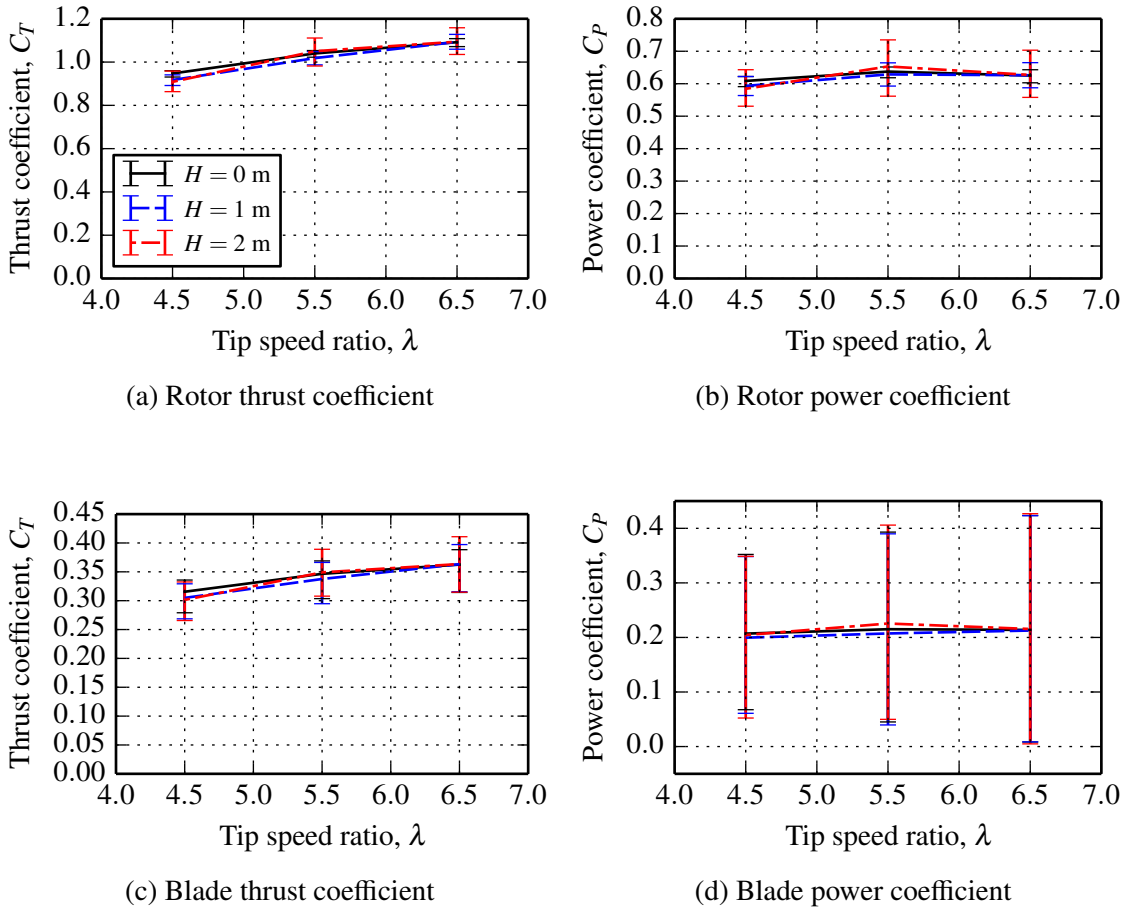

(a) Rotor thrust coefficient

(b) Rotor power coefficient

(c) Blade thrust coefficient

(d) Blade power coefficient

Figure 4.11: Blade and rotor thrust and power coefficients for waves of length $\lambda_w = 36$ m and heights $H = 0$ m, 1 m and 2 m. The error bars represent the 5th and 95th percentiles of the fluctuations in thrust and power.

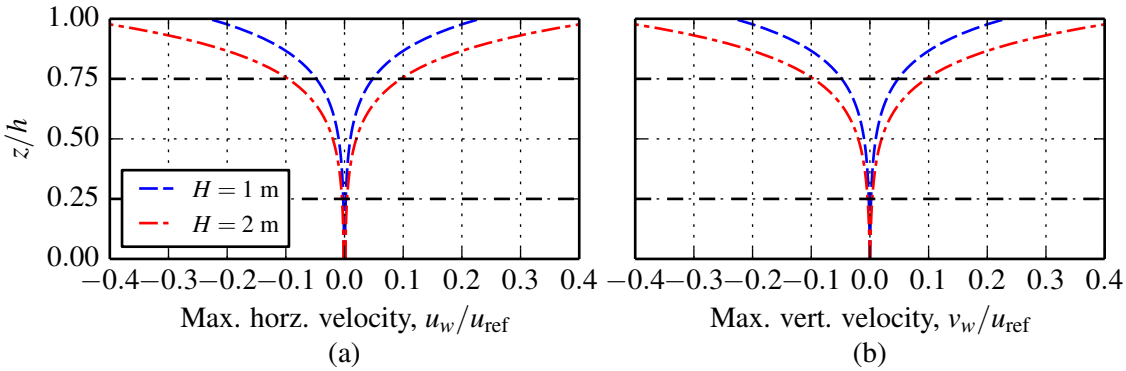

(a)

(b)

Figure 4.12: Maximum (a) horizontal and (b) vertical components of wave-induced velocity according to linear wave theory for different wave heights. The vertical extents of the rotor are marked out by the broken black lines. Note that these events are separated by a phase angle of $\alpha_w = \pi/2$.

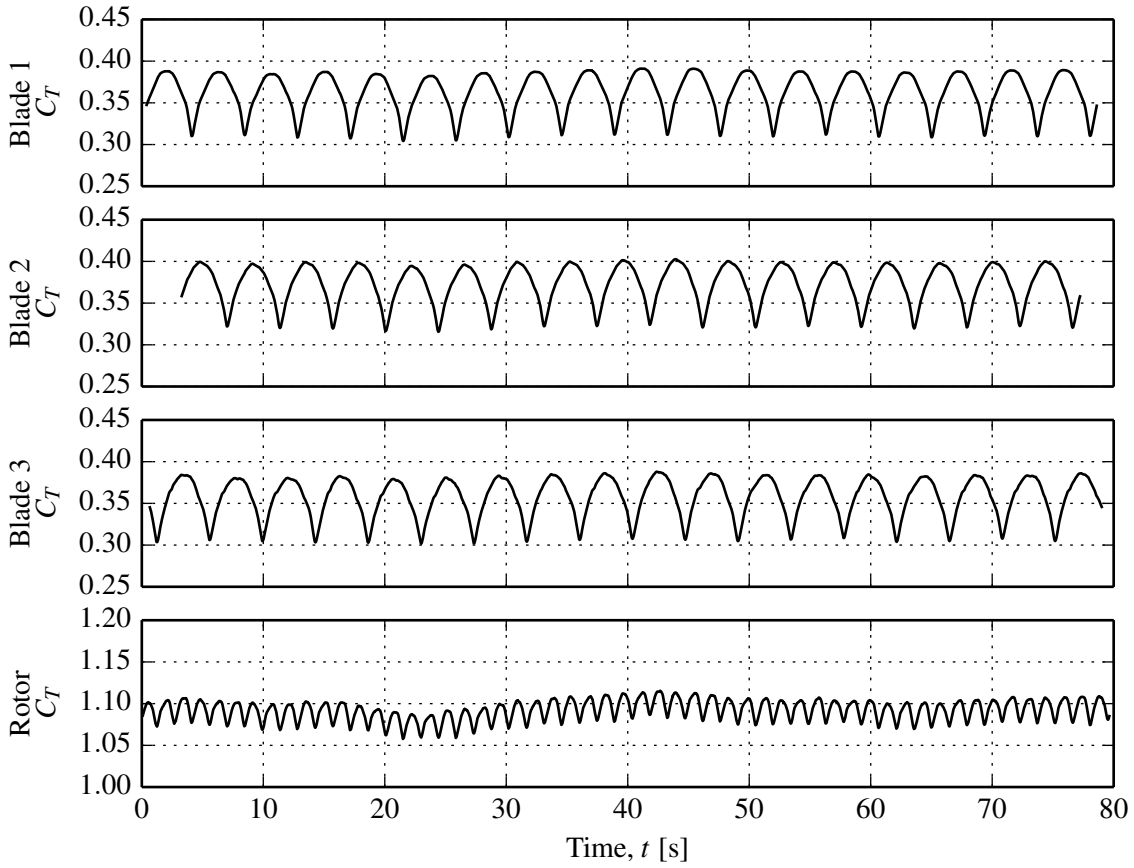

Figure 4.13: Histories of thrust loading on each blade and on the rotor for the deforming free surface case with no waves. The rotor speed is $\lambda = 6.5$ and the vertical scale is consistent across all plots.

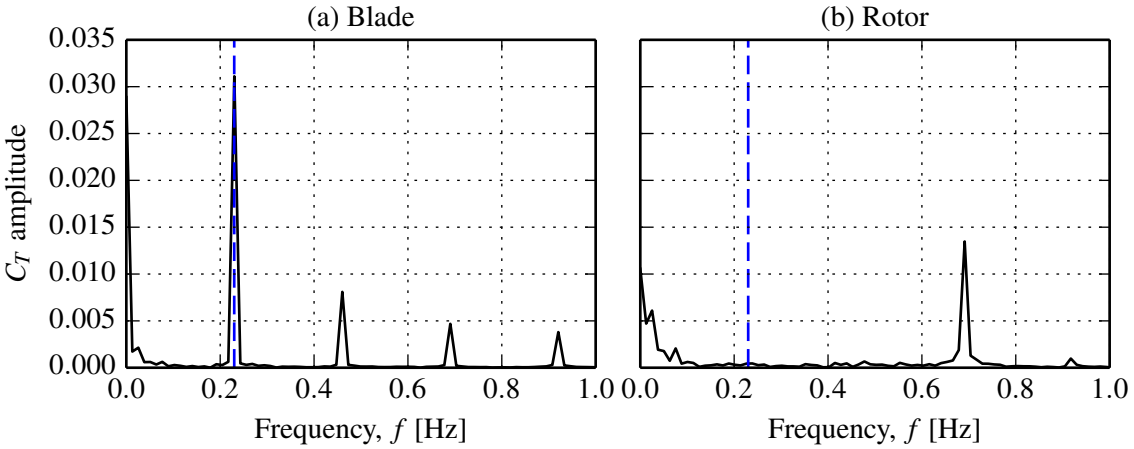

Figure 4.14: Frequency components of the (a) blade and (b) rotor thrust histories from figure 4.13. The broken blue line (– – –) marks frequency of the rotor, f_{rotor}. The normalised resolution is $\Delta f / f_{\text{rotor}} = 0.056$.

$20\,\mathrm{s} < t < 100\,\mathrm{s}$. The individual blades undergo large fluctuations in thrust due to the effect of the sheared velocity profile, as discussed in section 3.4 of chapter 3. A single frequency corresponding to the rotor speed is evident in the blade load histories, and a phase difference of $\theta = 120°$ exists between each due to the even distribution of blades about the rotor hub. When the thrust contributions of each blade are summed together, the unsteady components due to velocity shear cancel out. The lesser effect of the blade-tower interaction remains, occurring at three times the rotor frequency. Slight meandering of the rotor load history occurs due to low frequency error waves. These waves have two causes: the increase in water depth upstream of the turbine due to energy extraction, discussed in section 4.6, and imperfect damping of waves within the numerical beach zone.

A fast Fourier transform (FFT) (Cooley and Tukey, 1965) is applied to the blade and rotor load histories in figure 4.14 to identify the frequency components and ascertain their relative strengths. The frequency-domain output from the FFT is scaled and normalised so that the signal power in each frequency bin is representative of the magnitude of the corresponding load fluctuations, with some losses due to low frequency noise and spectral leakage. The processed FFT output is reported as 'C_T amplitude' or 'C_P amplitude', highlighting the relationship to the magnitude of the unsteady components in the thrust and power histories. Frequency resolution is calculated as $\Delta f = 1/T_{\mathrm{interval}}$, where T_{interval} is the total length of the signal. The normalised frequency resolution is

$$\frac{\Delta f}{f_{\mathrm{cycle}}} = \frac{1}{N_{\mathrm{cycles}}} \tag{4.20}$$

where f_{cycle} is the frequency of the feature of interest (i.e. wave or rotor), and N_{cycles} is the number of cycles of the feature of interest in the time interval. Normalised frequency resolution is reported in the captions of all frequency spectra reported here.

As expected, a single frequency is observed for the blade loading history at $f_{\mathrm{rotor}} = \lambda u_{\mathrm{ref}}/2\pi R = 0.23\,\mathrm{Hz}$, with higher harmonics occurring at integer multiples of the fundamental frequency. When the blade loads are summed, the rotor frequency component

is cancelled out, and the tower effect is observed at $f_{\text{tower}} = 3f_{\text{rotor}} = 0.69\,\text{Hz}$. The low frequency error waves appear in the frequency spectrum in the range $f < 0.1\,\text{Hz}$.

When linear waves of $H = 1\,\text{m}$ and λ_{w} are introduced, the loading histories become more complex, as shown in figure 4.15. The wave loading occurs at a different frequency to that of the rotor, resulting in a slight modulation of the blade load histories. The frequency of this modulation, or 'beating', is equal to the difference between the rotor and wave frequencies,

$$f_{\text{beat}} = |f_{\text{wave}} - f_{\text{rotor}}| \,. \tag{4.21}$$

The rotor and wave frequencies are readily identified in the blade load frequency plot in figure 4.16. Harmonics occur at integer multiples of these frequencies, and some low frequency content arises due to error waves in the domain. The observed wave frequency ω is calculated as

$$\omega = \sigma + k u_{\text{fs}} \tag{4.22}$$

where σ is the intrinsic wave frequency calculated from the dispersion relation (equation 4.12). For the current case of $\lambda = 36\,\text{m}$ waves superimposed on a current with free surface velocity of $u_{\text{fs}} = 2.2\,\text{m}\,\text{s}^{-1}$, the observed frequency is $\omega = 0.27\,\text{Hz}$. This frequency is identified by the red dash-dot line in figure 4.16. From this figure it is clear that a sheared velocity profile causes greater fluctuations in thrust than free surface waves for this operating case.

When the blade forces are summed in figure 4.15, the range of thrust fluctuation is reduced slightly, but appears to contain higher frequency components. Frequency analysis of the thrust history on the rotor in figure 4.16 (b) shows that this small reduction in thrust fluctuation is due to the cancelling out of the shear effect at the rotor frequency. Free surface waves have a greater influence on the rotor as a whole, and will have a negative impact on the fatigue life of the rotor power shaft and the turbine support structure. The higher frequency component in the rotor load history is due to the blade-tower interaction, similarly to the case without waves. The effect of error waves in the computational domain

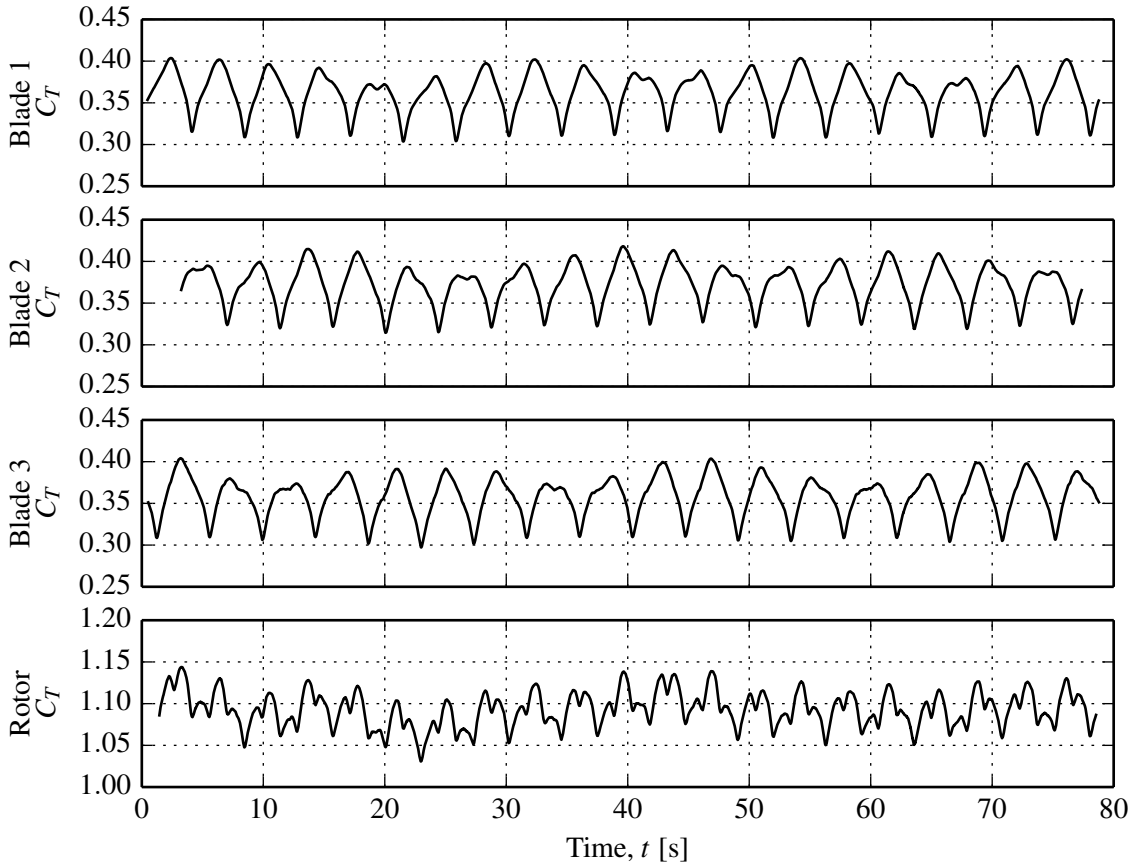

Figure 4.15: Histories of thrust loading on each blade and on the rotor for waves of length $\lambda_w = 36$ m and height $H = 1$ m. The rotor speed is $\lambda = 6.5$ and the vertical scale is consistent across all plots.

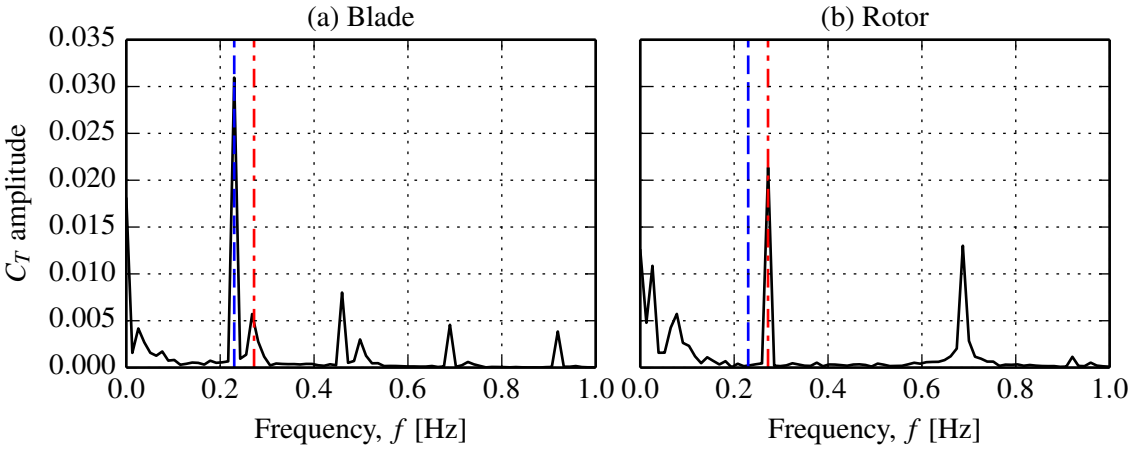

Figure 4.16: Frequency components for the (a) blade and (b) rotor thrust histories from figure 4.15. The broken blue line (– – –) marks frequency of the rotor, f_{rotor}, and the dash-dot red line (– · –) marks the wave frequency, f_{wave}. The normalised resolution of the primary frequency components are: $\Delta f / f_{\text{rotor}} = 0.056$, $\Delta f / f_{\text{wave}} = 0.047$.

is again evident for this operating case, firstly as the meandering of the rotor loading history, and secondly as the low frequency content in the blade and rotor frequency spectra.

4.8 Effect of wave length

The effect of wave length on turbine performance is presented in figure 4.17, where thrust and power are compared for waves of height $H = 1\,\mathrm{m}$ and wavelengths $\lambda_\mathrm{w} = 36\,\mathrm{m}$ and 72 m. Mean values of thrust and power on a single blade and the full rotor are not significantly affected by a change of wavelength. Unsteady blade and rotor loading is increased generally, as indicated by the error bars which represent the 5^{th} and 95^{th} percentile loads. This increase can be explained by examining profiles of maximum wave-induced velocity, shown in figure 4.18. In the region where the rotor lies, $0.25h < z < 0.75h$, the magnitudes of the horizontal velocity u_w and vertical velocity u_w profiles are greater for the $\lambda_\mathrm{w} = 72\,\mathrm{m}$ case.

The quality of the thrust loading histories on the blades and rotor operating at $\lambda = 6.5$ in waves of $H = 1\,\mathrm{m}$ and $\lambda_\mathrm{w} = 72\,\mathrm{m}$ are examined in further detail in figure 4.19. A more pronounced, higher frequency beat occurs here relative to the $\lambda_\mathrm{w} = 36\,\mathrm{m}$ case previously examined in figures 4.15 and 4.16, due to a larger difference between the wave and rotor frequencies. In fact, the wave frequency is now lower than the rotor frequency, as shown in figure 4.20 (a), and causes fluctuations similar in magnitude to the sheared velocity profile. The waves move slowly enough that a given wave can influence a single blade over a full revolution. When a rotor blade is in phase with a wave crest, i.e. the rotor is close to its azimuth as a wave passes through the rotor plane, the streamwise velocity will be increased and maximum blade thrust will occur. This occurs at times $t = 10\,\mathrm{s}$, 30 s and 50 s for ‘Blade 1’ in figure 4.19. The maximum blade load is reduced if the blade is in phase with a wave trough, as streamwise velocity will be reduced, and is observed at $t = 20\,\mathrm{s}$, 40 s and 60 s. The minimum blade loads are affected in a similar manner, but to a lesser extent because the induced velocities reduce with depth, as shown in figure 4.18.

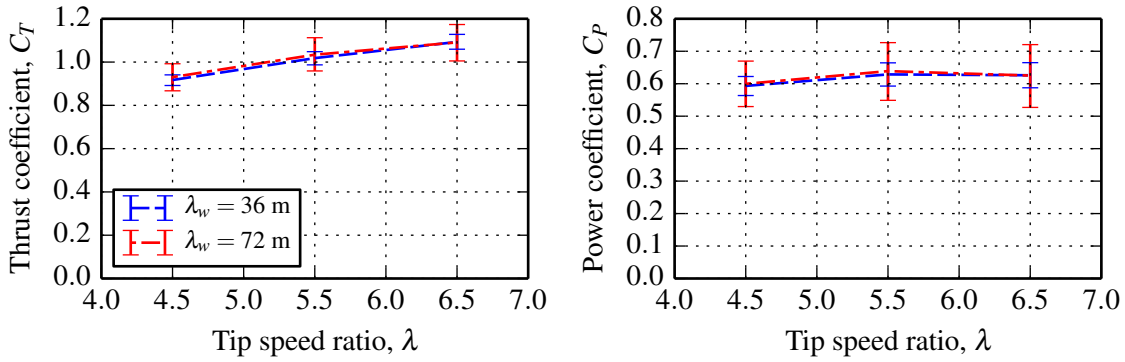

(a) Rotor thrust coefficient

(b) Rotor power coefficient

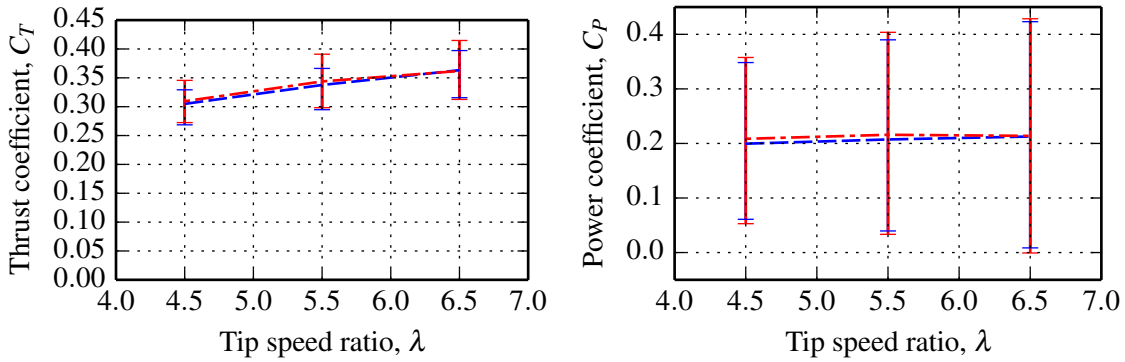

(c) Blade thrust coefficient

(d) Blade power coefficient

Figure 4.17: Blade and rotor thrust and power coefficients with free surface wavelengths of $\lambda_w = 36$ m and 72 m. The error bars represent the 5$^{\text{th}}$ and 95$^{\text{th}}$ percentiles of the fluctuations in thrust and power.

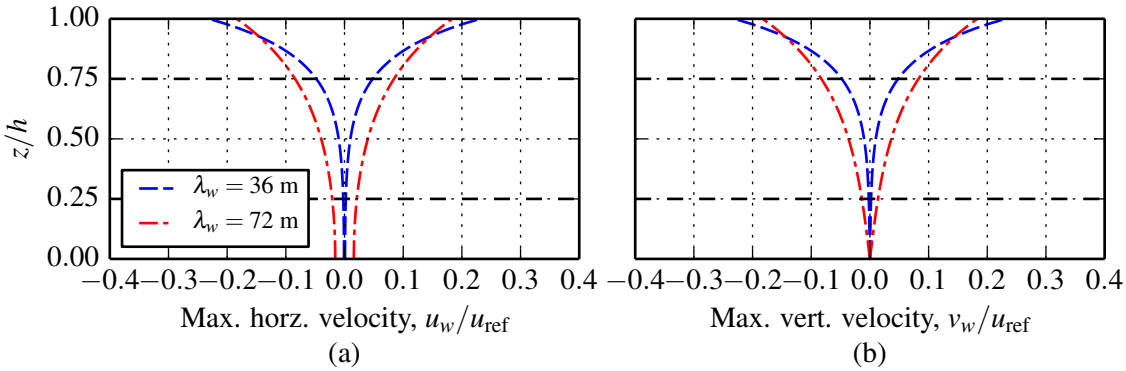

(a) (b)

Figure 4.18: Maximum (a) horizontal and (b) vertical components of wave-induced velocity according to linear wave theory for different wave lengths. The vertical extents of the rotor are marked out by the broken black lines. Note that these events are separated by a phase angle of $\alpha_w = \pi/2$.

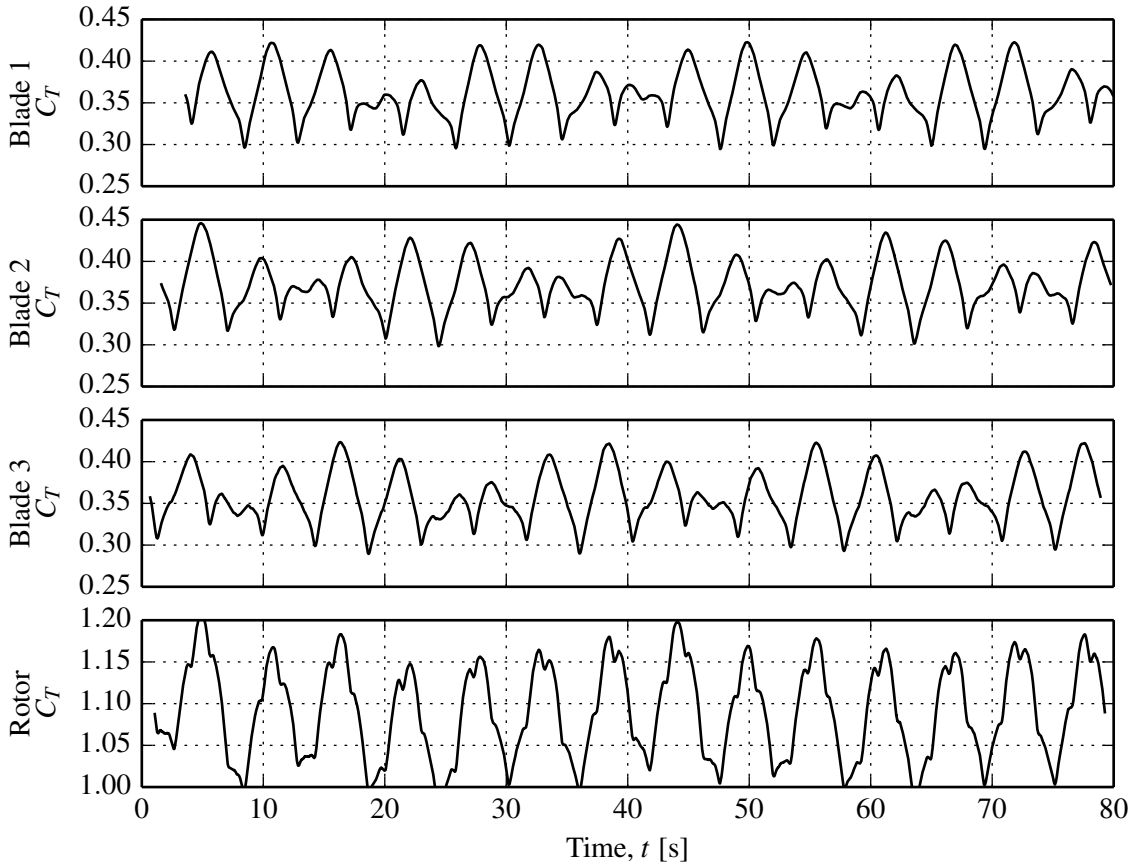

Figure 4.19: Histories of thrust loading on each blade and on the rotor for waves of length $\lambda_w = 72$ m and height $H = 1$ m. The rotor speed is $\lambda = 6.5$ and the vertical scale is consistent across all plots.

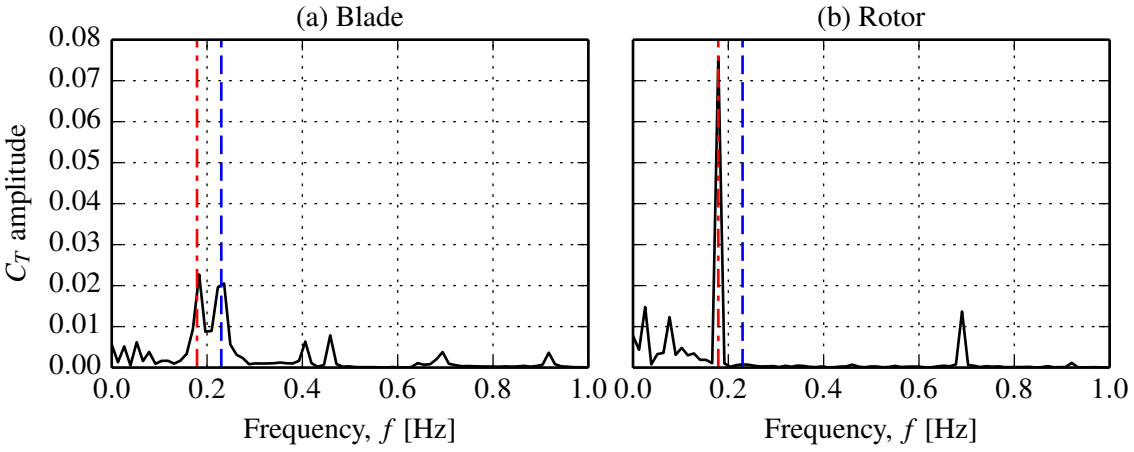

Figure 4.20: Frequency components for the (a) blade and (b) rotor thrust histories from figure 4.19. The broken blue line (– – –) marks frequency of the rotor, f_{rotor}, and the dash-dot red line (– · –) marks the wave frequency, f_{wave}. The normalised resolution of the primary frequency components are: $\Delta f / f_{\text{rotor}} = 0.056$, $\Delta f / f_{\text{wave}} = 0.072$.

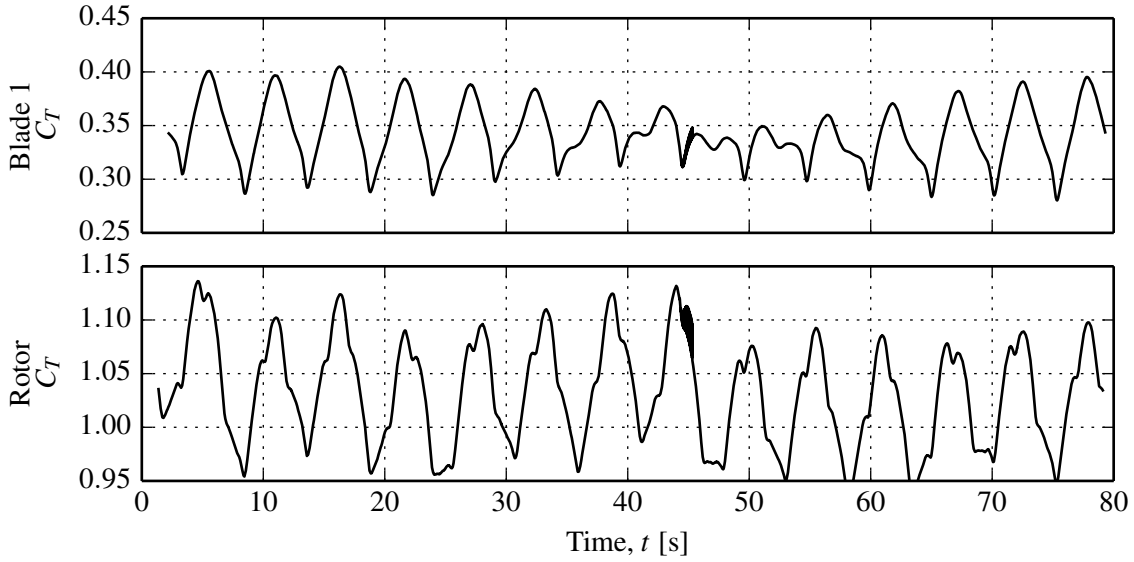

Figure 4.21: Histories of thrust loading on a single blade and on the rotor for waves of length $\lambda_w = 72\,\text{m}$ and height $H = 1\,\text{m}$. The rotor speed is $\lambda = 5.5$ and the vertical scale is consistent across all plots.

The increase in unsteady rotor load with wavelength can be seen by comparing rotor load histories (figures 4.15 and 4.19) and frequency spectra (figures 4.16 (b) and 4.20 (b)). As wavelength increases, the effect of the wave extends to greater depths, as shown in the comparison of velocity profiles in figure 4.18. At $\lambda_w = 72\,\text{m}$ the profile across the entire rotor is affected by wave motion, and hence the entire rotor is loaded in phase with the waves. Additional higher frequency loading is still evident in figure 4.20 (b) due to the blade-tower interaction.

The interaction between the rotor and wave frequencies is explored further in figures 4.21 and 4.22, where the turbine is operating at $\lambda = 5.5$ and the wave conditions are $\lambda_w = 72\,\text{m}$ and $H = 1\,\text{m}$. In this case the wave frequency, $f_{\text{wave}} = 0.178\,\text{Hz}$, is very close to the rotor frequency, $f_{\text{rotor}} = 0.195\,\text{Hz}$. A long wavelength beat, with a low frequency of $f_{\text{beat}} \approx 0.016\,\text{Hz}$ (equation 4.21) is observed on the rotor blade history.

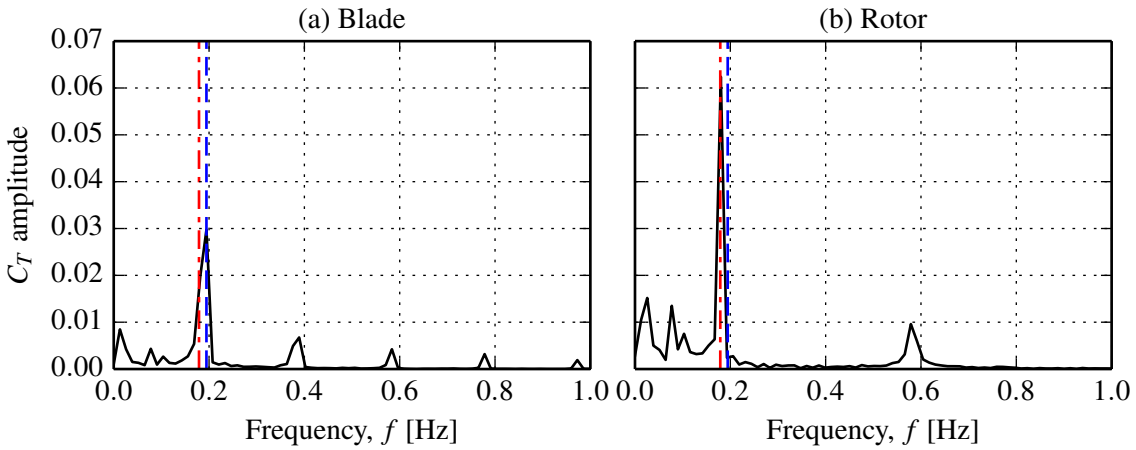

Figure 4.22: Frequency components for the (a) blade and (b) rotor thrust histories from figure 4.21. The broken blue line (– – –) marks frequency of the rotor, f_{rotor}, and the dash-dot red line (– · –) marks the wave frequency, f_{wave}. The normalised resolution of the primary frequency components are: $\Delta f / f_{\text{rotor}} = 0.067$, $\Delta f / f_{\text{wave}} = 0.072$.

4.9 Conclusions

The rigid lid model from chapter 3 is extended to include free surface waves using the volume-of-fluid method. Unsteady inflow profiles of velocity and fluid phase are prescribed at the inlet boundary, based on linear wave theory combined with the previously-developed sheared flow model.

Turbine performance is compared for the deforming and rigid free surface models. The power and thrust curves for the turbine are offset slightly to higher tip speed ratio. Power is slightly increased and thrust is slightly reduced when the free surface is allowed to deform, indicating that the rotor blades operate at a higher lift-to-drag ratio for a given tip speed ratio. Large fluctuations in blade torque are observed which are attributed to buoyancy due to the hydrostatic pressure gradient. These fluctuations would be greatly reduced for neutrally-buoyant blades.

Mean rotor power and thrust are not significantly affected by changes to wave height. However thrust and torque fluctuations increase with wave height, as the magnitudes of induced velocities in the upper portion of the water column are increased. Frequency analysis indicates that velocity shear is the primary source of fatigue loading on a rotor blade. The effect of shear is cancelled out over the full rotor due to axial symmetry, and

wave loading becomes the dominant cause of unsteady loads on the rotor.

Blade and rotor load fluctuations also increase with wave length, but mean values are not affected. The induced velocity profile increases in magnitude and extends deeper into the water column as wavelength is increased. The influence of waves on unsteady blade loading becomes similar in magnitude to that of velocity shear. Unsteady rotor loads also increase greatly — a doubling of wavelength results in a threefold increase in rotor thrust.

The interaction of the rotor and wave frequencies is also examined. When the difference between these frequencies is small, long-period modulation of the blade loading history is observed. Positive interference between the wave crest and blade position results in increased thrust loading.

The results of the current computational model highlight the additional unsteady loads introduced by free surface waves. Such loading will have a negative consequence for the fatigue life of the rotor blades, power shaft and support structure, and should be considered in structural design.

Chapter 5

Design and analysis of a bi-directional ducted turbine

5.1 Introduction

Many prominent tidal turbine designs feature a ducted rotor. The duct is variously claimed to accelerate the flow through the rotor via a venturi effect (thereby increasing power), to align yawed flow with the rotor axis, and to protect the blades from debris suspended in the flow (Clean Current Power Systems Inc., 2014; OpenHydro Group Ltd., 2014; Lunar Energy, 2014).

The primary objective of this chapter is to assess the claims of improved performance of ducted turbines. A secondary objective is to identify geometrical features which are beneficial for ducted turbine performance, through examination of a range of candidate designs.

In order to set practical limits to the scope of this study, certain constraints are placed on the duct geometry. For example, the duct is required to operate in the same manner for flood and ebb tidal currents, and the ratio of length to diameter should be similar to existing commercial designs. A range of two-dimensional duct profiles are produced within these constraints, and simulated in the same flow conditions using a RANS solver.

Device performance is assessed based on considerations of power and efficiency. The performance of the ducted designs relative to an unducted turbine is examined. Subsequently, subsets of the ducted designs are compared to assess the effects of duct curvature and thickness on performance.

An optimal duct design is then simulated at model scale for comparisons with physical tests carried out by a third party.

5.2 Ducted turbine design generation

The aims of this study are twofold: firstly to determine whether a ducted turbine outperforms a conventional bare turbine, and secondly to identify geometrical features which are beneficial to the performance of a ducted turbine. To this end, a series of duct geometries are devised, based on observations of industrial prototypes, and within certain constraints.

The first constraint is that the duct should be symmetric about the rotor plane to allow bi-directional operation without any yawing mechanism. While it is expected that uni-directional ducts would be most likely to improve turbine power output (Shives and Crawford, 2012) the added complexity and expense related to a yawing mechanism may outweigh any benefits. Secondly, the ratio of duct length L to diameter D is set to unity, which is similar to the Clean Current device (2014)*. Finally, all curved surfaces are constructed from circular arcs. This is a trade-off between simplicity of design, where straight sections and corners might be preferable, and hydrodynamic considerations, where corners are rounded by complex curves. An arc of radius $r_{\mathrm{LE}} = 0.0125D$ is used to represent the leading and trailing edges of all ducts. The inner and outer surfaces of each duct profile are constructed by joining the leading edge with straight lines or tangential arcs.

The candidate designs are presented in figure 5.1, where all dimensions are given in terms of the device radius R. The first profile, duct E, is produced by joining the leading

*Other prominent designs feature longer or shorter ducts (Lunar Energy, 2014; OpenHydro Group Ltd., 2014), but the effect of duct length to diameter is not examined here.

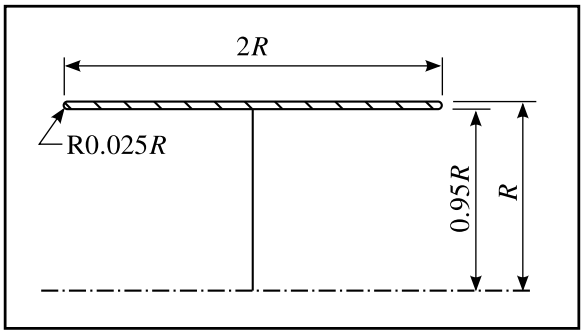

(a) Duct E

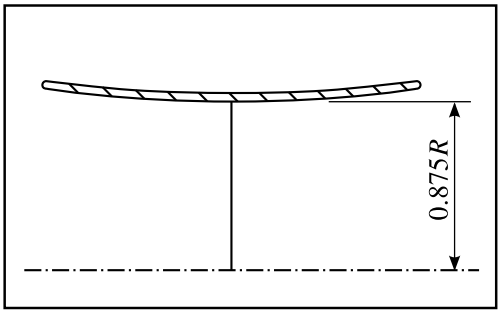

(b) Duct D

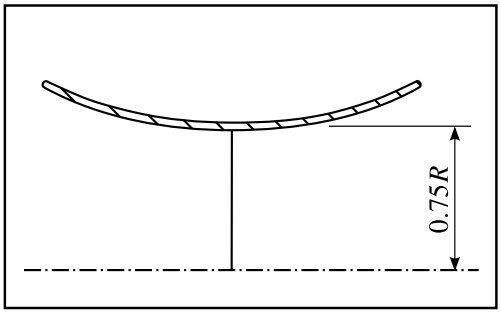

(c) Duct C

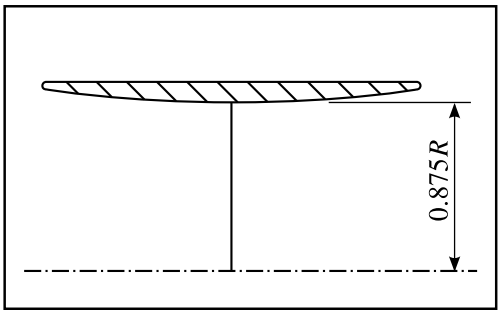

(d) Duct H

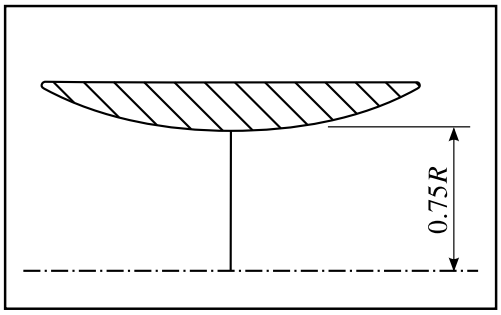

(e) Duct B

Figure 5.1: Profiles of ducts tested in parametric study, where $R = 10$ m.

and trailing edges with straight lines. Two series of designs are produced by perturbing the inner and outer surfaces of duct E. Ducts D and C are produced by joining the leading and trailing edges with parallel curved lines, producing thin profiles. Ducts H and B are produced by joining the leading and trailing edges with a straight outer surface, and a curved inner surface, leading to thick profiles.

5.3 Computational modelling

For this investigation, a 20 m diameter axial flow turbine is modelled in water of 40 m depth. Devices are spaced 60 m ($3D$) apart, resulting in a blockage ratio of $B = 0.131$.

Each device must be simulated at a range of operating points so that the points of peak power and efficiency are captured. As five candidate duct designs and one unducted device are to be compared, up to forty simulations may be necessary. Hence it is desirable to minimise the computational cost of the model while still capturing the pertinent physical features of the flow.

In this computational model, the flow is assumed to be steady, with a uniform velocity of $u = 2\,\mathrm{m\,s^{-1}}$. The resultant Reynolds number based on device diameter is $\mathrm{Re} = 4 \times 10^7$.

The primary effect of the rotor in a ducted turbine is the thrust it applies on the flow in the axial direction. As the focus of this comparative study is on duct performance, other features of rotor flow, such as non-uniform blade loading and swirl, are deemed less significant. Hence the rotor can be represented as a numerical porous disc (see section 1.4.1.1 for further discussion), which presents a resistance to the flow in the streamwise direction but does not impart swirl. The resistance of the disc in the axial direction takes the form of a momentum sink M,

$$M = \frac{1}{2} K \rho u_\mathrm{d}^2 \tag{5.1}$$

where ρ is the fluid density, K is the momentum loss factor and u_d is the local axial velocity at the disc. The momentum loss factor is varied within the range $0 < K < 5$ to emulate the thrust of a rotor at a range of angular speeds.

The problem can be further reduced by neglecting the support structure and converting the rectangular cross section of the flow through a single device into a circular cross section of equivalent area, as shown in figure 5.2. The flow through the circular section channel may be computed on a two-dimensional, rectangular, axisymmetric grid, marked by the broken line in the same figure.

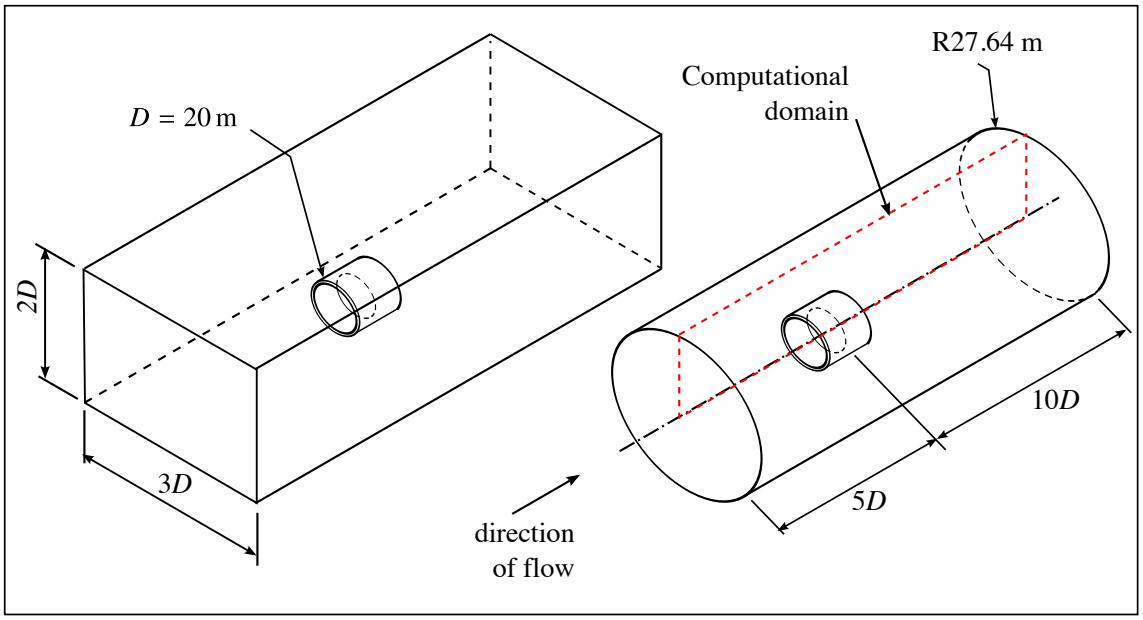

Figure 5.2: Illustration of simplification of three-dimensional rectangular domain (at left) to two-dimensional axisymmetric domain of equivalent blockage (red rectangle at right).

A uniform velocity of $2\,\mathrm{m\,s^{-1}}$ is prescribed at the upstream boundary, which is $5D$ from the rotor plane. At the same boundary, a turbulence intensity of $TI = 10\%$ and length scale of $l = 0.1D$ are specified, similar to the high turbulence case of Nishino and Willden (2012*a*). At the downstream boundary, $10D$ from the rotor plane, constant pressure of 0 Pa is applied. The inner radial boundary is assigned as the axis of symmetry as required by the two-dimensional axi-symmetric solver in ANSYS Fluent. A symmetry condition is set at the outer radial boundary.

5.3.1 Spatial resolution

The computational domain is discretised into quadrilateral elements using an unstructured multiblock approach. The same prototype grid, i.e. blocks and element numbers, is applied to each duct profile with only minor adjustments. A grid convergence study is carried out on duct C. Due to its thin profile and high curvature, this geometry is expected to be most senstive to spatial resolution. Following the method outlined by Roache (1998), the same flow case is simulated on a series of successively refined grids, and certain outputs of the model are checked to determine the degree of spatial convergence.

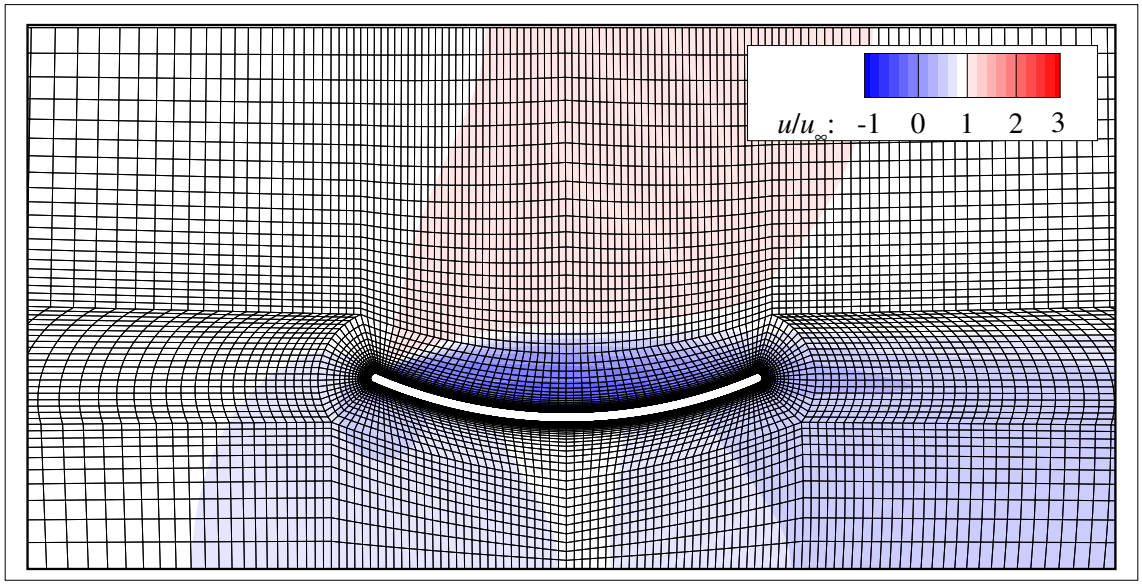

(a) The O-grid block enveloping the duct profile is visible here. The inner radial boundary (axis of symmetry) and outer radial boundary are both visible. The upstream boundary is five diameters to the left, and the downstream boundary is ten diameters to the right.

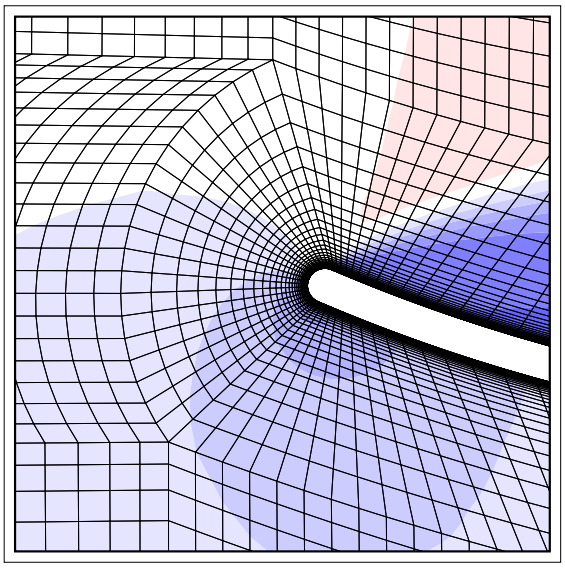

(b) Detail of transition between O-grid block and far-field rectangular blocks.

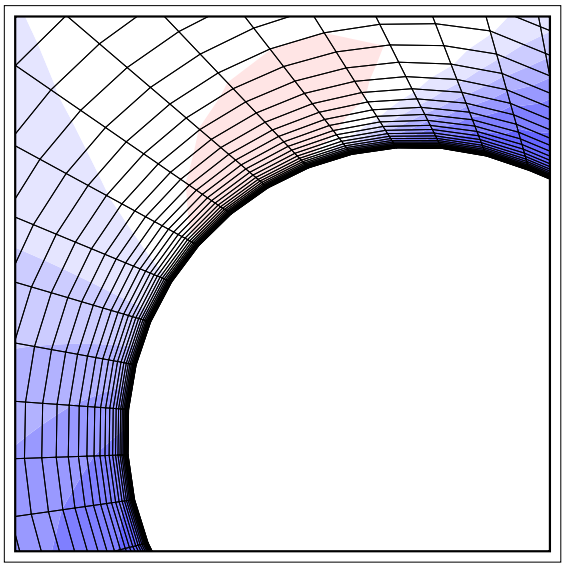

(c) Detail of resolution at leading edge.

Figure 5.3: Three views of grid III, showing (a) the general resolution around the device, (b) the transition from the duct O-grid to the far field grid and (c) the resolution at the leading edge. The coloured contours represent streamwise velocity normalised by the upstream value.

The coarsest grid for duct C, labelled grid III, is presented in figure 5.3. The gridlines are superimposed upon contours of normalised streamwise velocity u/u_∞ to give a qualitative indication of the flow field resolution. The upper figure (a) shows that the duct profile is enclosed in an O-grid, which extends approximately $0.15D$ from the duct surface. There are 40 elements in the wall-normal direction, 20 elements along the leading and trailing edges respectively, and 60 elements along the inner and outer surfaces respectively. The height of the elements adjacent to the duct surface is $h = 2.5 \times 10^{-5}D$, and each successive layer of elements within the O-grid region grows by a factor of 1.2. The nodes are uniformly distributed at the leading and trailing edges, but node spacing increases by a factor of 1.2 along the duct profile towards the disc plane. Rectangular blocks of elements are used to connect the curved O-grid region to the domain boundaries. Node spacing is matched across the interface between grid blocks, e.g. where an O-grid block meets a far-field block, and elements increase in size in the direction away from the duct by a constant factor (typically less than 1.05). There are 50 elements upstream and 100 elements downstream of the O-grid region. The regions between the inner and outer radial boundaries and the O-grid block are discretised with 10 and 20 elements respectively.

Two further grids are generated by subdividing each element in the base grid by a factor of $r = 2$ in each direction. Hence each element in grid III is subdivided into four child elements to produce grid II. The procedure is repeated on grid II to produce the highest resolution grid I. A consequence of this method of refinement is that for the higher resolution grids, the duct is slightly faceted: a length of curved surface which is approximated by a single element edge in grid III will be approximated by the same edge in grids II and I, but with two elements and four elements respectively. Using a consistent refinement ratio between grids, and refining in both the axial and radial directions, ensures that the aspect ratio remains constant across all grids. A constant aspect ratio is necessary to achieve order of convergence p close to the formal order of the discretisation scheme used in the solution of the governing equations (Salas, 2006).

A disc momentum loss factor of $K = 1$ is chosen as the operating point for the

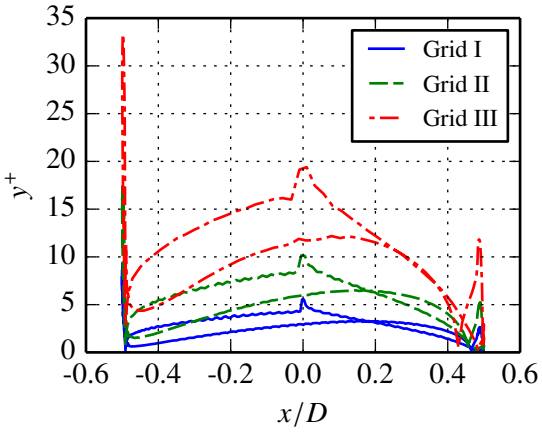

Figure 5.4: Profiles of non-dimensional wall distance y^+ at the surface of the duct for the grids used in the convergence study.

convergence study, as preliminary computations suggested that this point would correspond to peak power coefficient. All other simulation parameters, i.e. boundary conditions and solution methods, are consistent with the later comparative study of duct geometries.

The implementation of the k-ω SST turbulence model in ANSYS Fluent uses an enhanced wall model. As described in section 2.1.8, this means that a blending function is used in the boundary layer model between the laminar sublayer and the log-law region. Hence the error associated with wall-adjacent grid points being located in the buffer zone of the boundary layer (where non-dimensional wall distance is in the range $5 < y^+ < 30$ (Schlichting, 2000)) are mitigated. Profiles of y^+ at the surface of the duct are presented for grids I, II and III in figure 5.4.

Two metrics are used to determine convergence. Firstly, the mean streamwise velocity at the disc is reported, as device power is a function of this parameter*. Disc velocity is reported in non-dimensional form, normalised by the upstream velocity u_∞. Secondly, the drag (streamwise force) on the duct is examined, as it greatly affects the efficiency of the device (c.f. equation 5.10). Duct drag D_{duct} is presented as a coefficient, $C_{D\,\text{duct}}$, normalised by the free stream dynamic pressure and the total frontal area of the turbine

*To be precise, power is a function of the spatial average of the cube of streamwise velocity taken across the disc surface.

Table 5.1: Details of grids for duct C convergence study along with results for duct drag and mean disc velocity.

Grid	h	N_{elem}	C_D	u_{disc}/u_∞
III	$2.5 \times 10^{-5} D$	15700	0.423	0.9252
II	$1.25 \times 10^{-5} D$	62800	0.403	0.9215
I	$6.25 \times 10^{-6} D$	251200	0.398	0.9205

(including the duct where present), A_{tot},

$$C_{D\,\text{duct}} = \frac{D_{\text{duct}}}{\frac{1}{2}\rho u_\infty^2 A_{\text{tot}}}. \tag{5.2}$$

Disc velocity and duct drag are presented for each grid in table 5.1.

The error of a computational model can be expressed in the form of a Taylor expansion,

$$f_{\text{e}} = f_{\text{c}} + ch^p + \text{H.O.T} \approx f_{\text{c}} + ch^p \tag{5.3}$$

where f_e represents the exact solution for a model output parameter, f_c is the computed solution, h is a measure of the grid spacing, p is the order of convergence of the numerical scheme, c is a constant and H.O.T. are higher order terms. For a two-dimensional grid, equation 5.3 is valid only where the aspect ratio of each element remains constant across all grids (Salas, 2006). Roache (1998) derives the following formula to calculate the order of convergence from three grids with a consistent refinement ratio r,

$$p = \frac{\ln\left(\frac{f_{\text{III}} - f_{\text{II}}}{f_{\text{II}} - f_{\text{I}}}\right)}{\ln(r)} \tag{5.4}$$

where the Roman numerals correspond to the grids introduced previously. The observed polynomial order calculated by equation 5.4 may differ from the formal order of the numerical scheme due to factors such as non-uniform element spacing, grid skewness, and application of boundary conditions. The formal order of the current model is $p = 2$. The exact solution towards which the computations asymptote with increasing grid refinement

can be extrapolated using Richardson's method,

$$f_e = f_I + \frac{f_I - f_{II}}{r^p - 1}, \tag{5.5}$$

where the observed value of p from equation 5.4 is used, rather than the theoretical value of $p = 2$.

The numerical error of a fine grid solution can be computed with respect to a coarser grid as follows:

$$E = \frac{\varepsilon}{r^p - 1} \tag{5.6}$$

where ε is the normalised error $\left|f_I - f_{II}\right| / f_I$. Roache recommends the application of a factor of safety to E to produce the grid convergence index, GCI $= F_s E$. Where three grids have been used to estimate p, a factor of safety of $F_s = 1.25$ may be used.

The above convergence metrics are only valid if the set of computed solutions lie within the asymptotic range of convergence to the exact solution. This is true if successive GCI values differ only by a factor of r^p. Hence a ratio of GCI values may be defined as follows,

$$r_{GCI} = \frac{GCI_{I-II} r^p}{GCI_{II-III}} \tag{5.7}$$

for which a value of $r_{GCI} = 1$ indicates asymptotic convergence.

The above convergence metrics are presented in table 5.2 based on solutions for (a) disc velocity and (b) duct drag coefficient. Convergence study (b) produces an observed polynomial order of $p = 1.907$, which is very close to the formal order of accuracy of the discretisation scheme (second-order upwinding). The corresponding result from (a) is $p = 3.0$, which implies that the numerical errors are one order higher (i.e. smaller) than expected. However this is not necessarily the case; the value of p may be affected by factors such as grid skewness and uneven element spacing. Importantly, studies (a) and (b) report low grid convergence indices for the two finer grids (II and I), and the results are within the asymptotic range of convergence. Grid II is chosen as the basis for the

Table 5.2: Results of grid convergence study on duct C.

Metric	p	f_e	GCI $_{\text{I-II}}$ [%]	GCI $_{\text{II-III}}$ [%]	r_{GCI}
(a) u_{disc}/u_∞	3.000	0.9535	0.0195	0.156	1.001
(b) C_D	1.907	0.396	0.611	2.260	1.013

discretisation of each duct geometry in the subsequent parametric study. Recall that the geometry of duct C was slightly faceted by grid II in order to strictly maintain a constant aspect ratio for all elements. This requirement is no longer necessary for the parametric study, so the respective duct geometries can be captured as fully as the element spacing of grid II allows.

A bare disc of diameter $D = 20\,\text{m}$ is simulated for comparison with the various duct geometries. Another convergence study is carried out to determine the uncertainty of this model. Following the procedure outlined above, three grids of quadrilateral elements are produced, differing by a constant refinement factor of $r = 2$. The coarsest grid, labelled III, features 30 elements vertically along the disc. The element at the rotor tip has a height of $h_y = 5 \times 10^{-3} D$, and the elements increase in size towards the centre of the disc by a factor of 1.08. There are 40 elements between the rotor tip and outer radial boundary of the domain, increasing in size from $h_y = 5 \times 10^{-3}$ at the tip by a ratio of 1.07. The streamwise nodal spacing across the disc plane is $h_x = 0.018D$, increasing by a factor of 1.03 in the upstream direction (80 elements) and 1.02 in the downstream direction (130 elements). Preliminary computations suggest that peak power for the ducted turbine occurs around $K = 4$. However, the disc exerts high thrust on the flow at this operating point, introducing unsteadiness in the wake, and hence the degree of iterative convergence of the steady solver is reduced. As the effect on disc power is very small (good agreement is achieved with theory at high operating points later in figure 5.5), and the computational cost of the model must be minimised to facilitate the examination of a large number of cases, an unsteady solver is not used. An operating point of $K = 2$, corresponding to moderate thrust, is chosen for the grid convergence study. The three grids for the bare disc are presented in table 5.3 along with results for mean streamwise velocity.

The mean disc velocities calculated by the three grids agree to the third decimal point, indicating that even the coarsest grid resolves the flow with sufficient accuracy. Grid III is chosen for further simulations at a full range of disc operating points for comparison to the ducted turbine computations.

Comparisons are made with actuator disc theory in confined flow (Garret and Cummins, 2007; Houlsby et al., 2008) in figure 5.5. The disc operating point is presented in terms of induction factor,

$$a = \frac{u_\infty - u_{\text{disc}}}{u_\infty}. \tag{5.8}$$

where u_{disc} is the spatial average of velocity through the disc. Performance is reported in terms of the power coefficient,

$$C_P = \frac{P}{\frac{1}{2}\rho A_{\text{ref}} u_\infty^3} = \frac{\Delta p A_{\text{disc}} u_{\text{disc}}}{\frac{1}{2}\rho A_{\text{ref}} u_\infty^3} \tag{5.9}$$

where P is power, A_{disc} is disc area, u_{disc} is the spatial average of streamwise velocity across the disc, and A_{ref} is the reference area. The high turbulence case, corresponding to the later parametric study, predicts higher values of C_P than theory. This result is in qualitative agreement with Nishino and Willden (2012*a*) who show that at similar blockage (their $2.5D \times 2.5D$ case) an increase in freestream turbulence level leads to an increase in C_P. They attribute this increase in power to the enhanced mixing of the core and bypass flows. The increased shear acting on the interface between the core and bypass flows reduces the bypass velocity and increases the core velocity, thereby drawing a higher volume flux through the disc for a given momentum loss factor K (visible as a shift in operating point to the left in figure 5.5). The theoretical model treats the flow as inviscid

Table 5.3: Details of bare disc grids along with results for mean disc velocity.

Grid	h	N_{elem}	u_{disc}/u_∞
III	$5 \times 10^{-3} D$	14212	0.7516475
II	$2.5 \times 10^{-4} D$	56848	0.751551
I	$1.25 \times 10^{-4} D$	227392	0.751433

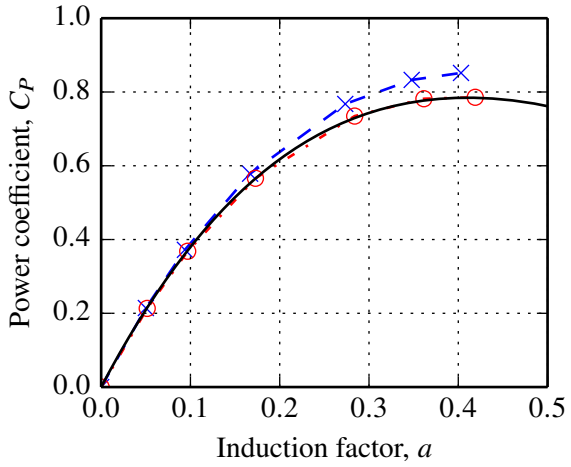

Figure 5.5: Comparison of computed and theoretical results for bare turbine. Black line: theoretical result from Garret and Cummins (2007); red circles: computed result for low free stream turbulence from convergence study; blue crosses: computed result for high free stream turbulence case.

and hence this effect is not taken into account. A very low freestream turbulence case is also compared in figure 5.5, where it lies on top of the theoretical curve.

5.4 Results

5.4.1 General effect of duct on performance

Power curves for the ducted devices and an unducted device are compared in figure 5.6 (a) at operating points $K = \{0, 0.25, 0.5, 1, 2, 3, 4\}$ (increasing from left to right along each curve). The reference area for the calculation of power coefficient (equation 5.9) is taken as the total frontal area of the device, including a duct where present. The unducted device which has been simulated for comparison has the same diameter as the external duct diameter, $D = 20\,\text{m}$ for consistency of blockage ratio. The importance of comparing device performance has been highlighted in the discussion of previous studies of ducted turbines in section 1.4.2.5.

All of the ducted devices exhibit peak power coefficients in the range $0.4 < C_P < 0.5$, whereas the unducted device achieves a maximum C_P of 0.85. Most of the duct designs accelerate the flow above the freestream velocity at low levels of rotor loading ($K < 0.5$),

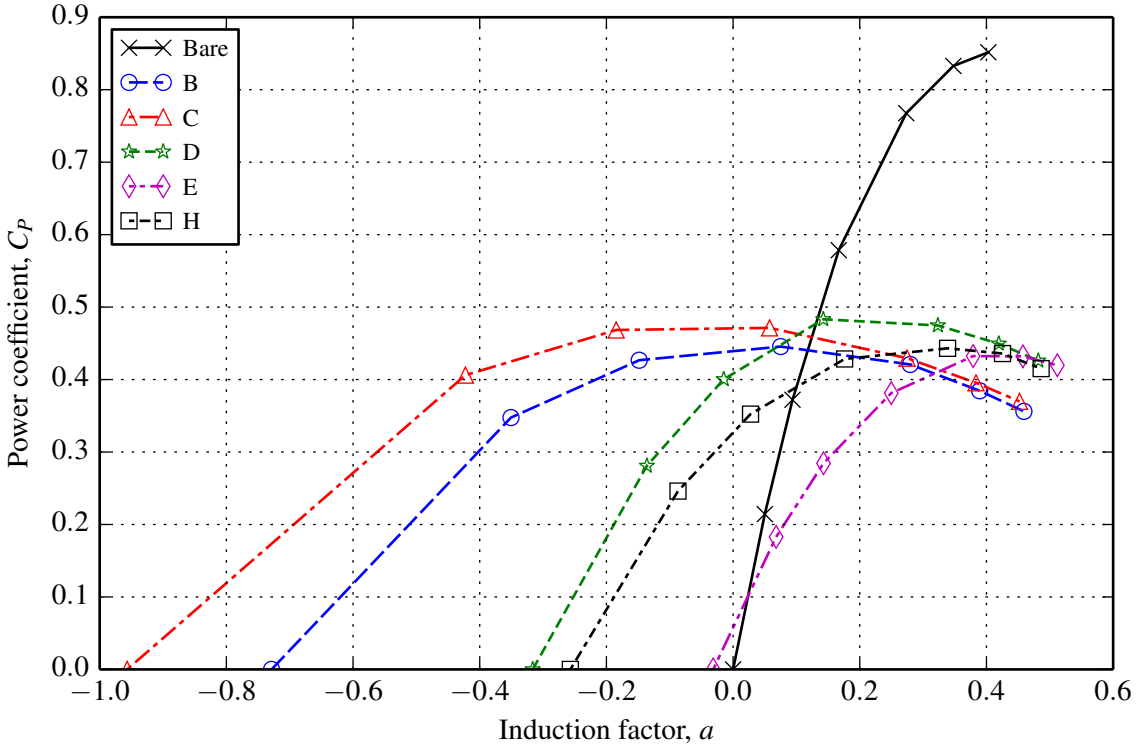

(a)

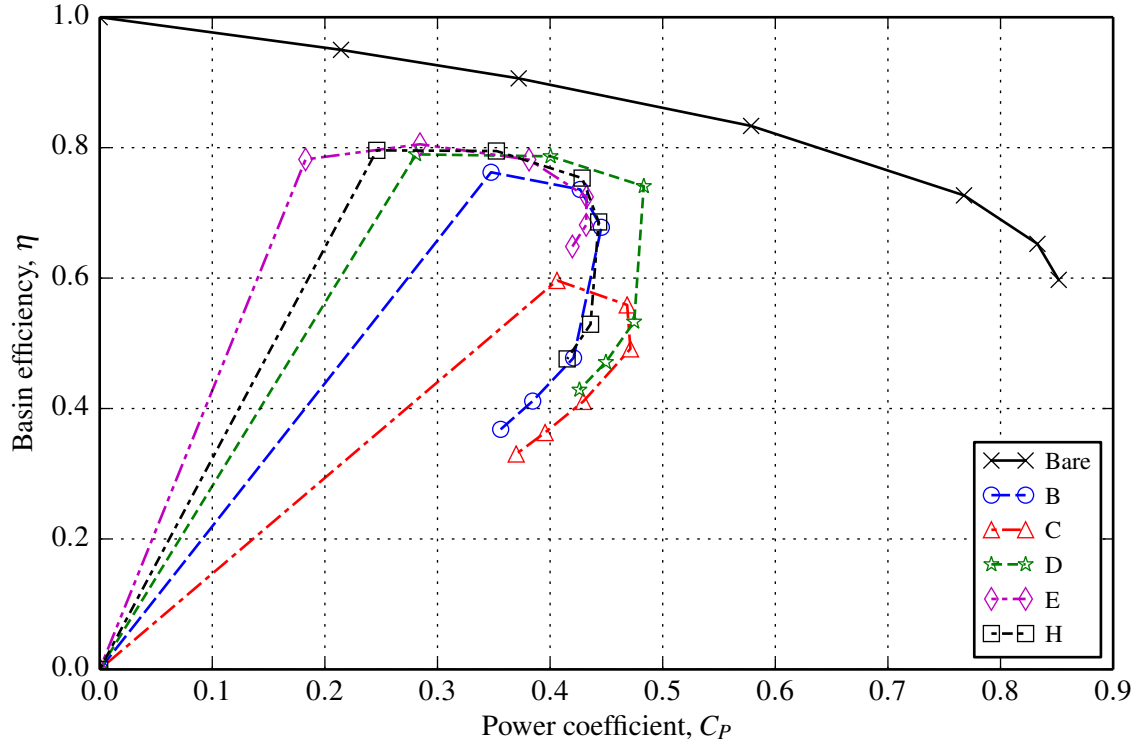

(b)

Figure 5.6: Comparisons of (a) power coefficient and (b) basin efficiency for the ducted turbines and the bare disc. The operating points correspond to momentum loss factors $K = \{0, 0.25, 0.5, 1, 2, 3, 4\}$, increasing in the clockwise direction.

as indicated by negative values of induction factor a. This increase in velocity at the rotor is a design intention; however such acceleration must outweigh any reduction in rotor area and pressure change in order to have a beneficial effect on power. While this does occur for devices B - D at operating points below $K = 0.5$, the unducted device has the highest peak power coefficient.

It is noted that similar geometries yield similar power curves. Highest flow acceleration is achieved by ducts B and C, which have the highest curvature. The power curve for duct E is similar to that of the bare disc, but peaks at a much lower power coefficient. The moderately curved ducts, D and H, perform similarly to each other, and their power curves lie between the straight duct E and the highly curved ducts B and C.

The broad, flat power curves for the ducted devices indicate that they perform well (relative to their maximum C_P value) across a broad range of operating points. However, peak power coefficient may be a more useful metric for comparison, as control methods can be employed to constrain turbine operation to a narrow operating range. Hence, the unducted turbine is the optimum device in this comparison.

The straight duct, E, performs similarly to the bare disc, in that it produces little acceleration at the $K = 0$ operating point

Another important performance metric for a tidal turbine is the ratio of useful power to total power lost from the flow. This term is denoted ‘efficiency’ here following Shives and Crawford (2010). The ‘useful power’ is the mechanical power transmitted to the shaft of the turbine, in the absence of mechanical losses. For a porous disc, it is calculated as $P_{\text{useful}} = T_{\text{disc}} u_{\text{disc}} = \Delta p A_{\text{disc}} u_{\text{disc}}$. The total power lost from the flow includes losses due to viscous effects such as flow separation from the duct and wake mixing as well as the useful mechanical power. Shives and Crawford (2010) show that this power is calculated by considering the total resistance to the flow, i.e. the thrust on the disc and duct, at the freestream velocity.

$$P_{\text{lost}} = (T_{\text{disc}} + T_{\text{duct}})\, u_\infty = (\Delta p A_{\text{disc}} + T_{\text{duct}})\, u_\infty \tag{5.10}$$

It is likely that regulators will limit the allowable change to water levels or flow speeds at a given tidal site. Any energy extracted from an open channel flow results in a reduction in water depth, whether that energy is converted to electrical power or lost to viscous action. Of course, a certain amount of viscous loss is necessary, such as that due to wake mixing resulting from the rotor thrust*. Any unnecessary losses, such as those associated with poor hydrodynamics of the supporting structure, should be minimised. Note that the current model simulates a tidal turbine within a rigid tunnel, so free surface deformation is not modelled.

The ideal operating point for a tidal turbine can be identified by considering both power coefficient and efficiency. Basin efficiency is presented as a function of power coefficient for each device in figure 5.6 (b). The momentum loss factor increases in a clockwise direction from $K = 0$ to $K = 4$ along the curves in this figure. Immediately we can see that all of the ducts examined have a detrimental effect on efficiency relative to the unducted device. In particular, a dramatic reduction in efficiency occurs for each ducted device at at a point in the range $1 < K < 2$. At higher values of disc resistance, very large reductions in efficiency are observed, while the power coefficient changes very little. The ideal operating point for the ducted devices is therefore just before the sharp drop in efficiency. This sudden drop is due to a change in the nature of the flow around the duct, as discussed by Belloni et al. (2013). Further discussion of this is given in section 5.4.3.

As observed in figure 5.6 (a), and discussed above, the peak power coefficients of each ducted device occur in the range $0.4 < C_P < 0.5$, whereas the unducted turbine has a much higher power coefficient. The cause of this limitation in power may be investigated by comparing physical properties of flow through a ducted and unducted device.

The cause of the power limitation affects all of the ducted devices to a similar degree, and hence is not strongly dependent on duct curvature. For comparison to the bare turbine, it is sensible to choose a device which does not introduce secondary effects such as flow acceleration or separation, which would add unnecessary complexity. Hence device E is

*In fact, the efficiency of a porous disc rotor model tends towards $\eta = 1.0$ with decreasing resistance, and consequently, decreasing useful power.

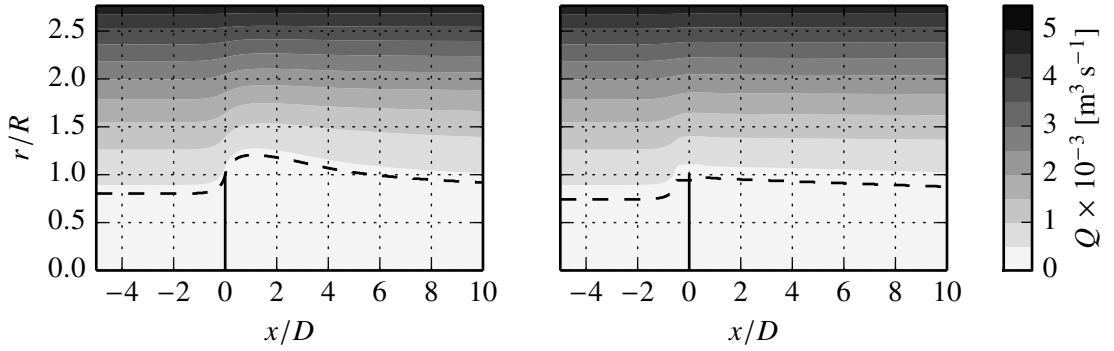

Figure 5.7: Contours of increasing volumetric flow rate for the unducted device at $K = 3$ (left) and device E at $K = 2$ (right). The broken line marks the streamtube which intersects the disc perimeter. The radial scale r/R is stretched relative to the axial scale x/D by a factor of 8.

chosen for comparison with the unducted device. As this duct has no camber, it does not provide any acceleration to the core flow, but it still has a peak power coefficient close to the maximum of all ducted devices considered.

The appropriate operating point at which to compare each device is chosen based on consideration of efficiency as well as power coefficient. Device E produces almost the same amount of power at momentum loss factors of $2 < K < 4$. However, the efficiency is reduced from $\eta = 0.72$ to $\eta = 0.65$ in this range. Hence the ideal operating point for device E is $K = 2$. The same argument is made in choosing $K = 3$ as the best operating point for the unducted device.

Defined in equation 5.9, power coefficient is a function of the area and velocity of the flow through the disc, as well as the pressure change in the flow as it passes through the disc. If a streamtube corresponding to the flow through the disc only is identified, representative values of area, velocity and pressure may be calculated for the flow passing through the disc, which may then be compared for different devices.

The patterns of the computed flow fields for the unducted device and device E is visualised in figure 5.7 as contours of volumetric flow rate $Q = u\pi r^2$ (i.e. streamtubes). The distance between streamtubes is a function of velocity and radial position. Streamtube spacing decreases in regions of increased velocity or radius.

The bounding streamtube marks the region of constant volumetric flow rate which

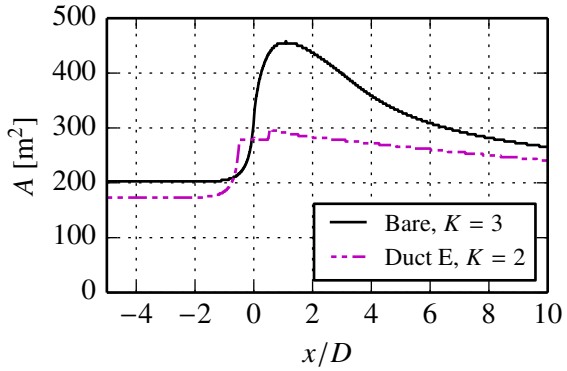

Figure 5.8: Streamtube area and for unducted device at $K = 3$ and device E at $K = 2$.

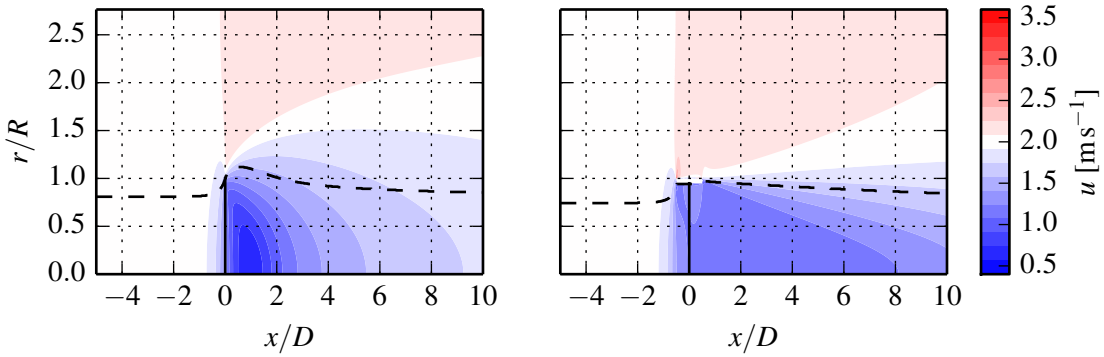

Figure 5.9: Contours of streamwise velocity for the unducted device at $K = 3$ (left) and device E at $K = 2$ (right). The upstream velocity is $u_\infty = 2\,\mathrm{m\,s^{-1}}$. The radial scale r/R is stretched relative to the axial scale x/D by a factor of 8.

passes through the rotor only for each case. The cross-sectional area of each streamtube is calculated from the radius and compared in figure 5.8, where the duct is observed to limit the flow expansion downstream of the disc.

Contours of streamwise velocity u for the unducted device and duct E are compared in figure 5.9. The streamtube which bounds the rotor flow, identified from figure 5.7, is superimposed. The volumetric flow rates through each streamtube are compared in figure 5.10. The increased rate of wake recovery in the unducted case is consistent with the expansion and subsequent relaxation of the streamtube, observed in figure 5.8.

The static pressure fields of the unducted device and device E are presented in figure 5.11. A representative streamtube pressure $\bar{p}$ is defined as the average value of static pressure in the radial direction at each axial location. Using the radial location r as a

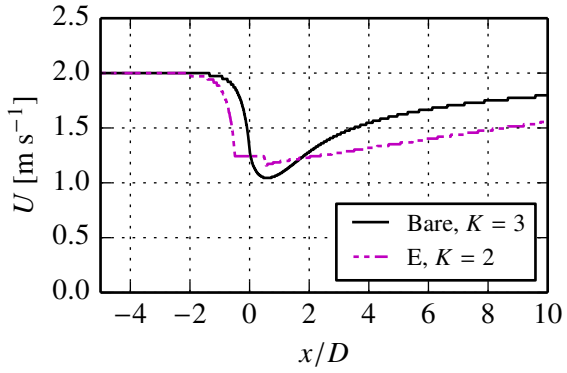

Figure 5.10: Streamtube mean streamwise velocity for unducted device at $K = 3$ and device E at $K = 2$.

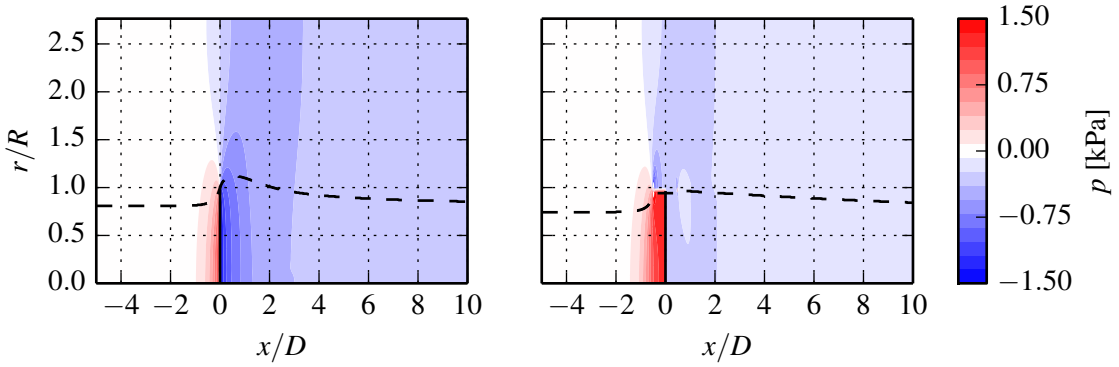

Figure 5.11: Contours of static pressure for the unducted device at $K = 3$ (left) and device E at $K = 2$ (right). The radial scale r/R is stretched relative to the axial scale x/D by a factor of 8.

weighting criterion, the representative streamtube pressure is calculated as

$$\bar{p} = \frac{\sum_{i=1}^{n} r_i p_i}{\sum_{i=1}^{n} r_i}. \tag{5.11}$$

Streamwise profiles of streamtube pressure for the bare disc and duct E are compared in figure 5.12.

Numerical values for streamtube area, velocity and pressure change across the rotor are listed in table 5.4. From this table, as well as figures 5.8, 5.10 and 5.11, it is evident

Table 5.4: Comparison of area, velocity, pressure and C_P for the unducted device and device E.

Device	K	A_{disc} [m^2]	U_{disc} [m s^{-1}]	Δp_{disc} [Pa]	C_P	η
Unducted	3	314.16	1.30	2380	0.833	0.727
E	2	283.53	1.23	1626	0.432	0.725

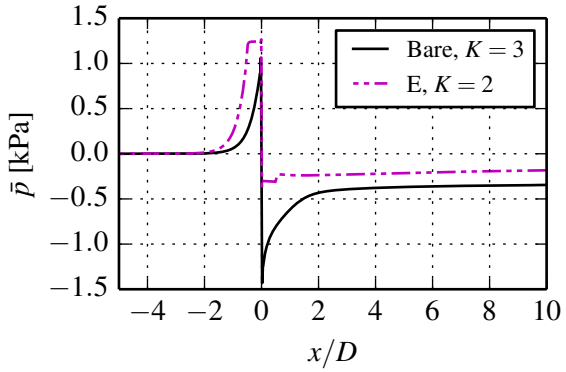

Figure 5.12: Streamtube mean pressure for unducted device at $K = 3$ and device E at $K = 2$.

that the pressure change across the disc is affected most significantly. The rotor of device E is 10% smaller than the unducted case. This is necessary for blockage to be constant between the two devices; both devices have an equal total frontal area of $A = 314.16\,\mathrm{m}^2$.

Figures 5.7, 5.9 and 5.11 show that the flow field upstream of each device is quite similar: there is an increase in pressure and area and a decrease in velocity as the flow approaches the turbine. However, differences arise at the turbine and in the downstream region. In the unducted case, the streamtube continues to expand as it passes through the rotor, accompanied by a large reduction in static pressure to a level below that far downstream. Downstream of the unducted rotor, the streamtube reduces in size, in balance with velocity and pressure recovery. The pressure reduction across the ducted rotor is limited on the downstream side. This is because the duct constrains the flow to be parallel (see figure 5.7), and hence a difference in pressure between the duct and the downstream flow cannot be supported. This effect is also observed for the curved duct geometries in the following sections. Additionally, the reduced area and velocity through the ducted rotor are equivalent to a reduced volumetric flow rate, reflected in the streamtube area at $x = -5D$ in figure 5.8.

5.4.2 Effect of duct curvature

The effects of particular geometrical features on the performance of a ducted turbine may be examined by selecting subsets of the devices tested. By comparing devices E, D and

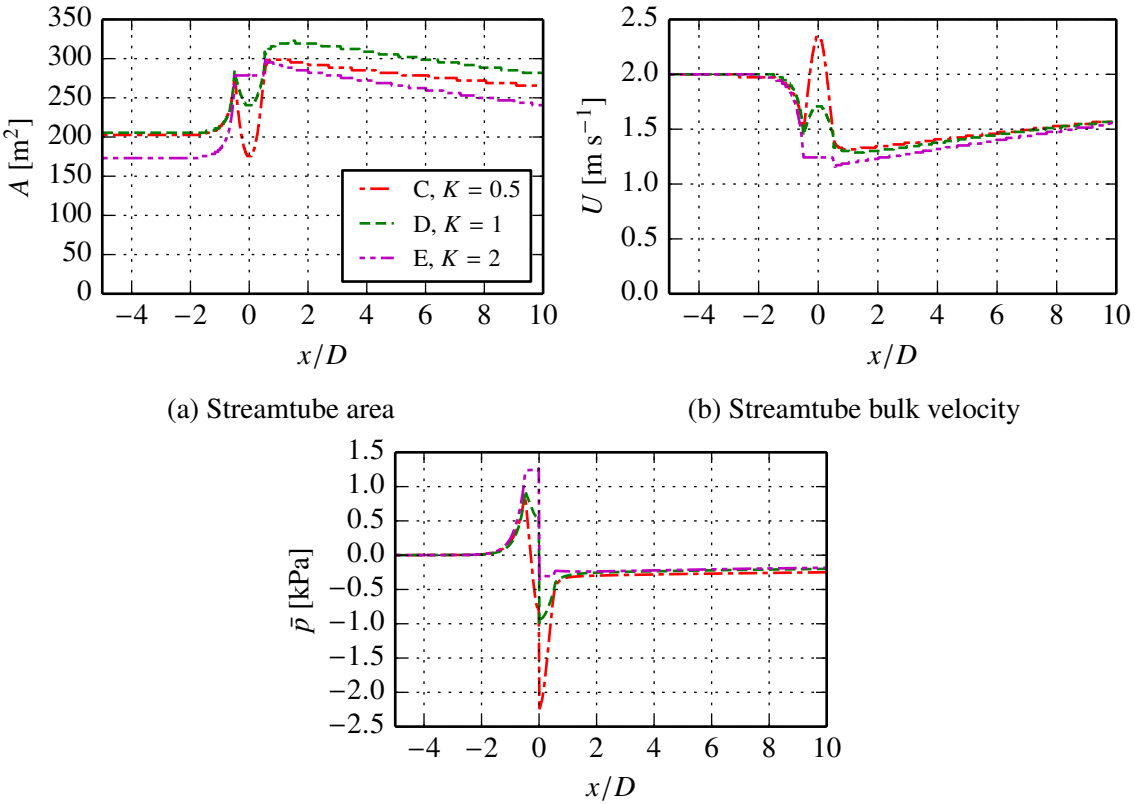

(a) Streamtube area

(b) Streamtube bulk velocity

(c) Streamtube mean pressure

Figure 5.13: Variation of streamtube area, velocity and pressure in the streamwise direction for ducts C, D and E, showing the effect of duct curvature.

Table 5.5: Comparison of area, velocity, pressure and C_P for devices C, D and E at operating points corresponding to peak performance.

Device	K	A_{disc} [m^2]	U_{disc} [m s^{-1}]	Δp_{disc} [Pa]	C_P	η
C	0.5	176.71	2.34	1483	0.468	0.559
D	1	240.53	1.71	1542	0.483	0.741
E	2	283.53	1.23	1626	0.432	0.725

B, the effect of camber on performance can be studied. The degree of profile curvature increases from duct E, which is not curved, to duct C, which is most curved. In the absence of a rotor, and provided the internal flow remains attached, increased duct curvature will result in higher flow speed at the duct throat. However, the active area of the device (i.e. the rotor area) is reduced correspondingly. Additionally, if a resisting force is presented to the flow, as a rotor would provide, the acceleration effect will be mitigated. These three features of throat velocity, rotor area and rotor resistance influence the generated power and the device efficiency in a complex way.

Each of these devices are assessed at their optimum operating point, which is chosen based on considerations of power coefficient C_P and efficiency η. The chosen operating points are $K = 0.5$ for device C, $K = 1$ for device D, and $K = 2$ for device E. It can be seen in figure 5.6 (b) that the operating points of devices C and E do not coincide with the point of maximum C_P. In these cases, a neighbouring operating point with a slightly lower C_P and a significantly higher η are deemed optimal.

Streamwise profiles of streamtube area, velocity and pressure are presented in figure 5.13, and the corresponding numerical values at the disc are listed in table 5.5. We can see that device D performs best in terms of power coefficient and efficiency. Device C does accelerate the flow through the rotor as intended by its design. However the area and resistance of the rotor are lower than the other devices and these factors outweigh the increase in throat velocity. Additionally, the efficiency of this device is much lower than the others; this will be investigated in section 5.4.3. Device E exhibits the highest streamtube area and pressure change at the disc. In this case the power is limited by the velocity through the disc: no acceleration is provided by this duct.

Ducts D and E are both operating at reasonably high values of efficiency. At higher momentum loss factors K, the efficiency drops dramatically. The relationship between geometry, disc resistance and efficiency is now investigated.

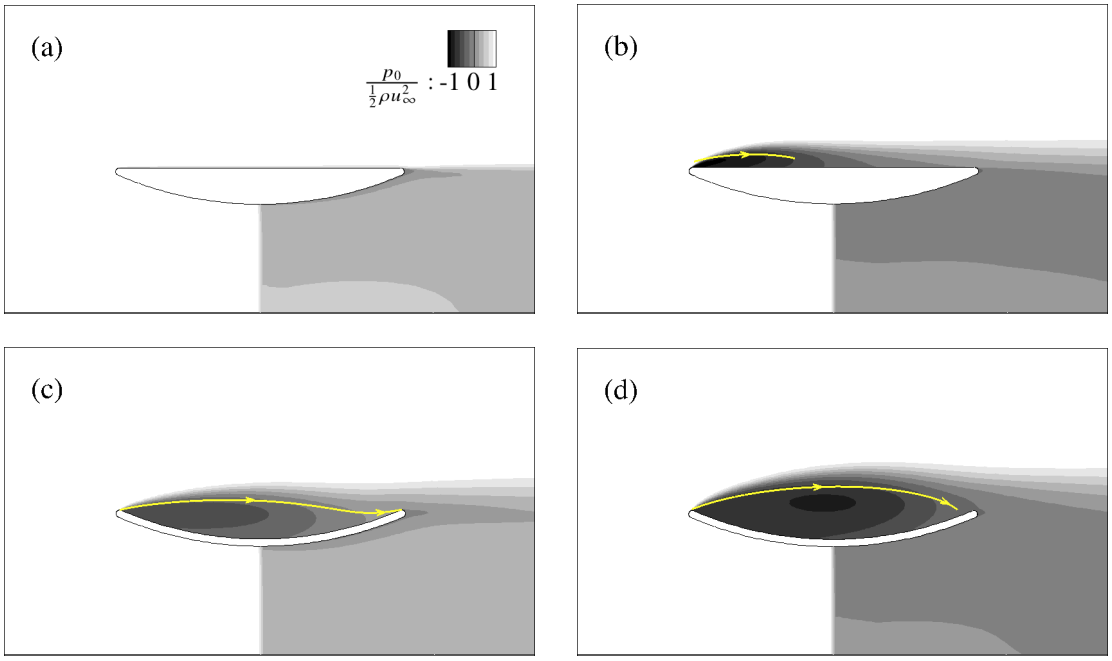

Figure 5.14: Contours of total pressure p_0, normalised on freestream dynamic pressure, for devices B (upper row) and C (lower row) at momentum loss factors of $K = 0.5$ (left hand side) and $K = 2$ (right hand side). Darker shades correspond to lower total pressure, i.e. greater local energy loss. For each case, the static pressure component has been shifted to a common upstream value. The yellow streamline indicates the edge of the recirculation zone.

5.4.3 Efficiency of ducted turbines

Figure 5.6 (b) shows that there is a sharp reduction in efficiency at a particular operating point for each device. As the disc resistance is increased above $K = 0$, the power and efficiency increase accordingly. When the efficiency reaches a maximum value, the power continues to increase. As power reaches a maximum value, and begins to reduce, there is a dramatic drop in efficiency. The cause for this change in efficiency is investigated by comparing the flow around a ducted turbine at low and high levels of disc resistance.

Contours of total pressure for devices B and C at low and high levels of disc resistance are presented in figure 5.14. The static pressure component of total pressure for each case has been shifted to achieve a common upstream value. The same colour scale is used across the four figures, with darker shades corresponding to lower static pressure. Where present, the recirculating region outside the duct is marked with a yellow streamline.

Ducts B and C are illustrated in the upper and lower figure rows respectively. The left

hand figures correspond to a low rotor resistance of $K = 0.5$, and the right hand figures correspond to a higher resistance of $K = 2$.

In each case, the energy transferred to the porous disc is indicated by a step change in total pressure within the duct. Areas of viscous loss, where kinetic energy is converted to heat, are visible as dark shades at the exterior and directly downstream of the duct.

At low rotor resistances, e.g. plots (a) and (c), the flow approaches the duct almost head-on, and either follows the contours of the duct (devices B, E, H), or separates beyond the leading edge (devices C, D). The static pressure upstream of the rotor increases with rotor resistance, reducing the axial velocity and increasing the radial velocity. The stagnation point migrates from the leading edge along the inner-surface of the duct, consequently affecting the flow around the leading edge. For the flat-sided devices, B, E and H, the flow separates from the leading edge, resulting in a recirculation zone where viscous losses are increased, shown in plot (b). The sharp reduction in efficiency observed for these devices is due to the onset of flow separation in the range $1 < K < 2$. For the concave devices, C and D, separation occurs much earlier, with a resultant increase in size of the recirculation region, as shown in plot (d). For these devices, a small change to the point of separation has a large effect on the recirculation zone and consequently the efficiency.

The performance of flat-sided and concave duct profiles are now compared. Streamtube-averaged plots of area A, mean velocity U and mean pressure p are presented for ducts B and C in figure 5.15 at their optimum operating point of $K = 0.5$. We can see from figure 5.1 that the only difference between these geometries is the external surface. However a slightly higher disc velocity and pressure jump are observed for duct C in figure 5.15 and table 5.6. Figure 5.14 shows that at $K = 0.5$ a region of separated flow exists outside duct C, which is not present for duct B. The effective blockage is therefore higher for

Table 5.6: Comparison of area, velocity, pressure and C_P for devices B and C.

Device	K	A_{disc} [m^2]	U_{disc} [m s^{-1}]	Δp_{disc} [Pa]	C_P	η
B	0.5	176.71	2.28	1395	0.427	0.736
C	0.5	176.71	2.34	1483	0.468	0.559

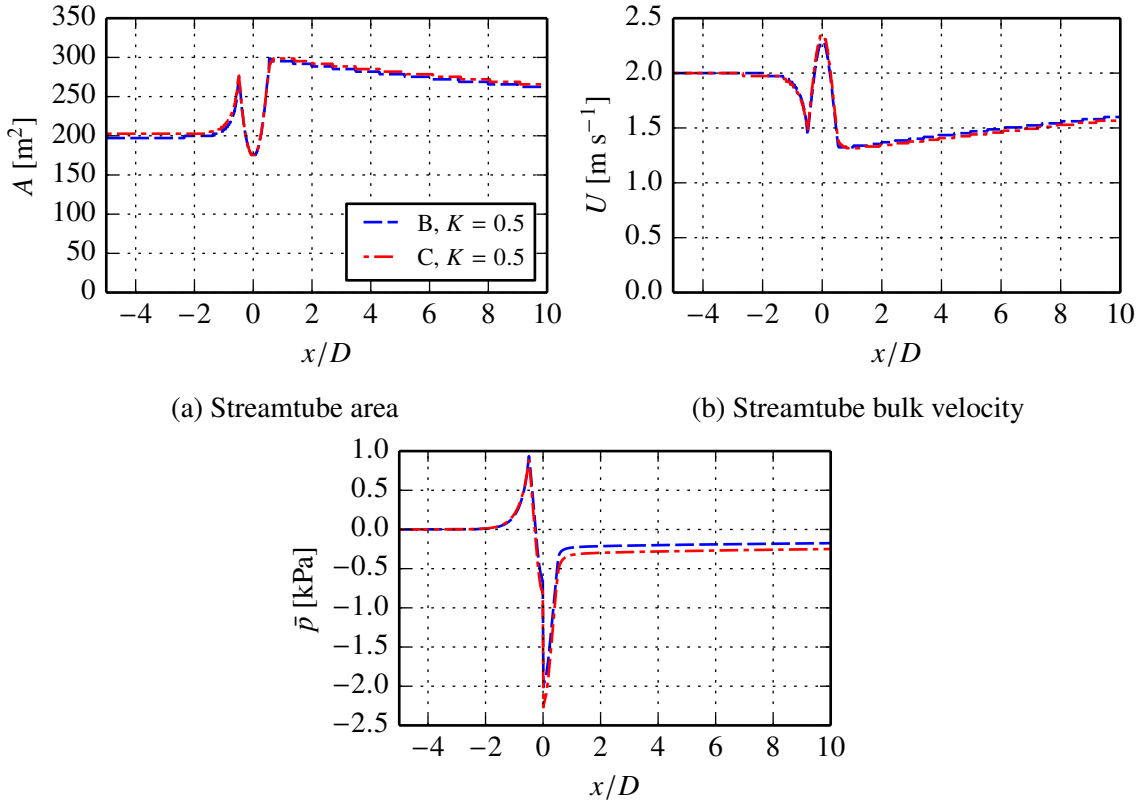

(a) Streamtube area

(b) Streamtube bulk velocity

(c) Streamtube mean pressure

Figure 5.15: Comparison of streamtube variables for ducts B and C, showing the effect of duct thickness.

duct C, and consequently the core and bypass flows are accelerated slightly. The pressure change is modelled as a function of the velocity at the disc, $\Delta p = \frac{1}{2}\rho U_{\text{disc}}^2$, and hence is higher for duct C than duct B. This results in a higher power coefficient of $C_P = 0.43$ for duct C. While flow separation at the leading edge has beneficial consequences for device power, it reduces device efficiency greatly. The small increase in power (4.9%) is achieved at the cost of a 26.3% reduction in efficiency as shown in table 5.6. Device B is a more favourable design due to the improved efficiency.

While there is a direct trade-off between profile thickness and device efficiency for ducts B and C, this is not the case for ducts D and H. Unlike the comparison between devices B and C, the concave profile (D) is superior to the flat-sided profile (H), as the increase in peak power coefficient (11.6%) outweighs the reduction in efficiency (1.3%) (table 5.7).

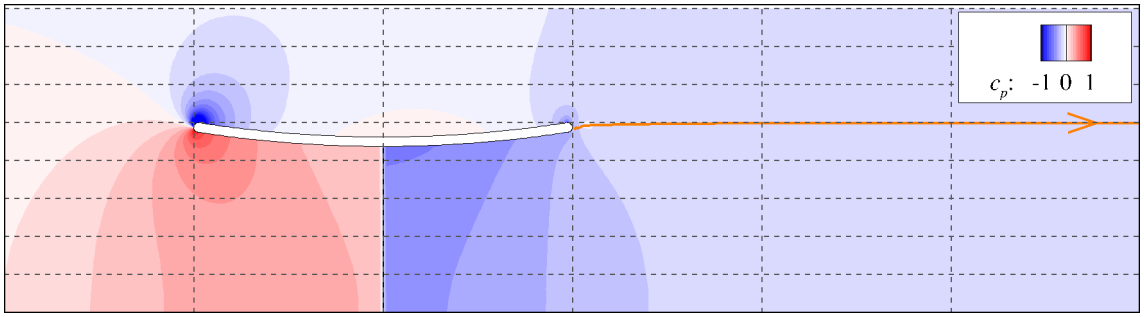

(a) Duct D at $K = 1$.

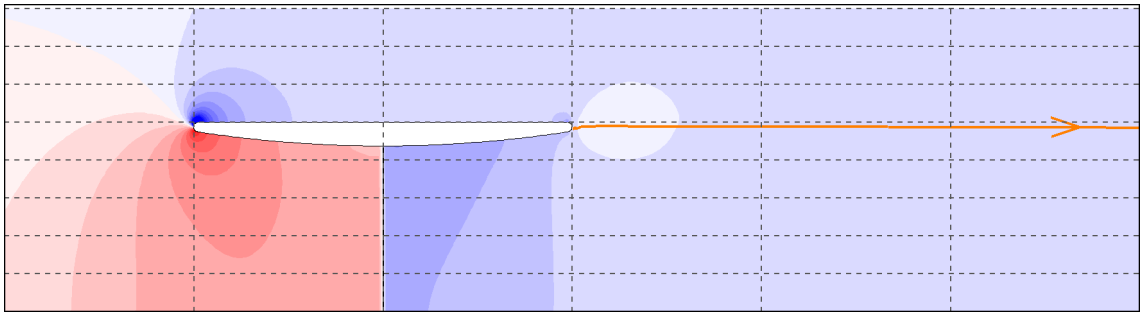

(b) Duct H at $K = 1$.

Figure 5.16: Flow expansion downstream of the device is visible by comparing the orange streamline against the rectangular grid. Although the expansion downstream of duct D is only slightly greater than that downstream of duct H, there is a marked effect on disc pressure change, disc velocity, and power. The contours of pressure coefficient c_p highlight the reduced pressure just downstream of the disc.

The concave curvature of the external surface of duct D is very slight, and at the operating point for maximum C_P ($K = 1$) the bypass flow remains attached. The flow follows the camber of the duct profile and departs from the trailing edge at an outward angle with respect to the axial direction. This enables a pressure gradient to be supported between the duct exit and the downstream boundary. The pressure field and downstream flow expansion of duct D and H are compared in figure 5.16. Pressure is expressed as the coefficient c_p,

$$c_p = \frac{p - p_\infty}{\frac{1}{2}\rho u_\infty^2} \tag{5.12}$$

where p is the local static pressure and p_∞ is the freestream value. An orange streamline highlights the larger expansion of the wake of duct D relative to duct H. This expansion is slight, but can be observed clearly by reference to the rectangular gridlines in each figure.

To illustrate the relationship between flow curvature and pressure change, we consider

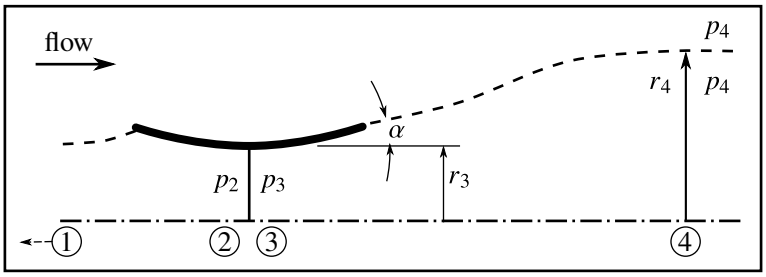

Figure 5.17: Schematic diagram of one-dimensional inviscid flow passing through a ducted turbine. The broken line represents the streamtube separating the core and bypass flows.

a one-dimensional inviscid flow between the rotor plane (station 3) and the point of pressure equalisation downstream (station 4). By continuity within the streamtube, shown in figure 5.17, the velocity will reduce as the streamtube expands. Correspondingly, the static pressure will increase to satisfy conservation of energy. If the angle at which flow departs from the trailing edge, α, is increased, the change in cross sectional area between the disc and point of pressure equalisation, $\Delta A_{34} = \pi\left|r_3^2 - r_4^2\right|$, will increase. The pressure change, $\Delta p_{34} = \left|p_3 - p_4\right|$, must also increase. The pressure far downstream is not greatly affected by small changes in duct curvature (it is more sensitive to total device thrust). Hence the pressure change Δp_{34} is reflected in a reduced level of static pressure at station 3, just downstream of the disc.

The reduced pressure downstream of the disc for device D allows for a greater pressure change across the disc, as shown in figure 5.18 (c). Plots (a) and (b) in the same figure indicate that the volumetric flow rate through the disc is increased. Device D has a higher streamtube area upstream and a higher mean disc velocity than device H. The values of disc area, velocity and pressure change are listed in table 5.7.

Note that this effect, where the duct imparts radial momentum to the flow at the trailing edge, is only possible for low external curvature and moderate disc resistance, where the

Table 5.7: Comparison of area, velocity, pressure and C_P for devices D and H.

Device	K	A_{disc} [m^2]	U_{disc} [m s^{-1}]	Δp_{disc} [Pa]	C_P	η
D	1	240.53	1.71	1540.49	0.483	0.741
H	1	240.53	1.64	1414.29	0.428	0.753

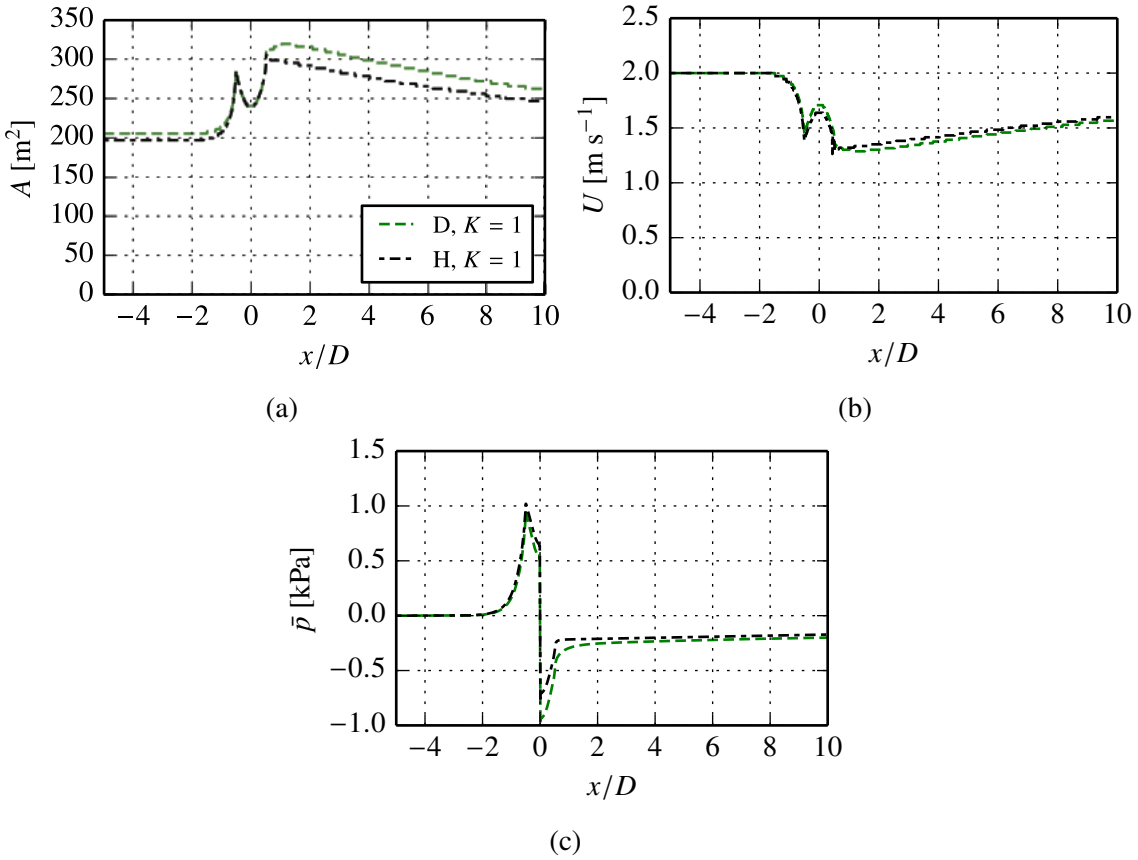

Figure 5.18: Comparison of (a) streamtube area, (b) streamtube volumetric flow rate and (c) streamtube pressure for ducts D and H.

bypass flow remains attached. If separation was triggered at the leading edge, perhaps by surface imperfections or freestream turbulence, this beneficial effect would be lost.

5.5 Three-dimensional computational model

5.5.1 Introduction

Within the PerAWaT project, researchers at the University of Manchester and Électricité de France (EDF) constructed and tested a physical model of a ducted tidal turbine. The experimental methods are described here as they have only previously been documented in a confidential industrial report (Fleming, McIntosh, Willden, Stallard and Feng, 2013). A three dimensional computational model of a ducted turbine is then developed for comparison to this experimental data.

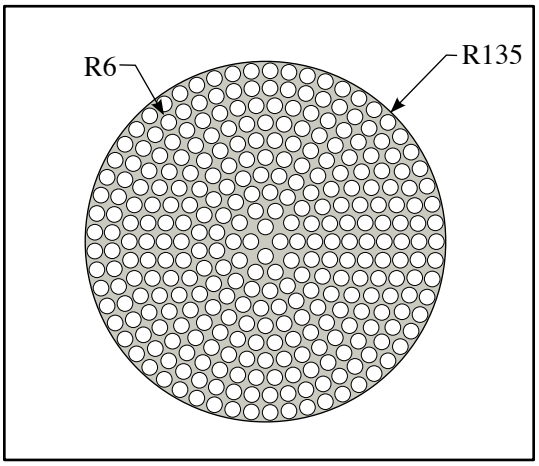

Figure 5.19: Schematic diagram of a typical porous disc with porosity $k = 1.61$ and resistance coefficient $K = 0.9$. Dimensions are in millimetres.

5.5.2 Experimental methods

5.5.2.1 Test description

A model scale ducted turbine was tested at a range of operating points in an open channel measuring 1.5 m wide with a water depth of 0.8 m*.

Three turbine models were tested: a ducted turbine, and two bare turbines. One of the bare turbine models had a diameter corresponding to the rotor of the ducted turbine, and the diameter of the second bare turbine model corresponded to the outer diameter of the ducted turbine.

The model duct was constructed from glass-filled polyamide 12 by a rapid-prototyping method. The duct profile was based on device H from the preceding study in section 5.4. The profile in figure 5.1 (d) was scaled down by a factor of 1.555×10^{-2} to fit a porous disc of diameter $D_{\text{disc}} = 0.27$ m. The resulting model had an external diameter and length of $D = L = 0.311$ mm, corresponding to a blockage ratio of $B = 0.063$.

5.5.2.2 Porous disc rotor model

For both the unducted and ducted turbine models, the rotor was represented physically by a porous disc (see figure 5.19), which presents a similar resistance to flow in the streamwise

*The tests reported in section 2.2.1 were also carried out in this channel.

direction for a given rotor operating point. A benefit of the porous disc model in this situation is that it allows for consistent comparison between unducted and ducted turbines. McIntosh et al. (2011) show that a rotor designed for operation within a duct will have different twist and chord distributions to one designed for operation in isolation.

The swirl which would be imparted by a real rotor is not reproduced by a porous disc. For this investigation into the effect of a duct, swirl is considered to be of secondary importance relative to streamwise thrust (provided no interior separation occurs at the downstream side of the duct). The resistance of a porous disc is governed by its porosity, k, defined as the ratio of open area (holes) to solid area.

$$k = \frac{A_{\text{open}}}{A_{\text{solid}}} \tag{5.13}$$

Hence a porous disc can represent a rotor at a single operating point only. In order to represent the full range of operating states, a set of discs of varying porosity must be used. To enable comparison with the numerical porous disc model used in the computational study, the disc resistance is measured in terms of a resistance coefficient K, defined as

$$K = \frac{T}{\frac{1}{2}\rho A_{\text{disc}} u_{\text{disc}}^2}. \tag{5.14}$$

Note that the resistance coefficient K of a physical porous disc is analogous to the momentum resistance factor K of a numerical porous disc and may be compared directly. Sets of 270 mm and 311 mm diameter discs were manufactured from 6 mm thick acrylic with a range of porosities. The resistance coefficients K for each disc porosity k were determined through preliminary testing, and are listed in table 5.8. Discs 1 - 5 were tested with and without a duct, while discs 6 and 7 match the blockage of the ducted turbine.

The porous discs listed in table 5.8 are used to represent three turbines. The set of 270 mm discs are used in combination with the model scale duct to represent a ducted turbine. The blockage of this device in the water channel is $B = 6.3\%$. The same discs are also tested in isolation, representing a 270 mm unducted turbine ($B = 4.8\%$). Finally, the

two 311 mm discs represent a bare turbine with equivalent blockage to the ducted turbine, $B = 6.3\%$.

5.5.2.3 Flume characterisation

The baseline flow in the EDF flume in the absence of a turbine was characterised prior to the experimental campaign, and is discussed in detail in section 2.2.1. The streamwise velocity at the rotor centreline for this case was 0.55 ms^{-1} and velocity and turbulence profiles have been presented previously in figures 2.5 and 2.6.

5.5.2.4 Performance measurement

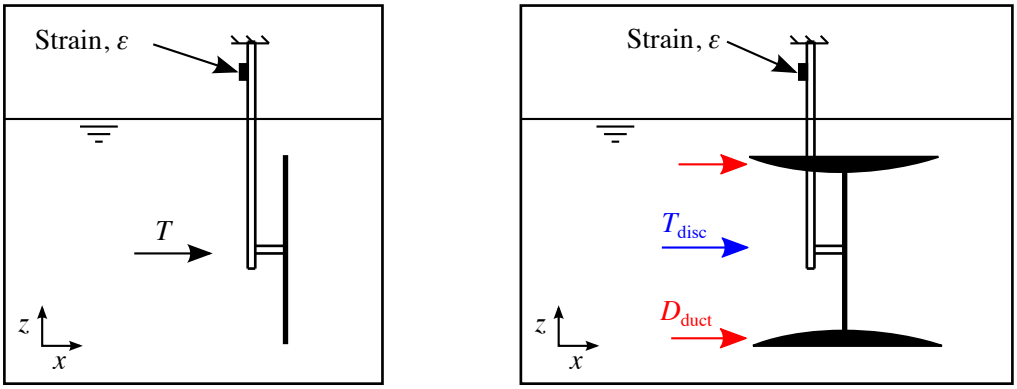

(a) (b)

Figure 5.20: Diagram of support tower for (a) the unducted disc and (b) the ducted disc.

The model turbine was supported from above by a 15 mm diameter tower with an embedded strain gauge, as indicated in figure 5.20. The strain gauge was calibrated prior

Table 5.8: List of porous discs with porosity and resistance coefficient.

Disc	Diameter, D [m]	Porosity, k	Resistance coefficient, K
1	0.27	2.15	0.6
2		1.61	0.9
3		1.00	1.8
4		0.30	10.0
5		0.22	16.0
6	0.311	1.00	1.8
7		0.30	10.0

to each test to determine the (linear) relationship between voltage output and thrust. Strain is sampled at 200 Hz for 120 seconds during each test. Prior to the connection of a turbine model (a ducted/unducted porous disc) to the tower for each test, the hydrodynamic thrust on the tower alone was measured. This residual drag was subtracted from subsequent measurements with the model turbine. Thrust is normalised on the upstream centreline velocity of $u_{\text{ref}} = 0.55\,\text{m}\,\text{s}^{-1}$.

$$C_T = \frac{T}{\frac{1}{2}\rho u_{\text{ref}}^2 A}, \tag{5.15}$$

In the case of a ducted turbine it was not possible to isolate the thrust on the disc alone, as there was no measurement of strain between the disc and duct. However, if a computational model can be developed which matches the experimental conditions and accurately predicts the total thrust on the device, it can be used to reasonably estimate the disc thrust.

5.5.3 Computational model

The ducted devices in section 5.2 were simulated at full scale in uniform flow with low ambient turbulence. The present experiments are carried out at reduced scale in vertically and horizontally sheared flow. The simplification of the full scale model into a two-dimensional problem by assuming axisymmetric flow in a cylindrical domain is not appropriate at model scale due to the velocity shear. Hence a three-dimensional computational model, capable of simulating horizontal and vertical sheared velocity profiles, is generated. As with the full scale simulations, an assumption of steady flow is made; therefore unsteady phenomena such as vortex shedding from the duct, disc and support structure will not be captured.

The computational domain consists of a rectangular channel of width and height corresponding to the flume width and water depth respectively, extending $5D$ upstream and $10D$ downstream of the rotor plane, as shown in figure 5.21. The duct geometry is generated by revolving the profile of the scaled duct H in figure 5.1 (d). In each computational simulation, the area blockage is equivalent to the corresponding experimental run.

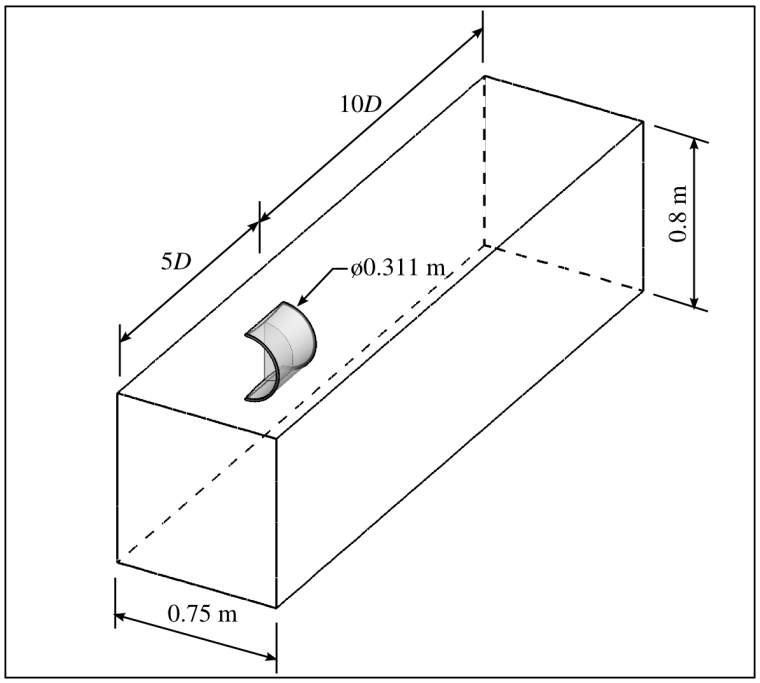

Figure 5.21: Isometric view of the computational model of the ducted turbine at model scale.

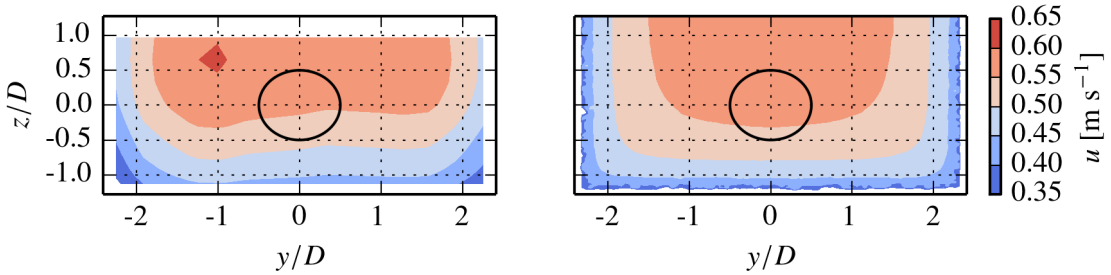

Figure 5.22: Comparison of measured (left) and computed (right) velocity profiles for the model scale turbine tests.

The velocity profile upstream of the turbine is sheared in the horizontal and vertical directions, due to the rough sides and floor of the flume. The sheared flow model from section 3.2.3 is used here, with modifications to allow horizontal and vertical profiles to be combined. A fully-developed turbulent velocity profile is generated numerically by assuming a linear variation of shear vertically from a given value τ_w at the channel bed to $\tau = 0$ at free surface, and horizontally from τ_w at the channel sides to $\tau = 0$ at the vertical midplane. Two values are required to describe the profile: a reference velocity, taken at the centreline of the flume (coincident with the turbine centreline), and a bed roughness coefficient, $c_f = \tau_w / \left(\frac{1}{2}\rho u^2\right)$. A friction coefficient of $c_f = 0.005$ is found to

Table 5.9: Size limits for triangular and tetrahedral elements in the base grid for the current three dimensional computational model.

Region	Element type	Max edge length
Leading edge	Triangular	$10^{-3}D$
Trailing edge		$2.5 \times 10^{-3}D$
Duct flank		$0.025D$
Duct near field	Tetrahedral	$0.05D$
$y < w/4$		$0.1D$
$w/4 < y < w/2$		$0.2D$

fit the undisturbed velocity profile at the vertical midplane of the flume. The resulting two-dimensional profile is compared with the experimental case in figure 5.22.

Profiles of turbulent kinetic energy k_t and specific dissipation rate ω are also prescribed at the upstream boundary. These profiles are derived from the velocity profile using an algebraic turbulence model, which is described in section 3.2.3.

A shear force of $\tau_w = c_f \frac{1}{2}\rho u^2$ per unit area is applied at the channel bed and walls to sustain the velocity and turbulence profiles. A symmetry boundary condition is applied along the vertical midplane of the turbine so that only one side of the channel needs to be modelled geometrically. The free surface is represented by a symmetry boundary condition at the upper boundary of the domain. Any deformation of the free surface due to power extraction is considered secondary to the current comparisons of ducted and unducted turbine performance. At the downstream boundary, a uniform pressure of $p = 0\,\text{Pa}$ is applied.

The rotor is modelled as a numerical porous disc, as described previously in section 1.4.1.1. The turbines are simulated at momentum loss coefficients $K = \{0.6, 0.9, 1.8, 10, 16\}$ for consistency with the resistance coefficients of the physical model.

5.5.3.1 Spatial discretisation

The domain is discretised with an unstructured grid of three-dimensional tetrahedral elements, as described in chapter 2. The maximum edge length of the triangular surface elements at the leading edge of the duct is $10^{-3}D$, so that this surface is resolved by at

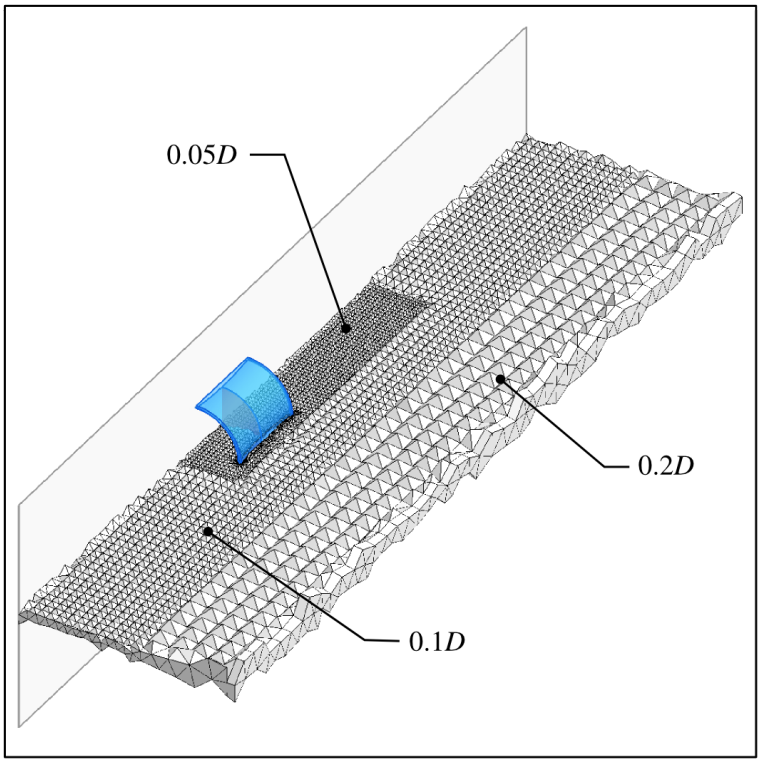

Figure 5.23: Isometric view of base grid showing the tetrahedral elements at a horizontal plane at mid-depth.

least 32 elements along its circumference. Preliminary computations revealed that ducted device performance was less sensitive to trailing edge resolution, so a larger element edge size of $2.5 \times 10^{-3} D$ is prescribed here, resolving the trailing edge curvature with at least 16 elements circumferentially. Surface elements grow from the leading and trailing edges to a maximum edge length of $0.025D$ on the inner and outer surfaces of the duct. A maximum tetrahedral element edge length of $0.05D$ is prescribed in a cuboidal region which encloses the ducted turbine and extends three diameters downstream. Outside this region, two further element size limits are set. In the region which encloses the turbine, extending from $y = 0$ to $y = s/4$, where s is channel width, a maximum element size of $0.1D$ is allowed. Away from the turbine, between the planes $y = s/4$ and $y = s/2$, the maximum element edge length is $0.2D$. These zones, where the maximum element size is controlled, are visible in figure 5.23, and the element sizes are listed in table 5.9.

Wall functions are used to model the boundary layer at the duct surface. The target dimensionless wall distance is $y^+ > 25$. Five layers of prism elements are generated, with

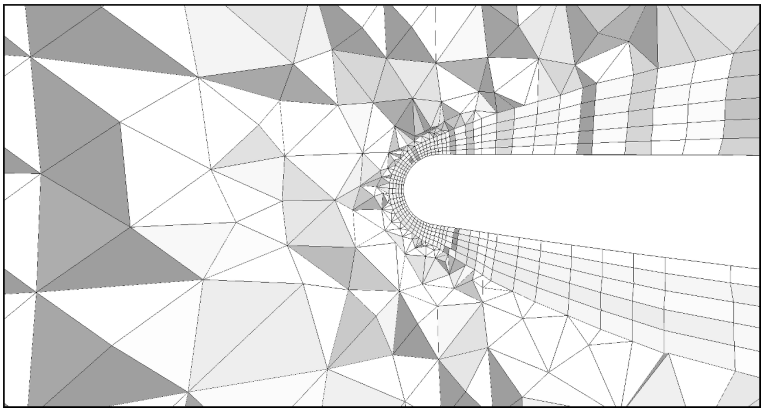

Figure 5.24: Close-up view of base grid showing resolution in the vicinity of the leading edge of the duct.

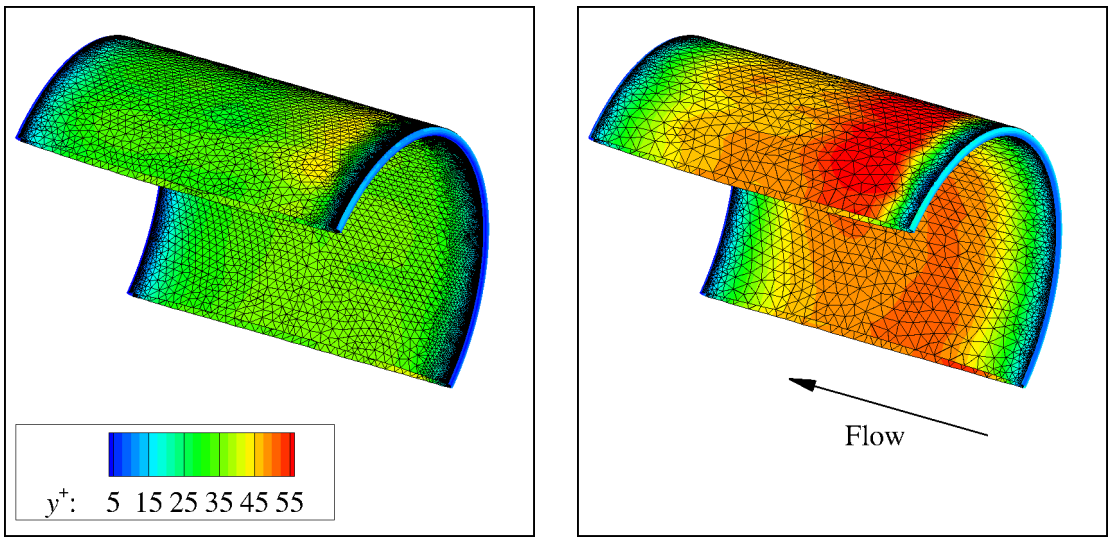

(a) (b)

Figure 5.25: Contours of dimensionless wall distance y^+ on the (a) the base grid and (b) the coarse grid. The surface mesh at the leading edge is not shown for clarity.

a scaling factor of 1.1 between each layer. The prism-generating algorithm prioritises a smooth transition between the uppermost layer of prism elements and the adjacent tetrahedral mesh, allowing the heights of the wall adjacent prisms to float. The resulting mesh topology at the leading edge is presented in figure 5.24. Contour plots of y^+ on the duct surface are shown for the base mesh (and a coarse mesh) in figure 5.25. Although non-dimensional wall distance values of $5 < y^+ < 25$ are observed near the leading and trailing edges, this is not expected to adversely affect the solution due to the use of enhanced wall functions in the k-ω SST turbulence model in ANSYS Fluent, as discussed

Table 5.10: Comparison of duct drag $C_{D\,\mathrm{duct}}$ and normalised disc velocity $u_{\mathrm{disc}}/u_\infty$ for 3D and 2D simulations of model scale test case.

Grid	y^+	N_{elem}	$C_{D\,\mathrm{duct}}$	$u_{\mathrm{disc}}/u_\infty$
3D coarse	$y^+ < 60$	2.5×10^5	0.134	0.804
3D base	$y^+ < 40$	2×10^6	0.136	0.805
2D	$y^+ < 2$	14100	0.140	0.826

in section 2.1.8.

Ideally, each three-dimensional element should be divided at the midpoint of each edge, producing eight child elements (whether the parent element is tetrahedral or prismatic). The resulting refined mesh would contain 8 times more elements, approximately 16×10^6 in the current case, which increases the computational load beyond the available resource. Conversely, a coarse mesh which shares the same nodal locations as the base mesh would contain only 2.5×10^5 elements, and may not capture the geometry adequately. In presenting the grid convergence index (GCI), Roache (1997) suggests that it is not necessary to use a refinement factor of $r = 2$, but it should of course be greater than $r = 1$. With this in mind, a coarse mesh is generated by scaling all element edge size limits by a factor of $r = 1.5$. Predictions of duct drag coefficient $C_{D\,\mathrm{duct}}$ and average normalised velocity at the disc $u_{\mathrm{disc}}/u_\infty$ are produced on the coarse and base grids to allow a grid convergence index to be calculated.

The test case for this mesh sensitivity study is modified to allow comparison with a two-dimensional model based on that presented in section 5.3.1, which exhibited low discretisation error. While blockage and Reynolds number remain consistent with the experiment, the flume velocity profile is not modelled. A uniform flow velocity of $u = 0.55\,\mathrm{m\,s^{-1}}$, a uniform turbulence intensity of $TI = 10\%$ and a length scale of $l = 0.1D$ are applied at the upstream boundary.

The scale of the 2D axisymmetric model from section 5.3.1 is reduced so that the duct now measures $R = 0.311$ m in diameter. The outer radial boundary of the domain is modified to match the blockage of the experiment, where $B = 0.063$. The topology of the

coarse grid III is used here. While grid III achieves a dimensionless wall distance in the range $10 < y^+ < 20$ at full scale, it is expected to achieve a much lower value of $y^+ < 1$ at model scale, where the Reynolds number is greatly reduced. The results of the three grids are presented in table 5.10.

When solutions from only two grids are available, the observed order of the numerical scheme cannot be calculated. The formal order of convergence ($p = 2$ in this case) may be used, but a larger factor of safety of $F_s = 3$ should be applied when calculating the grid convergence index (Roache, 1998). The relative error for the base grid is calculated using equation 5.6, where the refinement ratio is $r = 1.5$ and order of convergence is $p = 2$. The base grid convergence index is then calculated as $\mathrm{GCI}_{\mathrm{base}} = F_s E$. Values of $\mathrm{GCI}_{\mathrm{base}}$ for duct drag and average disc velocity are presented in table 5.11, indicating that discretisation error is acceptably low.

5.5.4 Results

The effect of the duct on turbine performance is now examined. Initially, computations and measurements of the thrust on each device are compared to determine how well the computational model performs. The computed power is then presented for case and the effect of the duct is discussed.

5.5.4.1 Comparison of computed and measured thrust

Computed predictions and experimental measurements of thrust are presented in figure 5.26. For both datasets, turbine operating point is described in terms of the disc resistance coefficient K rather than induction factor a, which was used previously in section 5.2. This

Table 5.11: Grid convergence indices for the 3D unstructured grid based on mean disc velocity and duct drag coefficient.

Metric	$\mathrm{GCI}_{\mathrm{base}}$ [%]
$u_{\mathrm{disc}}/u_\infty$	1.36
$C_{D\,\mathrm{duct}}$	2.97

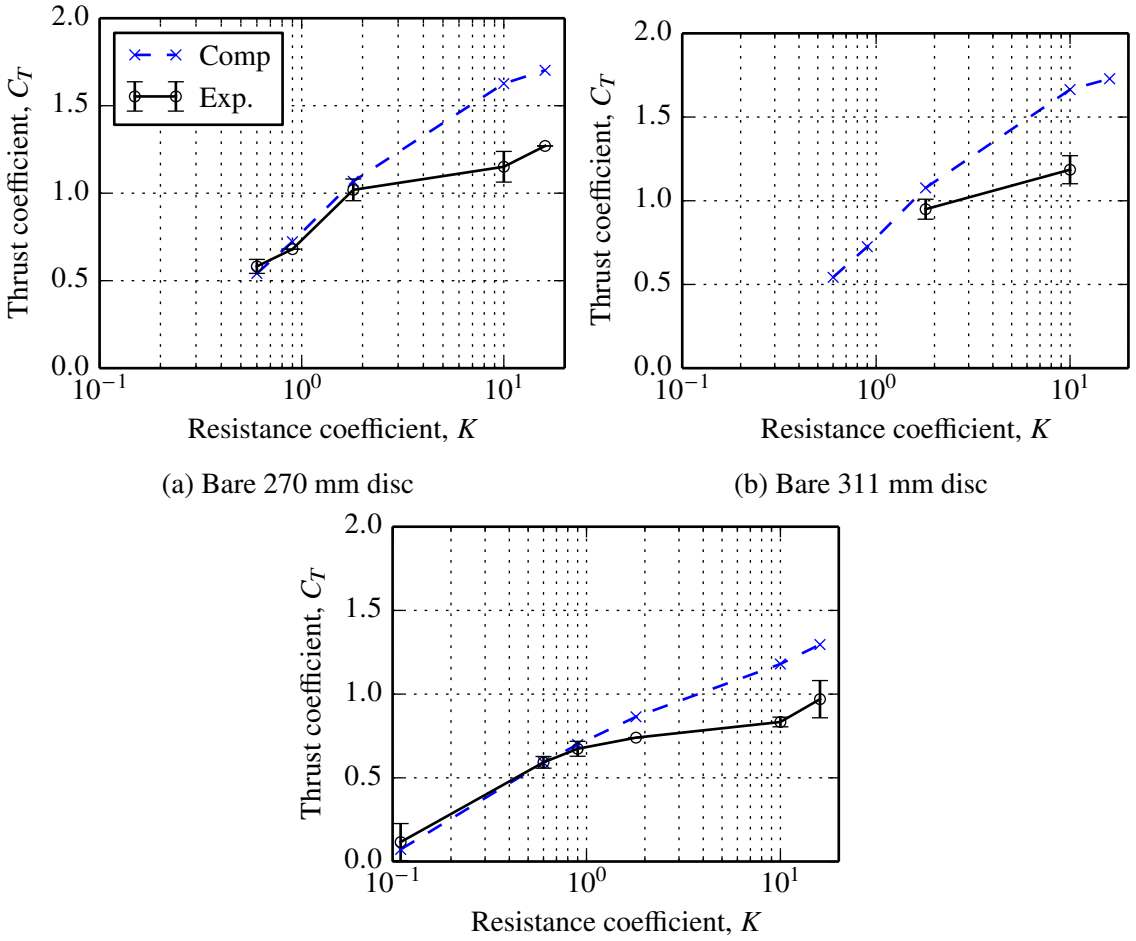

(a) Bare 270 mm disc

(b) Bare 311 mm disc

(c) Ducted 270 mm disc

Figure 5.26: Comparison of computed and measured thrust on the three devices. Note that in (b) the 311 mm disc is simulated at 5 operating points but tested at only two operating points.

is because unnecessary uncertainty would be introduced by estimating the induction factor from the measured thrust coefficient. As described previously, the thrust on the tower in isolation is subtracted from the measured thrust for each operating point, leading to the thrust on the disc alone. In the case of the ducted disc, the reported thrust is that on the disc and duct, but not the tower. As the experimental thrust fluctuates during the sampling period, error bars are used to represent each operating point. The centre of each error bar symbol corresponds to the mean of the thrust signal, and the length of each tail represents one standard deviation. For certain operating points, raw data was not available, so the mean value as provided by the experimentalists is used, and the error bar length is set to zero. These points are $K = 0.9$ and $K = 16$ for the 270 mm bare disc (figure 5.26 (a)), and

$K = 1.8$ for the ducted 270 mm disc (figure 5.26 (c)).

Good agreement in thrust is observed for low-to-moderate levels of resistance coefficient, where $K < 1.8$. For the range $K > 1.8$, thrust is over-predicted by the computational model. This divergence of computed and measured thrust for low porosity discs reflects a limitation in the physical model rather than the numerical model. Numerical and physical porous disc models are intended to emulate an ideal turbine, i.e. a turbine which removes streamwise momentum from the flow without viscous losses. At low-to-moderate disc resistance, both models behave as intended. Streamwise momentum is extracted from the flow, and while viscous losses are present in the shear layer where the flow separates from the disc edge, the relative effect of viscosity is negligible and the resulting wake is steady. As the resistance of a physical disc is increased (by reducing the number of holes), the disc approaches the behaviour of a solid disc, where viscous forces are more significant, triggering vortex shedding and unsteady separation from the disc. This mode of behaviour is no longer representative of an ideal turbine, and the physical model is no longer valid.

Graham (1976) shows that vortex shedding occurs for a rectangular porous strip above $K = 4$, which is consistent with the deviation in numerical and physical thrust observed here. The limiting C_T for a solid disc in the current conditions can be calculated for comparison to the current results. Yeung (2010) presents experimental data from a variety of sources to examine the drag of a solid disc in confined flow. The same author develops the following model to predict the thrust of a solid disc for a given blockage B (Yeung, 2009),

$$C_T = 0.831 \left(\frac{(1 + 0.831B) - \sqrt{(1 - 0.831B)^2 - 8B(1 - B)^6}}{4B(1 - B)^6} \right). \tag{5.16}$$

The result of this model should represent the upper limit for porous disc drag, as porosity is reduced to zero (i.e. a solid disc).

For the lower blockage case of $B = 0.045$, corresponding to the 270 mm disc, equation 5.16 yields a limiting thrust of $C_{T\,\mathrm{solid}} = 1.41$. This value lies below the maximum computed thrust for a numerical porous disc (which continues to represent an ideal rotor) of $C_T \approx 1.7$ in figure 5.26 (a). Measured thrust on the low-porosity ($K > 10$) discs in the

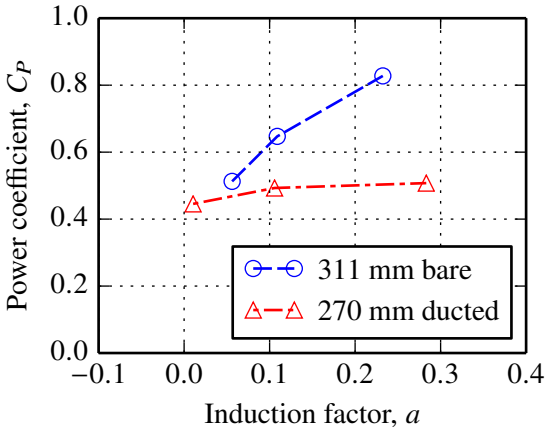

Figure 5.27: Comparison of computed power coefficient for bare and ducted discs.

same figure are below the solid disc value of $C_T = 1.41$ but appear to tend towards this limit. Similar behaviour is observed for the 311 mm disc in figure 5.26 (b), where the blockage ratio is $B = 0.063$. The theoretical limit in this case is $C_{T\,\text{solid}} = 1.49$. Computed maximum thrust for an ideal porous disc is above this threshold, while measured thrust for the porous disc at of resistance $K = 10$ is below this limiting value. Further tests of lower porosity discs and a solid disc would be required to verify this analysis.

As device power could not be measured directly from the experimental data, we rely on the computational model to determine the effect of the duct at model scale. Comparisons are made at disc resistances of $K = \{0.6, 0.9, 1.8\}$ only, where the computational and physical models report the same device thrust. The operating point is represented in this case by the induction factor a (defined in equation 5.8) to allow direct comparison with the results in section 5.2 for a tidal turbine at full scale.

In figure 5.27 the duct power coefficient is normalised on the total frontal area of the device, i.e. the area based on the maximum external diameter of the duct (311 mm). This is compared with simulations of a bare disc of diameter 311 mm, which has an equivalent frontal area. The same trend which was observed earlier at full scale (c.f. figure 5.6), is repeated here. The duct reduces the power at the moderate resistances tested, and the curves indicate that the ducted device may produce more power at very low disc resistance ($K < 0.6$). The ducted device exhibits a very broad range of operating points where C_P is

close to maximum. However, if a rotor can be controlled to operate close to peak C_P, the bare device is considered superior.

5.6 Conclusions

The objectives of the first part of this study were to assess the performance of a ducted turbine relative to an unducted turbine and to identify beneficial features of a duct. A series of bi-directional duct designs were produced by combining circular arcs and altering camber and thickness. These devices, along with a bare turbine, were each simulated under the same flow conditions using a simplified two-dimensional RANS model. Turbine performance was assessed in terms of power and efficiency. The unducted turbine outperformed all of the ducted turbines, achieving a power coefficient of $C_P = 0.83$ and an efficiency of $\eta = 0.73$ at its optimum operating point. The best-performing ducted device, D, achieved a power coefficient of only $C_P = 0.48$ at its best operating point. The corresponding efficiency at this operating point was relatively high at $\eta = 0.74$, as leading edge flow separation did not occur. Note that the results of this comparison between bare and ducted rotors are not general: an idealised rotor model has been used, and the effect of blockage ratio has not been examined.

The area, mean pressure and bulk velocity were calculated at each streamwise location in the streamtube bounding the rotor flow. Comparisons of these parameters show that a duct limits flow expansion downstream of the disc, thereby reducing the pressure reduction behind the disc and the volumetric flux through the disc, ultimately limiting the power coefficient of the device. The ducted devices undergo a sudden reduction in efficiency when the disc resistance is increased beyond a certain point. At this point, dependent on duct geometry, the flow separates from the leading edge. Kinetic energy is lost to heat through viscous action in the recirculating region which develops outside the duct, resulting in reduced efficiency.

Physical testing of a ducted porous disc has been carried out by a third party. The

thrust on the disc, and duct where present, was derived from a strain gauge embedded in the support shaft. A three-dimensional computational model developed to match the blockage and flow conditions of the flume. Good agreement in thrust was observed for unducted and ducted discs at low to medium resistance. The reason for the divergence in thrust results at higher resistance is that the physical disc approaches the behaviour of a solid disc due to viscous behaviour, while numerical disc continues to emulate an ideal rotor. Within the range of agreement with the experiment, the numerical model shows that device power is reduced by a duct at model scale.

The primary conclusion of this study is that an unducted turbine outperforms a bi-directional ducted turbine in terms of power and efficiency. If a duct is to be designed for a tidal turbine for other reasons, such as alignment of flow and protection of blades, a thin duct profile with slight camber performs best.

Chapter 6

Conclusions

A three dimensional computational model of a full scale axial flow tidal turbine has been used to investigate the effects of a range of realistic environmental conditions on turbine performance. The model, which is based on the Reynolds averaged Navier-Stokes (RANS) equations, has been developed using the commercial flow solver ANSYS Fluent.

The rotor of the turbine is directly resolved using a body-fitted grid, and motion is enabled through the introduction of a sliding mesh interface between the rotor geometry and the channel boundaries.

The boundary conditions and dimensions of the domain are modified to reproduce a range of operating conditions based on observations of tidal channel flows. Self-sustaining profiles of sheared velocity and turbulence profiles are generated using an existing method, where the prescribed velocity and turbulence profiles are maintained by a shearing force at the channel bed. The inter-device spacing of an infinite fence of turbines is modified by changing the width of the computational domain and prescribing periodic boundary conditions at the lateral boundaries. The periodic conditions at the lateral boundaries also enable the simulation of yawed flow.

A deforming free surface is introduced using a two-phase model, where the passage of air above the free surface is included. Linear wave theory is combined with the existing sheared flow model and applied as a boundary condition to the channel, allowing turbine

operation in a combination of sheared flow and free surface waves to be examined. This is the first time, to the author's knowledge, that such a flow has been reproduced successfully in a RANS model.

In a separate study, the performance of bi-directional ducted tidal turbines is investigated. In an effort to identify an optimum profile for a bi-directional duct, a series of candidate designs are generated parametrically. A two dimensional axi-symmetric RANS model is developed to examine device performance in confined flow conditions. A three-dimensional model is subsequently produced for comparison to existing experimental data.

Key findings from each of these investigations are now presented.

6.1 Key findings

6.1.1 Tidal turbine performance in sheared, confined and yawed flow

6.1.1.1 Effect of shear

- The thrust and power of a tidal turbine is higher in sheared flow than in a uniform flow of the same volumetric flow rate. This is due to the higher kinetic flux through the swept rotor area in the sheared velocity profile.

- The unsteady loading on a turbine blade is greatly increased in sheared flow. The rotor encounters a greater range of freestream velocities when passing between the high velocity flow in the upper portion of the sheared profile and the low velocity flow near the channel bed. This type of fatigue loading should be accounted for in the structural design of tidal turbine blades.

- The rate of wake recovery is increased in sheared flow. The high velocity flow in the upper portion of the sheared profile is accelerated further in the bypass flow due to blockage effects, generating a stronger shear layer at the edge of the

wake. Additionally, the sheared velocity profile supports a higher level of ambient turbulence, which enhances wake mixing.

- Turbine performance in sheared flow is also dependent on elevation. Mean power and thrust are reduced when the device is positioned close to the channel bed. However, the amplitude of unsteady loads on the rotor blades is increased due to the higher gradient in velocity in this region. Additionally, the rate of wake mixing is reduced, as a shear layer cannot form beneath the wake. A compromise is highlighted between the higher mean power and thrust attainable at high elevation in sheared flow, and the increased overturning moment on the supporting structure. Despite the increase in the relative size of the support structure, device efficiency (power-to-thrust ratio) is improved slightly, as the increase in power outweighs the increase in parasitic drag.

6.1.1.2 Effect of flow confinement

- When the lateral spacing of a row of turbines is reduced, mean thrust and power are increased due to the blockage effect, where the higher velocity in the bypass flow enables a greater pressure change across the rotor plane.

- The higher bypass velocity results in greater shear in the wake between the bypass and core flows, enhancing wake mixing.

6.1.1.3 Effect of flow alignment

- Rotor thrust and power are reduced in yawed flow, as the blades operate at off-design local flow angles for significant sections of a revolution.

- Unsteady blade loads in yawed flow are similar in relative magnitude to those in aligned flow if the velocity profile is consistent. However, at high yaw angles, an additional perturbation of the blade loading can occur in the ‘upstream’ portion of a revolution due to an interaction with the turbine nacelle.

- Device efficiency is reduced in yawed flow. Parasitic drag is increased due to the side-on interaction of the flow with the nacelle, which is expected to cause unsteady vortex shedding.

- A small but consistent distortion of the wake was observed in the yawed flow cases. This is a consequence of the rotating wake interacting with its images in the bed and free surface planes.

6.1.2 Effect of free surface waves

- Large differences in blade torque are observed in a comparison of rigid and deforming free surface models, in the absence of waves. A hydrostatic pressure gradient is present for the deforming free surface case, and exerts buoyancy forces on the rotor blade (which is modelled as a void) as it rotates.

- Thrust and torque fluctuations on the rotor and blades increase with wave height, but mean values are not affected. Frequency analysis indicates that unsteady rotor loading is dominated by wave-induced velocities, but the sheared velocity profile remains the dominant influence on unsteady blade loading.

- Blade and rotor load fluctuations also increase with wavelength, but mean values are not affected. The induced velocity profile increases in magnitude and extends deeper into the water column as the wavelength is increased. The influence of waves on unsteady blade loading becomes similar in magnitude to that of velocity shear. Unsteady rotor loads also increase greatly — a doubling of wavelength results in a threefold increase in rotor thrust fluctuations.

- The interaction of the rotor and wave frequencies is also examined. When the difference between these frequencies is small, long-period modulation of the blade loading history is observed. Positive interference between the wave crest and blade position results in increased thrust loading.

6.1.3 Performance of a ducted tidal turbine

- The primary conclusion of this study is that an unducted turbine outperforms a bi-directional ducted turbine in terms of power and efficiency. If a duct is to be designed for a tidal turbine for other reasons, such as alignment of flow and protection of blades, a thin duct profile with slight camber performs best.

- The unducted turbine was found to outperform all of the ducted turbines examined in a comparison at constant blockage. The best-performing ducted device achieves a peak power coefficient of approximately 45% of the unducted device.

- Comparisons of streamtube area, velocity and pressure for the flow through the ducted device show that a duct limits flow expansion downstream of the rotor. The pressure reduction behind the disc and the volumetric flux through the disc are reduced as a result, ultimately limiting the power coefficient of the device.

- Ducted devices undergo a sudden reduction in efficiency when the disc resistance is increased beyond a certain point. At this point, dependent on duct geometry, the flow separates from the leading edge. Kinetic energy is lost to heat through viscous action in the recirculating region that develops outside the duct, resulting in reduced efficiency.

6.2 Future work

Suggestions for future work based on the findings of this thesis are presented in this section.

6.2.1 Full scale rotor model

- This study has highlighted the magnitudes of the unsteady components of blade loading in sheared flow. For example, distributions of shear force and bending moment along a rotor blade over a revolution have been calculated. This data could be used as an input to fatigue calculations for the design of a tidal turbine blade.

- The downstream boundary was located six diameters from the rotor plane. A lower-order rotor model which is less computationally demanding, e.g. an actuator line method, could be used to simulate the rotor. The downstream length of the computational domain could then be increased, and the effect of shear, blockage and yaw on the development of the far wake could be examined.

- The current computational model uses wall functions to model the boundary layers at the rotor surfaces. The effect of this assumption on rotor performance could be examined (assuming the same computational resource) by producing matching axi-symmetric models: one using wall functions and the other with resolved boundary layers. Rotor motion could be simulated using a moving reference frame method.

6.2.2 Waves model

The current model of free surface waves on sheared open channel flow is a new development, and could be improved in many areas.

- Comparisons of a rigid and deforming surface showed that the rotor blades can undergo large fluctuations in torque due to buoyancy. In the field, it is more likely that tidal turbine blades are neutrally-buoyant, and hence such torque fluctuations will not be an issue. Neutrally-buoyant blades could be simulated in the current model by discretising the interior of the rotor geometry and assigning solid material properties to that region. The density of the new solid could be set to that of water.

- Discrepancies in prescribed and observed wave height of 10% – 15% were observed in the simulated wave cases. These could possibly be reduced by increasing the vertical resolution in the vicinity of the free surface.

- Further testing of the wave damping zone at the outlet boundary is required to determine an appropriate length for wave damping. Results from the current study suggest that the length of the damping zone should be increased when higher or longer waves are modelled.

- The current parametric study was limited, in that only three wave conditions were examined. With some improvements to wave resolution and damping, this model could be employed to investigate a much wider range of wave conditions.

Bibliography

Abbot, I. H. and von Doenhoff, A. E. (1959), *Theory of Wing Sections*, Dover, New York.

Adcock, T. A. A., Draper, S., Houlsby, G. T., Borthwick, A. G. L. and Serhadlioglu, S. (2013), 'The available power from tidal stream turbines in the Pentland Firth', *Proc. R. Soc. A* **469**(2157), 20130072.

Afgan, I., McNaughton, J., Rolfo, S., Apsley, D., Stallard, T. and Stansby, P. (2013), 'Turbulent flow and loading on a tidal stream turbine by LES and RANS', *International Journal of Heat and Fluid Flow* **43**(0), 96 – 108.

Airy, G. B. (1841), Tides and waves, *in* H. Rose, ed., 'Encyclopaedia Metropolitana, Mixed Sciences', Vol. 3.

Ammara, I., Leclerc, C. and Masson, C. (2002), 'A viscous three-dimensional differential/actuator-disk method for the aerodynamic analysis of wind farms', *J. Sol. Energy Eng.* **124**(4), 345–356.

ANSYS Inc. (2012*a*), *ANSYS FLUENT 14.5 Theory Guide*, Canonsburg, PA, USA.

ANSYS Inc. (2012*b*), *ANSYS FLUENT 14.5 User's Guide*, Canonsburg, PA, USA.

ANSYS Inc. (2012*c*), *ANSYS ICEM CFD 14.5 User Manual*, Canonsburg, PA, USA.

Atlantis Resources (2014).

URL: *http://atlantisresourcesltd.com*

Atwater, J. F. and Lawrence, G. A. (2010), 'Power potential of a split tidal channel', *Renewable Energy* **35**(2), 329 – 332.

Bahaj, A., Molland, A., Chaplin, J. and Batten, W. (2007), 'Power and thrust measurements of marine current turbines under various hydrodynamic flow conditions in a cavitation tunnel and a towing tank', *Renewable Energy* **32**(3), 407 – 426.

Bai, L., Spence, R. G. and Dudziak, G. (2009), Experimental and computational analysis of a model horizontal axis tidal turbine, *in* 'Proc. 8th European Wave and Tidal Energy Conference, Uppsala, Sweden'.

Batten, W., Bahaj, A., Molland, A. and Chaplin, J. (2008), 'The prediction of the hydrodynamic performance of marine current turbines', *Renewable Energy* **33**(5), 1085 – 1096.

Batten, W. M. J., Harrison, M. E. and Bahaj, A. S. (2013), 'Accuracy of the actuator disc-rans approach for predicting the performance and wake of tidal turbines', *Phil. Trans. R. Soc. A* **371**(20120293).

Belloni, C. (2013), Hydrodynamics of ducted and open-centre tidal turbines, PhD thesis, University of Oxford.

Belloni, C. S., Willden, R. H. and Houlsby, G. T. (2013), 'A numerical analysis of bidirectional ducted tidal turbines in yawed flow', *Marine Technology Society Journal* **47**(4), 23–35.

Betz, A. (1920), 'Das Maximum der theoretisch möglichen Ausnützung des Windes durch Windmotoren', *Zeitschrift für das gesamte Turbinenwesen* **26**, 307–309.

Bradshaw, P., Ferriss, D. H. and Atwell, N. P. (1967), 'Calculation of boundary-layer development using the turbulent energy equation', *Journal of Fluid Mechanics* **28**, 593–616.

Bryden, I. G., Couch, S. J., Owen, A. and Melville, G. (2007), 'Tidal current resource assessment', *Proc. IMechE Part A: J. Power and Energy* **221**(2), 125–135.

Buckland, H. C., Masters, I., Orme, J. A. and Baker, T. (2013), 'Cavitation inception and simulation in blade element momentum theory for modelling tidal stream turbines', *Proceedings of the Institution of Mechanical Engineers, Part A: Journal of Power and Energy* **227**(4), 479–485.

Burton, T., Sharpe, D., Jenkins, N. and Bossanyi, E. (2001), *Wind Energy Handbook*, John Wiley & Sons.

Butterfield, C., Musial, W., Scott, G. and Simms, D. (1992), 'NREL Combined Experimental Final Report — Phase II'. National Renewable Energy Laboratory, Golden, Colarado, USA.

Buvat, C., Martin, V., Menon, J.-M. and Fil, C. (2012), 'Performance of tank tests with physical scale model of horizontal-axis turbine device installed'. Energy Technologies Institute. PerAWaT report WG4 WP1 D4.

Carbon Trust (2011), 'UK Tidal Current Resource and Economics'.
URL: *www.carbontrust.com*

Cebeci, T. and Smith, A. (1974), *Analysis of turbulent boundary layers.*, Academic Press, New York.

Chaudhry, M. H. (2007), *Open-Channel Flow*, Springer.

Churchfield, M. J., Lee, S., Michalakes, J. and Moriarty, P. J. (2012), 'A numerical study of the effects of atmospheric and wake turbulence on wind turbine dynamics', *Journal of Turbulence* p. N14.

Churchfield, M. J., Li, Y. and Moriarty, P. J. (2013), 'A large-eddy simulation study of wake propagation and power production in an array of tidal-current turbines', *Philosophical*

Transactions of the Royal Society A: Mathematical, Physical and Engineering Sciences **371**(1985).

Clean Current Power Systems Inc. (2014).
URL: *www.cleancurrent.com*

Consul, C. A., Willden, R. H. J. and McIntosh, S. C. (2013), 'Blockage effects on the hydrodynamic performance of a marine cross-flow turbine', *Philosophical Transactions of the Royal Society A: Mathematical, Physical and Engineering Sciences* **371**(1985).

Cooley, J. W. and Tukey, J. W. (1965), 'An algorithm for the machine calculation of complex Fourier series', *Math. Comp.* **19**, 297–301.

Courant, R., Friedrichs, K. and Lewy, H. (1928), 'Über die partiellen Differenzengleichungen der mathematischen Physik', *Mathematische Annalen* **100**(1), 32–74.

Cummins, P. F. (2013), 'The extractable power from a split tidal channel: An equivalent circuit analysis', *Renewable Energy* **50**(0), 395 – 401.

Divett, T., Vennell, R. and Stevens, C. (2013), 'Optimization of multiple turbine arrays in a channel with tidally reversing flow by numerical modelling with adaptive mesh', *Phil. Trans. R. Soc. A* **371**(20120251).

Draper, S., Adcock, T. A. A., Borthwick, A. G. L. and Houlsby, G. T. (2014), 'An electrical analogy for the Pentland Firth tidal stream power resource', *Proc. R. Soc. A* **470**(20130207).

Draper, S., Houlsby, G., Oldfield, M. and Borthwick, A. (2010), 'Modelling tidal energy extraction in a depth-averaged coastal domain', *Renewable Power Generation, IET* **4**(6), 545–554.

Draper, S., Stallard, T., Stansby, P., Way, S. and Adcock, T. (2013), Laboratory scale experiments and preliminary modelling to investigate basin scale tidal stream energy extraction, *in* 'Proc. 10th European Wave and Tidal Energy Conference, Aalborg, Denmark'.

EIA (2014), 'Annual Energy Review 2014'. U.S. Energy Information Administration.

Ferrer, E. and Munduate, X. (2007), 'Wind turbine blade tip comparison using CFD', *Journal of Physics: Conference Series* **75**(1), 012005.

Fleming, C. F., McIntosh, S. C. and Willden, R. H. J. (2011), Design and analysis of a bi-directional ducted tidal turbine, *in* 'Proc. 9th European Wave and Tidal Energy Conference, Southampton, UK'.

Fleming, C. F., McIntosh, S. C. and Willden, R. H. J. (2013), Tidal turbine performance in sheared flow, *in* 'Proc. 10th European Wave and Tidal Energy Conference, Aalborg, Denmark'.

Fleming, C. F., McIntosh, S. C., Willden, R. H. J., Stallard, T. and Feng, T. (2013), 'Experimental and computation investigations into ducted porous discs and rotors at low blockage'. Energy Technologies Institute. PerAWaT report WG4 WP3 D3.

Foreman, K. and Gilbert, B. (1983), 'A free jet wind tunnel investigation of DAWT models'. RE-668, SERI/TR 01311-1.

Foreman, K., Maciulaitis, A. and Gilbert, B. (1983), Performance predictions and recent data for advanced DAWT models, *in* 'ASME Solar Energy Division Meeting', p. 10.

Gant, S. and Stallard, T. (2008), Modelling a tidal turbine in unsteady flow, *in* 'Proceedings of the Eighteenth International Offshore and Polar Engineering Conference, Vancouver, BC, Canada'.

Garret, C. and Cummins, P. (2007), 'The efficiency of a turbine in a tidal channel', *Journal of Fluid Mechanics* **588**, 243–251.

Garrett, C. and Cummins, P. (2005), 'The power potential of tidal currents in channels', *Proc. R. Soc. A* **461**, 2563–2572.

Garrett, C. and Cummins, P. (2007), 'The efficiency of a turbine in a tidal channel', *Journal of Fluid Mechanics* **588**, 243–251.

Gómez-Iradi, S., Steijl, R. and Barakos, G. N. (2009), 'Development and validation of a cfd technique for the aerodynamic analysis of hawt', *Journal of Solar Energy Engineering* **131**(3), 031009–031009.

Graham, J. M. R. (1976), 'Turbulent flow past a porous plate', *Journal of Fluid Mechanics* **73**, 565–591.

Gunn, K. and Stock-Williams, C. (2013), 'On validating numerical hydrodynamic models of complex tidal flow', *International Journal of Marine Energy* **3–4**(0), e82 – e97. Special Issue – Selected Papers - EWTEC2013.

Hand, M., Simms, D., Fingersh, L., Jager, D., Cotrell, J., Schreck, S. and Larwood, S. (2001), 'Unsteady Aerodynamics Experiment Phase VI: Wind Tunnel Test Configurations and Available Data Campaigns'. National Renewable Energy Laboratory, Golden, Colarado, USA.

Hansen, J., Sato, M., Ruedy, R., Lo, K., Lea, D. and Medina-Elizade, M. (2006), 'Global temperature change', *Proc. Natl. Acad. Sci.* **103**, 14288–14293.

Hansen, M. O. L., Sorensen, N. N. and Flay, R. G. J. (2000), 'Effect of placing a diffuser around a wind turbine', *Wind Energy* **3**, 207–213.

Houlsby, G., Draper, S. and Oldfield, M. (2008), 'Application of Linear Momentum Actuator Disc Theory to Open Channel Flow'. Report No. OUEL 2296/08.

Hu, D., Hua, O. and Du, Z. (2006), 'A study on stall-delay for horizontal axis wind turbine', *Renewable Energy* **31**(6), 821 – 836.

Hunter, W., Nishino, T. and Willden, R. H. (2013), Investigation of tidal turbine arrays using 3d reynolds-averaged navier-stokes simulations, *in* 'Proc. 10th European Wave and Tidal Energy Conference, Aalborg, Denmark'.

IPCC (2014), Contribution of Working Group III to the Fifth Assessment Report of the

IPCC, *in* 'Climate Change 2014: Mitigation of Climate Change', Intergovernmental Panel on Climate Change.

Jeong, J. and Hussain, F. (1995), 'On the identification of a vortex', *Journal of Fluid Mechanics* **285**, 69–94.

Joukowsky, N. E. (1920), 'Windmill of the NEJ type', *Transactions of the Central Institute for Aero-Hydrodynamics of Moscow* .

Kang, S., Yang, X. and Sotiropoulos, F. (2014), 'On the onset of wake meandering for an axial flow turbine in a turbulent open channel flow', *Journal of Fluid Mechanics* **744**, 376–403.

Kepler Energy Ltd. (2014).
URL: *www.keplerenergy.co.uk*

Lanchester, F. W. (1915), 'A contribution to the theory of propulsion and the screw propeller', *Transactions of the Institution of Naval Architects* **57**, 98–116.

Lissaman, P. (1983), 'Low-reynolds-number airfoils', *Annual Review of Fluid Mechanics* **15**(1), 223–239.

Lunar Energy (2014).
URL: *www.lunarenergy.co.uk*

MacKay, D. J. C. (2009), *Sustainable Energy — Without The Hot Air*, UIT, Cambridge, England.

Malki, R., Masters, I., Williams, A. J. and Croft, T. N. (2014), 'Planning tidal stream turbine array layouts using a coupled blade element momentum – computational fluid dynamics model', *Renewable Energy* **63**(0), 46 – 54.

Marine Current Turbines (2014).
URL: *www.marineturbines.com*

Mason-Jones, A., O'Doherty, D., Morris, C. and O'Doherty, T. (2013), 'Influence of a velocity profile & support structure on tidal stream turbine performance', *Renewable Energy* **52**(0), 23 – 30.

Mason-Jones, A., O'Doherty, D., Morris, C., O'Doherty, T., Byrne, C., Prickett, P., Grosvenor, R., Owen, I., Tedds, S. and Poole, R. (2012), 'Non-dimensional scaling of tidal stream turbines', *Energy* **44**(1), 820 – 829.

McIntosh, S. C., Fleming, C. F. and Willden, R. H. J. (2011), Optimal axial flow tidal turbine design, *in* 'Proc. 9th European Wave and Tidal Energy Conference, Southampton, UK'.

McNaughton, J. (2013), Turbulence modelling in the near-field of an axial flow tidal turbine using *Code_Saturne*, PhD thesis, University of Manchester.

McNaughton, J., Afgan, I., Apsley, D. D., Rolfo, S., Stallard, T. and Stansby, P. K. (2014), 'A simple sliding-mesh interface procedure and its application to the CFD simulation of a tidal-stream turbine', *International Journal for Numerical Methods in Fluids* **74**(4), 250–269.

McSherry, R., Grimwade, J., Jones, I., Mathias, S., Wells, A. and Mateus, A. (2011), 3d cfd modelling of tidal turbine performance with validation against laboratory experiments, *in* 'Proc. 9th European Wave and Tidal Energy Conference, Southampton, UK'.

Menter, F. R. (1994), 'Two-equation eddy-viscosity turbulence models for engineering applications', *AIAA Journal* **32**(8), 1598–1605.

Menter, F. R., Kuntz, M. and Langtry, R. (2003), Ten Years of Industrial Experience with the SST Turbulence Model, *in* 'Turbulence, Heat and Mass Transfer 4', Begell House, CT, USA, pp. 625 – 632.

Menter, F. R., Langtry, R. B., Likki, S. R., Suzen, Y. B., Huang, P. G. and Völker, S. (2004),

'A correlation-based transition model using local variables—part i: Model formulation', *Journal of Turbomachinery* **128**(3), 413–422.

Miley, S. J. (1982), A catalogue of low Reynolds number airfoil data for wind turbine applications, Technical Report RFP-3387 UC-60, Dept. of Aerospace Engineering, Texas A&M University.

Myers, L. and Bahaj, A. (2009), Near wake properties of horizontal axis marine current turbines, *in* 'Proc. 8th European Wave and Tidal Energy Conference, Uppsala, Sweden'.

NASA (2014), "Surface Temperature Analysis", Goddard Institute for Space Studies. Data available from http://data.giss.nasa.gov/gistemp/.

Nezu, I. (2005), 'Open-channel flow turbulence and its research prospect in the 21st century', *Journal of Hydraulic Engineering* **131**(4), 229–246.

Nezu, I. and Rodi, W. (1986), 'Open-channel measurements with a laser doppler anemometer.', *J. Hydraul. Eng.* **112**(5), 335–355.

Nicholls-Lee, R., Turnock, S. and Boyd, S. (2013), 'Application of bend-twist coupled blades for horizontal axis tidal turbines', *Renewable Energy* **50**(0), 541 – 550.

Nishino, T. and Willden, R. H. (2012*a*), 'Effects of 3-D channel blockage and turbulent wake mixing on the limit of power extraction by tidal turbines', *International Journal of Heat and Fluid Flow* **37**(0), 123 – 135.

Nishino, T. and Willden, R. H. J. (2012*b*), 'The efficiency of an array of tidal turbines partially blocking a wide channel', *Journal of Fluid Mechanics* **708**, 596–606.

Nishino, T. and Willden, R. H. J. (2013), 'Two-scale dynamics of flow past a partial cross-stream array of tidal turbines', *Journal of Fluid Mechanics* **730**, 220–244.

NOAA (2014), Trends in atmospheric carbon dioxide, Earth System Research Laboratory, National Oceanic and Atmospheric Administration. Data available from http://www.esrl.noaa.gov/gmd/ccgg/trends/.

Ocean Renewable Power Company (2014).

URL: *www.orpc.co*

O'Doherty, T., Mason-Jones, A., O'Doherty, D. M., Byrne, C. B., Owen, I. and Wang, Y. X. (2009), Experimental and computational analysis of a model horizontal axis tidal turbine, *in* 'Proc. 8th European Wave and Tidal Energy Conference, Uppsala, Sweden'.

OpenHydro Group Ltd. (2014).

URL: *www.openhydro.com*

Patankar, S. V. and Spalding, D. (1972), 'A calculation procedure for heat, mass and momentum transfer in three-dimensional parabolic flows', *Int. J. of Heat and Mass Transfer* **15**(10), 1787–1806.

Petit, J. R., Jouzel, J., Raynaud, D., Barkov, N. I., Barnola, J.-M., Basile, I., Bender, M., Chappellaz, J., Davis, M., Delaygue, G., Delmotte, M., Kotlyakov, V. M., Legrand, M., Lipenkov, V. Y., Lorius, C., Pepin, L., Ritz, C., Saltzman, E. and Stievenard, M. (1999), 'Climate and atmospheric history of the past 420,000 years from the Vostok ice core, Antarctica', *Nature* **399**, 429–436.

Phillips, D. (2003), An investigation on diffuser augmented wind turbine design, PhD thesis, University of Auckland.

Prandtl, L. (1925), 'Bericht über Untersuchungen zur ausgebildeten Turbulenz', *Z. Angew. Math, Meth.* **5**, 136–139.

Prandtl, L. (1945), 'Über ein neues Formelsystem für die ausgebildete Turbulenz', *Nacr. Akad. Wiss. Gottingen, Math-Phys. Kl.* pp. 6–19.

Rawlinson-Smith, R., Bryden, I., Folley, M., Martin, V., Stallard, T., Stock-Williams, C. and Willden, R. (2010), The PerAWaT project: Performance Assessment of Wave and Tidal Array Systems, *in* 'Proc. 3rd International Conference on Ocean Energy, Bilbao, Spain'.

Roache, P. J. (1997), 'Quantification of uncertainty in computational fluid dynamics', *Annu. Rev. Fluid. Mech.* **29**, 123–60.

Roache, P. J. (1998), *Verification and validation in computational science and engineering.*, Hermosa Publishers, New Mexico.

Salas, M. D. (2006), 'Some observations on grid convergence', *Computers & Fluids* **35**, 688–692.

Schlichting, H. (2000), *Boundary Layer Theory*, 8th edn, Springer-Verlag.

Schluntz, J. and Willden, R. H. (2013), The effect of rotor design on the power output of closely packed tidal turbines, *in* 'Proc. 10th European Wave and Tidal Energy Conference, Aalborg, Denmark'.

Schluntz, J. and Willden, R. H. J. (2014), 'An actuator line method with novel blade flow field coupling', *Wind Energy* (under review) .

Schmitt, F. G. (2007), 'About boussinesq's turbulent viscosity hypothesis: historical remarks and a direct evaluation of its validity', *Comptes Rendus MÃl'canique* **335**(9âĂŞ10), 617 – 627. Joseph Boussinesq, a Scientist of bygone days and present times.
URL: *http://www.sciencedirect.com/science/article/pii/S1631072107001386*

Serhadlıoğlu, S., Adcock, T. A., Houlsby, G. T., Draper, S. and Borthwick, A. G. (2013), 'Tidal stream energy resource assessment of the Anglesey Skerries', *International Journal of Marine Energy* **3–4**(0), e98 – e111. Special Issue – Selected Papers - EWTEC2013.

Shives, M. and Crawford, C. (2010), Overall efficiency of ducted tidal current turbines, *in* 'OCEANS 2010', pp. 1–6.

Shives, M. and Crawford, C. (2012), 'Developing an empirical model for ducted tidal

turbine performance using numerical simulation results', *Proceedings of the Institution of Mechanical Engineers, Part A: Journal of Power and Energy* **226**(1), 112–125.

Solomon, S., Qin, D., Manning, M., Chen, Z., Marquis, M., Averyt, K., Tignor, M. and Miller, H. (2007), Contribution of Working Group I to the Fourth Assessment Report of the Intergovernmental Panel on Climate Change, Cambridge University Press.

Sørensen, J. N. and Shen, W. Z. (2002), 'Numerical modeling of wind turbine wakes', *Journal of Fluids Engineering* **124**(2), 393–399.

Sørensen, N. N., Michelsen, J. A. and Schreck, S. (2002), 'Navier-Stokes predictions of the NREL Phase VI rotor in the NASA Ames 80 ft × 120 ft wind tunnel', *Wind Energy* **5**(2-3), 151–169.

Stallard, T., Collings, R., Feng, T. and Whelan, J. (2013), 'Interactions between tidal turbine wakes: experimental study of a group of three-bladed rotors', *Phil. Trans. R. Soc. A* **371**(1985), 20120159.

Sun, X., Chick, J. and Bryden, I. (2008), 'Laboratory-scale simulation of energy extraction from tidal currents', *Renewable Energy* **33**(6), 1267 – 1274.

Tidal Generation Ltd. (2014).
URL: *http://www.alstom.com/power/renewables/ocean-energy/tidal-energy/*

Turnock, S. R., Phillips, A. B., Banks, J. and Nicholls-Lee, R. (2011), 'Modelling tidal current turbine wakes using a coupled RANS-BEMT approach as a tool for analysing power capture of arrays of turbines', *Ocean Engineering* **38**(11-12), 1300 – 1307.

van Kuik, G. A. (2007), 'The Lanchester-Betz-Joukowsky limit', *Wind Energy* **10**(3), 289–291.

Vennell, R. (2010), 'Tuning turbines in a tidal channel', *Journal of Fluid Mechanics* **663**, 253–267.

Vennell, R. (2011), 'Tuning tidal turbines in-concert to maximise farm efficiency', *Journal of Fluid Mechanics* **671**, 587–604.

Verdant Power (2014).

URL: *www.verdantpower.com*

Versteeg, H. K. and Malalasekera, W. (1995), *An Introduction to Computational Fluid Dynamics: The Finite Volume Method*, Pearson Education Ltd.

Viterna, L. A. and Corrigan, R. D. (1981), Fixed pitch rotor performance of large horizontal axis wind turbines, *in* 'DOE/NASA Workshop on Large Horizontal Axis Wind Turbines, Cleveland, OH, USA', pp. 69–85.

Whelan, J. I., Graham, M. R. and Pieró, J. (2009), 'A free-surface and blockage correction for tidal turbines', *J. Fluid Mech.* **624**, 281–291.

Wilcox, D. C. (1994), *Turbulence Modeling for CFD*, DCW Industries, Inc.

Yeung, W. W. H. (2009), 'On pressure invariance, wake width and drag prediction of a bluff body in confined flow', *Journal of Fluid Mechanics* **622**, 321–344.

Yeung, W. W. H. (2010), 'On the Relationships Among Strouhal Number, Pressure Drag, and Separation Pressure for Blocked Bluff-Body Flow', *Journal of Fluids Engineering* **132**(2), 021201–021201.

Youngs, D. L. (1982), Time-dependent multi-material flow with large fluid distortion, *in* K. W. Morton and M. J. Baines, eds, 'Numerical Methods for Fluid Dynamics', Academic Press, New York, pp. 273–285.